UNIVERSITÉ DE STRASBOURG

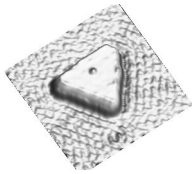

ÉCOLE DOCTORALE DE PHYSIQUE ET CHIMIE-PHYSIQUE

Institut Pluridisciplinaire Hubert CURIEN (IPHC), UMR7178

THÈSE présentée par :

Xitzel SÁNCHEZ CASTRO

soutenue le : **31 mars 2015**

pour obtenir le grade de : **Docteur de l'Université de Strasbourg**

Discipline/ Spécialité : Physique des particules

Production de mésons K^0_S et de baryons Lambda associés à des hadrons chargés de haut p_T dans les collisions Pb-Pb du LHC à $\sqrt{s_{NN}}$ = 2.76 TeV avec l'expérience ALICE

Comparaison entre les processus durs et «soft» liés à la production de hadrons

THÈSE dirigée par :

M. KUHN Christian	Directeur de Recherche, CNRS/IN2P3 - IPHC

RAPPORTEURS :

M. GRANIER DE CASSAGNAC Raphaël	Directeur de Recherche, CNRS/IN2P3 - LLR
Mme. PETERSEN Hannah	Professeur, FIAS

AUTRES MEMBRES DU JURY :

M. BAUDOT Jérôme	Professeur, IPHC
M. CHRISTAKOGLOU Panagiotis	Chercheur, NIKHEF

A Ma. de la Luz†
A mi familia

Acknowledgements

Doing my doctoral studies in a foreign country has been one of the most gratifying, fruitful and challenging experiences in my life. It passed in the blink of an eye. Now that this period has finished, I look back and I see how my doctoral research shaped me while I was shaping it up.

I am deeply grateful to my thesis director Dr. Christian Kuhn that offered me the possibility to be part of the ALICE-Strasbourg group as a doctoral student four years ago, helping me with all the papers and processes of settling in France and who encouraged me during all these years. The results in this dissertation were attainable thanks to all the member of the ALICE-Strasbourg group: Dr. Iouri Belikov who was always there to help me with the coding of my analysis and to discuss the technical and the physics-related questions that I had; Dr. Boris Hippolyte that provided me with his valuable remarks on the importance of my analysis and with all his comments and suggestions on how to improve my plots and presentations; Dr. Antonin Maire that guided me during the approval sessions of the ALICE Collaboration and gave me feedbacks, constructive comments and discussions on the analysis note, the manuscript and the results; Dr. Levente Molnar with whom I had the opportunity to work during my service task and he shared with me his opinions on my presentations and thesis; Dr. Fouad Rami that provided me with his comments and questions during the writing process of my thesis and the preparation of my defence; and Vít Kučera who was always willing to discuss our results and to came up with new questions. Merci à tous pour votre soutien!

Special thanks to the jury members for their comments, questions and discussions about my thesis: Prof. Dr. Jérôme Baudot, Dr. Panagiotis Christakoglou, Dr. Raphaël Granier de Cassagnac and Prof. Dr. Hannah Petersen.

Many thanks to all the people I met in Strasbourg and at CERN with whom I shared incredible working experiences, entertaining chats and unforgettable moments.

También quisiera agradecer enormemente a John P. Ottersbach que fue complice de esta aventura y que, a pesar de estar a más de 500 kilómetros de distancia, siempre me dio su apoyo, atención, comprensión, cariño, consejos y más. Vielen Dank John!

This doctoral research was founded by CNRS and Région Alsace.

Contents

Introduction

Decades of ultra-relativistic heavy-ion collision experiments at different interaction energies (SPS, RHIC and LHC colliders) have proven that strongly-interacting matter at very high energy density does exist in a state where quark and gluon degrees of freedom are liberated (what is usually referred to as the quark-gluon plasma (QGP)). The phase transition between hadronic matter and the QGP has been predicted by lattice quantum chromodynamics to happen at a critical temperature T_c in the range of 145-185 MeV. The initial expectations were that the QGP at high temperature is a weakly-interacting gas of quarks and gluons. Nowadays, comparisons between the experimental measurements and the theoretical models indicate that the QGP is a strongly-coupled plasma, the constituents of which have a very short mean free-path and exhibit a high degree of collective behavior. This state of matter has also been shown to absorb a considerable fraction of the energy of the traversing fast-partons. Theoretical representations of the QGP describe it as a quasi equilibrated medium with a small ratio of shear viscosity to entropy density, hence a nearly perfect liquid.

In ultra-relativistic heavy-ion collisions, a volume with high energy density can be created involving a large number of constituents. It is from this region, which consists of (locally) thermalized matter, that more than 90% of the final produced hadrons, at low and intermediate transverse momentum, originate. According to many observations, it is this bulk of matter (whose hadronization mechanisms and dynamical expansion are subject to strong collective effects) that is believed to be a QGP as long as its temperature is above T_c. The dimensions of this bulk of matter, hence the collective phenomena associated to the QGP, decrease when going from central to peripheral heavy-ion collisions and, at first order, they are supposed to vanish in pp collisions; consequently measurements in pp collisions are used as 'hadronic references'. Nonetheless, recent studies on pp collisions at LHC energies point to a more complex picture of the involved interactions where possible collective effects could develop.

From the inclusive measurements at the LHC, and previously at RHIC, within the intermediate transverse momentum range ($2 < p_{\mathrm{T}} < 6$ GeV/c), an enhancement of the ratio of baryons to mesons ($\Lambda/\mathrm{K}^0_{\mathrm{S}}$ in particular) has been observed in heavy-ion collisions by comparison with the pp measurements. The magnitude of the enhancement diminishes when going from the most central collisions to the most peripheral ones where it vanishes, i.e. the baryon-to-meson ratio becomes compatible to the one measured in pp collisions. At the beginning, these measurements were often interpreted as 'direct' hints that recombination (or coalescence) mechanisms represent a major actor, in competition with parton fragmentation processes, in the hadron formation scenario, thus evidencing a high level of partonic degrees of freedom in the created medium. Today, without supporting one particular explanation, these features suggest at least

that the baryon-to-meson ratio enhancement is a bulk effect produced by collective phenomena in the hadronization mechanisms and in the expansion dynamics (radial flow) of the QGP.

The aim of this dissertation is to validate this hypothesis experimentally, and furthermore to examine if other phenomena, not related to the collective behavior of the bulk but rather to a modification of the hard processes between partons and of the parton fragmentation mechanisms in the medium, may also contribute to the baryon-to-meson enhancement. To achieve this goal, differential measurements are needed and performed in this work by means of two-hadron angular correlations. With this method, in principle, it is possible to disentangle the hadrons produced from hard-parton scattering by parton fragmentation from the ones emerging from the bulk. The hadrons from the first category are selected by associating their emission to the one of a high-p_{T} particle (named *trigger particle*). This energetic trigger particle is expected to be part of a 'jet' of collimated hadrons originated from a hard-parton scattering. Thus the emission direction of the *associated particles* has to be within a given range of azimuthal angle and pseudo-rapidity in the vicinity of the emission direction of the trigger particle. The hadrons coming from the bulk are the ones whose emission direction is far away from the one of any high-p_{T} particle.

The present dissertation work is based on the analysis of Pb–Pb data provided by the LHC at $\sqrt{s_{\mathrm{NN}}} = 2.76$ TeV and recorded with ALICE (A Large Ion Collider Experiment) in 2011. The two-hadron correlation distributions are constructed with charged primary particles ($5 < p_{\mathrm{T}} < 10$ GeV/c) as trigger particles, and the $\mathrm{K}^0_{\mathrm{S}}$ and Λ strange hadrons in the range $2 < p_{\mathrm{T}} < 7$ GeV/c as associated particles. $\mathrm{K}^0_{\mathrm{S}}$ and Λ are selected for these investigations because they can be measured over a wide p_{T} range thanks to the topological reconstruction of their weak decay. Results on the $\Lambda/\mathrm{K}^0_{\mathrm{S}}$, related to the bulk matter and to the production by parton fragmentation, will be presented for different intervals of centrality of the collision (0-10% and 20-40% centrality classes). They will be compared to inclusive measurements performed for Pb–Pb and pp collisions with ALICE as well as to results obtained by CDF in jet samples of $\mathrm{p\overline{p}}$ collisions.

In the first Chapter of the thesis, the theoretical background related to quantum chromodynamics, heavy-ion collisions and the quark-gluon plasma, as well as the experimentally observed baryon-to-meson enhancement will be introduced. In Chapter 2, the ALICE detector and the main subsystems involved in the analysis will be briefly described. Chapter 3 concerns the description of the selections applied in order to perform the two-hadron angular correlations, as well as the various steps and corrections used to construct these correlations. Chapter 4 contains the main results of the data analysis (the yield per trigger of the associated $\mathrm{K}^0_{\mathrm{S}}$ and Λ, in the bulk and the near-side peak regions, and the corresponding $\Lambda/\mathrm{K}^0_{\mathrm{S}}$ ratios) and detailed information about the evaluation of the systematic uncertainties. At last, Chapter 5 is devoted to a discussion of the results and followed by a summary of the main conclusions.

1. Quark-gluon plasma: overview and some probes

"On ne voit bien qu'avec le coeur.
L'essentiel est invisible pour les yeux."
Antoine de Saint-Exupéry

The quantum chromodynamics theory predicts that under extreme temperatures and densities, the hadronic matter can undergo a phase transition to a plasma of quasi-free quarks and gluons, a state which could have existed during the first microseconds after the big bang. The corresponding conditions can be recreated in laboratories via heavy-ion collisions provided by high-energy ring accelerators such as, for example, the Large Hadron Collider.
In this first chapter, we briefly review historical developments of high-energy particle physics. Next, we remind the main features of the strong interaction and the quantum chromodynamics theory. Then, we present the QCD phase diagram and discuss its exploration by means of high energy heavy-ion experiments. We also study the evolution of the colliding system before, during and after the creation of the quark-gluon plasma. Finally, in the last section of the chapter, we emphasize the importance of hadronization mechanisms and collective flow effects at play in understanding the origin of the baryon-to-meson enhancement observed in heavy-ion collisions, which is the main subject of this dissertation.

1.1 A brief summary of particle physics

The understanding of our environment and the seek of knowledge have played an important role in the evolution of the human beings. Up to this day, with that abstract comprehension, we have been capable of predicting certain facts and proposing description of the world that surrounds us.
The beginning of particle physics can be traced back to ancient greek philosophers. They developed ideas of the matter, asking questions like: what are the fundamental components of matter? How can they be classified? Is the matter continuous or discontinuous? Around 460 B.C., Democritus and Leucippus, the two founders of ancient atomic theory, proposed the possible existence of smallest indivisible bodies which everything else is composed of: *the atoms*. Moreover, the atoms move in the infinite void and can combine into clusters which form the universe [1].
For centuries, all these ideas remained speculative and were lacking any connection with experiment and practice in general. The subject of the matter's constituents gained a radical boost in 1897 with the discovery of the electron by J. J. Thomson with his experiments on the deflection

of cathode rays by electric and magnetic fields [2, 3]. Based on this, J. J. Thomson proposed a representation of the atomic structure named *plum pudding model*, where neutral-charged atoms were composed of negative charged corpuscles (electrons) permeated throughout a homogeneous mass of positive electricity to balance the charge [4, 5]. Later on, scatterings of α and β particles, performed by Hans Geiger and Ernest Marsden under the direction of Ernest Rutherford, revealed a different description of the atom where the positive charge is concentrated in its centre [6].

During the first years of the 20th century, a new age for Physics began with the foundation and the development of quantum theory. The starting point was the postulate of Max Planck about the quantized electromagnetic energy spectra present in the blackbody radiation[1] [7, 8]. Soon after, in 1905, Albert Einstein confirmed Planck's formulation with the description of the photoelectric effect by assuming "quanta" of energy (*photons*) for the electromagnetic radiation [9]. Then, in 1913, Niels Bohr proposed his atomic model bringing together Rutherford's model with Max Planck's quantum postulate: the electrons are constrained to individual circular orbits around the positive charge. In the model, electrons are allowed to jump from one orbit to another but not to be in between [10].

The enrichment of the formalism of the quantum mechanics continued. In 1925, Wolfgang Pauli proposed the *exclusion principle* where two electrons[2] can not occupy the same quantum state [11]. During the same year, Werner Heisenberg constructed the matrix description of quantum mechanics, and in 1927 his proposition about the *uncertainty principle* set the limits with which the position and velocity of a particle can be simultaneously determined [12]. In 1926, Erwin Schrödinger formulated the representation of the wave function providing thus the possibility to calculate the energy levels of atoms [13]. Later, the relativistic description of quantum mechanics was developed and the prediction of antiparticles was derived with P. A. M. Dirac's equation in 1930 [14, 15]. The existence of the positron was confirmed by Carl D. Anderson only two years later[16]. Many other contributions were made, but their review is beyond the scope of the present thesis.

The great advances of theory of quantum mechanics evolved alongside experimental discoveries. In 1932, James Chadwick found an evidence for neutral particles inside the atom's nucleus which were named *neutrons* [17]. During the same period, the experimental observation of the β-decay of nuclei[3] and the problem of spin-conservation of some nuclei motivated W. Pauli to assume the existence of a massless neutral $^1/_2$–spin particle to explain those phenomena. Later this new particle was called *neutrino* [18]. The first evidence for the existence of the neutrino was obtained in the Savannah River Plant during the 1950's through the *inverse* β-decay reaction [19]. With the studies of cosmic rays and with the development of particle accelerators in 1950's and 1960's many new hadrons were discovered. Some of these particles revealed a strange behavior since they were produced on a short-time scale ($\approx 10^{-23}$ s) and they decayed relatively slowly, motivating the scientific community to propose *strangeness* as a new property to describe these particles [20]. In 1961, Murray Gell-Mann, and independently Yuval Ne'eman, proposed a symmetry scheme based on the unitary group of symmetries SU(3) to classify the recently discovered hadrons, known as the *eightfold way* [21, 22], where *baryons* are arranged in octets and decuplets

[1] With the energy E being a multiple of the quantity h: $E = \nu h$, where ν is the frequency of the electromagnetic radiation.

[2] Later, the exclusion principle was extended to fermions.

[3] The neutron decay ($n \rightarrow p + e^- + \nu$) is behind this process.

whereas *mesons* in octets and singlets [20, 23, 24]. They also included the classification of the hadrons by strangeness and electrical charge.

To improve the classification of hadrons, in 1964, Gell-Mann and George Zweig proposed that baryons and mesons are composed states of *quarks* [25, 26], by then hypothetical particles. Baryons are formed by three quark states and mesons by quark-antiquark states. The quarks belonged to a triplet (*up, down* or *strange*) with $^1/_2$-spin and fractional electrical charge of that of the electron or proton. In 1969, experiments of high-energy inelastic electron-positron scattering, performed at the Stanford Linear Accelerator Center (SLAC), provided the first evidence that protons have an internal structure [27, 28].

However, in the quark model, the Δ^{++} baryon composed by three *up* quarks all with spin $^1/_2$ seemed to violate W. Pauli's exclusion principle. This fact led Oscar Wallace Greenberg to propose a new type of charge carried only by the quarks, the *color charge* with three possible states: *red, blue,* and *green* [29]. In 1965, Moo Young Han and Yoichiro Nambu proposed that the color charge is based on SU(3), introducing 8 gauge vector fields for the "superstrong" interactions responsible for forming baryons and mesons [30]. Posteriori, these gauge vector fields would be known as *gluons*.

The subsequent discoveries of the 20th century were even more interesting. In 1974, the J/Ψ meson was detected almost simultaneously in two laboratories (SLAC and BNL[4]), followed by the possible existence of a fourth quark which was called *charm*. The following years, several baryons and mesons described with charm quark content state were detected providing a strong support to the quark model [20]. A few years after a new heavy meson, the upsilon Υ, was added to the list with the fifth type of quark content named *bottom*[5]. The sixth and last quark, the *top* quark, was detected in proton-antiproton collisions several years later, in 1995, by the CDF and DZero experiments [31, 32] at the Fermi National Accelerator Laboratory (Fermilab).

While developing the theory of the β-decay, it was conjectured that the mediator responsible for this process was of weak interaction. Glashow, Weinberg and Salam constructed a theory (the electroweak theory) with three intermediate vector bosons, two of them being charged ($W^{\pm}$) and one neutral (Z), with predicted masses of 82 ± 2 GeV/c^2 and 92 ± 2 GeV/c^2 [20], respectively. These particles were searched by many experiments at several accelerators, however their discovery became only possible with the achievements in the accelerator technology applied in the proton-antiproton ring accelerator (Super Proton Synchrotron (SPS)) at Organisation européenne pour la recherche nucléaire (CERN) in 1981. It was in January of 1983 that the first results of the $W^{\pm}$ boson were presented publicly by the UA1 and UA2 experiments [33, 34]. Later, in June of the same year, the UA1 experiment made public announcement about the observation of the Z decay [35].

As the technology was improving with time, high-energy physics entered new territories by colliding heavier and heavier accelerated nuclei instead of leptons or hadrons. At the mid-eighties, the SPS ring succeeded in accelerating relatively light nuclei such as oxygen and sulphur aiming at observing for first time a deconfined state of quarks and gluons: the quark-gluon plasma (QGP). However the experiments did not obtain any real evidence of this state of matter predicted by theoreticians. A decade later, with the acceleration of lead beams in the SPS, the first experimental signatures of the quark-gluon plasma were observed [36, 37, 38]. It was shown that

[4]Brookhaven National Laboratory.

[5]Sometimes, it is referred as well as *beauty*.

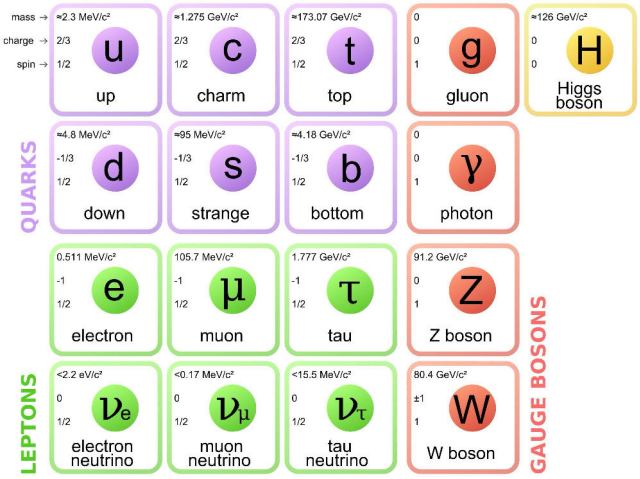

Figure 1.1: Elementary particles in the Standard Model organized by family. Information about its properties (mass, charge and spin) is also included.

at all collision energies the pion/baryon and strangeness/pion ratios indicate saturation with the size of the colliding nuclei and are in quantitative agreement with the calculations made under assumption that a QGP [39]. In 2000, BNL also studied heavy-ion collisions with Au and Cu nuclei at center-of-mass energies per nucleon pair of nucleons of $\sqrt{s_{\mathrm{NN}}} = 200$ GeV. Their observations allowed for the first detailed studies of phenomena related to the creation of hot deconfined matter [40, 41]. The measurements showed a suppression of the the inclusive hadron spectra and two-particle azimuthal correlations at moderate and high-p_{T}, in central RHIC Au–Au collisions, relative to scaled nucleon-nucleon collisions. And in the soft-sector, observations of a strong elliptic flow were in agreement with expectations based on ideal hydrodynamic flow [41].
With the construction of the Large Hadron Collider (LHC), a new frontier of high-energy physics was reached. One of the most recent results, and expected from the last decades, is the observation of the Higgs boson by the ATLAS and CMS collaborations [42, 43]. The public announcement was made at CERN the 4th of July 2012. The Higgs boson could finally complement the general description of the particle interactions and the origins of the particle masses. The LHC at CERN also provided a new record for the hottest state of matter ever created in a laboratory. In October 2010 Pb nuclei were successfully collided at center-of-mass energy of 2.76 TeV, enabling for a better characterization and more precise measurements of the phenomena related to the quark-gluon plasma.

The Standard Model (SM) brings together the quantum field theory and the principles of symmetry provided by the group theory combining electromagnetism, weak and strong forces into a single universal force[6]. It describes the interactions between the gauge bosons (photon, $W^{\pm}$, Z and gluons with spin 1 and the 0-spin Higgs) and the fundamental $^1/_2$–spin fermions (leptons and quarks) [44]. These fundamental constituents are shown in Figure 1.1 with their characteristics of mass, spin and electrical charge. As one can see in the figure, the light up, down and strange quarks have masses below the typical quantum chromodynamics energy scale $\Lambda_{\mathrm{QCD}} \approx 250$ MeV.

[6]The gravitational force turns out to be extremely weak, almost negligible, in comparison with the rest of the interactions at this energy scale, e.g. a factor 10^{-38} with respect to the strong force.

The rest of the quarks (charm, bottom and top) are much heavier. In fact, hadron masses are much larger than the sum of the masses of constituent quarks within them. The largest fraction of hadron masses is thus generated by the strong color field binding the partons together [45].

1.2 Quantum chromodynamics Lagrangian

The strong interaction between gluons and quarks is described by quantum chromodynamics (QCD) that is a non-Abelian $SU(3)_C$ gauge theory based on the color charge.
The invariant form of the QCD Lagrangian is [46]

$$\mathcal{L}_{\text{QCD}} = \sum_f \bar{\Psi}_f \Big(i\gamma^\mu (\partial_\mu - i g_s \frac{\lambda^a}{2} A^a_\mu) - m_f \Big) \Psi_f - \frac{1}{4} Tr[G^{\mu\nu} G_{\mu\nu}], \tag{1.1}$$

here, g_s is the dimensionless gauge coupling constant of the strong interaction. G_μ are the eight different colored field strength tensors expressed as [47]

$$G^a_{\mu\nu} = \partial_\mu A^a_\nu - \partial_\nu A^a_\mu - g_s f^{abc} A^b_\mu A^c_\nu \tag{1.2}$$

In the relation 1.1, the factor $\frac{1}{2}\lambda^a$ $(a = 1, 2, ..., 8)$ denotes the generators of the fundamental representation of the $SU(3)_C$ algebra. The matrices are traceless and satisfy the commutation relations:

$$\Big[\frac{\lambda^a}{2}, \frac{\lambda^b}{2} \Big] = i f^{abc} \frac{\lambda^c}{2} \tag{1.3}$$

with f^{abc} the $SU(3)_C$ structure constants, which are real and totally antisymmetric.
Under local $SU(3)_C$ transformation $\theta_a(x)$, the quark and the gluon field transforms as [48]:

$$\Psi^\alpha_f \rightarrow \Psi^\alpha_f + i \Big(\frac{\lambda^a}{2} \Big)_{\alpha\beta} \delta\theta_a(x) \Psi^\beta_f \tag{1.4}$$

$$G^a_\mu \rightarrow G^a_\mu + \frac{1}{g_s} \partial_\mu \big(\delta_a(x) \big) - f^{abc} \delta_b(x) G^c_\mu \tag{1.5}$$

Expanding the terms 1.4 and 1.5 in the expression 1.1 of the QCD Lagrangian, one obtains terms of the gluon self-interactions in cubic and quadratic contributions [47, 48] reflecting the non-Abelian nature of QCD. This feature results in an interesting observation that we will be discussed in the next section.

1.3 Asymptotic freedom

In early 1970's, David J. Gross worked together with Frank Wilczek on the β-function for the Yang-Mills theory that would relate to the effective coupling constant α_s as:

$$\frac{\partial \alpha_s(Q^2)}{\partial \ln(Q^2)} = \beta \Big(\alpha_s(Q^2) \Big) \tag{1.6}$$

Simultaneously, Hugh David Politzer performed similar theoretical studies. Since QCD is a non-Abelian theory, gluons can interact with themselves through the color charge. As an important consequence, the strong interaction requires higher order corrections to be taken into account in calculations based on any perturbative approach. The corresponding studies led to the discovery

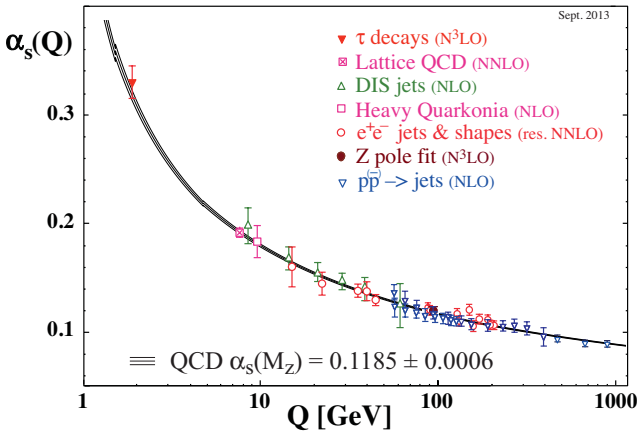

Figure 1.2: Summary of measurements of the strong coupling α_s as a function of the energy scale Q [46, 50].

that QCD is an asymptotically free theory [49].
The coupling g_s is a parameter in the QCD Lagrangian depending on the mass scale μ and it is related to the effective coupling constant as:

$$\alpha_s = \frac{g_s^2}{4\pi} \tag{1.7}$$

When considering a quark-gluon interaction with more than one-gluon exchanges, the theoretical calculations are treated in a perturbative way introducing correction terms of the order of $1/Q^2$, with Q being the momentum transfer in the interaction. In the limit of large momentum transfer, the modification to the coupling constant leads to the correction [20]:

$$\alpha_s(Q^2) = \frac{\alpha_s(\mu^2)}{1 - b_0\,\alpha_s(\mu^2)\ln(Q^2/\mu^2)} \tag{1.8}$$

with $b_0 = \frac{1}{12\pi}(11N_C - 2N_f)$, where N_C is the number of colors and N_f is the number of quark flavors. The first factor of b_0 comes from the anti-screening interactions while the second factor represents the screening loop. For three color charges, b_0 is always positive: $b_0 = 11N_C - 2N_f > 0$.
Considering perturbation theory of first order where the QCD coupling constant is sufficiently small ($\alpha_s \ll 1$) gives

$$\alpha_s(Q^2) \cong \frac{12\pi}{(11N_C - 2N_f)\ln(Q^2/\Lambda^2_{\mathrm{QCD}})} \tag{1.9}$$

where Λ^2_{QCD} is the QCD scale.
From the equation 1.9, the coupling becomes weaker[7] at larger momentum transfer ($Q \to \infty$), that is equivalent to going to shorter distances. This behavior of the coupling is called *asymptotic freedom*.
One remark is needed: at the limit $Q \to \Lambda_{\mathrm{QCD}}$, the expression 1.9 diverges, but this is only because the perturbative approximation for $\alpha_s(Q^2)$ becomes not valid. Complicated interactions

[7] The interaction between quarks vanishes.

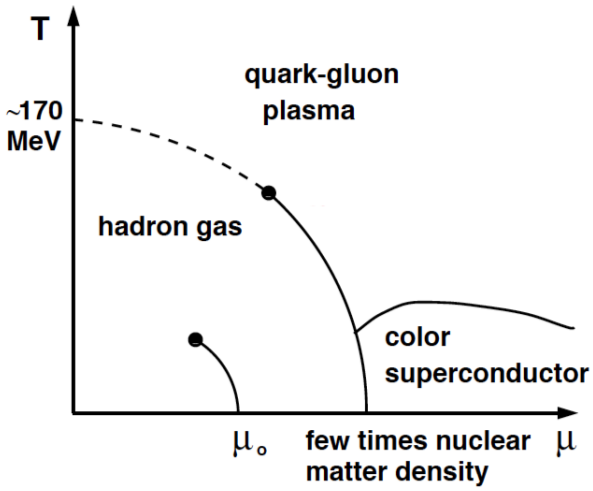

Figure 1.3: Phase diagram of QCD matter [52].

(mainly dominated by gluons) lead to stronger and stronger binding as we pull apart one quark from another: the anti-screening of the gluons overcomes the screening due to quarks, resulting in the growth of the coupling constant as the distance increases [51]. This property of the running coupling leads to the phenomenon of *quark confinement* at large distances.
Measurements of the coupling constant α_s have been performed at different energy scales Q^2 from different scattering processes and reactions using QCD perturbation theory[8], e.g. e^+e^--annihilation, deep inelastic scattering, hadronic τ-decays and others. The experimental results on $\alpha_s(Q)$ are shown in Figure 1.2 [50]. They are in a good agreement with the QCD prediction of asymptotic freedom and confinement.

1.4 QCD phase diagram

The main objective of heavy-ion physics is to explore the QCD phase transitions in different conditions and accessible regions. The diagram representing the various phases of nuclear matter is shown in Figure 1.3 with thermodynamical variables of temperature (T) and net baryon chemical potential (μ).
At low values of μ and high temperatures, the QCD matter enters into a phase corresponding to a state of deconfined quarks and gluons and the restoration of chiral symmetry. This region of the QCD diagram is the place that can be explored with the ultra-relativistic heavy-ion collisions at the LHC. Lattice QCD calculations predict that the system experiences a smooth transition (*crossover*), i.e. without any discontinuity of the order parameters when the critical transition temperature (T_c) is reached [53]. The crossover is driven by the large change in the degrees of freedom from the hadronic phase to the QGP. For the description of the system below and above the critical temperature, it is necessary to determine the corresponding equation of state, which means to describe the pressure (p), energy density (ϵ), trace anomaly ($I = \epsilon - 3p$) and entropy

[8]The processes are based on next-to-leading order (NLO) and next-to-next-to-leading order (NNLO) perturbation QCD.

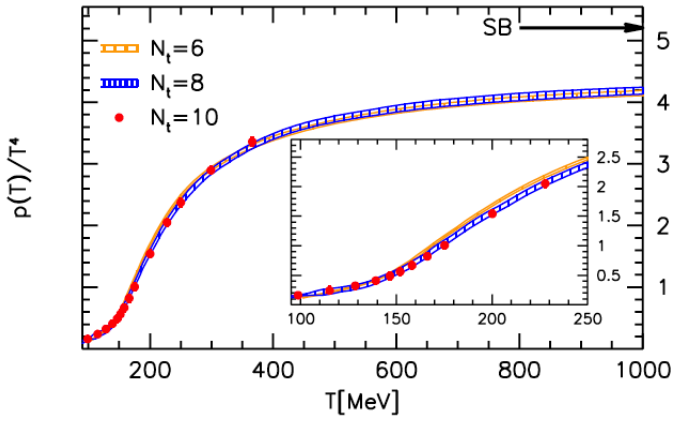

Figure 1.4: Results of lattice QCD about the pressure as function of the temperature, in the region of $\mu \sim 0$, with different lattice spacing (N_t) [64]. The horizontal arrow indicates the limit for the Stephan-Boltzmann pressure.

$(s = (\epsilon + p)/T)$ as a function of temperature and chemical potential [54]. The latest lattice QCD results by the Wuppertal-Budapest collaboration for the pressure normalized by T^4 is shown in Figure 1.4. A clear change in p/T^4 is observed in the temperature range of 145-185 MeV when the liberation of quarks and gluons happens. The results are performed for different lattice spatial sizes indicated by N_t. Another model has predicted a T_c value of 154 ± 9 MeV [55].
The QCD phase diagram contains a critical point that separates the end of the first-order phase transition at high densities from the crossover at low densities and high temperatures. The non-monotonic behavior of μ/T would signal the first order transition of the QCD matter [56]. The low energy program at the Relativistic Heavy Ion Collider (RHIC) named Beam Energy Scan (BES) was proposed to cover the region where this point is expected to lie [57]. The future Facility for Antiproton and Ion Research (FAIR) program will pursue this research to determine the critical point [58]. Other experiments like the Nuclotron-based Ion Collider fAcility (NICA) at the Joint Institute for Nuclear Research (JINR) [59, 60] and the Japan Proton Accelerator Research Complex (J-PARC) at the Japan Atomic Energy Agency (JAEA) [61] could also provide new insights about the critical point. Various model predictions do not locate exactly the critical point but they give a wide range in the phase diagram where it can be found. For further information see reference [56].
As seen in Figure 1.3, more exotic phase transitions in the cold dense matter are predicted to happen in astrophysical phenomena, e.g. in the core of neutron stars. One of the predicted states of matter is the Color Superconductor. It is created when the baryon density is high and quarks at the QCD ground state condensate to form Cooper pairs [61, 62, 63].

1.5 Stages of heavy-ion collisions

In this section we describe the evolution of heavy-ion collisions, from the pre-collision state passing through the quark-gluon plasma phase up to the final-state particles, which are observed

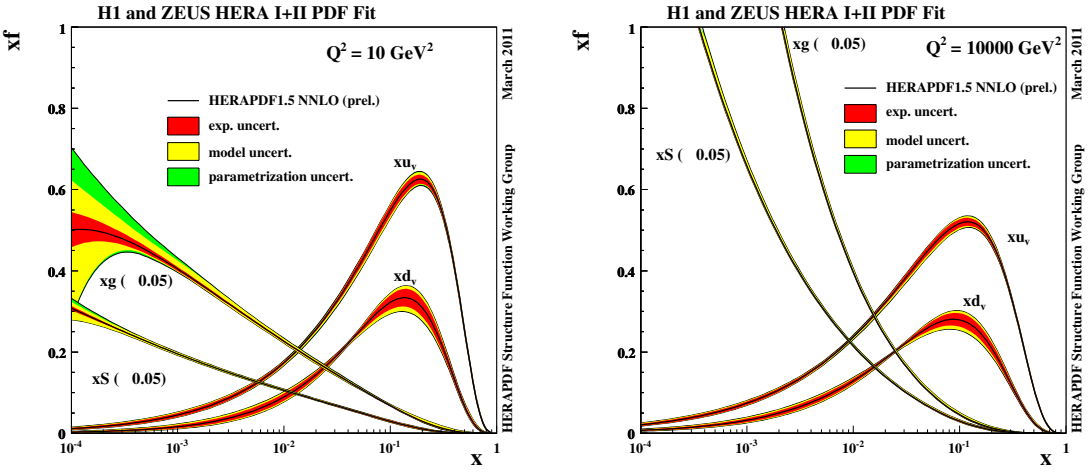

Figure 1.5: Parton distribution functions obtained for two different energy scales. The results are from the analysis of the HERA combined data [66].

experimentally.

Describing the evolution of hadron-hadron collisions has proven to be challenging due to the complexity of its internal structure represented by the parton distribution functions (PDFs). The knowledge of these functions is obtained via deep-inelastic scattering experiments, where the hadron structure is tested with $\mathrm{e} + \mathrm{p} \rightarrow \mathrm{e} + \mathrm{X}$ interactions. In Figure 1.5, the PDFs results from HERA[9] data are shown as function of the Bjorken x-factor, for different factorization scales. The measurements are of a high precision for the low-x sea quarks and gluons [65].

Prior a hadron-hadron (heavy-ion) collision, inside a proton (nucleon), virtual partons can be generated via gluon-gluon interactions. These virtual partons have energies and momenta of the order of Λ_{QCD} in the reference frame, consequently having a time scale magnitude about $\tau \sim 1/\Lambda_{\mathrm{QCD}}$. In high-energy colliders, hadrons (nuclei) are accelerated ($\gamma \gg 1$) boosting the virtual partons to a time scale $\sim \gamma/\Lambda_{\mathrm{QCD}}$ which is larger than the times of the collision process. Therefore, these virtual partons are separated from the vacuum in the boosted frame and can eventually participate during the collision [67].

Additionally, in perturbative QCD, parton evolution proceeds via bremsstrahlung favoring the emission of soft and collinear gluons, i.e. $x \gg 1$ and relative small $k_\perp$[10] [67]. The emitted virtual partons can also radiate gluons again and again with smaller longitudinal momentum fractions than the accelerated hadrons (nucleons) and which occupy approximately the same transverse size than the parent parton. This process increases the number of soft gluons (small x) at a fixed Q^2. In heavy-ion collisions, the former mechanism is more important than in hadron-hadron collisions due to the large number of nucleons in the nuclei. However, the gluon distribution in a QCD bound state cannot continuously grow at small Bjorken x without violating unitarity.

[9] In an attempt to improve the PDFs, the H1 and ZEUS measurements have been combined.

[10] The probability of the bremsstrahlung emission is:

$$\mathrm{d}P_{\mathrm{Brem}} \simeq C_R \frac{\alpha_s(k_\perp^2)}{\pi^2} \frac{\mathrm{d}^2 k_\perp}{k_\perp^2} \frac{\mathrm{d}x}{x}$$

having two singularities when $k_\perp \rightarrow 0$ and $x \rightarrow 0$, enhancing the gluon emission at small $k_\perp$ and/or x [67].

At some point, the gluon fusion will balance the growth. The scale at which the probability of gluon interactions in the nucleus wave function becomes of the order of unity determines the saturation scale Q_s which is theoretically described by the color glass condensate (CGC) formalism [67, 68, 69].

At ultra-relativistic energies, the nuclei are affected by the Lorentz-contraction with a factor $\gamma \sim 100$ along the longitudinal direction. As already explained in this section, at the low values of the Bjorken x-factor, the parton distribution functions of a nucleon are dominated by virtual gluon production (see Figure 1.5). Therefore the initial state of the collision can be seen as a gluon-saturated medium where $k_\perp = 2$ GeV for gluons with $x = 10^{-4}$ in the nucleus [67].

Immediately after the collision, the dominant interactions are the hard parton scatterings which involve large momentum transfer about $Q^2 \sim p_\perp^2 \gg 1$ GeV^2, consequently their production can be calculated in perturbative QCD. These interactions develop in a relative short time[11] of $\tau_{\text{form}} \simeq \sqrt{Q^2}$. Processes like direct-photon, heavy quark and vector boson production and jets occur during this early stage of the collision.

Around $\tau \sim 0.2$ fm/c, and specially in head-on collisions, the constituents of the large density interaction region rescatter enough for approaching a thermal equilibrium. Thermalization happens at a relative short time about $\tau \sim 1$ fm/c. The state of this thermalized matter with partonic degrees of freedom is known as the quark-gluon plasma. This stage of the heavy-ion collisions is estimated to last up to 8-15 fm/c (for Au–Au at $\sqrt{s_{\text{NN}}} = 200$ GeV, see e.g. [70]).

Assuming the hadronic matter, before the QGP, can be approximated by an ideal gas of massless pions. Then, the pressure and energy density as function of the temperature can be described by Stefan-Boltzmann statistics [71, 72]

$$P_\pi = g_{\text{DOF}} \frac{\pi^2}{90} T^4 \qquad \text{and} \qquad \epsilon_\pi = g_{\text{DOF}} \frac{\pi^2}{30} T^4. \tag{1.10}$$

In the previous expression, the degeneracy factor of the degrees of freedom (DOF) for a gas of pion is $g_{\text{DOF}} = 3$, that accounts for the three charge states of the pion: $\pi^\pm$ and π^0. Using the MIT bag model [73], the corresponding expressions for the quark-gluon plasma are

$$P_{\text{QGP}} = g_{\text{DOF}} \frac{\pi^2}{90} T^4 - B \qquad \text{and} \qquad \epsilon_{\text{QGP}} = g_{\text{DOF}} \frac{\pi^2}{30} T^4 + B, \tag{1.11}$$

where B represents the bag pressure taking into account the difference between the physical vacuum and the ground states of the quarks [72]. During the QGP phase, there is a rapid increase of the numbers of degrees of freedom when the confined partons are liberated. By considering only two flavors and three colors the number of degrees of freedom in the QGP phase is $g_{\text{DOF}} = \left\{ 2 \times 8 \times \frac{7}{8} (3 \times 2 \times 2 \times 2) \right\}$. In the MIT bag model, the temperature at which the transition to partonic degrees of freedom happens when the pion gas pressure equals the QGP pressure, hence $T_c = \left(\frac{45}{17\pi} \right)^{1/4} B^{1/4}$. Considering a bag pressure value of $B^{1/4} \simeq 0.2$ GeV, the critical temperature for the phase transition is $T_c \simeq 150$ MeV [72].

It has been seen the large energy density deposited during the collision is redistributed by the strongly interacting partons. Due to the corresponding thermal pressure, the system expands as a medium with collective behavior.

As the medium is expanding, the temperature of the system decreases. At a certain temperature the partonic medium will hadronize, i.e. the quarks and gluons will be bound together

[11] As it is specified by the uncertainty principle.

again inside hadrons. From theoretical models, the hadronization is expected to occur at the temperature of the order of T_c where the crossover happens.
After hadronization, the medium continues expanding and the hadrons keep rescattering with each other until the *freeze-out* stage where the interactions stop and the hadrons decouple. There exist two kinds of the freeze-out. One where the hadron composition of the system will not change anymore (*chemical freeze-out*), but the kinematic interactions will continue though. The second one takes place at a time ∼20 fm/c, the elastic interactions will stop (*kinetic freeze-out*) and the hadrons will reach the detector.
The kinetic freeze-out temperature can be extracted by fitting the measured transverse momentum spectra. In the frame of the fluid, the expression is

$$\frac{\mathrm{d}N}{2\pi p_{\mathrm{T}}\mathrm{d}p_{\mathrm{T}}\mathrm{d}y} \propto \frac{\mathrm{d}N}{\mathrm{d}y}\exp[m_{\mathrm{T}}\cosh(y-\eta)/T]. \tag{1.12}$$

1.6 Hadronization mechanisms and collective effects

We know that free quarks and gluons can not be observed in nature, but are bound together inside hadrons. The process the quarks and gluons undergo to create hadrons is known as hadronization. In this section, two of such mechanisms will be reviewed: the parton fragmentation and the parton coalescence/recombination (the second one still needs to be confirmed). These hadronization mechanisms as well as the phenomena related to the collective expansion of the medium are important elements to achieve the final goal of this dissertation, since the previous processes are involved in the observed two-hadron correlation features.

1.6.1 Parton fragmentation

A hard-scattering is usually considered as a $2 \to 2$ process between two incoming elementary particles (partons in the case of hadron-hadron or heavy-ion collisions) that generates two outgoing partons with large transverse momenta. These partons will eventually fragment into groups of hadrons moving roughly in the directions of the original partons, forming what is commonly known as *jets of hadrons* [74].
The parton fragmentation is a complex process turning a parton that carries color charge into colorless hadrons produced at relatively low energy scale where the QCD coupling constant is large and the perturbative theory cannot be used anymore [75]. The fragmentation function $D_i^h(z, Q)$ characterizes the probability for a hadron with momentum $\mathbf{p}_h$ to be produced from the parton i and carrying momentum fraction z of the momentum $\mathbf{p}_i$ [75, 76]

$$z \equiv \frac{\mathbf{p}_i \cdot \mathbf{p}_h}{|\mathbf{p}_i|^2}. \tag{1.13}$$

These functions are either extracted from the experimental data, or obtained from parametrized expressions constrained to certain requirements and having parameters determined from data [76]. An usual parametrization for light hadron at an initial scale μ_0 is

$$D_i^h(x, \mu_0^2) = N x^\alpha (1-x)^\beta \Big(1 + \gamma(1-x)^\delta\Big). \tag{1.14}$$

Frequently, the term involving γ and δ is left out. The parameter μ_0 is around 1 GeV^2 for light quarks and gluons and m_Q^2 for heavy quarks [46].

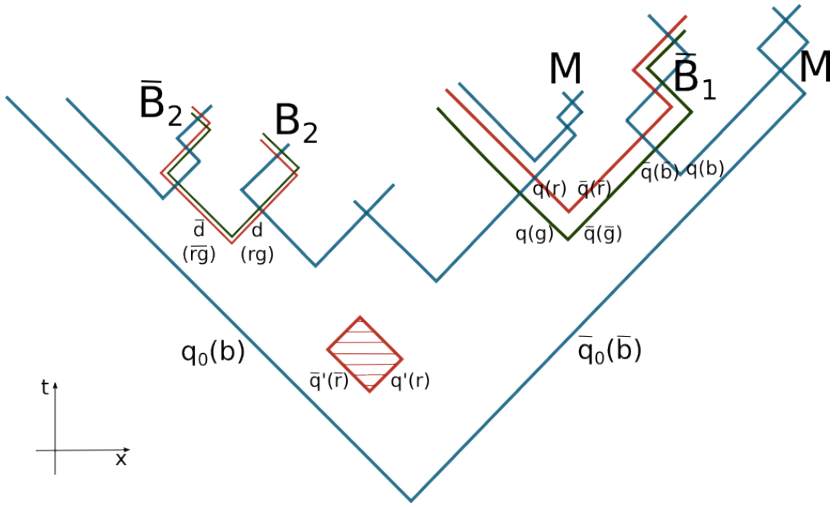

Figure 1.6: Illustration about the string breaking originated form the color field between a quark-antiquark pair. The lines represent the expansion in time-space of the quark with color change (red, blue or green as the representative color of the lines). The stretching of the color field makes it energetically favorable to produce pairs of $q\bar{q}$ and diquarks $d\bar{d}$ (with $d = q_1q_2$). The quarks are further bounded into mesons (M) and baryons (B).

The widely used picture of the non-perturbative parton fragmentation is the mechanism described by the Lund string model where the color binding force between two nearby partons (qg, $q\bar{q}$, gg) is represented as a flux tube. The idea of the color flux tube can be seen as a massless relativistic string with a linear force field [77, 78]. The amount of energy in the string per unit of length is $\kappa = 1$ GeV/fm ≈ 0.2 GeV^2.
In a system with one quark and one antiquark ($q_0\bar{q}_0$), it is assumed that these partons are associated to the end-points of the string, and that (hard) gluons are associated with the energy and momentum carrying *kinks*[12] on the string. In the formed system, in its centre of mass frame, the quark will be moving in the $+z$ direction whereas and the antiquark in the $-z$ one. When pulling apart the pair $q_0\bar{q}_0$ the flux tube is stretched, and consequently there will be a moment when it would become energetically more favorable to break the string and create a new pair of quark-antiquark ($q_1\bar{q}_1$). The breaking of the string is constrained by the energy and momentum contained in the string. In the simplest sketch, the partons will be grouped to form mesons with content $q_0\bar{q}_1$ and $q_1\bar{q}_0$ (see Figure 1.6).
The breaking of the stringlike force-field in the Lund string fragmentation model is a stochastic process. In this way, the probability $\mathcal{M}$ for creating a quark q with transverse mass m_T is

$$|\mathcal{M}|^2 \sim \exp(-\pi\, m_T^2/\kappa) = \exp(-\pi\, m^2/\kappa)\exp(-\pi\, \mathbf{p}_T{}^2/\kappa). \tag{1.15}$$

The created $q\bar{q}$ pair is a distance l apart such that the energy stored in the string is $\kappa l = 2m_T$. Furthermore, the expression 1.15 defines the flavor and the transverse properties of the fragmentation leading to a suppression of heavier flavor production with respect to up and down quarks. For $s\bar{s}$ pair the suppression factor is $\sim \frac{1}{3}$, while for $c\bar{c}$ is $\sim 10^{-11}$ [77].

[12] Curving the string what is supposed to be straight.

The formation of baryons within a jet of hadrons is difficult to model and yet is not completely understood. The Lund model proposes that the baryons are formed after the creation of a diquark-antidiquark (q_1q_2-$\bar{q}_1\bar{q}_2$) pair system, in a similar way as the previously-presented $q\bar{q}$ pair in this section, where the two quarks in the diquark are in a color antitriplet state although not as a fundamental unit [79]. Following this procedure, the baryon ($q_0q_1q_2$) and antibaryon ($\bar{q}_0\bar{q}_1\bar{q}_2$) pairs are always nearest neighbors in rapidity. Additionally, since baryons have a symmetric wave function, the model assumes that the final state of baryons fulfills this requirement by taking into account the probability for different flavor and spin states for the quarks [78]. One of the features of the expression 1.15 is that the probability of baryon creation is less than the one for the meson.
An alternative mechanism for baryon production has been proposed in the string model by means of fluctuations in the color field. The basic assumption is that the confined force field could contain regions where quantum color fluctuations ($q'\bar{q}'$) pops out. The produced fluctuations either could correspond to the "wrong" color state leading to the final annihilation of the $q'\bar{q}'$ pair; or could form the right color state that would allow the pair to survive.
If the original outcoming $q_0\bar{q}_0$ pair encounters the color fluctuation ($q_1\bar{q}_1$) and its color field breaks creating the $q_2\bar{q}_2$ pair within the fluctuation region, then the quark q_2 will be dragged towards the quarks forming the state $q_0q_1q_2$ and $\bar{q}_2$ toward the antiquarks, resulting in a possible baryon-antibaryon production.
If the fluctuation is large in space-time scale, it is possible that an additional quark-antiquark pair is produced inside the fluctuation region. Thus, the baryon and the antibaryon are separated in rapidity by a meson. The Lund fragmentation scheme for baryons, previously described, is usually known as the *popcorn mechanism*.

The hadron production via parton fragmentation is important in colliding systems with a small density of particles created at the final state, e.g. e^+e^- and pp collisions. However, increasing the density of particle in the interacting region, as the one created in heavy-ion collisions, leads to other possible scenarios for hadronization, such as coalescence/recombination models that will be introduced in the next subsection.

1.6.2 Parton coalescence/Recombination model

The parton coalescence or recombination models [80, 81, 82, 83] propose an alternative way for hadron formation in the quark-gluon plasma where the degrees of freedom are partonic. This model aims to describe the hadron spectra and the collective dynamics observed at RHIC energies in Au–Au collisions in a large momentum range from 0 to 5–7 GeV/c.
In the parton coalescence approach, three quarks or one quark-antiquark pair that happen to emerge close each to other in a densely populated phase space can form a baryon or a meson, respectively [84]. In the model, it is assumed that the QGP partons are in local chemical equilibrium and dominate the transverse momentum below a certain p_{T}-threshold, p_0, with the spectra of the thermal partons following a Boltzmann distribution (exponential function) [81]. In the expanding medium expected for heavy-ion collisions, the specific recombination of partons into hadrons would occur in a space-like hypersurface $\sum_{\mathrm{f}}$. In the most simple description of parton coalescence this hypersurface is constant in time. Also, the details of the dynamical process are discarded [80]. The expected number of hadrons h at freeze-out is characterized by

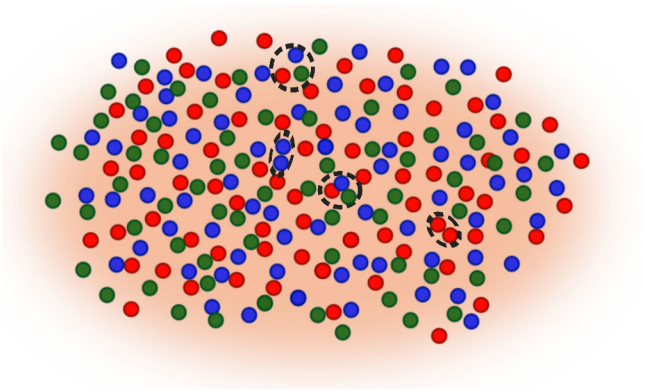

Figure 1.7: Representation of the coalescence mechanism in the hot and dense medium where comoving partons gather to form a meson (quark-antiquark state) or a baryon (three-quarks state).

the density matrix of the parton system on $\sum_{\mathrm{f}}$ as $\hat{\rho}_{\mathrm{f}}$:

$$N_h = \int \frac{\mathrm{d}^3 P}{(2\pi)^3} \langle h; \mathbf{P} | \hat{\rho}_{\mathrm{f}} | h; \mathbf{P} \rangle \tag{1.16}$$

where $|h; \mathbf{P}\rangle$ is the hadron wave function with momentum $\mathbf{P}$.
The information about the hadron bound state is schematically encoded in the phase space distributions for quarks and antiquarks, $w_q(\mathbf{x}, \mathbf{p})$ and $w_{\bar{q}}(\mathbf{x}, \mathbf{p})$, respectively. These distributions are also known as Wigner distribution functions and satisfy the normalization requirement $\int d^3\mathbf{x}\, d^3\mathbf{p}\, w_{q,\bar{q}}(\mathbf{x}, \mathbf{p}) = N_{q,\bar{q}}$ [81]. It is also important to mention that the model neglects space-momentum correlation between partons in the density matrix.
The general form of the transverse momentum spectrum of a meson consisting of $n = 2$ (anti-)quarks can be written as

$$\frac{\mathrm{d}N_{\mathrm{H}}}{\mathrm{d}^2 P_{\mathrm{T}}} = g_{\mathrm{H}} \int \prod_{i=1}^{n} \frac{\mathrm{d}^3 \mathbf{p}_i}{(2\pi)^3 E_i} p_i \cdot \mathrm{d}\sigma_i w_q(x_i, p_i) f_{\mathrm{H}}(x_1 \ldots x_n; p_1 \ldots p_n) \delta^{(2)} \Big(P_{\mathrm{T}} - \sum_{i=1}^{n=2} p_{\mathrm{T},i} \Big). \tag{1.17}$$

The factor g_{H} represents the statistical factor for forming a hadron from colored quarks and antiquarks of spin $^1/_2$ and $\mathrm{d}\sigma$ is the space-like hypersurface. The hadron Wigner function $f_{\mathrm{H}}(x_i; p_i)$ describes the spatial and momentum distribution of quarks in a hadron [85]. The expression 1.17 can be trivially extended for baryons by considering $n = 3$. For simplicity, in the previous relation the quark flavor indices are omitted. Also, it is noticeable in the expression 1.17 that the valence parton transverse momentum[13] sum up to the hadron P_{T}. An illustration of coalescence between partons is given in Figure 1.7.
The Wigner function for a meson considered by Greco *et al.* is

$$f_{\mathrm{M}}(x_1, x_2; p_1, p_2) = \frac{9\pi}{2} \Theta\big(\Delta_x^2 - (x_1 - x_2)^2\big) \Theta\big(\Delta_p^2 - (p_1 - p_2)^2 + (m_1 - m_2)^2\big). \tag{1.18}$$

In the previous expression, Δ_x and Δ_p are the spatial and momentum coalescence radii, considering the hadron is formed in a sphere of radius Δ_x. These two parameters satisfy together the

[13] In this section, we refer the momentum of the hadron with uppercase P, while for the partons with lower case p.

uncertainty relation, $\Delta_x \Delta_p > \hbar$, and are taken to be different for baryons and mesons with values $\Delta_p = 0.45$ GeV and $\Delta_p = 0.24$ GeV [86], respectively. The corresponding Wigner function for the baryon can be found in [81, 86]. It should also be mentioned that the coalescence occurs between collinear partons, i.e., partons moving in the same direction.

In some recombination models, the gluons are not contemplated as partons to hadronize directly but need to convert to $q\bar{q}$ pairs. Thus, only (anti-)quark distributions are considered for the coalescence process [83].

A more complex description of parton coalescence was introduced by allowing the high transverse momentum minijet partons to recombine with the partons from the quark gluon plasma. It was suggested to be essential for understanding the measured inclusive hadron spectra at moderate and high transverse momenta [85]. Compared to the thermal partons, the minijet partons follow a power-law spectrum since they are produced by semihard and hard scatterings.

Greco *et al.* [81] allow small coalescence probabilities of minijet partons with the thermalized partons by weighting them with the large number of lower transverse momentum minijet partons. In contrast, Hwa *et al.* [83, 87, 88] introduce the individual contribution of partons coming from either the thermalized medium ($\mathcal{T}$) or produced in a shower of minijets ($\mathcal{S}$). Under this approach, the meson content combines in the following scheme: $\mathcal{TT} + \mathcal{TS} + (\mathcal{SS})_1 + (\mathcal{SS})_2$, where the subindices in the $\mathcal{SS}$ terms indicate that the two partons are produced in the same shower (index 1) or in separated showers (index 2) emerging from different hard scatterings but nearby hard partons. The authors claim that the $(\mathcal{SS})_2$ term is important only when the density of hard partons is extremely high [83], e.g. at LHC energies [88]. A similar description applies for baryons.

In heavy-ion collisions, the interaction of the fast partons with the dense medium leads to energy loss via the mechanism of gluon bremsstrahlung. For this reason, relatively recent coalescence models consider this effect by using quenched minijet distributions for partons with $p_{\mathrm{T}} > p_0$ in the coalescence process [85] or including a parameter that describes the average fraction of partons that escape from the dense medium and are able to hadronize outside [83, 89]. Additionally Greco *et al.* have suggested the conjecture that adding the fact that the minijet partons can scatter with the thermalized medium, and considering that thermal partons dominate below p_0, then those minijet partons with momentum around p_0 could thermalize with the QGP partons [81].

The coalescence model implementing the considerations mentioned above has been able to qualitatively describe several collective phenomena observed in heavy ion collisions in the intermediate p_{T}-range, such as the hadron spectra, the flavor ordering of the elliptic flow and the baryon-to-meson enhancement (p/π, $\Lambda/\mathrm{K}^0_{\mathrm{S}}$). These phenomena are discussed in the following subsection.

1.6.3 Collective flow

Collectivity in heavy-ion collisions can be observed as the emission of a large number of particles at a common velocity field originated from thermalization phase and the high pressure gradients generated by the dense regions of compressed matter [90].

The study of collective flow provides insights on the evolution of heavy-ion collisions, the properties of the initial state, the creation of the quark-gluon plasma and giving experimental information about the equation of state and the transport properties of the QGP.

The collective flow can be classified into different components. The flow component along the

beam direction, is referred to as *longitudinal flow*, while the component in the plane transverse to the beam is called *transverse flow* or *anisotropic flow* depending on the azimuthal angle.

Transverse flow

The particles created in the thermalized source (*fireball*) can be emitted perpendicularly to the beam direction with a common velocity field which is independent of the azimuthal angle.
The radial transverse expansion that the medium undergoes can be described by hydrodynamics. For this description, the only required assumption is that just before the expansion the medium has reached local thermal equilibrium, i.e. the temperature and the pressure vary slowly in the vicinity around the point.
The initial conditions of the collision imply the initial transverse velocity of the fluid is zero, yet the interactions between particle generate a non-zero acceleration of the fluid. Applying the thermodynamic laws, the acceleration component in the x-axis is [91]

$$\frac{\partial v_x}{\partial t} = -\frac{1}{(\epsilon + P)}\frac{\partial P}{\partial x} = -c_s^2 \frac{\partial \ln s}{\partial x}, \tag{1.19}$$

where v_x is the x-component of the flow velocity, s represent the entropy and c_s is the sound velocity in the fluid, with $c_s = (\partial P/\partial \epsilon)^{1/2}$. The y-component follows a similar relation. The thermal pressure at early times of the expansion is large, hence the pressure gradients. However, from Equation 1.19, the large force $-\nabla \mathbf{P}$ is compensated by the term $\epsilon + P$, resulting into a linear increase of the transverse velocity [91].
Studying the transverse-momentum (or transverse-mass) particle spectra provides information on the collective transverse expansion of the emitting source [90]

$$\frac{\mathrm{d}N}{2\pi\, p_T\, \mathrm{d}p_T\, \mathrm{d}p_z} \propto \exp\Big(\frac{-m_T u_0 + p_T u}{T}\Big). \tag{1.20}$$

If we consider the absence of flow in the medium ($u = 0$ and $u^0 = 1$), all hadron spectra follow the same Boltzmann distribution:

$$\frac{\mathrm{d}N}{2\pi\, p_T\, \mathrm{d}p_T} \propto \exp\Big(-\frac{m_T}{T}\Big), \tag{1.21}$$

thus the kinetical-freeze-out temperature T of the fireball can be immediately extracted. However, since the medium presents an explosive expansion, the quantity T is related to the following factors of the transverse expansion [90]

$$T = T_{\text{thermal}} + m\langle\beta_t\rangle^2, \tag{1.22}$$

where the $\langle\beta_t\rangle$ term is the velocity of the transverse flow.
In the non-relativistic limit, the kinetic energy associated to the collective motion is $mv^2/2$, leading heavier particles to show a larger effective temperature T. This clearly gives a positive contribution to the slope resulting in a flatter momentum spectra, i.e., the larger the inverse slope, the larger the effect due to the collective transverse flow.

Anisotropic flow

In non-central nucleus-nucleus collisions, the overlapping collision region is approximately elliptic. Consequently, the interactions among the constituents of the thermalized medium generate a pressure gradient, transforming the initial coordinate space anisotropy into a momentum anisotropy in the final state (*anisotropic flow*). The initial conditions provide a larger pressure gradient in the direction of the minor axis of the interacting region rather than the major one, causing that particles emitted along that direction acquire larger p_{T} [92]. The hadron rescattering in the final collision phase [93] and/or partonic energy loss[14] [94] can also contribute to the flow components.

Experimentally, the emission of the particles is measured with respect to the reaction plane Ψ_{RP}, formed by the beam axis z and the impact parameter vector. The particle distribution can be written in a form of Fourier series [95] in the plane transverse to the beam direction:

$$E\frac{\mathrm{d}^3N}{\mathrm{d}^3p} = \frac{1}{2\pi}\frac{\mathrm{d}^2N}{p_{\mathrm{T}}\mathrm{d}p_{\mathrm{T}}\mathrm{d}y}(1+\sum_{n=1}2v_n\cos[n(\varphi-\Psi_{\mathrm{RP}})]). \tag{1.23}$$

The v_n terms represent the magnitude of the nth order harmonics. The first term of the Fourier decomposition is named *direct or longitudinal flow* (v_1), the second term is the *elliptic flow* (v_2), while the third one is known as the *triangular flow* (v_3). The v_3 and the higher-order terms are referred as higher harmonics. Although a direct measurement of the reaction plane Ψ_R is not possible, experimental estimations can be extracted from the data. The estimated reaction plane is referred as the event plane. The event flow vector $\mathbf{Q_n} = ((|Q_n|\cos(n\Psi_n), |Q_n|\sin(n\Psi_n)))$ and the event plane angle Ψ_n can be determined independently for each harmonic of the anisotropic flow using the following formulae:

$$\begin{aligned} |Q_n|cos(n\Psi_n) &= \sum_i w_i\cos(n\varphi_i), \\ |Q_n|sin(n\Psi_n) &= \sum_i w_i\sin(n\varphi_i), \end{aligned} \tag{1.24}$$

where the i index goes over all the primary particles in the event, φ_i is the azimuthal angle of the particle i and the weights, w_i, depend to a large extent on the details of the experimental analysis [95].

During the last years, studies of the anisotropic flow at the LHC showed that event-by-event ($\langle v_n\rangle$) fluctuations are significant ingredients of the collision dynamics [96]. Therefore, alternative methods, that eliminate the uncontrolled bias in the measurement introduced by these fluctuations, have been proposed to extract the flow components, e.g., the particle azimuthal correlations known as *cumulant* method [97] or the scalar-product [98, 99, 100] method which differ slightly from the event-plane method.

Experimental results at RHIC energies for Au–Au collisions show a mass ordering of the elliptic flow for low p_{T} values ($p_{\mathrm{T}} < 1$ GeV/c), with smaller v_2 for heavier particles, i.e., $v_2^{\pi} > v_2^{K} > v_2^{p}$ [101, 102]. Qualitatively, this dependence of the particle mass is predicted by hydrodynamical

[14] Partons going into a direction where the interaction zone is less extended will suffer less energy loss.

Figure 1.8: ALICE measurements of the elliptic flow and higher harmonics (v_3 and v_4) for unidentified charged particles as a function of transverse momentum for various centrality classes [106].

calculations [103, 104]. However, for $p_{\mathrm{T}} > 2$ GeV/c, the mass ordering is broken and v_2 presents larger values for baryons than for mesons. It was also observed that, if v_2 and p_{T} are scaled by the number of constituent quarks (n_q) in the hadron, the v_2 for different hadron species becomes similar.

One of the first experimental observations at LHC energies was that the p_{T}-integreated v_2 for inclusive charged particles increases by about 30% compared to RHIC Au–Au collisions at 200 GeV [105]. In addition, the first published measurements of higher harmonic flow (up to n=5) in heavy-ion collisions were obtained with the ALICE detector [106, 107]. Figure 1.8 shows the ALICE results of the p_{T}-dependence v_2, v_3 and v_4 for unidentified charged particles in Pb–Pb collisions at $\sqrt{s_{\mathrm{NN}}} = 2.76$ TeV for different centrality intervals. For very central events (0-5%), the observed v_3 has larger values than the elliptic flow in the p_{T}-interval above 2 GeV/c, while for larger centralities v_2 dominates with respect to the other flow harmonics in all the p_{T}-range. For very central events (0-5%), it is observed that the maximum value for v_3 and v_4 stays almost at the same amplitude. The CMS [108, 109] and ATLAS [110, 111] results on anisotropic flow and also higher harmonics are in agreement with the ALICE results.

Another interesting result was reported in [107] showing that long $\Delta\eta$ correlation (*near-side ridge*) of the two-particle angular distributions (in an interval $0.8 < |\Delta\eta| < 1.8$) can be described with the sum of the contributions from the Fourier harmonics v_n obtained from the particle-pairs. The same conclusion was derived by the ATLAS collaboration within a pseudo-rapidity range of $2 < |\Delta\eta| < 5$ [110].

The constituent quark scaling of the v_2 observed at RHIC energies was tested also at the LHC. Figure 1.9 shows the ALICE results on the elliptic flow parameter scaled to the number of constituent quarks (n_q) for different particles species as a function of the scaled transverse

Figure 1.9: The $(m_T - m_0)/n_q$ dependence of the quark-scaling elliptic flow (v_2/n_q) for identified hadrons for Pb–Pb collisions at $\sqrt{s_{\rm NN}} = 2.76$ TeV in the centrality intervals 0-5% (left panel) and 30-40% (right panel) measured with ALICE [112].

kinetic mass $(m_T - m_0)/n_q$, where $m_T = \sqrt{p_{\rm T}^2 - m_0^2}$ is the transverse mass. This representation is introduced to extend the scaling to low values of transverse momentum. The v_2 values were extracted with the Scalar Product method using a pseudo-rapidity gap of $|\Delta\eta| > 0.9$ for Pb–Pb collisions at $\sqrt{s_{\rm NN}} = 2.76$ TeV [112]. The ALICE data present deviations between the scaled v_2 for different identified particles, suggesting that quark scaling does not hold for LHC energies. In semi-peripheral Pb–Pb collisions, in the interval 30-40% and for $p_{\rm T} > 3$ GeV/c, the scaled v_2 for identified particles tend to merge into two separate groups depending if the hadron is a baryon or a meson [112].
In pPb collisions at $\sqrt{s_{\rm NN}} = 5.02$ TeV, CMS and ATLAS collaborations reported a ridge-like structure in two-hadron angular correlations [113, 114]. More so, using the pPb results, it was also possible to extract anisotropic coefficients, v_n, for charged and identified particles [113, 115]. Furthermore, the azimuthal correlations measured with CMS have been described by the theoretical work of Dusling *et al.* using the CGC model [116].

1.6.4 Baryon-to-meson enhancement

In heavy-ion collisions at RHIC and LHC energies, an enhanced production of baryons compared to mesons has been observed with respect to what is measured in proton-proton (pp) collisions at similar or even higher collision energy. This occurs in the $p_{\rm T}$ range from 2 up to ∼6 GeV/c [117, 118, 119, 120]. This phenomenon is illustrated with the ALICE results of $\Lambda/{\rm K}^0_{\rm S}$ in Pb–Pb collisions at LHC energies are shown in Figure 1.10. At $p_{\rm T} \sim 3$ GeV/c, this ratio is about 3 times larger in central Pb–Pb collisions as compared to the pp result. Moreover, the magnitude of the peak of the $p_{\rm T}$-differential $\Lambda/{\rm K}^0_{\rm S}$ decreases with the centrality of the collision, reaching a value for the most peripheral collision (80-90%) equivalent to that of pp collisions. Due to the fact this effect is the highest in the most central Pb–Pb collisions, where the largest bulk of matter is created and which is not present in pp collisions, these observations have been interpreted as the results of the collective nature of the hadronization processes and the dynamical expansion of the bulk.

Figure 1.10: $\Lambda/\mathrm{K}^0_\mathrm{S}$ ratio measured by ALICE in Pb–Pb collision at $\sqrt{s_{\mathrm{NN}}} = 2.76$ TeV for different centrality intervals [117]. Results from pp collisions are also plotted for comparison.

In [117], comparisons of the ALICE result with the $\Lambda(\overline{\Lambda})/\mathrm{K}^0_\mathrm{S}$ from the STAR experiment are presented. It can be clearly seen that the $\Lambda/\mathrm{K}^0_\mathrm{S}$ ratio at LHC energies peaks at ∼3 GeV/c for central collisions, whereas the peak in Au–Au collisions is located at lower p_T of about 2 GeV/c. This feature is seen for different centrality selections. This shift in the position of the maximum is in qualitative agreement with the increase of the radial flow at larger collision energies [121, 122]. Several models have been proposed to explain such a baryon-to-meson enhancement, but none relies on a single mechanism. Instead, these models generally include an interplay between various particle production mechanisms to describe the enhancement.

In a pure hydrodynamics picture, the baryon-to-meson enhancement originates from the mass-dependent ordering of the flow. Baryons, being heavier particles than mesons, receive larger flow contribution to their momenta and are therefore relocated to higher p_T compared with mesons. For the $\Lambda/\mathrm{K}^0_\mathrm{S}$ ratio in Pb–Pb collisions, hydrodynamics only describes data in a small (at low) p_T range. Around 2 GeV/c, the curve of the hydrodynamics model starts deviating from data [117]; the predicted values continue increasing at higher p_T, which is not seen for the experimental data. As already discussed in previous sections of this chapter, the hadrons produced by a hard scattering, in the intermediate and high-p_T region, decouple from the medium at early times during the collision, and so the hydrodynamical expansion does not substantially affect these hadrons anymore. As a consequence, the baryon-to-meson ratio is expected to reach a maximum value then decrease as the p_T of the hadrons increases, reproducing thus the experimentally observed trend.

Within the coalescence/recombination approach, the baryon-to-meson enhancement could be interpreted as the consequence of the exponential shape of the p_T distribution of partons in the quark-gluon plasma [84, 86]. As explained in subsection 1.6.2, when the partonic degrees of freedom become dominant, the kinematical properties of the formed hadrons are built as

the sum of those of the valence quarks. As a result, a meson with transverse momentum p_{T} originates from partons with an average transverse momentum of about $p_{\mathrm{T}}/2$, while baryons of the same momentum p_{T} are produced out of partons from a considerably more populated kinematical region around $p_{\mathrm{T}}/3$ [84]. Thus, the relative production of baryons with respect to mesons becomes larger for that p_{T}-range. At high transverse momenta, coalescence would cease to be the dominant hadronization mechanism and the production by parton fragmentation takes over. Consequently, the interplay between these two hadronization mechanisms would result in a peak of the baryon-to-meson ratio as function of p_{T}.
Theoretical results on $\overline{\mathrm{p}}/\pi^-$ [81] were obtained for RHIC energies by calculating separately the hadron spectrum under two different assumptions, either having contributions from thermal partons and hadrons from independent fragmentation of partons originating from minijets, or allowing also the coalescence between these two classes of partons. The latter contribution showed to enhance the ratio significantly, with a good description of the PHENIX data [123]. In [80], the results from the model of Greco *et al.* applied to the STAR results of $\Lambda/2\mathrm{K}^0_{\mathrm{S}}$ show a good qualitative agreement with the data. The theoretical results by Fries *et al.* are also included in the comparison [80]: under this coalescence approach the baryon-to-meson p_{T}-dependence reproduces the peak, but the calculation overestimates the data of $\Lambda/2\mathrm{K}^0_{\mathrm{S}}$.
Further, the STAR results on $\Lambda/\mathrm{K}^0_{\mathrm{S}}$ and Ω/ϕ were compared to the recombination approach proposed by Hwa *et al.* [87]. The recombination curves reproduce the ratio at low p_{T} and bear the shape of the baryon-to-meson enhancement whereas the peak is obtained at larger transverse momentum values than for experimental data. Recently, the description for the ALICE data on p/π^+ and $\Lambda/\mathrm{K}^0_{\mathrm{S}}$ for the 0-5% centrality selection in Pb–Pb collisions was published [89]. However, these results seem to describe only the experimental p/π^+ for a small p_{T}-range (between 1 and 2 GeV/c), and do not agree with the ratio measured for strange hadrons.
In addition to the bulk-matter and jet production, the event generator EPOS2.17v3 takes into account the interactions between the jet hadrons and the transverse fluid [124]. The key elements of the model are the flux tubes (associated to pomeron exchanges and being mainly longitudinal) that moves transversely to the collision axis. The idea of flux tubes comes from the string fragmentation picture. The flux tubes increase substantially the amount of multiple interactions between the incoming particles taking part in the collision [125]. The scenario becomes more complicated for heavy-ion collisions.
To describe the baryon-to-meson enhancement, the EPOS model introduces the concept of the string segment[15]. EPOS2.17v3 includes three scenarios for the evolution of the string segment depending on its energy [124, 125]:

1. Without enough energy to escape out of the medium, the string will evolve hydrodynamically and will eventually hadronize as soft hadrons.

2. With sufficient energy, it will escape out of the bulk and will be observed as a jet.

3. The string could be produced inside the medium, or near the surface, carrying as much energy as necessary to appear as a jet. However, in the process of going through the medium, the string will be affected by the flow. The later situation will push more Λ than the kaons, giving it additional momentum.

[15] These segments are produced when the flux tube breaks.

Figure 1.11: $\Lambda/\mathrm{K}^0_\mathrm{S}$ ratio obtained with the ALICE experiment in p–Pb collisions at $\sqrt{s_\mathrm{NN}} = 5.02$ TeV (left panel) and in Pb–Pb collisions at $\sqrt{s_\mathrm{NN}} = 2.76$ TeV (right panel). The results are presented for two multiplicity (centrality) classes for p–Pb (Pb–Pb) collisions [128].

The EPOS2.17v3 has provided the best description of the $\Lambda/\mathrm{K}^0_\mathrm{S}$ results from the ALICE collaboration [124] at different centralities ranges. The position in p_T and the value of the $\Lambda/\mathrm{K}^0_\mathrm{S}$ maximum are the same as in the Pb–Pb data.

Another Monte Carlo model, HIJING/BB2.0 proposes alternative mechanisms leading to the baryon-to-meson enhancement [126]. The model is based on a two component geometrical model of minijet production and soft interactions, incorporating nuclear modification of the parton distribution functions and jet-quenching. In this model, the baryon-to-meson enhancement is attributed to new transport dynamics of the topological field configurations. The origin of this phenomenon is related to the interplay of the strong longitudinal color fields created by the saturation scale of multiple longitudinal flux tube overlapping in combination with dynamical baryon junctions and gluon loops.

HIJING/BB2.0 results for $\overline{\mathrm{p}}/\pi^-$ and p/π^+ ratios for central (0-12%) Au–Au collisions at $\sqrt{s_\mathrm{NN}} =$ 200 GeV/c are published in [126]. The results on $\overline{\mathrm{p}}/\pi^-$ provided a good description of the STAR data up to high-p_T. However, the model overestimates p/π^+ above $p_\mathrm{T} > 3$ GeV/c. The same model tries to reproduce the $\overline{\mathrm{p}}/\pi^-$ and $(\Lambda + \overline{\Lambda})/2\mathrm{K}^0_\mathrm{S}$ for central (0-5%) and peripheral (70-80%) Pb–Pb collisions at the LHC energies [117]. But, these calculations noticeably overestimate the experimental results on $(\mathrm{p}+\overline{\mathrm{p}})/(\pi^+ + \pi^-)$ and $\Lambda/\mathrm{K}^0_\mathrm{S}$ obtained by ALICE.

In the proposed model of Sapeta *et al.* [127], the baryon-to-meson enhancement has contribution from medium modification of the jet hadrochemistry on top of the contribution from coalescence and parton fragmentation mechanisms. These two latter elements are the underlying events (background composition) of the event. The in-medium modification of the parton fragmentation manifests itself as a consequence of an increase of the probability of parton splitting, affecting thus the distribution of the invariant mass of partons at the end of the parton shower. The results

lead to an increase of soft particles and also to the modification of the hadron composition within the quenched jet where heavier hadrons become more abundant. In [127], it is found that the particle ratios, especially the $\mathrm{p}(\overline{\mathrm{p}})/\pi^{\pm}$, show to be significantly enhanced at high-p_{T} ($p_{\mathrm{T}} > 5$ GeV/c) in the calculations with in-medium modified jets with respect to those considering only vacuum jets. In summary, the increase of the parton-splitting probability leads to a baryon-to-meson enhancement at high-p_{T} values.
To complete the overview of the baryon-to-meson enhancement phenomenon, let us mention that the ALICE $\Lambda/\mathrm{K}^0_{\mathrm{S}}$ result in the largest multiplicity class obtained for p–Pb collisions at $\sqrt{s_{\mathrm{NN}}} = 5.02$ TeV also exhibits an enhancement with respect to smaller multiplicity events for the same collision system [128]. Figure 1.11 shows the $\Lambda/\mathrm{K}^0_{\mathrm{S}}$ ratios for p–Pb and Pb–Pb collisions at LHC energies. It is interesting to note that the position of the maximum of the $\Lambda/\mathrm{K}^0_{\mathrm{S}}$ ratio is located at the same p_{T} of about 3 GeV/c as in most central Pb–Pb collisions, despite the fact that the amplitude of the maximum is smaller. This could imply two possible interpretations: either p–Pb collision system at LHC energies approaches somehow a thermalized state comparable to that in heavy-ion collisions, or the baryon-meson enhancement in Pb–Pb contains contributions from cold nuclear matter effects and/or from fluctuations associated to the initial state.

1.7 Purpose of the present dissertation

The baryon-to-meson enhancement has shown to be a very interesting phenomenon with many possible theoretical interpretations about its origins. A priori, this effect is thought to be related to collective phenomena in the bulk, as mentioned before in section 1.6.4. Therefore, the fundamental question is to know whether this effect could also arise partially from a modification of the hard-processes and of the parton fragmentation mechanism inside the bulk.
To validate these hypotheses, this doctoral work addresses the origin of the baryon-to-meson enhancement by separating the hadrons ($\mathrm{K}^0_{\mathrm{S}}$ and Λ) produced in association with parton fragmentation (and therefore correlated with high-p_{T} particles) from those emerging from the thermalized phase (see Figure 1.12). The investigation procedure is based on the construction of the two-hadron angular correlation distributions, in φ and η, using charged high-p_{T} particles as trigger particles and $\mathrm{K}^0_{\mathrm{S}}$ and Λ hadrons as the associated particles. Our purpose will be achieved by obtaining the $\Lambda/\mathrm{K}^0_{\mathrm{S}}$ ratio of the particles produced in correlation with charged high-p_{T} particles coming from hard-parton scatterings, and comparing it to the $\Lambda/\mathrm{K}^0_{\mathrm{S}}$ ratio related to the particles emerging from the bulk. The details about the techniques to follow and selections to apply will be described along the next chapters.

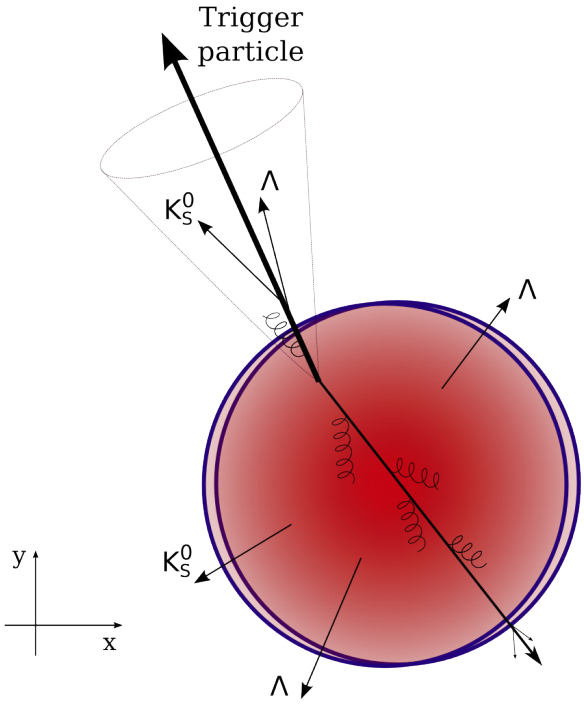

Figure 1.12: Illustration of the production of K^0_S and Λ in correlation to a hard-parton scattering (described by the long arrows). The representation of the hadrons emerging from the bulk of matter is also included. The collision between two heavy-ions (represented by the circles) is seen in the transverse plane with respect to the beam direction.

2. ALICE: key to wonderland

"Mira las cosas que se van, recuérdalas,
porque no volverás a verlas nunca."
José Emilio Pacheco

During the last decades we have witnessed outstanding advances in particle physics emerging from collider experiments. These new results have only become possible due to highly optimized detector designs. As mentioned before, the goal of ultra-relativistic heavy-ion collisions is to study the phenomena related to the quark-gluon plasma, and the ALICE detector is playing a key role in this research field.
The Large Hadron Collider and the ALICE detector will be presented in this chapter. We will review in detail the main ALICE subsystems involved in the trigger selection, track and vertex reconstruction used for the analysis presented in this thesis.

2.1 The Large Hadron Collider

The Large Hadron Collider was placed in the 27-km-long and 100-meters-underground tunnel that was constructed for the former Large Electron-Positron Collider (LEP) at CERN, located on the Franco-Swiss border. The accelerator consists of two rings where the beams are kept in orbit by superconducting electromagnets, traveling in opposite directions and passing eight crossing points as possible interactions regions. The four largest LHC experiments (ALICE, ATLAS, CMS and LHCb) are located at four of the eight interactions points [129] (see Figure 2.1). There are also other smaller experiments (TOTEM, LHCf, MoEDAL).
The purpose of the LHC is to collide proton-proton and light and heavy (such as Pb) ion beams at unprecedented energies and luminosities to achieve frontier research in high-energy physics. In proton-proton collisions one of the goals was to observe for the first time the Higgs boson [42, 43] and characterize its properties, and to search for signs of new physics beyond the Standard Model. The Pb–Pb collisions are meant for the characterization of the hot and dense QCD matter (quark-gluon plasma).
A large luminosity, required for the physics goals at the LHC, is provided by high number of particles per bunch and a large quantity of bunches. The latter is determined by the machine radio-frequency (RF) cavities that operate at 400 MHz with a nominal space between bunches of 25 ns. Thus, the filling scheme of the LHC can provide a large number of buckets per beam (up to 35640 buckets) with 3564 bunches. However, because of restrictions in the beam injection, the synchronization on the beam dump gap and other machine operation conditions [130], the

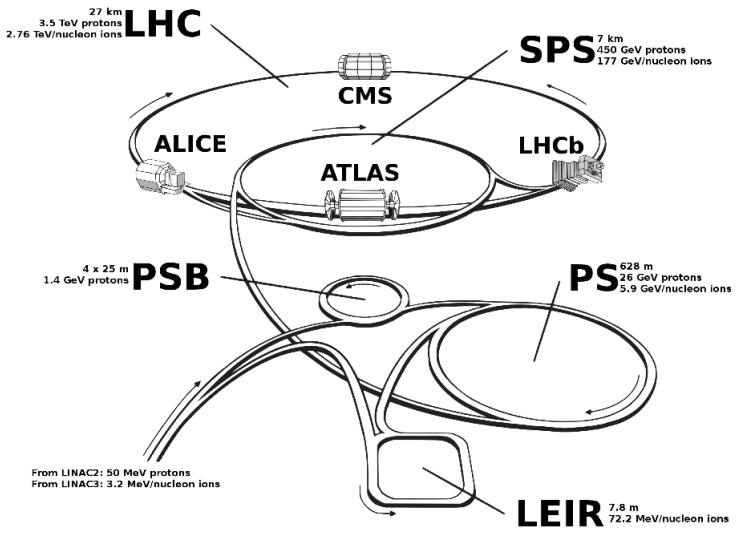

Figure 2.1: Large hadron collider scheme with the principal experiments [133].

maximum number of bunches is 2808 with a 25-ns separation. The first Pb ions were injected in the tunnel on the evening of November 4th in 2010, starting the Pb–Pb collisions era at the LHC. During the 2010 Pb run, the beam included 137 bunches. In 2011, the number of bunches for Pb beams reached 358. Together with a larger number of ions per bunch, this allowed for the increase of the integrated luminosity from 9 μb^{-1} [131] in 2010 to 146 μb^{-1} [132] in 2011. In Figure 2.2, we present a display of tracks from one of the first Pb–Pb collisions registered in ALICE. It gives a visual impression of the number of particles produced in a typical collision at LHC energies.

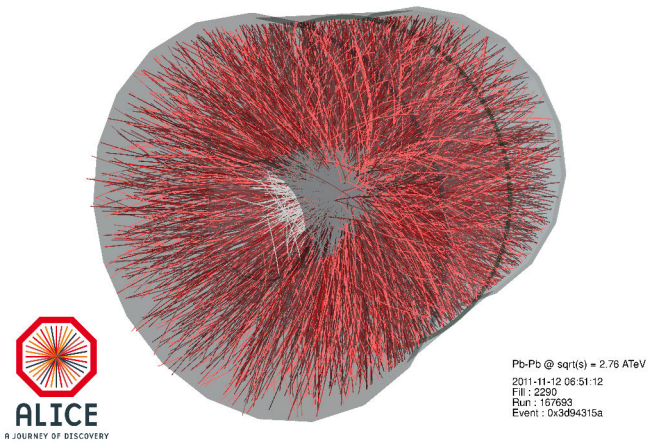

Figure 2.2: An event display of one Pb–Pb collision recorded with the ALICE detector in November 2010.

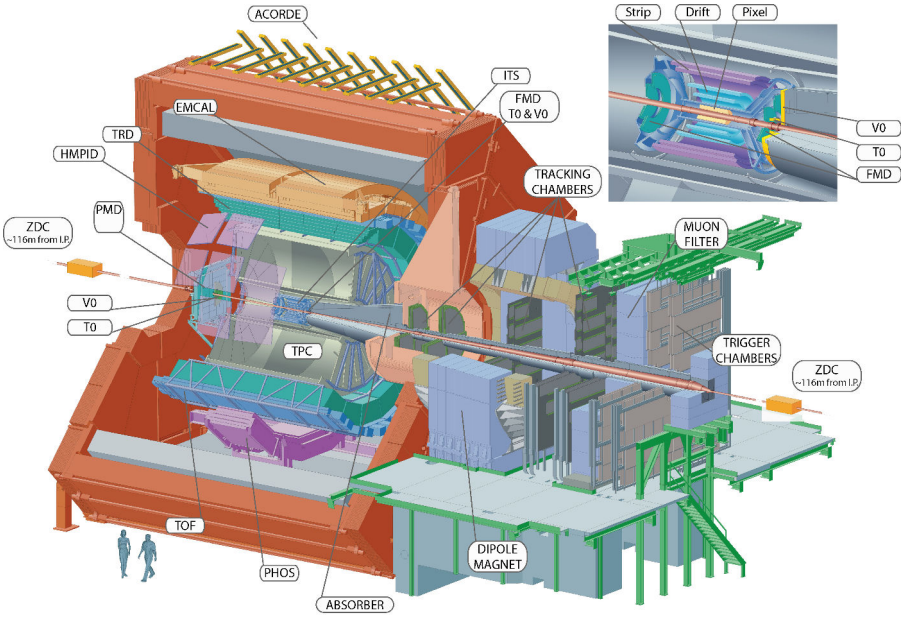

Figure 2.3: The layout of the ALICE experiment [134].

2.2 The main ALICE subsystems

The large multiplicity of particles produced in the most central Pb–Pb collisions is one of the principal constrains for the ALICE detector design [134]. After the first run of Pb–Pb collisions at the LHC, ALICE proved to have the requirements to perform the particle identification from low-p_{T} (from tens of MeV/c) for studying the collective effects of the medium, up to high values of the transverse momentum for jet reconstruction using the combination of all the sub-detectors [132]. This is possible due to the low material budget that reduces the multiple scattering at low-p_{T} (13% X0 up to the end of the TPC) and a large tracking lever arm of up to 3.5 m to guarantee a good resolution at high p_{T} (up to 100 GeV/c) [135].
ALICE is composed of 18 different subsystems (see Figure 2.3) [135]. Its overall dimensions are 16x16x26 m^3 with a total weight of approximately 10 000 tons. The central-barrel detectors are embedded in a large solenoid magnet that provides a magnetic field of 0.5 T to allow for track reconstruction at low p_{T}. The subsystems contained in this part of the detector are the Inner Tracking System (ITS), the Time Projection Chamber (TPC), the Time-of-Flight (TOF), the Ring Imaging Cherenkov (HMPID) and Transition Radiation (TRD) detectors, and the two calorimeters Photon Spectrometer (PHOS) and Electromagnetic Calorimeter (EMCal). The Muon Spectrometer located in the forward region consists of a complex arrangement of absorbers, a large dipole magnet, and 14 planes of tracking and triggering chambers. The forward region contains also several smaller subsystems: ZDC, PMD, FMD, T0 and VZERO. These detectors are used for global event characterization and triggering, they are located at small angles with respect to the beam. An array of scintillators (ACORDE) on top of the ALICE solenoid is used to trigger on cosmic rays. The global ALICE coordinate system is a right-handed coordinate system with the z-axis coinciding with the beam-pipe axis and going in the direction opposite to the muon arm, the y-axis going up, and the origin of coordinates defined by the intersection point of the z-axis and the central membrane plane of TPC [136].

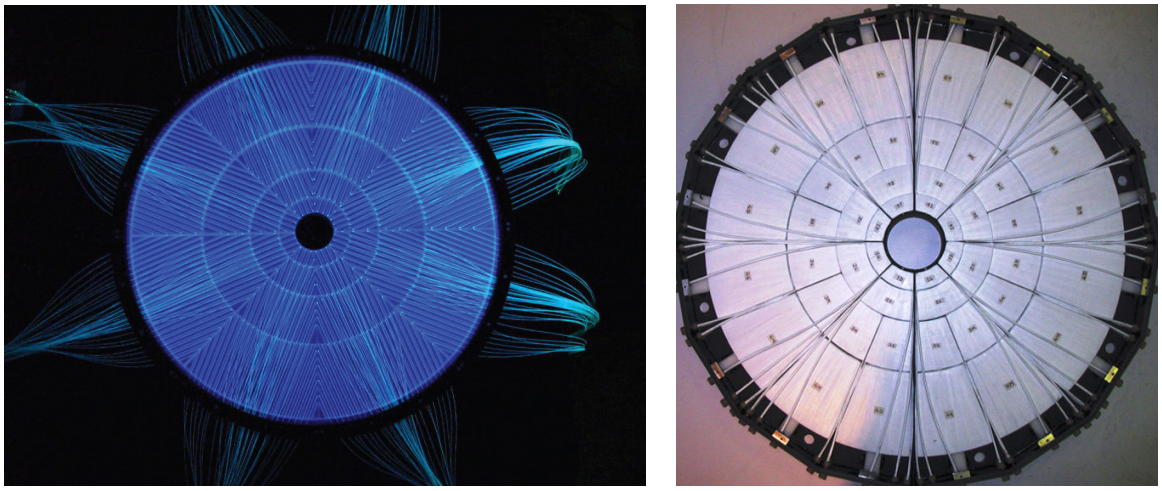

Figure 2.4: The two components of the VZERO detector: VZERO-A (left) and VZERO-C (right) [137]. Each device is divided in 8 sectors in the azimuthal angle and in four rings in the radial direction.

In the following sections, the main subsystems of ALICE involved in the doctoral work of this dissertation will be described in more detail.

2.3 VZERO detector

The VZERO system monitors the beam conditions and operates as a trigger detector that separates the beam-beam interactions from different sources of background. It is also used to determine the beam luminosity, the particle multiplicity, collision centrality and event plane direction in nucleus-nucleus collisions [137].
The VZERO system is composed of two plastic scintillator arrays (VZERO-A and VZERO-C) located at asymmetric positions, one on each side of the interaction point. The VZERO-A detector is at 329 cm from the interaction point, opposite to the muon spectrometer, and the VZERO-C is fixed at -90 cm in front of the hadronic calorimeter (see Figure 2.3). They cover small angles at a pseudo-rapidity range of $2.8 < \eta < 5.1$ and $-3.7 < \eta < -1.7$, respectively [135]. Each of the scintillator arrays is composed of four concentric rings of scintillators, and each ring is divided in eight sectors in the azimuthal plane, with a 45º coverage. The design of the VZERO detector is shown in Figure 2.4. The photons produced in the scintillator material are collected by wavelength shifting fibers. The collected signal is amplified by photomultipliers and then transferred to the front-end electronics to measure the pulse time (leading time) relative to the 40-MHz LHC bunch clock and to integrate the charge [138]. The individual channel time resolution, averaged over all signal amplitudes, is of the order of 1 ns for both arrays [137].
The VZERO subsystem is set with two types of trigger algorithms working independently for the VZERO-A and the VZERO-C arrays. The algorithm type is based on the time information from the counters and is used for separating beam-beam collisions from the background events (further details will be presented in subsection 3.1.2). The second algorithm is based on the total

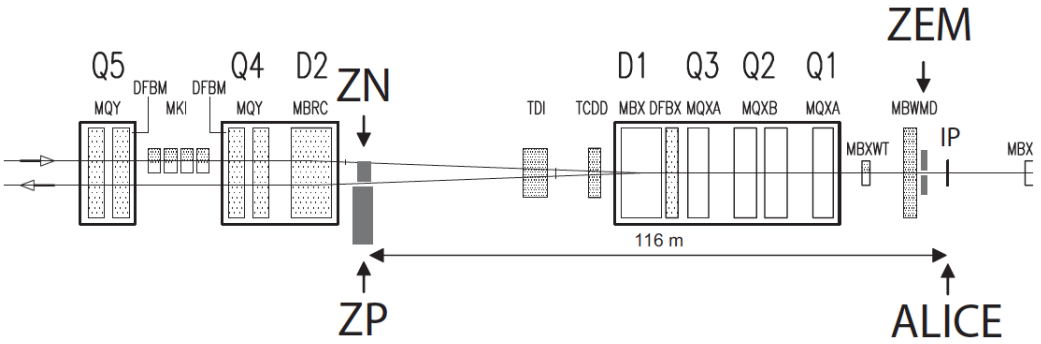

Figure 2.5: Configuration of the zero degree calorimeter (ZP and ZN) and the electromagnetic calorimeters (ZEM) with respect to the interaction point (IP) in ALICE [135].

amplitude of the signals collected by each array allowing for triggering on collision centralities in Pb–Pb runs [135, 137].

2.4 Zero Degree Calorimeter

The Zero Degree Calorimeter (ZDC) was built to measure the energy carried away by the non-interacting nucleons (*spectators*) in the forward direction of the heavy-ion collision, providing information about the multiplicity of the event [139]. Besides, it can estimate the reaction plane in nuclear collisions and can also be used as a triggering detector thanks to its very fast response of about 13 ns.

The ZDC is composed of two set of hadronic and electromagnetic calorimeters. The hadronic calorimeters are quartz fibers sampling calorimeters with silica optical fibers as active material embedded in a dense absorber. Its functioning is based on the detection of the Cherenkov radiation produced by the charged particles of the shower in quartz fibers [140].

The spectator protons are separated from the neutrons by beam optics of the LHC machine (set of magnets along the beam pipe). Therefore, the hadronic calorimeter is made to measure both protons and neutrons with two distinct detectors: the ZN for spectator neutrons, placed between the beam pipes at 0^{o} relative to the LHC axis, and the ZP for spectator protons, placed externally to the outgoing beam pipe on the side where positive particles are deflected (see Figure 2.5). The hadronic ZN and ZP are located at 116 m on either side of the interaction point with dimensions about $7.04 \times 7.04 \times 100$ cm^3 and $12 \times 22.4 \times 150$ cm^3, respectively. Together they cover the pseudo-rapidity region of $|\eta| > 8.7$ [135].

To complement the set, two small electromagnetic calorimeters (ZEM) are placed on both sides of the LHC beam pipe at about 7 m from the collision (opposite to the muon arm). They cover a pseudo-rapidity range $4.8 < |\eta| < 5.7$. The peripheral (>30% centrality) and central A–A collisions are detected as similar events with the ZDCs because in peripheral events the nuclear fragments are bound into fragments that stay in the beam pipes. Therefore, the ZEM helps discriminating between central and peripheral collisions by means of photons generated from π^0 decays whose energy increases monotonically with centrality. The ZEM fibers and plates are oriented at 45^{o} with respect to the LHC axis. This choice maximizes the detector response,

because Cherenkov light production has a pronounced peak around 45°.

2.5 Inner tracking system

Due to its intrinsic distance to the primary beam-beam interaction, the Inner Tracking System (ITS) is one of the fundamental pieces in ALICE. It provides the following important tasks: delivering one of the trigger responses during the collision data taking, participating in the tracking procedure by reconstructing low-p_{T} charged particles as standalone tracks, improving the spatial and momentum resolution of the tracks, determining the primary vertex position and providing particle identification capabilities [134, 141].
The ITS is made of six cylindrical layers of silicon detectors (see Figure 2.6), parallel to the beam axis, located at radii between 3.9 and 43 cm and covering a pseudo-rapidity range from -0.9 up to 0.9 with full azimuthal coverage. The six ITS layers use different technology: the first two layers are made of silicon pixel detectors (SPD), the third and fourth layers are based on silicon drift detectors (SDD) and the two outer layers are the silicon strip detectors (SSD). The layers are positioned according to the optimization of the track finding efficiency and the impact parameter resolution [141]. Especially, the innermost layer has the minimum distance to be compatible with the beam pipe radius. The beam pipe is a 800 mm-thick beryllium cylinder of 6 cm outer diameter, coaxial with the ITS detector layers. The position of the outermost ITS layer is determined by the track matching with the TPC.
The four outer layers have analogue readout and therefore can be used for particle identification via $\mathrm{d}E/\mathrm{d}x$ measurement in the non-relativistic ($1/\beta^2$) region (to be described in detail in section 2.9).
The silicon detectors used to measure ionization densities (drift and strips) must have a minimum thickness of approximately 300 mm to provide acceptable signal-to-noise ratio. Thus, the ITS has a material budget contribution about 7.18% of radiation length (X/X_0) [135].

In the next subsections, the design of the ITS component and their functions will be described in more detail.

Silicon pixel detectors

The silicon pixel detector forms the two innermost cylindrical layers of the ITS. It plays a fundamental role for the determination of the position of the primary vertex as well as for the measurement of the impact parameter of secondary tracks originated from the weak decays of strange, charm, and beauty particles [134]. The SPD was designed to have a high-granularity and an excellent spatial precision to operate under the condition of large-track density (up to 90 particles/cm^2).
The layers are located at radial distance of 3.9 cm and 7.6 cm from the beam line and provide a pseudo-rapidity coverage of 2.0 and 1.4 unities, respectively. These detectors are formed of hybrid silicon pixels in a two-dimensional matrix with a structure[1] of 256×160 cells of 50 μm $\times$ 425 μm ($r\varphi \times z$) pixel dimensions. Longer sensor cells are used in the boundary region to ensure coverage between readout chips. The sensor matrix has an active area of 12.8 mm ($r\varphi$) by 70.7 mm (z). The front-end chip reads out a sub-matrix of 256 ($r\varphi$) and 32 (z) detector cells. The SPD

[1] The structure is called a ladder.

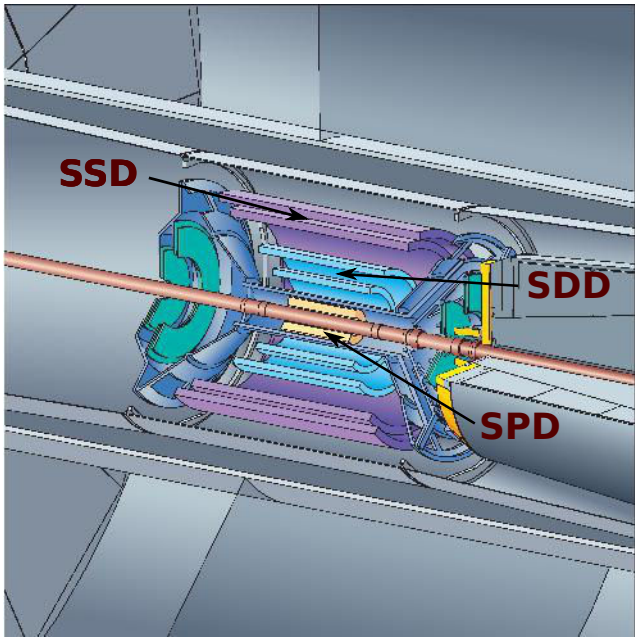

Figure 2.6: Illustration of the inner tracking system in ALICE and its six different layers: the silicon pixel detectors (SPD), the silicon drift detectors (SDD) and the silicon strip detectors (SSD).

includes 240 ladders with 1200 front-end chips for a total of 9.8×10^6 cells [135].
Each of the chips provides a fast signal (about 800 ns) whenever a pixel cell (or a group of them) detects a hit above the threshold. The signals from the 1200 chips are combined in a programmable logic unit which supplies a trigger signal [142].
The fraction of SPD channels active during the 2010 and 2011 data taking was 70% for the inner and 78% for the outer layer, leading to azimuthal inhomogeneity in the track detection and reconstruction conditions.

Silicon drift detectors

The silicon drift detectors are the two intermediate layers of the ITS. They are constructed to have a good quality for tracking and to provide particle identification with the energy loss ($\mathrm{d}E/\mathrm{d}x$). The detector measures the transport time of the transversing particle via the cloud of electrons generated through its interaction with the material and drifted towards the read-out anodes.
The two SDD layers are placed on the average radius of 14.9 and 23.8 cm. They consist of 14 and 22 ladders, having an active area about 7.53×7.25 cm^2 each [141]. The sensitive area of the detectors is separated into two drift regions by the central cathode strip. A high voltage of -2.4 kV is applied to the cathode. For each region, a series of parallel drift cathode strips (291 p^+ cathodes with 120×70 μm^2 pitch) cover the two detector surfaces generating a constant electrostatic field (drift field) parallel to the surface. The overall detector performance does not depend significantly on the applied voltage in a range from -1.65 kV to -2.4 kV.
Moreover, each drift region has one row of 256 collection anodes with a pitch of 294 μm and three

rows of 33 point-like metal-oxide-semiconductor (MOS) charge injectors. The MOS injectors are introduced to calibrate the drift time and to monitor the uniformity of the drift velocity across the sensitive area which is very susceptible to the temperature: $v_{\text{drift}} \propto T^{-2.4}$ [135]. When working at a field of 600 V/cm, the drift speed of the charge cloud will be about 8 μm/ns with a maximal drift time of about 4.3 μs.
Other important elements of the SDD are the guard cathodes introduced to gradually scale the high potential of the drift cathodes down to the ground potential of the n^+ ring at the detector edge. The guard cathodes have a pitch of 32 μm. There is one guard cathode every two drift cathodes. Usually, the drifting charges are collected from the middle plane of the detector towards the surface by an array of n^+ anodes. Normally, this part of the drift region is referred to as the collection zone.
The space precision provided by the detector is better than 38 μm along $r\varphi$ over the whole detector surface, and the precision along the anode axis (z) is better than 30 μm over 94% of the detector surface and reaches 60 μm close to the anodes, where a fraction of clusters affects only one anode.

Silicon strip detectors

The fifth and sixth layers of the ITS are crucial for the matching of tracks from the TPC to the ITS. As well as the SDD, the strip detectors provide $\mathrm{d}E/\mathrm{d}x$ information for particle identification at low momentum.
The structure of the layers is about 768 double-sided silicon strip sensors with 300 μm thick and a 95 μm pitch. One side is constructed with p^- strips, while the other side consist of n^- strips. Each of these sensors has a rectangular shape corresponding to an overall area of 75×42 mm^2. The strips are 40 mm long and tilted by an angle of 17.5 mrad with respect to the short side of the detector, allowing a two-dimensional reconstruction of track position. The spacial precision in the two detector coordinates is typically of 15 μm in the x direction (orthogonal to the beam axis) and around 800 μm in the y direction (parallel to the beam axis in ALICE) [141].

2.6 Time projection chamber

The time projection chamber is the main tracking system in ALICE for the central acceptance ($|\eta| < 0.9$) with full azimuthal coverage. As a drift detector, the charged particles are detected through the ionization of the medium along its trajectory. The measured mean energy, deposited in the detector, per unit length ($\mathrm{d}E/\mathrm{d}x$) is used to identify principally electrons, pions, protons and charged kaons [134] as well as light (anti-)nuclei such as deuterons, $^3\overline{\mathrm{He}}$ and $^4\overline{\mathrm{He}}$ [135]. The TPC is also used to reconstruct the primary vertex position and to give an estimation of the multiplicity of particles generated during the collision.
The TPC is a large cylindrical drift detector whose dimensions extends radially from 85 to 247 cm, and from -250 to +250 cm along the beam direction (z-axis) [143]. It is filled with nearly 90 m^3 gas which consist of a mixture of Ne (85.7%), CO_2 (9.5%) and N_2 (4.8%) until the end of 2010, and Ne (90%) and CO_2 (10%) since the beginning of 2011. Thus, decreasing the gain and decreasing the risk of a detector breakdown in the 2011 LHC run conditions. The drift properties of the two mixtures practically stay equal [144]. The gas together with the field cage ensure

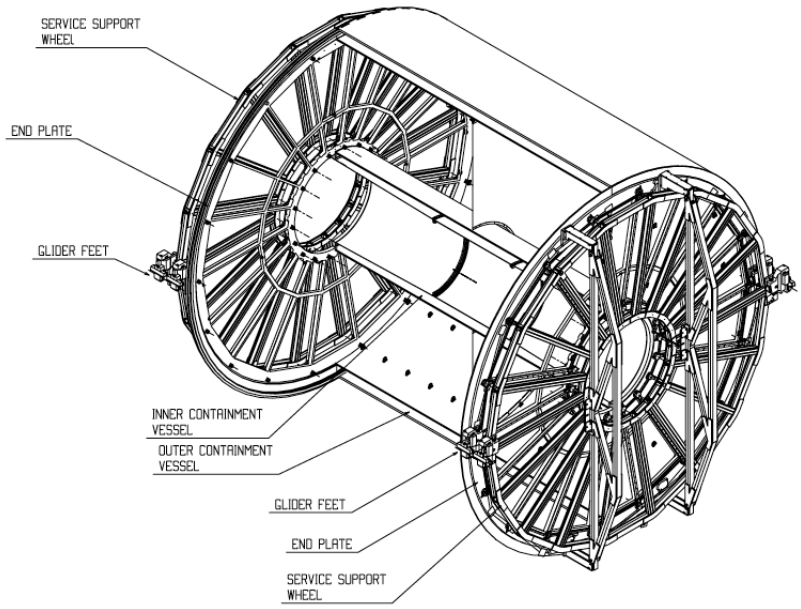

Figure 2.7: Diagram of the time projection chamber in ALICE [135].

a low material budget of less than 3% of the radiation length, keeping minimal the multiple scattering and the secondary-particle production [135].
The chamber is divided in two parts by a 22-μm-thick electrode located at the axial centre of the cylinder to which a high-voltage of -100 kV is applied. At both end-caps of the barrel, multi-wire proportional chambers with cathode segments (readout pad) are installed with 18 trapezoidal sectors each (see Figure 2.7) [134]. The active area varies radially from 84.8 to 132.1 cm and from 134.6 to 246.6 cm for the inner (IROC) and outer (OROC) read-out chamber, respectively. The inactive areas between neighboring inner chambers are aligned with those between neighboring outer chambers [135, 143]. A two-dimensional segmentation of the cathode plane provides the measurement of many individual space points per particle track in the r-φ-plane by sampling the time distribution of each pad signal. The IROC have a pad size of 4×7.5 mm^2. The total number of pads in the inner chamber is 5732, distributed over 64 pad-rows running parallel to the wires, i.e, located radially. The number of pads in the OROC is 10110, with a pad size of 6×10 mm^2 for $r < 198.6$ cm (64 rows) and 6×15 mm^2 for $r > 198.6$ cm (32 rows). In this chamber the pads are also oriented radially. The segmentation of the readout pad plane was chosen to optimize, in the high multiplicity environment of central Pb–Pb collisions, the momentum and dE/dx resolution. The radial dependence of the track density lead to two different readout chambers with a radial segmentation [143].
The readout chambers are multi-wire proportional chambers with cathode pad readout. They consist of a grid of anode wires above the pad plane, a cathode wire plane, and a gating grid. In the absence of trigger, the gating grid prevents the electrons to enter to the amplification region and the ions from the previous events to enter to the drift volume where they will cause field distortions leading to deteriorated tracking performance. The gate is opened only by the Level 1 trigger (6.5 μs after the collision) for the duration of one drift-time interval that is of 90 μs. It has been verified that the closed gate reduces the drift of electrons by a factor better than

10^5 [135].
The front-end electronics has about 560 000 readout pads of three different sizes: 4×7.5 mm^2 in the inner chambers, 6×10 mm^2 and 6×15 mm^2 in the outer chambers. The chambers deliver on their pads a current signal with a fast rise time (less than 1 ns), and a long tail due to the motion of the positive ions. The amplitude, which is different for the different pad sizes, has a typical value of 7 μA. Coplanarity between the two readout planes was checked by survey and adjusted for a mechanical precision of order ≤ 250 μm.
The TPC allows up to 159 position signals (clusters) for the particles transversing the detector. The recorded data of the clusters is used later to reconstruct the charged particle trajectory as well as to calculate the particle $\mathrm{d}E/\mathrm{d}x$ energy loss to identify the particle species of the track.
The TPC field cage in combination with the electrode provide a highly uniform electrostatic field. An insulating gas envelope of CO_2 in containment vessels surrounds the field cage. The drift field is chosen as a function of the intrinsic properties of the drift gas, affecting the drift velocity and the diffusion of primary ionization electrons in that gas. For the chosen gas mixture and conditions operation in ALICE, the electric drift field is of 400 V/cm allowing a drift velocity of 2.7 cm/μs. It is known that temperature variations cause local fluctuations in the gas density, hence in the velocity of drifting electrons. TPC is aiming for a thermal stability with $\Delta T \leq 0.1$ K in the drift volume [135].

2.7 Primary vertex determination

The reconstruction of the primary-vertex position in ALICE is done applying two methods. The first one uses only the information provided by the SPD layers of the ITS. Pairs of reconstructed points in the two layers, close in azimuthal angle in the transverse plane, are selected. With their z-coordinates, the z-position of the primary vertex is estimated using a linear extrapolation. The combination of the space points gives a distribution of z-primary-vertex position which is fitted to the sum of a Gaussian and a constant. The centroid of the Gaussian is used as the estimation of the primary vertex position [145]. Finally, a similar procedure is obtained in the transverse plane with selected point pairs within $4\sigma_{z_{\mathrm{vtx}}}$ around the estimated vertex location $z_{\mathrm{vtx}}^{\mathrm{SPD}}$. Despite the bending in the magnetic field, the x- and y-coordinates of the primary vertex are determined with a sufficient precision [136]. This first determination of the primary vertex is used as an input in the first stage of the track finding.
The resolution on the $z_{\mathrm{vtx}}^{\mathrm{SPD}}$ depends on the track multiplicity. For heavy-ion charged-particle densities, the vertex-position resolution is about 10 μm, and for the average pp collisions where $\langle \mathrm{d}N_{\mathrm{ch}}/\mathrm{d}\eta \rangle = 6-7$ the resolution is about 150 μm [135]. Whereas the resolution in the transverse plane 35 μm in Pb–Pb collisions [136] and about 50 μm in the high multiplicity pp collisions [132].
After track reconstruction, the position of the primary vertex is recalculated with a higher precision using the measured TPC and ITS track parameters. Each track is approximated with a straight line at the position of the closest approach to the nominal primary vertex position. Then, all possible track pairs (i, j) are considered and for each pair, the centre $C(i, j) \equiv (x_{ij}, y_{ij}, z_{ij})$ of the segment of minimum approach between the two lines is found [136]. The coordinates of the primary vertex are determined as

$$x_{\mathrm{vtx}} = \frac{1}{N_{\mathrm{pairs}}} \sum_{i,j} x_{ij}, \quad y_{\mathrm{vtx}} = \frac{1}{N_{\mathrm{pairs}}} \sum_{i,j} y_{ij}, \quad z_{\mathrm{vtx}} = \frac{1}{N_{\mathrm{pairs}}} \sum_{i,j} z_{ij}, \tag{2.1}$$

where N_{pairs} is the number of track pairs.

2.8 Tracking and reconstruction

With the signals left by each charged particle passing through the detectors, the position of the points in space where the particle has passed is measured. The track finding consist of assigning these space points to tracks during the reconstruction procedure, obtaining the particle's kinematics as well.
The method employed for track finding and fitting is the Kalman filter [146] which is performed in three stages, following an inward–outward–inward scheme as it is illustrated in Figure 2.8. This method depends critically on the determination, for each track, of a set of initial seed values for the track parameters and their covariance matrix.
The first inward stage of the overall tracking starts with the track candidates (*seeds*) in the outermost pad rows of the TPC (see Figure 2.8). The space-point positions are calculated from the centre of gravity of the two-dimensional clusters (in the pad-row and time directions) considering two cases: i) the track is originated in the primary interaction, ii) or it comes from a secondary interaction, decay, etc, (without the primary vertex constraint). Thus, the track parameters and their covariance matrices in the vicinity of the interaction point are calculated. The tracking procedure consists of the following steps [136]:

i) The state vector of the track parameters and their covariance matrix are propagated to the next pad row.

ii) A term related to the noise is added to the inverted covariance matrix which represent information loss due to stochastic processes.

iii) If the filter finds in the new pad row a space point compatible with the track prolongation, this measurement is added to the track parameters by updating its covariance matrix.

Only those tracks that have at least 20 TPC clusters (out of maximum 159 possible) and that miss no more than 50% of the clusters expected for a given track position are accepted. These are then propagated inwards to the inner TPC radius.
The reconstructed TPC tracks are then propagated to the outermost ITS layer and become the seeds for track finding in the ITS. The highest-momentum tracks are propagated first and then continue with the lower-momentum ones in order to make the most precise track-space point. The ITS tracker tries to prolong the TPC tracks as close as possible to the primary vertex. Assigning additional reconstructed ITS clusters, the estimation of the track parameters improves.
After all the track candidates from the TPC are assigned their clusters in the ITS, a special ITS stand-alone tracking procedure is applied to the rest of the ITS clusters. This procedure tries to recover the tracks that were not found in the TPC because of the p_{T} cut-off, dead zones between the TPC sectors, or decays [136].
When the ITS tracking is completed, the second tracking stage starts from the primary vertex position back to the outer layer of the ITS and then repeated towards the outer wall of the TPC. The tracks are refitted by the Kalman filter in the outward direction using the clusters found at the previous stage. For the track that was labelled by the ITS tracker as potentially primary,

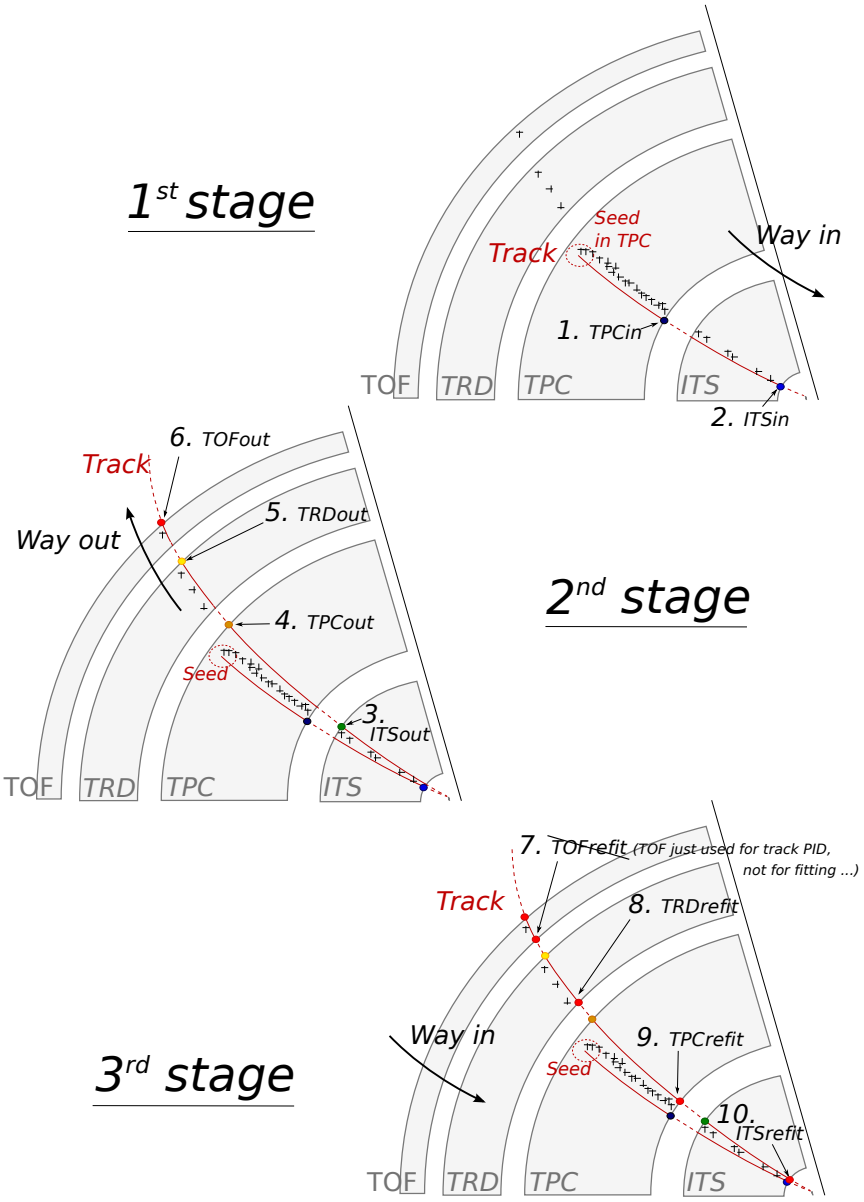

Figure 2.8: Representation of the three performed stages for track finding. The procedure follows an inward–outward–inward scheme. The detectors involved in each tracking stage are enumerated. Illustration taken from [147].

several particle-mass-dependent, time-of-flight hypotheses are calculated. These hypotheses are then used for the particle identification with the TOF detector. Once the outer radius of the TPC is reached, the precision of the estimated track parameters is sufficient to extrapolate the tracks to the TRD, TOF, HMPID, EMCal and PHOS detectors.

Finally, the Kalman filter is reversed one last time and all tracks are refitted from the outside inwards, in order to obtain the values of the track parameters at or nearby the primary vertex. The track's position, direction, inverse curvature, and its associated covariance matrix are determined.

The tracks that passed the final refit are used for the secondary vertex (V0, cascade, kink)

reconstruction. The reconstructed tracks (together with the PID information), kink, V0 and cascade particle decays are then stored.
ALICE has good track-finding efficiency for tracks down to $p_{\mathrm{T}} = 100$ MeV/c. Figure 2.9 shows the TPC tracking efficiency, defined as the ratio between the reconstructed tracks and generated primary particles in the simulation, as a function of transverse momentum for pp and Pb–Pb collisions. While the drop below a transverse momentum of 0.5 GeV/c is caused by energy loss in the detector material, the characteristic shape at larger p_{T} is determined by the loss of clusters in the dead zones between readout sectors.

Figure 2.9: Tracking efficiency of charged primary particles reconstructed only in the TPC. The results are obtained for pp collisions and Pb–Pb collisions at LHC energies [132].

2.9 Particle identification

The particle identification (PID) capabilities of ALICE are broad, consisting of different systems (ITS, TPC, TRD, TOF and HMPID) to distinguish charged pions, kaons, protons and electrons at different p_{T} intervals, each with a different momentum-dependent performance [132]. In this section we will review the applied technique for the main detectors in ALICE used for PID.

- ♢ The ITS uses the four outer layers to measure the deposited charge, thereby providing a $\mathrm{d}E/\mathrm{d}x$ measurement, specifically for low-p_{T} tracks ($p_{\mathrm{T}} < 0.7$ GeV/c) where the ITS is used for standalone tracking. The $\mathrm{d}E/\mathrm{d}x$ is estimated as a truncated mean: the average of the lowest two points of four points are measured, or a weighted sum of the lowest (weight 1) and the second-lowest points (weight $^1/_2$) [132], if only three points are measured in order to minimize the influence of Landau fluctuations. The resolution of the ITS $\mathrm{d}E/\mathrm{d}x$ measurement is about 11%, which allows for good π/K separation up to 450 MeV/c and for good p/K separation up to about 1 GeV/c.

Figure 2.10: Particle identification for Pb–Pb collisions at $\sqrt{s_{\mathrm{NN}}} = 2.76$ TeV for two systems in ALICE: the energy loss of the particles in the TPC (left panel) and the correlation $\beta = v/c$ observed by TOF (right panel) versus the momentum.

♢ The $\mathrm{d}E/\mathrm{d}x$ measurement in the TPC is treated in a similar way as in the ITS, using the truncated mean of the 65% lowest-amplitude pad-row samples [135]. Particle identification in the TPC is performed by simultaneously measuring the specific energy loss, charge, and momentum of each particle traversing the detector gas. The energy loss, described by the Bethe-Bloch formula, is parametrized by the function

$$f(\beta\gamma) = \frac{P_1}{\beta^{P_4}}\Big(P_2 - \beta^{P_4} - \ln\big(P_3 + \frac{1}{(\beta\gamma)^{P_5}}\big)\Big) \tag{2.2}$$

where β is the particle velocity, γ is the Lorentz factor, and P_{1-5} are fit parameters [132]. A clear separation between the different particle species at low momenta ($p_{\mathrm{T}} < 1$ GeV/c) can be seen in Figure 2.10 where the particles can be identified on a track-by-track basis. Still at higher momenta, particles can be separated on a statistical basis via multi-Gaussian fits.

♢ The TOF detector is a large area array of Multigap Resistive Plate Chambers. It measures the arrival time of particles with respect to the interaction time provided by the T0 detector. In Pb–Pb collisions, in the centrality range 0-70% the overall TOF resolution is 80 ps for pions with a momentum around 1 GeV/c. The detector provides a good separation up to 2.5 GeV/c for pions and kaons, and up to $p_{\mathrm{T}} < 4$ GeV/c for protons [148]. The left panel on Figure 2.10 illustrates the performance of the TOF detector by showing the measured velocity β distribution as a function of momentum (measured by the TPC). The background is due to tracks that are incorrectly matched to TOF hits in high-multiplicity Pb–Pb collisions [135].

♢ The HMPID is a Ring Imaging Cherenkov detector that covers $|\eta| < 0.6$ in pseudo-rapidity and 57.6° in azimuth, corresponding to 5% acceptance of the central barrel. The HMPID is devoted to the identification of the high-momentum particles, i.e. pions, kaons and protons in the range from 1 to 5 GeV/c. The identification is based on the Cherenkov angle θ of

the ring produced by charged tracks: $\cos\theta = 1/(n\beta)$ where n is the refractive index of the radiator [149]. The separation of kaons from other charged particles is achievable up to $p_{\mathrm{T}} < 3$ GeV/c for pions, and up to $p_{\mathrm{T}} < 5$ GeV/c for protons.

♢ One of the main tasks of the TRD is the discrimination of electrons above $p_{\mathrm{T}} > 1$ GeV/c from a large background of pions. Electrons are identified based on their specific energy loss and transition radiation. Although the ionization in the TRD gas (based on purified xenon) is larger than in the TPC (based on neon), the TRD $\mathrm{d}E/\mathrm{d}x$ measurement is only a complement to the TPC measurement because of the limited TRD track length. The precision on the $\mathrm{d}E/\mathrm{d}x$ in the TRD is estimated to be 18-20% [135].

The improvement on the particle identification in ALICE is achieved by combining the individual information of each detector. Figure 2.11 shows the pion-kaon (left panel) and kaon-proton (right panel) separation power of the ITS, TPC, TOF, and HMPID as a function of p_{T}. The separation is calculated as the distance Δ between the peaks divided by the Gaussian widths of the pion and the kaon response, respectively. The p_{T}-dependent results are presented in $|\eta| < 0.5$. At low $p_{\mathrm{T}} < 500$ MeV/c, the TPC and ITS provide the main separation. At intermediate-p_{T}, up to 3 (4) GeV/c for pions/kaons and 5 (6) GeV/c for protons, TOF (HMPID) provides more than 3σ statistical separation power. At higher-p_{T} in the TPC, the particle identification of pions, protons and kaons can be estimated by exploiting the relativistic rise of the energy loss [118, 132]. Additional to charged particle identification, photon identification in ALICE is performed either by reconstructing the electromagnetic shower developed in the PHOS and EMCal calorimeters, or by reconstructing electron-positron pairs originating from photons converted in the material ($\gamma \rightarrow \mathrm{e}^-\mathrm{e}^+$) of the inner detector with the ITS and TPC.
ALICE also identifies hadrons through their weak decay topology. This technique is used for strange hadrons, such as $\mathrm{K}^0_{\mathrm{S}}$, Λ and the multi-strange baryons Ξ and Ω, as well as for charmed hadrons. In all of these cases a full kinematical reconstruction of the decay into charged hadrons is used. In Section 3.4, we will review with more details the reconstruction technique for $\mathrm{K}^0_{\mathrm{S}}$ and Λ.

Figure 2.11: Separation power of hadron identification in the ITS, TPC, TOF, and HMPID as a function of the transverse momentum at midrapidity. The left panel shows the separation of pions and kaons, meanwhile the right panel corresponds to power separation of kaons and protons [132].

3. Two-hadron angular correlations: analysis method

"La inteligencia es como una flecha:
una vez que se aleja del arco, ya no la gobierna nadie.
Su vuelo depende de tu fuerza, pero también del viento y,
¿por qué no decirlo?, del destino que camina detrás de ella."
Ermilo Abreu Gómez

The two-hadron angular correlation method is a powerful technique to investigate hadron production in different collision systems [150, 151]. For heavy-ion collisions, this method can also provide information about the properties of the dense medium [152, 153, 154]. In this chapter, we will start by presenting the criteria used to select the events. Then, we will describe the selections and the procedure applied to construct the two-hadron angular correlation with the primary charged particles as trigger particles, and the K^0_S and Λ as associated particles. By selecting primary particles with high transverse momentum, we expect to isolate correlated hadrons produced by the fragmentation of a parton subsequently to a hard scattering. The two-hadron angular correlation will be extracted from Pb–Pb data taken during the 2011 period. Furthermore, performances related to tracking and reconstruction in the two-hadron angular correlations will be presented.

3.1 Event selection

For the two Pb–Pb periods (December 2010 and December 2011) provided by the LHC, the data taking conditions and strategy for the ALICE experiment were different. In both situations, the detector worked within all its capacity for the delivered luminosity which reached a value of $\mathcal{L} \simeq 9\ \mu b^{-1}$ in 2010 and $\mathcal{L} \simeq 146\ \mu b^{-1}$ in 2011. The probability of event pile-up[1] was less than 10^{-4} and 10^{-3}, respectively. The estimation of the total number of recorded nuclear collision events (of any centrality) by ALICE is of 56 millions during the 2010 Pb–Pb run and of 72 millions for the 2011 Pb–Pb run.

3.1.1 Online trigger

The collected events passed through an online trigger selection based on different signals in the detectors. The Minimum Bias (*MB*) online trigger consists of a combination of the particles detected in coincidence with the VZERO and the SPD detectors (presented already in Chapter 2). The *MB* triggers are defined as follows:

[1] Multiple beam-beam collisions in a single bunch-crossing.

Table 3.1: Online trigger selections for Pb–Pb runs in 2010 and 2011.

Trigger	Description
Minimum Bias (*MB*)	
V0AND	signals in VZERO-A and VZERO-C
3-out-of-3	signals in VZERO-A, VZERO-C and at least in two chips of the SPD
2-out-of-3	two signals combination in either VZERO-A, VZERO-C or/and at least in two chips of the SPD
MBZ	Minimum Bias and signals in both ZDC's
Centrality triggers	
CENT	VZERO based centrality trigger for Pb–Pb (0-10% centrality)
SEMI	VZERO based centrality trigger for Pb–Pb (0-50% centrality)

- ♢ *V0AND* with signals registered in coincidence with both the VZERO-A and the VZERO-C detectors

- ♢ *3-out-of-3* that needs one signal in VZERO-A, another in the VZERO-C and at least two chips fired in the SPD

- ♢ *2-out-of-3* with a combination of two conditions out of the following three possibilities: signal in the VZERO-A and/or signal in the VZERO-C and/or signal on two chips fired in the SPD

The *MB* trigger was used for the 2010 and the 2011 Pb–Pb runs. The mentioned triggering was complemented by demanding signals in the two ZDC detectors (*MBZ*) to reduce the large amount of background coming from one of the electromagnetic interactions generated between the Pb ions.
For the 2011 Pb–Pb run, the goal was to focus on the events with high multiplicity, thus there were two dedicated online triggers according to the signal threshold in the VZERO detector: 0-10% (*CENT*) and 0-50% (*SEMI*) centrality[2].
Other kinds of online triggers were applied for the 2011 run, e.g. selections based on rare signals using the TRD detector. Since we are neither studying heavy-flavor physics nor charged jets, this type of online-triggered events are not of interest in this analysis.
A summary of the online trigger selections is presented in Table 3.1.

3.1.2 Offline trigger and background rejection

A further selection is applied offline to the events satisfying the "online" trigger conditions which are calculated then with the offline information of the detectors. This allows rejecting events considered as background. There are several sources of instrumental and physical backgrounds affecting the quality of the events, therefore the task of the offline trigger selection is to identify

[2]For more details about the centrality information, see section 3.2.

Figure 3.1: Time distribution of signals registered in the VZERO-A detector. The time arrival is measured with respect to the beam crossing time [155]. The beam-gas interactions are detected at earlier times than the beam-beam collisions.

and to eliminate these contributions. Different subsystems are used to identify and remove background according to its classification:

- ◊ ***Beam-machine interactions***
  This kind of background implies two types of machine-induced interactions: beam-gas and beam-machine collisions. Inside the LHC beam pipe, after the vacuum is reached, some residual gas can still remain. As a consequence, some collisions between the Pb beam and the remaining molecules of gas can occur close to the experimental region, being then detected by the subsystems. Another type of contamination is produced by the interactions between the beam-halo and the mechanical structure of the accelerator. All the previous interactions can be identified with the time arrival registered in the VZERO detectors. Figure 3.1 shows the signal of the interaction in the VZERO-A detector [155]. The particles produced in the beam–beam interactions arrive at the VZERO-A detector at approximately 12 ns after the beam crossing time. The beam-machine interactions that occur outside the interaction region are detected at earlier times in the detector with respect to the particles produced in the beam-beam collisions. The contribution of this type of contamination is observed as secondary peaks in the distribution.

- ◊ ***Satellite collisions***
  Another contamination comes from the interaction of the main Pb bunches with the debunched ions, that are non-negligible in the case of the Pb beams. The beam injection at the LHC is such that there are 10 equidistant and empty radiofrequency (RF) buckets with a time interval between two nominal and filled bunches of 25 ns. However, the Pb ions can be displaced by one or more of the neighboring RF buckets generated at the level of the beam injection. The displacement occurs in multiples of the $(2.5\text{ ns}/2)c = 37.5$ cm that is outside the standard fiducial region i.e. primary vertex $|z_{\text{vtx}}| < 10$ cm [155]. Such satellite collisions can be rejected using the information of the ZDC. The correlation between the

Figure 3.2: Correlation between the sum and the difference of the times recorded by the neutron ZDC detector on each side of the interaction region [132].

sum and the difference of the times measured with the ZNA and ZNC in Pb–Pb collisions is shown in Figure 3.2. The large clusters at $t_{ZNA} - t_{ZNC} \sim 0$ and $t_{ZNA} + t_{ZNC} \sim 760$ ns correspond to the Pb-Pb interaction of the nominal RF bunches for each side. The rest of the small clusters placed along the diagonals represent the satellite collisions from the debunched ions that are rejected.

◇ ***Background contribution from electromagnetic processes***
The Pb beams generate an electromagnetic field around them which has a cross section of $\sigma_{\text{singleEMD}} = 187.4$ b and $\sigma_{\text{mutualEMD}} = 5.7$ b for single and mutual electromagnetic dissociation [156], much larger than the one for hadronic interactions. The main contaminations to the events which are coming from the physical electromagnetic processes are the photo-production that creates an e^+e^- pair, and the photo-nuclear interactions where one photon from the electromagnetic field of one nucleus interacts with the other nucleus. The single electromagnetic processes can be identified with the energy deposited in the ZNA and ZNC. An additional condition consisting of having a signal in the electromagnetic calorimeter close to the beam rapidity ZEM allows to distinguish an electromagnetic dissociation from hadronic interactions.

In Figure 3.3, we can observe the distribution of selected events as function of the centrality according to the offline trigger selection *MB*, *CENT* and *SEMI* for the 2011 Pb–Pb period. The shape of the global distribution reveals a drop in the centrality range from 8 to 12%, which needs to be corrected for the correlation studies (for more details see section 3.5).

3.1.3 Primary vertex selection for the 2011 Pb–Pb run

The selected events are required to have a position of the primary vertex ($|z_{\text{vtx}}^{trk}|$) of less than 10 cm away from the detector centre to ensure a uniform pseudo-rapidity acceptance ($|\eta| < 1.0$) and to be optimal for rejecting the beam-induced and electromagnetic backgrounds.

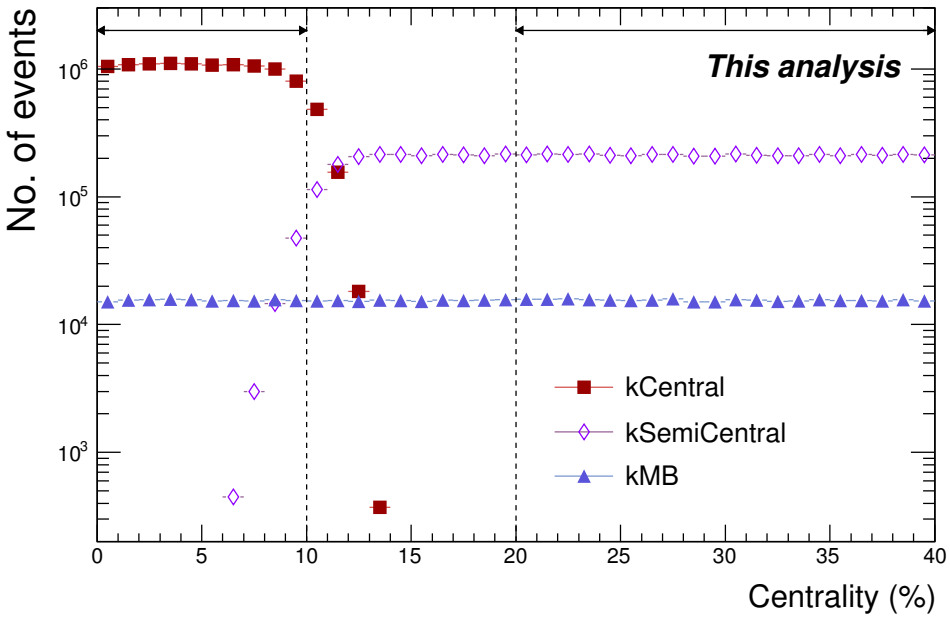

Figure 3.3: Centrality distribution for 2011 Pb–Pb data according to the offline trigger selection.

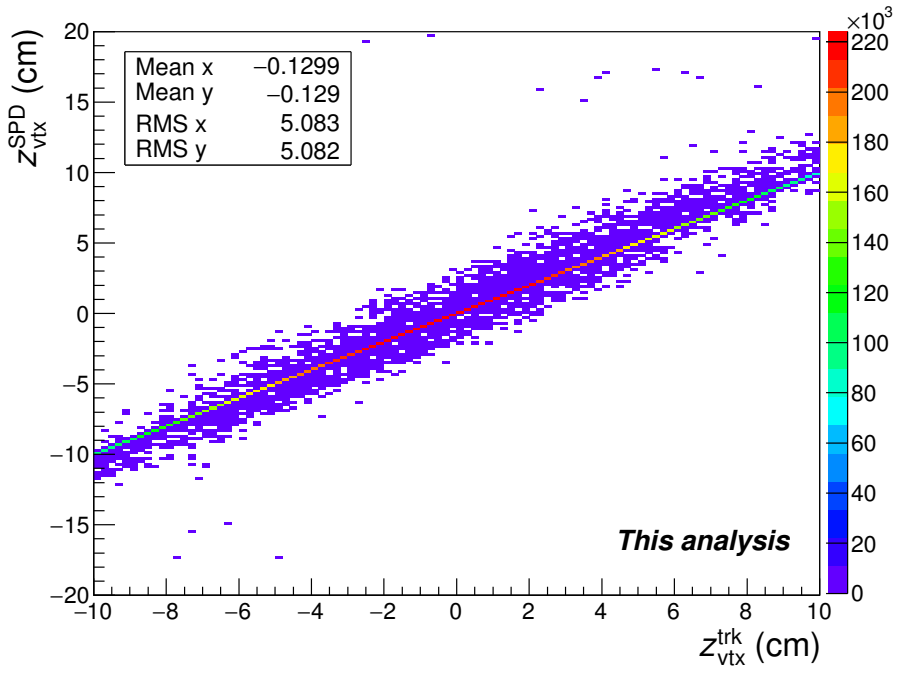

Figure 3.4: Correlation between the z primary vertex position measured with the SPD detector ($z_{\mathrm{vtx}}^{\mathrm{SPD}}$) and the one estimated with global tracks ($z_{\mathrm{vtx}}^{\mathrm{trk}}$).

In addition, for the 2011 data we required that the primary vertex position reconstructed with the two inner layers of the ITS (SPD) ($z_{\rm vtx}^{\rm SPD}$) is within 0.5-cm-distance from the primary vertex position reconstructed with tracks, i.e., $|z_{\rm vtx}^{\rm trk} - z_{\rm vtx}^{\rm SPD}| < 0.5$ cm, to avoid the potential bias from pile-up vertices caused by the increase of the luminosity from 0.03×10^{27} cm^{-2}s^{-1} in the 2010 run to 0.5×10^{27} cm $^{-2}$s^{-1}. The correlation between the positions of the primary vertex estimated with global tracks and with the SPD is shown in Figure 3.4.
The number of offline selected events, using the trigger condition listed in Table 3.1, is about 14×10^{6} for 2010 data and 25×10^{6} for 2011 data in the centrality range 0-90%. A more detailed information on the number of events in each selection step is summarized in Table 3.2 for the two Pb-Pb runs recorded by ALICE in the 0-10% and 20-40% centrality ranges.

Table 3.2: Number of selected events in each selection step for Pb–Pb collisions at $\sqrt{s_{\rm NN}} = 2.76$ GeV/c for the 2010 and 2011 periods.

Year	Description	No. Events	
		0-10%	20-40%
2010	Initial	1 585 036	3 171 448
	$\lvert z_{\rm vtx}^{\rm trk}\rvert < 10$ cm	1 584 933	3 171 342
2011	Initial	11 628 734	4 991 295
	$\lvert z_{\rm vtx}^{\rm trk}\rvert < 10$ cm	10 161 580	4 352 977
	Pile-up rejection	10 157 377	4 352 006

3.2 Centrality determination and the Glauber Model

The picture of heavy-ion collisions can be seen as a sum of multiple-scatterings of their elements, the nucleons. Thus, it would be natural to ask how many nucleons are involved in the collision. This can be estimated using a Glauber model [157], which provides a geometrical representation of the initial state of the interaction. Within this model the nuclei are described as nucleons distributed according to the nuclear density function, which is commonly parameterized by a Fermi distribution or modified Woods-Saxon as follows:

$$\rho(r) = \rho_0 \frac{1 + w(r/R)^2}{1 + \exp(\frac{r-R}{a})}. \tag{3.1}$$

The ρ_0 parameter represents the nucleon density and provides the all-inclusive normalization condition for the nuclear distribution that is $\int \rho(r) {\rm d}^3 r = A$, where A is the total number of nucleons in the nucleus. The parameter R in the previous equation is the radius of the nucleus and in case of ALICE it stands for the ^{208}Pb nucleus with a value of 6.62 ± 0.06 fm [155]. The parameter a is the skin thickness of the nucleus that indicates how quickly the nuclear distribution decreases at the surface; for ^{208}Pb, $a = (0.546 \pm 0.019)$ fm [155]. The parameter w is introduced to describe the deviations from a spherical shape of the nucleus, this parameter can be important for Au (at RHIC), but for Pb (at the LHC) $w = 0$ [155].

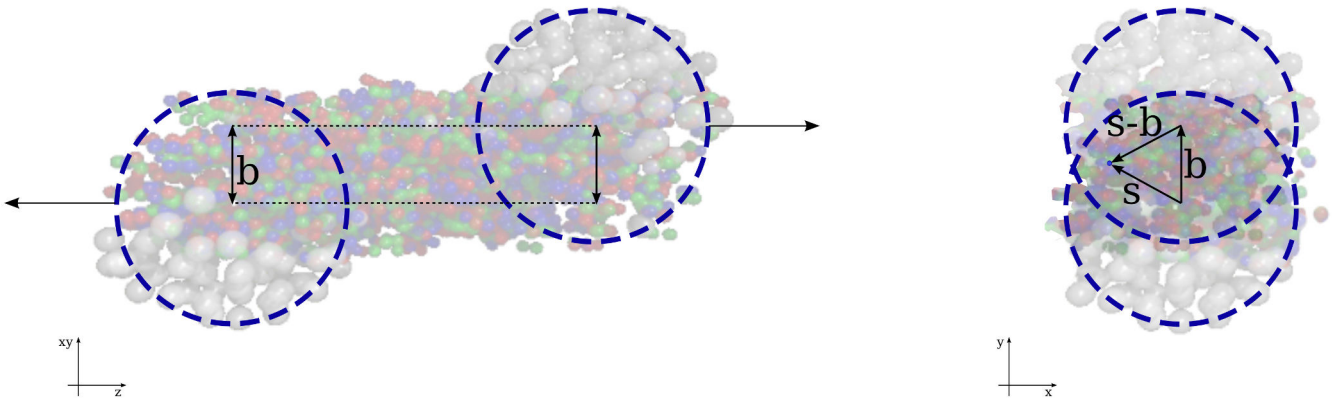

Figure 3.5: Graphical representation of a heavy-ion collision in the Glauber Model observed along the beam direction (z) (left illustration) and in the transverse plane to z (right illustration). The impact parameter (b) is defined as the distance between the centre of the two nuclei in the transverse plane.

On the theoretical side, the principal quantity to illustrate the centrality of a heavy-ion collision is the impact parameter vector ($\mathbf{b}$) defined as the distance between the center of the two nuclei in the transverse plane with respect to the beam axis. This is also used to establish the interacting volume between the nuclei (see Figure 3.5).
The Glauber Model treats the nuclear collision, involving a nucleus target A and a projectile B, as a superposition of binary nucleon-nucleon interactions expressed by the *nuclear overlap function* ($T_{AB}(\mathbf{b})$):

$$T_{AB}(\mathbf{b}) = \int T_A(\mathbf{s}) T_B(\mathbf{s}-\mathbf{b}) \mathrm{d}\mathbf{s}. \tag{3.2}$$

The term $T_A(\mathbf{s})$ is called *thickness function* and is obtained by integrating the nuclear distribution along the beam axis at a certain transverse distance $\mathbf{s}$: $T_A(\mathbf{s}) = \int \rho(\mathbf{s}, z)\mathrm{d}z$. $T_{AB}(\mathbf{s})$ represents the density of nucleons inside A at the distance $\mathbf{s}$ that will potentially interact with the nucleons in B located at a distance **s-b**. A geometrical representation of a heavy-ion collision can be seen in Figure 3.5. For symmetric collisions, e.g. Pb–Pb, one should consider $B = A$ in equation 3.2.
The number of binary nucleon-nucleon collisions (N_{coll}) occurring in the interacting volume is determined through the nuclear inelastic cross section $\sigma^{\mathrm{inel}}_{\mathrm{NN}}$, $N_{\mathrm{coll}} = \sigma^{\mathrm{inel}}_{\mathrm{NN}} T_{AB}(\mathbf{b})$. The number of participants (N_{part}) is defined as the number of nucleons that undergo at least one collision with the nucleons from the other nucleus. It can be calculated as

$$\begin{aligned} N_{\mathrm{part}}(\mathbf{b}) &= A \int T_A(\mathbf{s}) \Big\{ 1 - \Big[1 - T_B(\mathbf{s}-\mathbf{b}) \sigma^{\mathrm{inel}}_{\mathrm{NN}} \Big]^B \Big\} \mathrm{d}\mathbf{s} + \\ & \quad B \int T_B(\mathbf{s}-\mathbf{b}) \Big\{ 1 - \Big[1 - T_A(\mathbf{s}) \sigma^{\mathrm{inel}}_{\mathrm{NN}} \Big]^A \Big\} \mathrm{d}\mathbf{s}, \end{aligned} \tag{3.3}$$

the rest of the nucleons that do not suffer any interaction are known as spectators which are defined as $N_{\mathrm{spec}} = (A + B) - N_{\mathrm{part}}$.
The previous quantities $\mathbf{b}$, N_{coll}, N_{part} and N_{spec} can not be measured directly in the experiment. For that reason the experimental approach to infer the centrality of the event is to compare the

event multiplicity from data with the implementation of the Glauber Model. The most common approach is to use the Monte Carlo technique to obtain the quantities given by the model.
In the Glauber Monte Carlo, nucleons are considered to be far from each other with at least 0.4 fm distance between their centers and are stochastically placed following the nuclear density distribution of equation 3.1. In ALICE, the selection of the impact parameter is performed from the geometrical distribution $\mathrm{d}P/\mathrm{d}b = b$ within a range from 0 fm up to 20 fm $> 2R_{\mathrm{Pb}}$. During the simulation, the nucleons belonging to different nuclei suffer a collision when the distance between their centers is less than $d < \sqrt{\sigma_{\mathrm{NN}}^{\mathrm{inel}}/\pi}$. Moreover, it is assumed that nucleons travel in straight paths between the consecutive nucleon-nucleon collisions and that $\sigma_{\mathrm{NN}}^{\mathrm{inel}}$ is independent of previous interactions. A value of 64 ± 5 mb for $\sigma_{\mathrm{NN}}^{\mathrm{inel}}$ [155] was considered at the energy of 2.76 TeV.
The centrality of the collision (related to $b := |\mathbf{b}|$) is obtained as a fraction of the total hadronic interaction cross section σ_{AA}. The centrality percentile c in AA collisions is calculated via the geometrical Glauber model as follows:

$$c(b) = \frac{\int_0^b \mathrm{d}\sigma/\mathrm{d}b'\mathrm{d}b'}{\int_0^\infty \mathrm{d}\sigma/\mathrm{d}b'\mathrm{d}b'} = \frac{1}{\sigma_{AA}} \int_0^b \frac{\mathrm{d}\sigma}{\mathrm{d}b'}\mathrm{d}b'. \tag{3.4}$$

In ALICE, the centrality is defined as the percentile of the hadronic cross section corresponding to a particle multiplicity above a given threshold ($N_{\mathrm{ch}}^{\mathrm{THR}}$) or an energy deposited in the ZDC below a given value ($E_{\mathrm{ZDC}}^{\mathrm{THR}}$) in the ZDC energy distribution $\mathrm{d}\sigma/\mathrm{d}E'_{\mathrm{ZDC}}$ [155],

$$c \approx \frac{1}{\sigma_{AA}} \int_{N_{\mathrm{ch}}^{\mathrm{THR}}}^\infty \frac{\mathrm{d}\sigma}{\mathrm{d}N'_{\mathrm{ch}}}\mathrm{d}N'_{\mathrm{ch}} \approx \int_0^{\mathrm{E}_{\mathrm{ZDC}}^{\mathrm{THR}}} \frac{\mathrm{d}\sigma}{\mathrm{d}E'_{\mathrm{ZDC}}}\mathrm{d}E'_{\mathrm{ZDC}}. \tag{3.5}$$

The VZERO detector is used as the principal device to classify the collisions in centrality percentage. The reference point (or *anchor point*) for the absolute scale of the centrality corresponds to the amplitude of the VZERO that is equivalent to 90% of the hadronic cross-section [155]. One method to define the anchor point is to fit the experimental multiplicity distribution of the

Figure 3.6: Centrality classes of the Pb–Pb collisions in ALICE with the sum of VZERO amplitudes. The negative binomial distribution Glauber fit is shown as the red line [155].

Table 3.3: Requirements applied for two different trigger particle selections in the 2010 and 2011 Pb–Pb data, where Δ_{xy} and Δ_z are the impact parameters to the primary vertex in xy and z dimensions, respectively. The present analysis is performed with hybrid tracks. *This selection is only applied where the SPD ladders were on.

Trigger particle selections		
	Hybrid track	**TPC-only track**
Transverse momentum	$5 < p_{\mathrm{T}} < 10$ GeV/c	$5 < p_{\mathrm{T}} < 10$ GeV/c
$\lvert\eta\rvert$	< 0.7	< 0.7
SPD hit(s)*	Yes	—
Number of crossed TPC pad rows	≥ 70	≥ 70
χ^2/cluster in the ITS	< 36	—
χ^2/ cluster in the TPC	< 4	< 4
Crossed pad row / findable clusters	> 0.8	—
Reject kink daughters	Yes	Yes
Maximum distance to the primary SPD vertex d_{xy} (d_z)	$< 0.0105 + \frac{0.0350}{p_{\mathrm{T}}}$ cm (< 2 cm)	< 2.4 cm (< 3.2 cm)
Constrain to the primary SPD vertex	$\left(\frac{\Delta_{xy}}{d_{xy}}\right)^2 + \left(\frac{\Delta_z}{d_z}\right)^2 < 1$	$\left(\frac{\Delta_{xy}}{d_{xy}}\right)^2 + \left(\frac{\Delta_z}{d_z}\right)^2 < 1$
Refit in the ITS	Yes	—
Refit in the TPC	Yes	Yes

VZERO detector with the Monte Carlo Glauber model as shown in Figure 3.6. To perform the fit, one assumes a particle production based on the negative binomial distribution (NBD).
The obtained centrality resolution depends on the rapidity coverage of the detector used. The best centrality resolution is achieved when combining the VZERO-A and VZERO-C detectors which is about 0.5% in central collisions and about 2% in peripheral collisions. The resolution obtained with the SPD and the TPC ranges from 1% in central to 3% in peripheral collisions (80%).

3.3 Trigger particle selection ($h^{\pm}$)

The angular correlation studies presented in this dissertation are performed using primary charged particles as the trigger particles. In the next subsections, we will specify the conditions for selecting the corresponding tracks, as well as, some checks to know the quality of these tracks.

Table 3.4: Number of trigger particles for each centrality selection in 2010 and 2011 Pb–Pb data at $\sqrt{s_{\mathrm{NN}}} = 2.76$ TeV.

Centrality	2010 data	2011 data
0-10%	690×10^3	4.1×10^6
20-40%	762×10^3	1×10^6

3.3.1 Selection of trigger particle tracks

The track selection for the trigger particles is done through the requierements listed in the second column of Table 3.3. The selected tracks are commonly known as hybrid tracks because different track qualities are combined to ensure uniform $(\varphi - \eta)$-distribution in the regions where the SPD ladder were switched off. Among the conditions to keep good-quality tracks, we demand the track to be formed with at least one hit in the SPD ladders where the detector was active. The track should have a large number of crossed TPC pad rows, with a minimum value of the ratio of crossed TPC pad rows over findable clusters of about 0.8. The χ^2/cluster related to the track in the ITS (TPC) must be less than 36 (4) units. Also, the daughter particles of kinks[3] are rejected. The maximum distance of the track to the primary vertex position in the xy-plane has a p_{T}-dependence, thus the tracks are constrained to the primary SPD vertex. On the kinematical side, primary charged tracks are selected in the transverse momentum range from 5 to 10 GeV/c and with a pseudo-rapidity of ± 0.7 to maintain a uniform coverage in the detector acceptance[4].

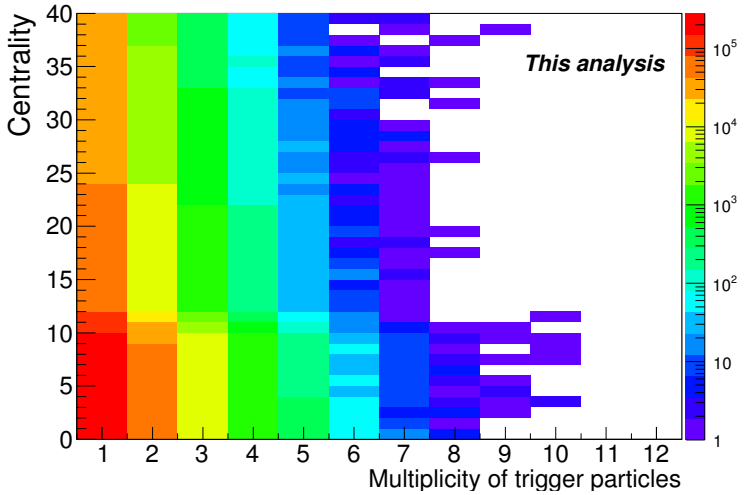

Figure 3.7: Number of trigger particles per collision for the 0 to 40% centrality class in 2011 Pb–Pb data at $\sqrt{s_{\mathrm{NN}}} = 2.76$ TeV.

[3] Pions and kaons identified via their weak decay (kink topology): $\pi \to \mu\nu$ and $\mathrm{K} \to \mu\nu$

[4] The same p_{T} selection for the trigger particles was done originally in the analysis of the K/π and the p/π ratios in jet and bulk. See reference [158].

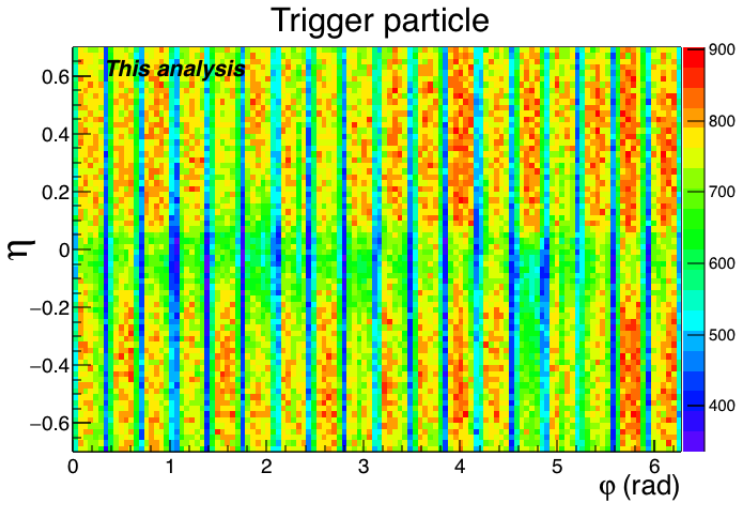

Figure 3.8: η vs φ distribution of the selected trigger particles in 2011 Pb–Pb data at $\sqrt{s_{\mathrm{NN}}} = 2.76$ TeV.

The number of trigger particles in the two Pb–Pb runs, 2010 and 2011, for different centrality selections is presented in Table 3.4. The 2011 data contains more statistics than the 2010 data for the most central collisions, which is a key point for this analysis. For this reason, the two-hadron angular correlations are performed with the 2011 Pb–Pb data.
The requirements related to different track selection criteria (TPC-only track) are listed in Table 3.3. Originally, the $h^{\pm}$-V0 correlations were obtained by selecting trigger particles as TPC-only tracks. However, studies about track splitting showed that hybrid tracks are the best option to perform the current angular correlation analysis. A more extended description will be presented in subsection 3.5.1.

3.3.2 Quality assurance for trigger particles

The amount of trigger particles per event in each centrality bin is illustrated in Figure 3.7. It is observed that the most probable configuration are one or two trigger particle(s) per event. It is also interesting to notice that the multiplicity of trigger particles decreases with decreasing event centrality.
We present the spatial distribution for the selected trigger particles in Figure 3.8. The distribution in η (see Figure 3.9.a) is approximately symmetric around zero. The small gaps observed in the φ-distribution are due to the boundaries between the TPC sectors (Figure 3.9.b) that have a coverage of 20° (~ 0.349 rad).
Studies with Monte Carlo data were performed to obtain the resolution for the three essential variables of the analysis: the track transverse momentum, its azimuthal angle and its pseudo-rapidity. To estimate the resolution, we calculate first the difference between the values obtained with the reconstruction procedure and the quantities coming from the Monte Carlo generation. Figure 3.10 shows the results for the two data taking periods, 2010 and 2011. For trigger particles having a p_{T} range from 5 to 10 GeV/c, the transverse momentum resolution for 2010 and 2011 data are of approximately 4% and 5%, respectively. For higher-p_{T} particles, the resolution in p_{T}

becomes poorer (of about 10-15%) [134]. For this reason, trigger particles with p_{T} larger than 10 GeV/c were not included in the analysis. The resolutions on η are taken as the root-mean square of the distributions with $(2.500 \pm 0.002) \times 10^{-3}$ and $(2.5392 \pm 0.0003) \times 10^{-3}$ units for 2010 and 2011 data, respectively. For the φ-variable, the resolution is about $(2.899 \pm 0.002) \times 10^{-3}$ radians in 2010 data and $(2.687 \pm 0.0003) \times 10^{-3}$ radians for the 2011 period.
In this analysis, the resolution on both η and φ was required to be better than 0.02 units. Note that under this condition, only a very small fraction (0.7%) of trigger particle tracks were rejected. The arrows in Figure 3.10.b) and 3.10.c) delimit graphically our choice. The (small) differences in the width of the distributions, between the two Pb–Pb runs, are due to the fact that the TPC-detector settings for the 2011 run were different from the ones of 2010 run.

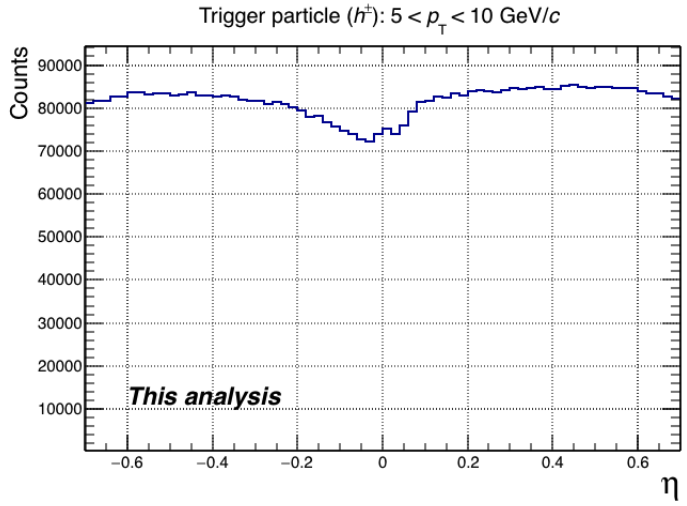

a)

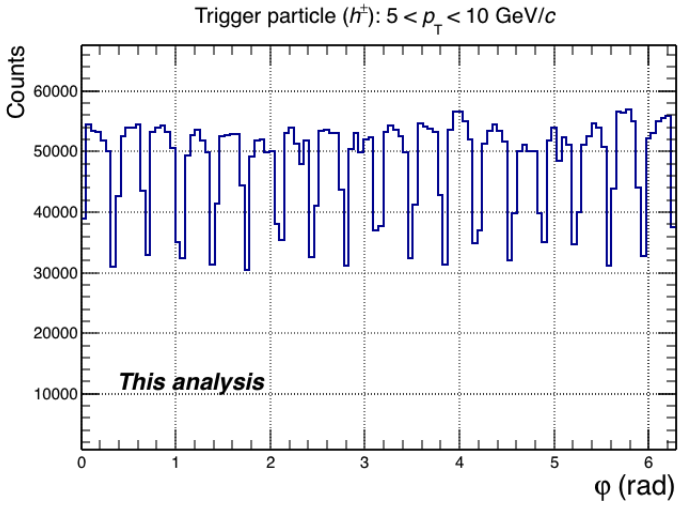

b)

Figure 3.9: a) Trigger particle's η-distribution b) Trigger particle's φ-distribution. Both distributions are shown for the 2011 Pb–Pb data.

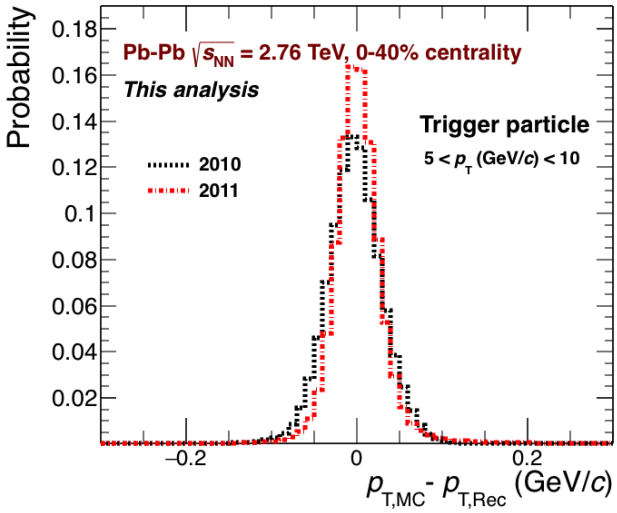

a)

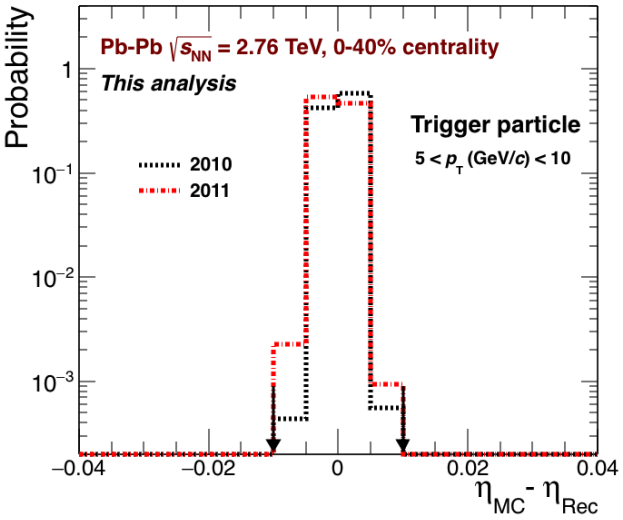

b) in $|\eta_{\mathrm{Trig}}| < 0.7$

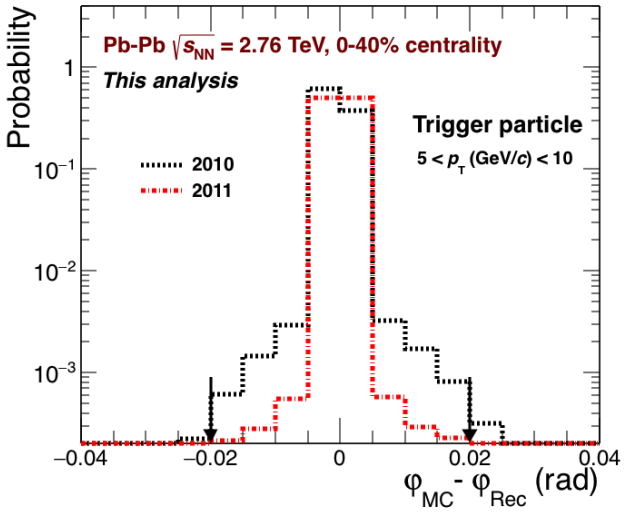

c) in $0 < \varphi_{\mathrm{Trig}} < 2\pi$

Figure 3.10: a) Distribution of the difference between the MC transverse momentum and the reconstructed track transverse momentum of the $h^{\pm}$ trigger particles. b) and c) same distributions for, respectively, the pseudo-rapidity and the azimuthal angle φ. The distributions are shown for 2010 and 2011 Pb-Pb data at at $\sqrt{s_{\mathrm{NN}}} = 2.76$ TeV in the 0-40% centrality selection.

3.4 Selection of the associated-particles (K^0_S and Λ)

The K^0_S and Λ strange and neutral hadrons are commonly known as 'V0 particles' because their largest branching ratio decay is into a positive and a negative particle (*daughter tracks*), leaving footmarks of a 'V' shape in the detector. In the following text we will use this term to refer to these hadrons. The properties of the single-strange hadrons K^0_S, Λ and the main particles that contain a Λ baryon in their decay channel (Σ^0, Ξ and Ω) are sorted in Table 3.5.

Table 3.5: Properties of the strange and multi-strange hadrons [46]. Information about the PDG mass (m_{PDG}), the proper decay length ($c\tau_{PDG}$) and the corresponding branching ratio (B.R.) for the corresponding decay channels are indicated.

Particle	Quark content	m_{PDG} (GeV/c^2)	$c\tau_{PDG}$ (cm)	Decay channel	B.R.
K^0_S	$d\bar{s}+\bar{d}s$	0.497	2.68	$\pi^+\pi^-$	69.2%
Λ	uds	1.115	7.98	$p\pi^-$	63.9%
Σ^0	uds	1.192	2.2×10^{-14}	$\Lambda\gamma$	100%
Ξ^0	uss	1.314	8.71	$\Lambda\pi^0$	99.5%
Ξ^-	dss	1.321	4.91	$\Lambda\pi^-$	99.8%
Ω^-	sss	1.672	2.46	ΛK^-	67.8%

3.4.1 K^0_S and Λ reconstruction

In ALICE, the V0 particles are reconstructed through their topological decay: $K^0_S \to \pi^+\pi^-$ and $\Lambda \to p\pi^-$. After selecting two reconstructed tracks in the TPC with opposite charge signals, the distance of closest approach between the two tracks is calculated (DCA), thus determining the decay point of the V0 candidate. The combination of pair of tracks whose DCA is larger than a given threshold are rejected. Further selections are applied to the V0 candidates. The information of each daughter track is propagated back to the primary interaction, requiring to have a minimum distance of closest approach to the primary vertex (b) to avoid selecting primary particles as daughter tracks. With the information of the momentum components of the tracks, the momentum and the mass of the V0 candidate is reconstructed following the conservation law of energy and momentum. In order to select primary V0 particles, the direction of the reconstructed momentum vector is required to point to the primary vertex position by applying a cut in the cosine of the pointing angle ($\cos(\theta_p)$). A graphical representation of the topological decay is shown in Figure 3.11 for the specific case of K^0_S.
The main advantage of working with these strange particles is that we can apply the same reconstruction technique for both K^0_S (meson) and Λ (baryon) over a wide momentum range from 0.4 GeV/c (0.6 GeV/c for Λ) to 12 GeV/c for the Pb–Pb data in ALICE [117]. This reconstruction technique also provided a good control of the systematic uncertainties. An example of the K^0_S and Λ reconstructed invariant mass is shown in Figure 3.12. More details about the signal extraction will be given in Section 3.5.

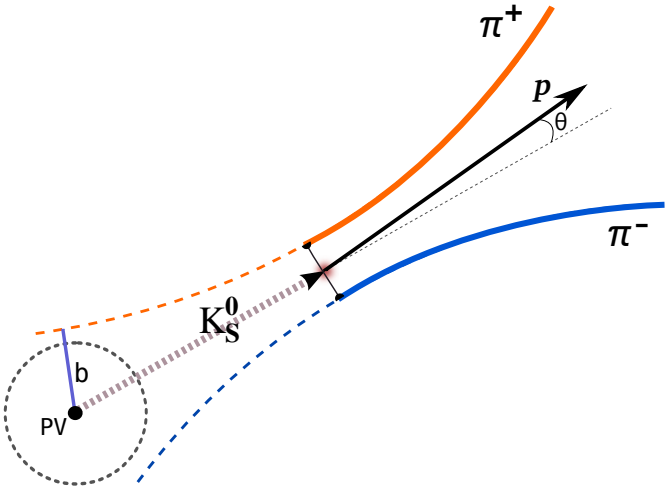

Figure 3.11: Illustration of the topological decay of the V0 particle.

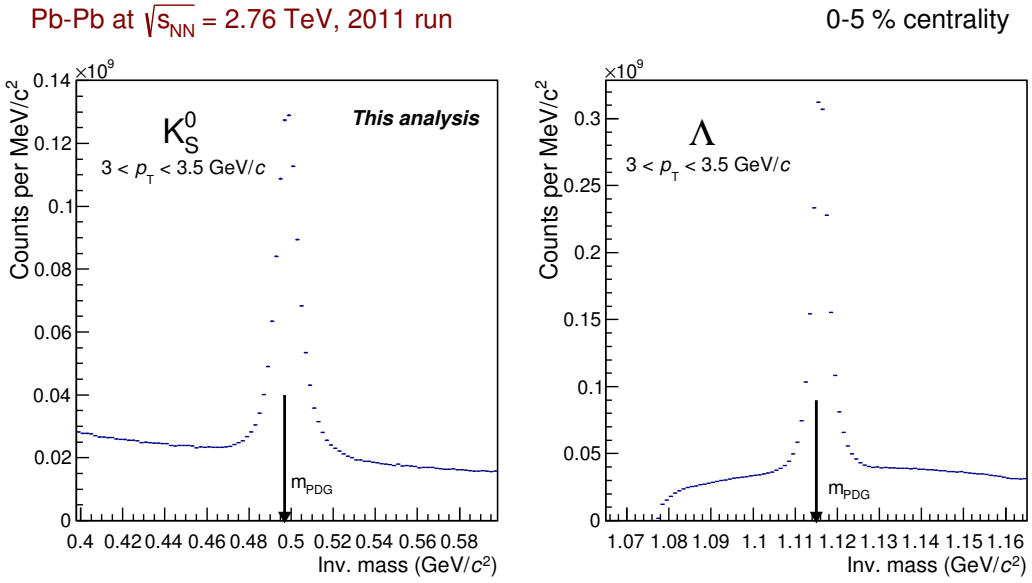

Figure 3.12: Reconstructed invariant mass distributions of K^0_S (left panel) and Λ (right panel) for Pb–Pb collisions at $\sqrt{s_{NN}} = 2.76$ TeV [117]. The distributions were obtained from the analysis of the data taken in 2011.

Table 3.6: Selections of daughter tracks and V0 candidates.

Daughter track selections	
Opposite charge for the daughter tracks	Yes
TPC refit	Yes
Number of crossed TPC pad rows	≥ 70
Pseudo-rapidity range	< 0.8
Transverse momentum range	> 0.16 GeV/c
Impact parameter with respect to the primary vertex (b)	> 0.1 cm
Distance of closest approach between the daughter tracks (DCA)	< 1 cm
Armenteros cut (for K^0_S)	$p_T^{arm} > 0.2\|\alpha^{arm}\|$
V0 candidate selections	
Pseudo-rapidity	$\|\eta\| < 0.7$
Cosine of the pointing angle ($\cos(\theta_p)$)	> 0.998
Transverse fiducial volume	$5 < r_T < 100$ cm
Pseudo-proper decay length ($l_T m/p_T$)	$< 3\, c\tau_{PDG}$

Track and topological selection

The default requirements applied for the daughter particles and the selection of the V0 candidates, used in this analysis, are listed in Table 3.6. A selection on the Armenteros-Podolanski variables was applied only for K^0_S, to prevent Λ and $\overline{\Lambda}$ from being reconstructed as background in the K^0_S invariant mass. This selection allows for a better control on the systematic uncertainties. The Armenteros-Podolanski variables, p_T^{arm} and α^{arm}, are based on the simple properties of two-body decays. Here, p_T^{arm} is the projection of the positive (negative) daughter momentum on the plane perpendicular to the V0 momentum, and $\alpha^{arm} = (p^+_{\parallel} - p^-_{\parallel})/(p^+_{\parallel} + p^-_{\parallel})$, where $p^+_{\parallel}$ ($p^-_{\parallel}$) is the projection of the positive (negative) daughter momentum on the momentum of the V0 particle [117]. To select K^0_S, the relation $p_T^{arm} > 0.2|\alpha^{arm}|$ is required (see Figure 3.13).
The position in the transverse plane, r_T, of the reconstructed secondary vertex[5] was required to be within a fiducial 'volume' of 5-100 cm. The lower value was chosen to minimize systematic effects introduced by efficiency corrections [117]. To decrease even more the background contribution, the selection in the pseudo-proper decay length ($l_T m/p_T$) was introduced in the transverse plane.
The two-hadron angular correlation distributions were obtained for K^0_S and Λ with transverse momenta within the range 2-7 GeV/c, where the baryon-to-meson enhancement has been observed from inclusive Pb–Pb collisions [117].

Distribution and resolution in φ and η

The K^0_S and Λ distributions of the geometrical variables φ and η are shown in Figure 3.14 for different p_T-ranges. As previously seen with the trigger particles, the φ-distributions present

[5] Position at where the particle decays.

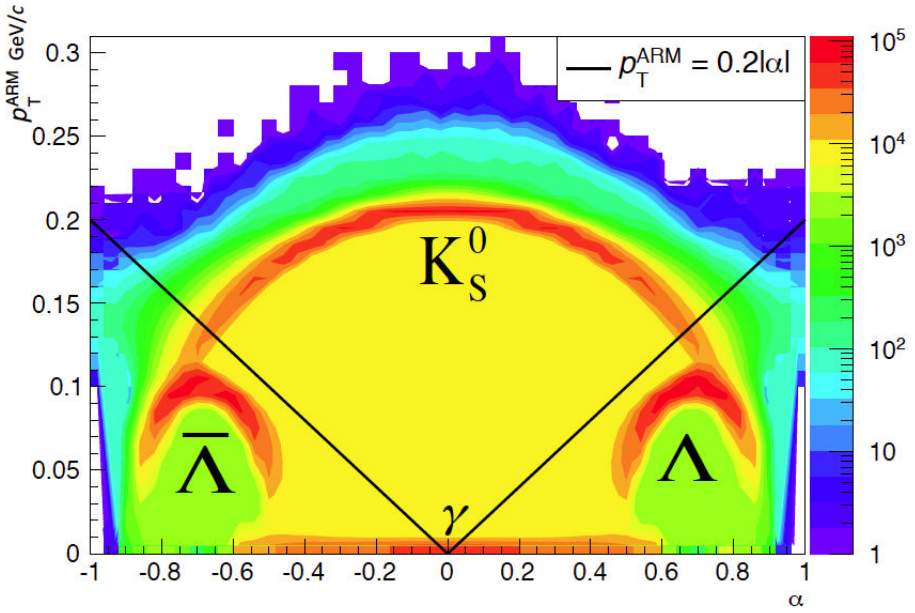

Figure 3.13: Distribution of the Armenteros-Podolanski variables ($p_{\mathrm{T}}^{\mathrm{arm}} vs. \alpha^{\mathrm{arm}}$). The highest density regions represent the kinematical decay of the V0 particles ($\mathrm{K}^0_{\mathrm{S}}$, Λ and $\overline{\Lambda}$) and the γ-conversion. The continuous line ($p_{\mathrm{T}}^{\mathrm{arm}} = 0.2|\alpha^{\mathrm{arm}}|$) delimits the area for selecting only $\mathrm{K}^0_{\mathrm{S}}$ candidates [159].

some regular gaps corresponding to the TPC sectors. In the case of V0 particles, the pseudo-rapidity distribution is not uniform over the whole selected η-range. We observe that, below $p_{\mathrm{T}} < 4$ GeV/c, there is a significant drop at the edges of the distribution, which is particularly visible for the lowest p_{T} values. This effect is due to the loss of a daughter track outside the detector acceptance.

The resolution in φ and pseudo-rapidity was obtained for $\mathrm{K}^0_{\mathrm{S}}$ and Λ using MC simulated events using the HIJING event generator. The distribution of the difference between the MC azimuthal angle (pseudo-rapidity) and the reconstructed azimuthal angle (pseudo-rapidity) is plotted in Figure 3.16 (Figure 3.15) for two different p_{T} ranges 2-3 GeV/c and 5-7 GeV/c. The corresponding RMS values of the distributions for such variables are shown in Table 3.7 for the 2010 and 2011 data. We observe that the resolutions for neutral strange hadrons have larger values than to the ones observed for the primary charged particles.

As already mentioned in section 3.3, the arrows pointing to the values ± 0.02 in the Figures 3.15 and 3.16 represent the range with 99.3% of resolution in the respective variables. We can consider this limit as a rough estimation for the resolution.

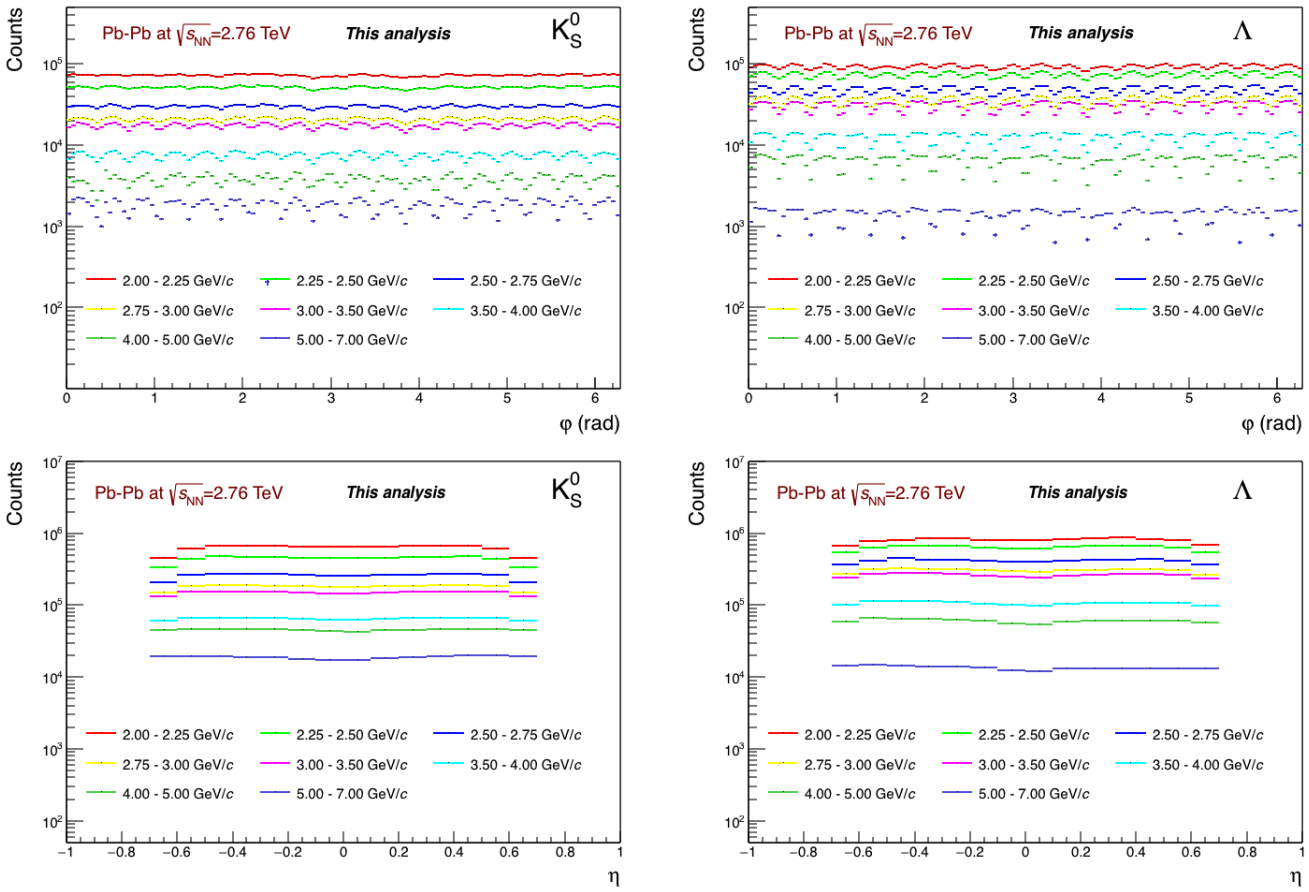

Figure 3.14: Distributions in the azimuthal angle (φ) (upper panels) and in pseudo-rapidity (η) (lower panels) of the inclusive K^0_S and Λ production in the p_T-bins used in the angular correlation studies.

Table 3.7: Resolution of the η and φ variables for K^0_S and Λ obtained from the RMS of the distributions in Figures 3.15 and 3.16.

p_T (GeV/c)	K^0_S		Λ	
	RMS_η 2010 (2011) $\times 10^{-3}$	RMS_φ (rad) 2010 (2011) $\times 10^{-3}$	RMS_η 2010 (2011) $\times 10^{-3}$	RMS_φ (rad) 2010 (2011) $\times 10^{-3}$
2-3	3.731 ± 0.005 (3.923 ± 0.002)	4.052 ± 0.006 (4.074 ± 0.002)	4.454 ± 0.011 (4.559 ± 0.004)	4.881 ± 0.009 (4.848 ± 0.004)
5-7	3.506 ± 0.019 (3.693 ± 0.007)	4.000 ± 0.021 (4.437 ± 0.009)	3.086 ± 0.028 (3.695 ± 0.013)	4.041 ± 0.028 (4.690 ± 0.017)

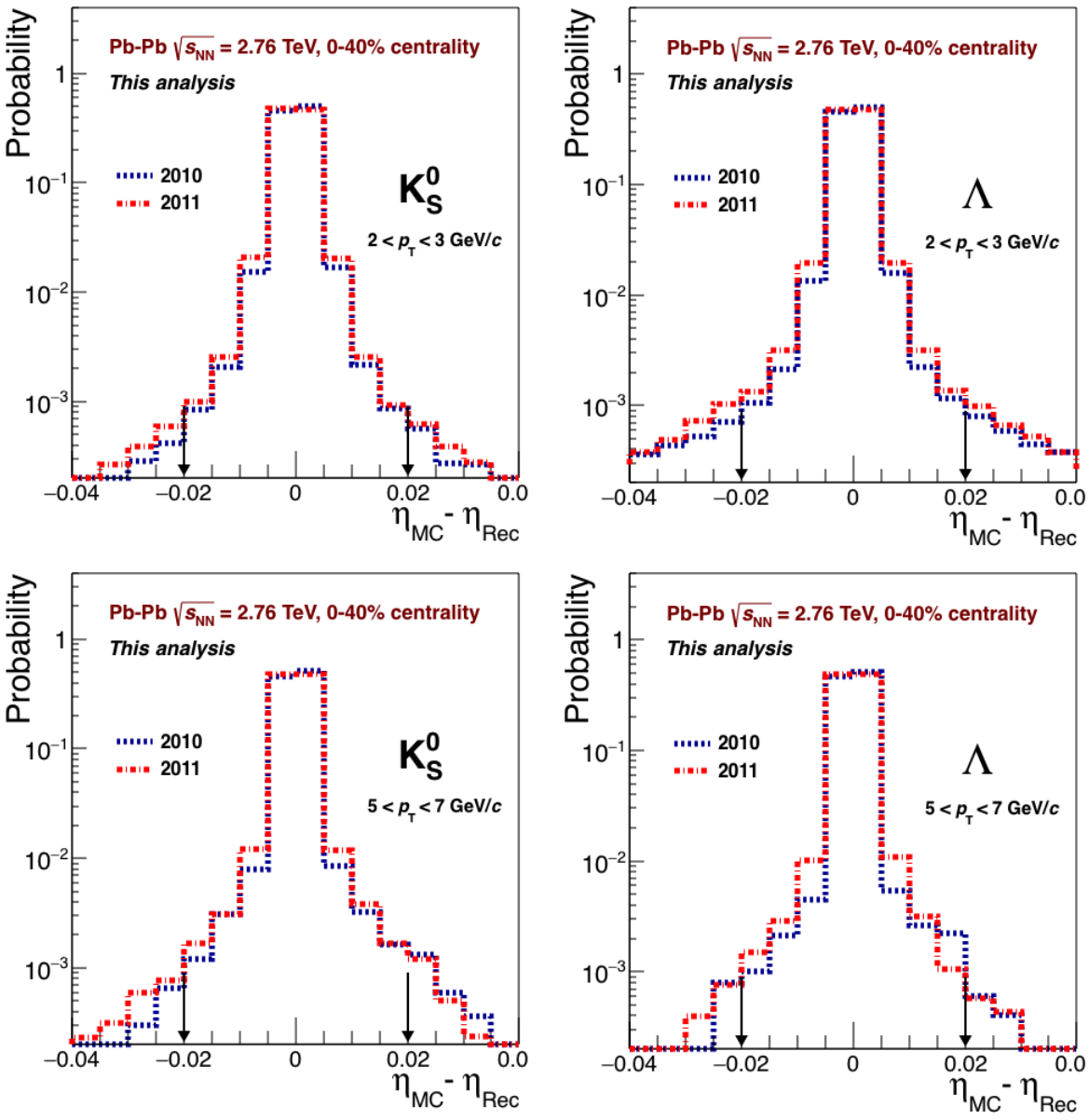

Figure 3.15: Resolution in **pseudo-rapidity** for K^0_S (left panels) and Λ (right panels) in two different p_T-ranges: 2-3 GeV/c (upper panels) and 5-7 GeV/c (lower panels). The arrows delimit the best resolution to be considered for this variable. $\overline{\Lambda}$ are not considered.

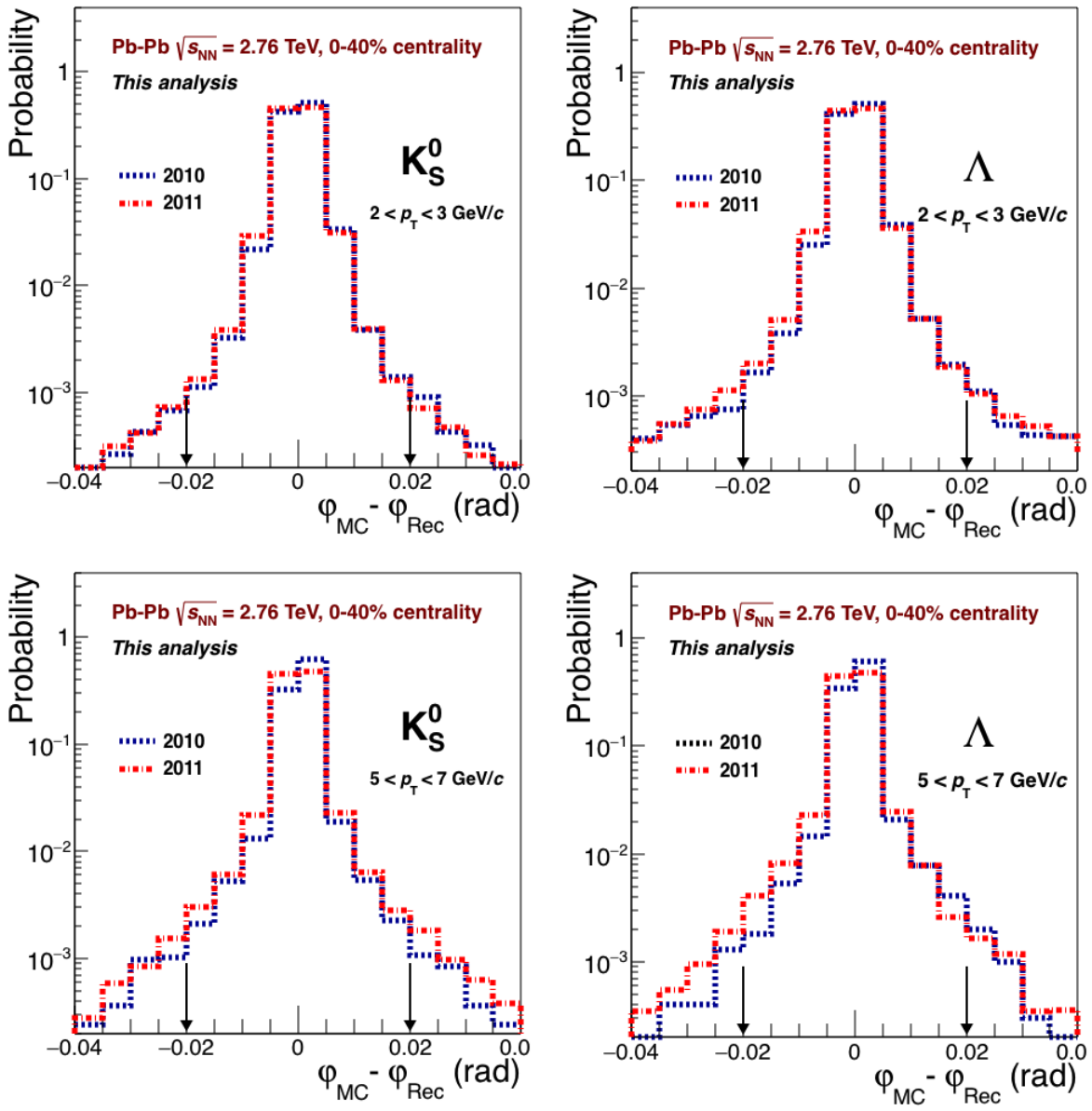

Figure 3.16: Resolution in the φ **angle** for K^0_S (left panels) and Λ (right panels) in two different p_T-ranges: 2-3 GeV/c (upper panels) and 5-7 GeV/c (lower panels). The arrows delimit the best resolution to be considered for this variable.

Invariant mass resolution for K^0_S and Λ

The invariant mass distribution obtained for each hadron (as shown in Figure 3.12) can be fitted with a Gaussian function (with the mean fixed at the PDG mass value of the hadron) plus a second order polynomial to describe the combinatorial background. From the fit result of the Gaussian function, we can extract the invariant mass resolution represented by the Gaussian width (σ).

Figure 3.17 shows the invariant mass resolution of K^0_S and Λ for the two centrality selections 0-5% and 20-40%. The p_T-binning is the same as the one used previously in [117]. It is observed that σ depends on p_T, since the larger the transverse momentum, the worse the p_T-resolution. For the Λ baryon, the invariant mass width increases slightly in the 2011 run with respect to the 2010 data. This feature is mainly due the different run conditions for the TPC. For K^0_S, the invariant mass is similar for both runs.

A fit to a linear polynomial function was performed in the transverse momentum range from 2 to 8 GeV/c. To obtain the best results, the likelihood option in ROOT was used. The information of the fit results for 2010 and 2011 Pb–Pb data are added to each panel on Figure 3.17 (see

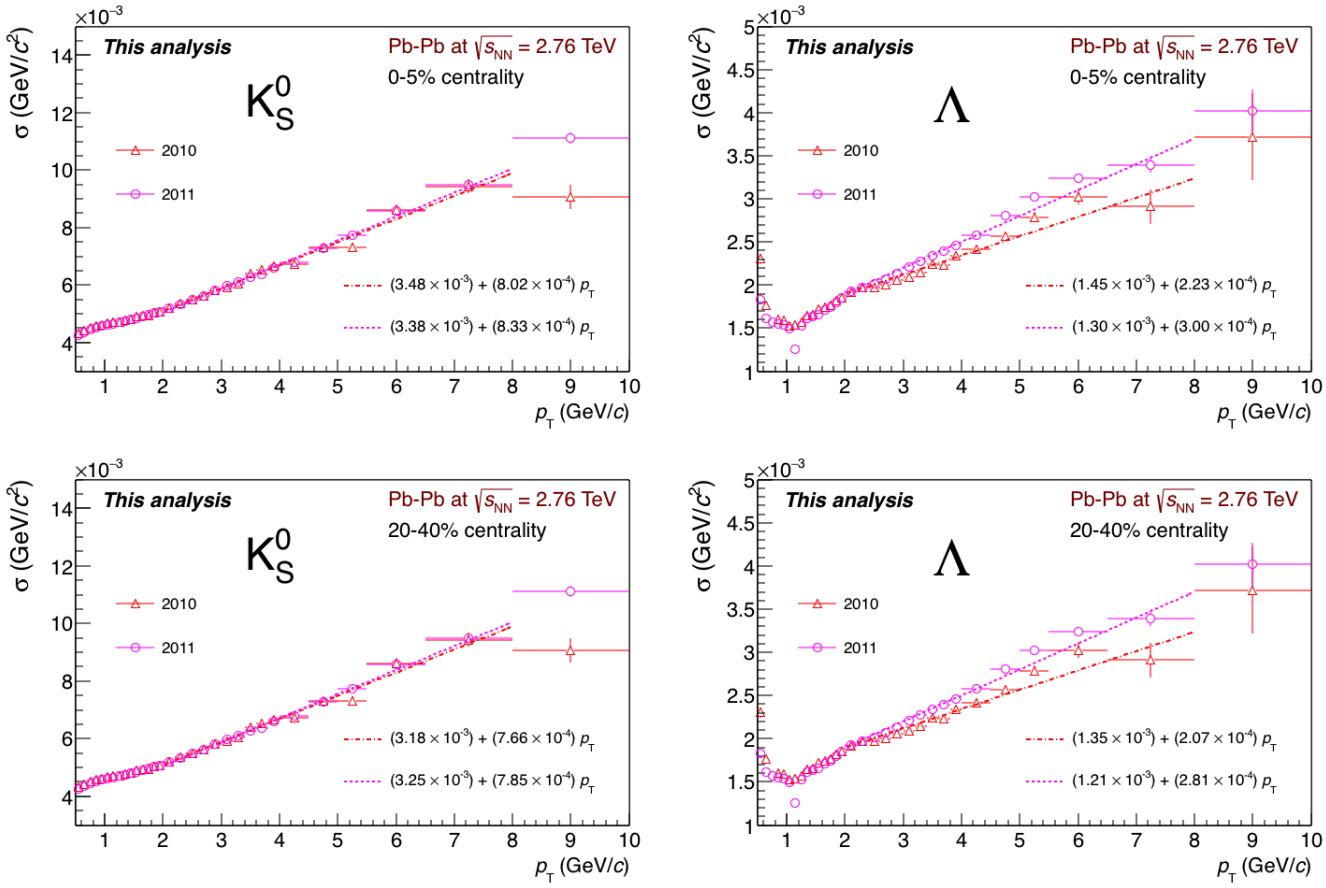

Figure 3.17: Invariant mass width of the K^0_S (upper panels) and Λ (lower panels) for 0-5% centrality (left panels) and 20-40% centrality (right panels). The results are presented for the Pb–Pb data of the 2010 and 2011 runs. The $\overline{\Lambda}$ is not considered for the results.

the lower right corner). The dashed-dotted red line corresponds to the 2010 data fit, while the dotted magenta line is for 2011 data.

Efficiency×Acceptance×B.R. of inclusive primary V0 candidates

The reconstruction efficiency for K^0_S and Λ has been studied with MC simulated events using the HIJING event generator and the GEANT3 code. One of the important ingredient to estimate this reconstruction efficiency is the MC spectrum of the generated particles in HIJING. Figure 3.18 shows the K^0_S and Λ generated MC p_T-spectra used in the evaluation of the reconstruction efficiency for 2010 and 2011 data. Only particles generated by HIJING are included, i.e. the injected particles mentioned in 3.4.1 are rejected. The distributions are normalized to the total number of counts and the bin width in p_T, thus the principal information to extract from these plots is the probability density of the V0 particles to be produced at a given p_T range in the Monte Carlo generator. The main difference between the two generated datasets is observed at high-p_T ($p_T > 3$ GeV/c) for K^0_S and Λ in the shown centralities. This effect comes from the different settings in the generation of the HIJING events. In the MC 2010 dataset the V0 particle production was set with the θ-range from 45° to 135° ($|\eta| < 0.88$) and a p_T-range from zero to 10 GeV/c, while in the MC 2011 dataset the former variables were changed to a rapidity selection within ±1.2 and the p_T range was extended up to 30 GeV/c.

The reconstruction efficiency was evaluated as the ratio defined in Equation 3.6. The denominator is the total amount of generated hadrons in Monte Carlo data within the pseudo-rapidity selection of ±0.7 as a function of p_T. The Λ baryons produced by Σ^0 decays are also considered as primary generated particles, since, at the reconstruction level it is not possible to disentangle the Λ's produced in these electromagnetic decays from the Λ's produced directly in the primary collisions. The numerator in the ratio of Equation 3.6 is the number of reconstructed particles that pass the selection cuts and match the Monte Carlo identity of the respective particle to remove the combinatorial background contribution. Figure 3.19 shows the obtained reconstruction efficiency (eff) multiplied by the detector acceptance (Accep) and the branching ratio (B.R.) (see Table 3.5), for K^0_S and Λ measured in both 2010 and 2011 data taking periods. It is observed that the eff × Accep. × B.R. has a dependence in pseudo-rapidity, which is more evident for large values in $|\eta|$ and at transverse momenta below 4 GeV/c (see Figure 3.20).

$$\text{eff} \times \text{Accep.} \times \text{B.R.}\ (p_T) \;=\; \frac{\text{MC associated particles}\ (p_T \mid |\eta_{\text{Gen}}| < 0.7)}{\text{MC generated particles}\ (p_T \mid |\eta_{\text{Gen}}| < 0.7)}. \tag{3.6}$$

In the equation 3.6, an invariant mass selection of $\pm 4\sigma$ is considered in the numerator as applied in the signal extraction for the reconstructed data. The σ values are taken from the fit functions obtained in the previous subsection. It has been noted that the efficiencies evaluated in the invariant mass and with a looser selection in the integrated invariant mass, over the range from 0.398 to 0.598 GeV/c^2 for K^0_S and from 1.065 to 1.165 GeV/c^2 for Λ candidates, lead to differences of less than 4% for K^0_S (less than 3% for Λ) at a transverse momentum of 7 GeV/c .

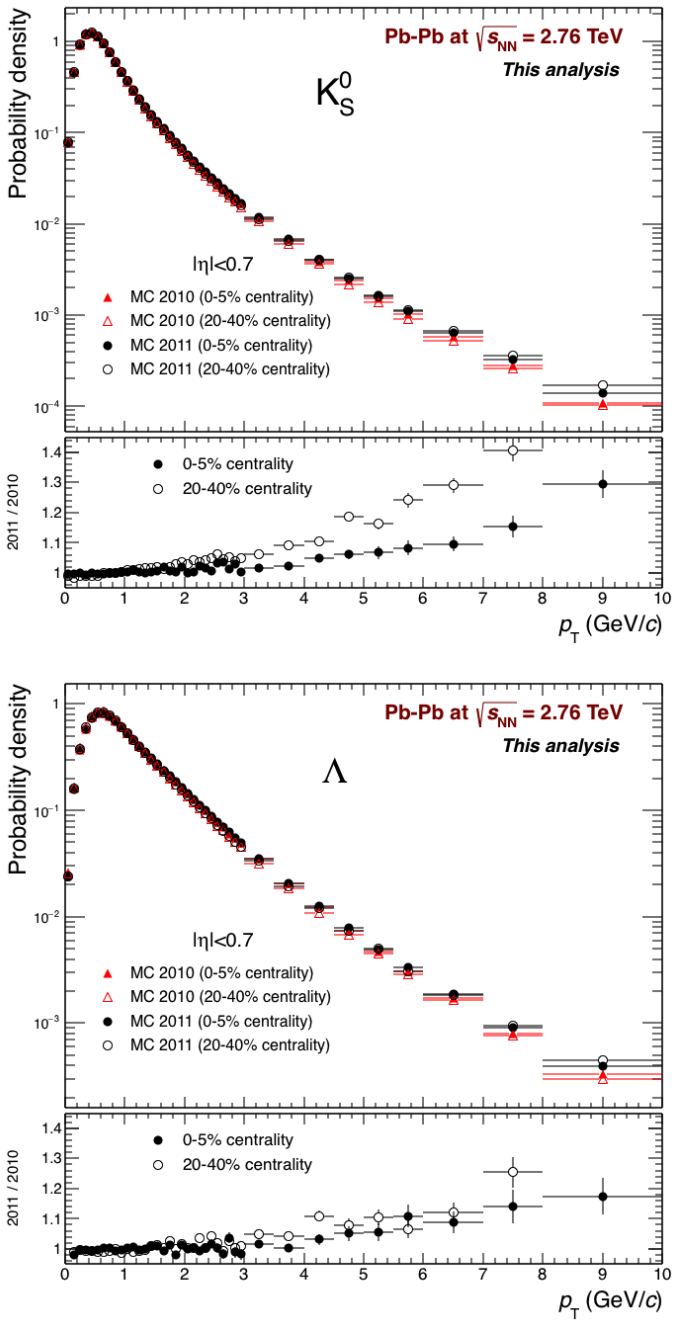

Figure 3.18: Probability density for K^0_S (upper panel), and Λ (bottom panel), to be produced at a given p_T in true Monte Carlo. The distributions are shown for two event centrality intervals, 0-5% and 20-40%. The $\overline{\Lambda}$ particles are not included.

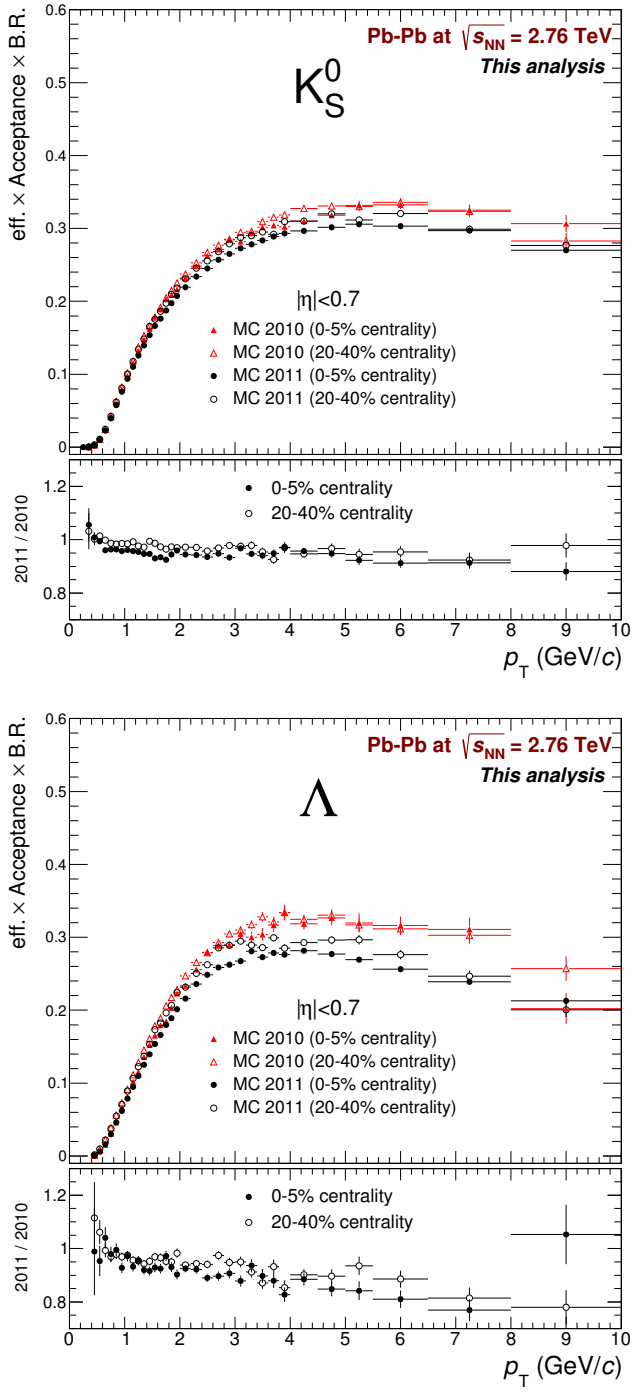

Figure 3.19: Efficiency×Acceptance×B.R. of K^0_S (upper panel) and Λ (bottom panel) for both data taking periods (see text for details). This is shown for two centrality selections 0–5% and 20–40%. The baryon $\overline{\Lambda}$ is not included in the efficiency estimation.

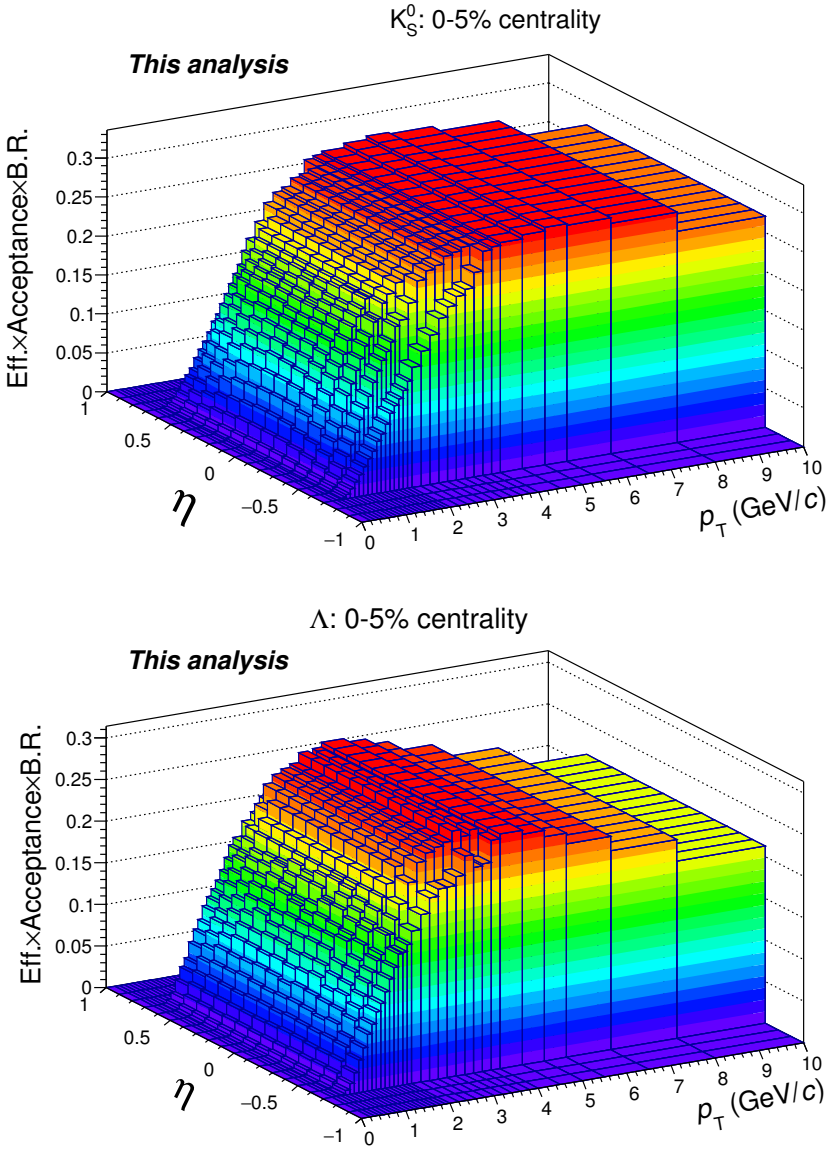

Figure 3.20: Efficiency×Acceptance×B.R. as function of pseudo-rapidity and transverse momentum of K^0_S and Λ for the 2011 data taking period in the 0–5% centrality selection. The baryon $\overline{\Lambda}$ is not considered in the efficiency estimation.

3.4.2 Feed-down contribution (Decay of Ξ into Λ)

Decays of Ξ and Ω multi-strange hyperons contribute to the production of Λ baryons. A fraction of Λ's produced via these decays survive the topological cuts used in the analysis to select primary Λ's. It is therefore important to correct the raw lambda yield for the feed-down contribution.

An estimation of the Λ feed-down (fd) from Ξ^- and Ξ^0 is presented in [117]. To correct the raw yield for the feed-down contribution, it is necessary to obtain a Monte Carlo matrix that correlates in p_T the production of the Λ feed-down with its Ξ mother. After the reconstructed Λ passes the selection cuts, we verify if the baryon is a decay product from Ξ using the MC information. If this happens to be the case, the feed-down **FD** matrix is filled with the information of the p_T^{Λ} vs p_T^{Ξ} (left panel in Figure 3.21). The ratio of the raw p_T spectra of Ξ in experimental data to the one in the Monte Carlo data is obtained. The values of this ratio are used to re-weight the **FD** matrix to obtain the final feed-down contribution to the Λ raw yield, as a function of p_T (see equation 3.7).

$$fd(p_T^{\Lambda}) = \sum_{i,j} \mathrm{FD}_{\mathrm{Raw}}(i,j)\, \frac{\text{Corrected yield}^{\Xi}_{\mathrm{Data}}(p_{T,j})}{\text{True yield}^{\Xi}_{\mathrm{MC}}(p_{T,j})}. \tag{3.7}$$

The results show that the feed-down contribution is $\sim 25\%$ at $p_T^{\Lambda} \sim 1$ GeV/c and it decreases down to $\sim 10\%$ at high p_T, with an estimated error of the feed-down of about 5% for all the p_T-ranges. In addition, the feed-down contribution is found to be centrality-independent.

Because of their much lower production rate, the feed-down contribution from Ω decays is found to be negligible.

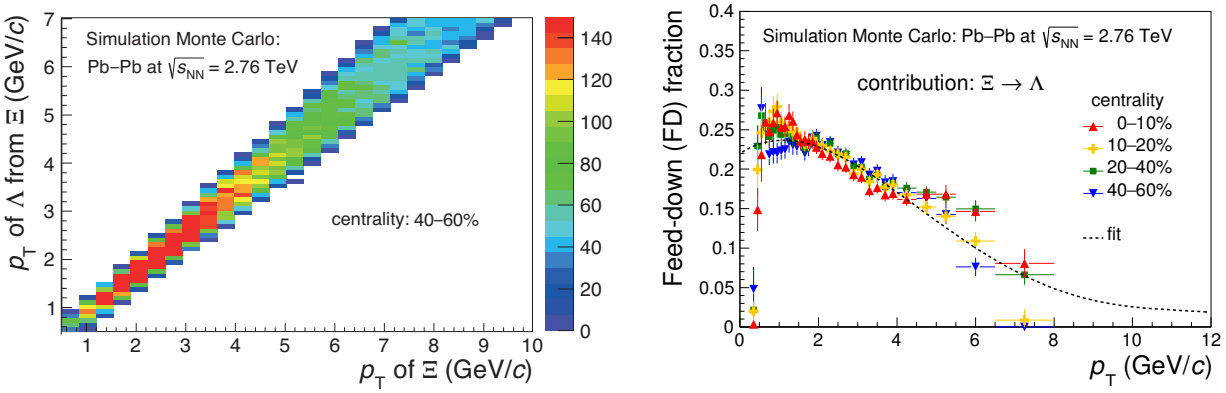

Figure 3.21: Monte Carlo results for the correlation between the transverse momentum of the Λ particle coming from a Ξ decay and the transverse momentum of the mother Ξ (left panel). Correction factor of the Λ feed-down obtained from [117] for different centrality selections (right panel).

3.5 Construction of $h^{\pm}$-V0 correlations

To get the angular correlation distribution $1/N_{\mathrm{Trig}}\,\mathrm{d}^2N/\mathrm{d}\Delta\varphi\,\mathrm{d}\Delta\eta$, the following method is applied.

◇ ***Centrality determination***

The events are classified according to the collision centrality. We perform the angular correlations in two different centrality intervals: {0–10%, 20–40%}.

For the centrality interval 0–10%, because of the large particle multiplicity, the analysis is done in sub-intervals of 0–5% and 5–10%, to have a more accurate correction of the correlation distributions. Once all the corrections are performed, the two-dimensional angular correlations are added to construct the final distribution corresponding to the 0–10% centrality class.

◇ ***Trigger particles***

In each event, the trigger particles (charged primary particles, $h^{\pm}$) are selected according to the cuts presented in subsection 3.3. This is done in the interval from 5 to 10 GeV/c in the transverse momentum of the trigger particles. The upper limit of 10 GeV/c is introduced because the p_{T} resolution for tracks with higher p_{T} is poorer and also due to the lack of statistics of trigger particles at high p_{T}. The selected trigger particles are required not to be a daughter track from a V0 candidate. In the analysis, this rejection is done by comparing the track ID between the trigger particle track and the daughter track.

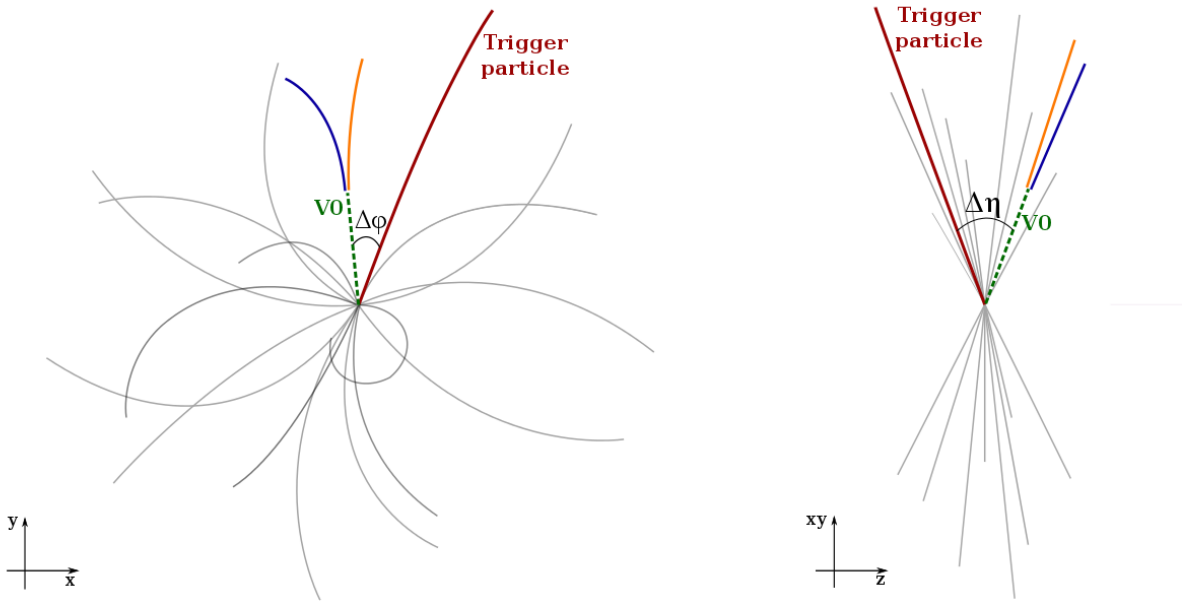

Figure 3.22: Representation of the angular correlations between the trigger particle and the associated particle ($\mathrm{K}^0_{\mathrm{S}}$ or Λ). The left picture represent the correlation in the azimuthal angle ($\Delta\varphi$), while the correlation in pseudo-rapidity ($\Delta\eta$) is illustrated in the right scheme.

This is needed to remove the potential non-physical auto-correlations.

◇ K^0_S ***and*** Λ ***candidates***
The K^0_S and Λ candidates are reconstructed in the event with a transverse momentum between 2 to 7 GeV/c as described before in subsection 3.4.1. The transverse momentum of the associated particle should be lower than the one of the trigger particle, i.e, $p_{\mathrm{T,Assoc}} < p_{\mathrm{T,Trig}}$.

◇ ***Raw angular correlations***
The angular correlations are studied in eight different p_{T} intervals of the associated particles and defined as follows:

$$\{2.0\text{–}2.25,\ 2.25\text{–}2.5,\ 2.5\text{–}2.75,\ 2.75\text{–}3.0,\ 3.0\text{–}3.5,\ 3.5\text{–}4.0,\ 4.5\text{–}5.0,\ 5.0\text{–}7.0\}\ \mathrm{GeV}/c.$$

This binning is chosen to obtain the yield per trigger in the bulk. However, the binning used to get the associated-to-jet yield considers the merging of the first four bins into two: 2.0–2.5, 2.5–3.0 GeV/c. The principal motivation is to have larger statistics for a better definition of the peak structure that appears from the particles produced in association to the trigger particle.
For a given 2-cm-wide interval of the primary vertex position, within the 20-cm span range of z_{vtx}, the raw angular correlations between the trigger particles and the V0 candidates in the azimuthal angle and in pseudo-rapidity are constructed as (see Figure 3.22):

$$\Delta\varphi = \varphi_{\mathrm{Trig}} - \varphi_{\mathrm{Assoc}} \text{ and } \Delta\eta = \eta_{\mathrm{Trig}} - \eta_{\mathrm{Assoc}}.$$

The reconstructed invariant mass of V0 candidates is then saved for each $\Delta\varphi \times \Delta\eta$ area. The V0 candidates kept for the correlation distributions have an invariant mass range from 0.398 to 0.598 GeV/c^2 for K^0_S candidates and from 1.065 to 1.165 GeV/c^2 for Λ candidates. We will denote these correlation distributions as $(\mathrm{d}^2N_{\mathrm{Candidates}}/\mathrm{d}\Delta\varphi\mathrm{d}\Delta\eta)|_{z_{\mathrm{vtx,i}}}$, where *Candidates* stand for signal plus background contributions in the specified invariant mass intervals.

◇ ***On-the-fly analysis corrections***
The raw angular correlations are corrected by the two following factors:

1. A weight considering the non-flat centrality distribution in the centrality bin 9-10% (see Figure 3.23). This weight is obtained by fitting the centrality distribution in the range 0-9% centrality to a constant and by dividing the result by the number of entries in the centrality bins 9-10%. The purpose is to increase the contribution of the 9-10% bin to the same level as the 0-9% centrality distribution.
2. The reconstruction efficiency (eff × Accep × B.R.) as function of the pseudo-rapidity and the transverse momentum as showed in Figure 3.20. To avoid the η-fluctuations of the efficiency, the η-integrated efficiency was used in the η-range where the efficiency shows to be constant. For example, above 4 GeV/c in p_{T} the efficiency is taken as the integral in $|\eta| < 0.7$.

The $\overline{\Lambda}$ candidates are not considered for the current angular correlation analysis.

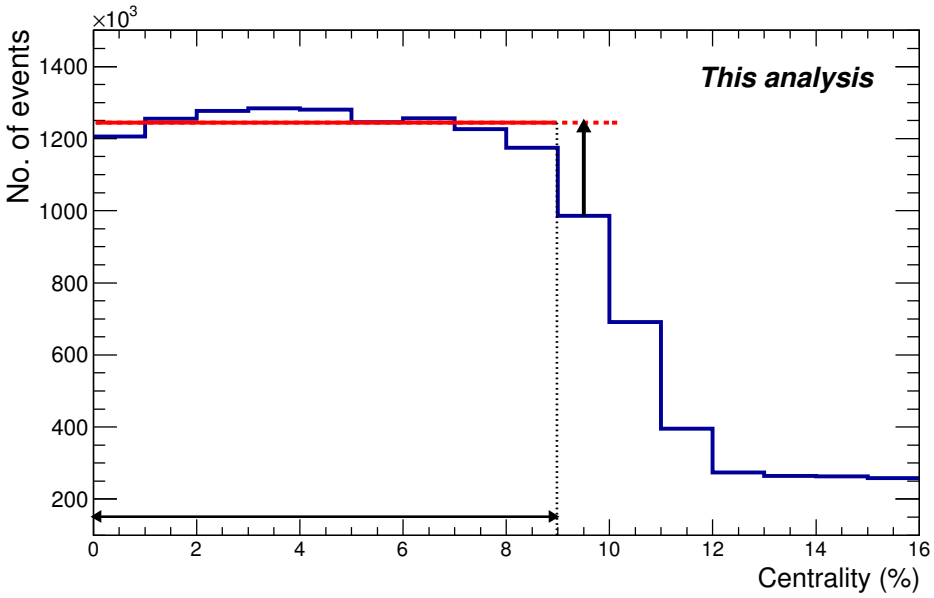

Figure 3.23: Event centrality distribution in the 0-16% range for the 2011 Pb–Pb collisions. A step in the distribution is visible within the range vale 9-12% of centrality. This feature is caused by the online trigger centrality selection during the 2011 data taking. The continuous and dashed red lines represent the centrality range in this analysis. The non-uniformity of the distribution in the 9-10% centrality interval is scaled to the average level of the 0-9% centrality range as indicates with the vertical arrow.

◊ ***Pair-acceptance correction with event mixing***

After the trigger and the associated particles are selected, we correct the two-dimensional angular correlations for the limited acceptance of the detector which leads to losses of trigger-associated pairs. For example, this loss is reflected when the final particles (trigger particle or the decay products of the V0 particles) traverse the inefficient boundaries of the TPC sectors, or simply, they end-up outside the acceptance of the detector ($|\eta| > 0.8$). In the two cases, the particles can not be recovered in the reconstruction part.

The pair-acceptance correction is applied by using the mixed-event technique for the previously mentioned intervals of centrality, z position of the primary vertex and transverse momentum of the associated particles.

To construct the mixed-event distributions, we consider approximately 1000 trigger particles for each interval in centrality and $z_{\rm vtx}$. About 1.7×10^6 events, with at least, one V0 particle, were used for the associate particle. Then, the distance in φ and η between the trigger particles and the V0 candidates coming from two different events ($\rm ev_1$ and $\rm ev_2$) is calculated:

$$\Delta\varphi_{\rm ME} = \varphi_{\rm Trig}|_{\rm ev_1} - \varphi_{\rm Assoc}|_{\rm ev_2} \text{ and } \Delta\eta_{\rm ME} = \eta_{\rm Trig}|_{\rm ev_1} - \eta_{\rm Assoc}|_{\rm ev_2}.$$

The events $\rm ev_1$ and $\rm ev_2$ belong to the same interval of centrality and $z_{\rm vtx}$ to ensure similar acceptance for both events.

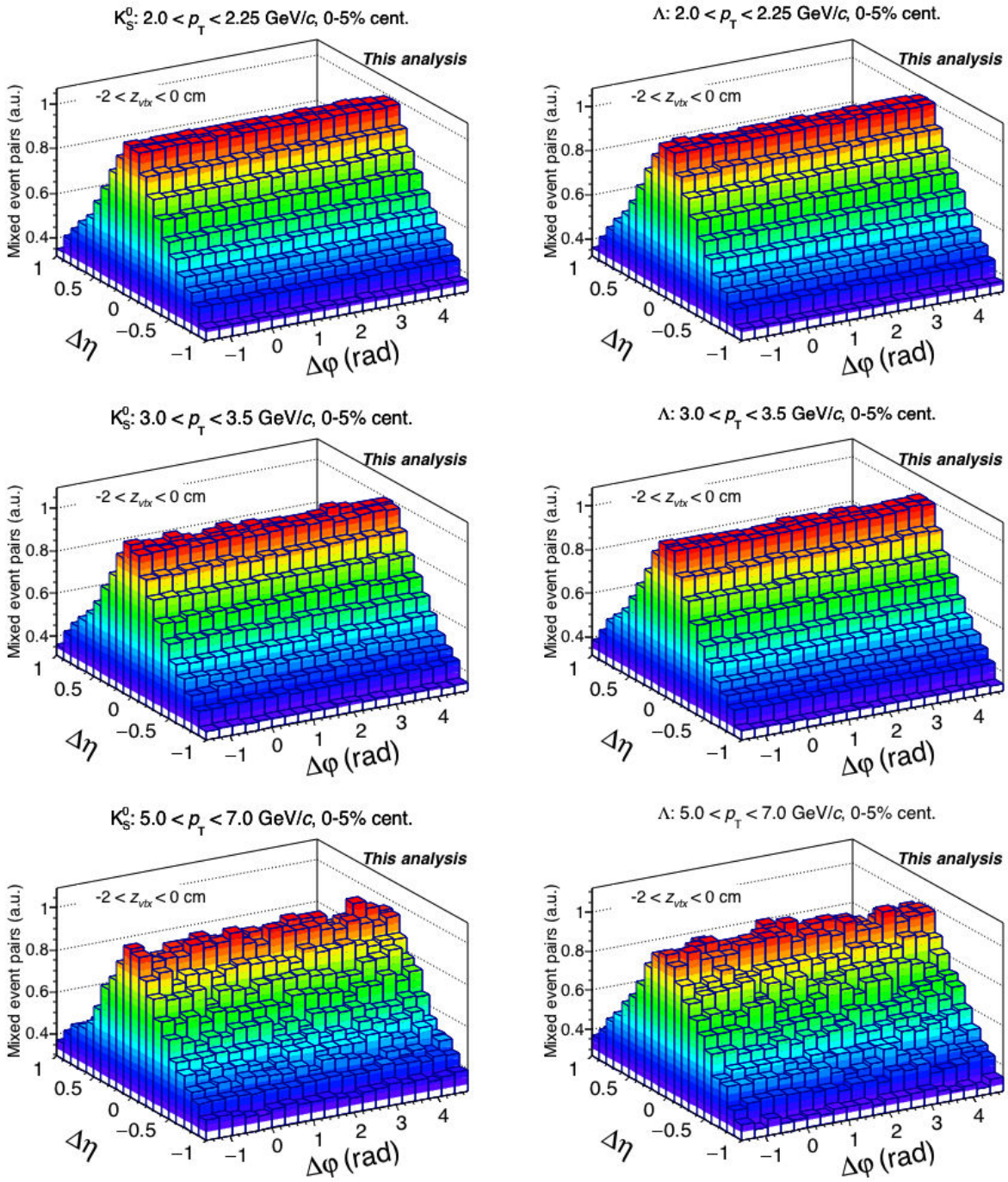

Figure 3.24: Mixed-event distributions for K^0_S candidates (left distributions) and Λ candidates (right distributions), for events with z-vertex position $-2 < z_{\mathrm{vtx}} < 0$ cm. The results are presented for different p_T ranges of the associated particle: $2.0 < p_\mathrm{T} < 2.25$ GeV/c (upper panels), $3.0 < p_\mathrm{T} < 3.5$ GeV/c (middle panels) and $5.0 < p_\mathrm{T} < 7.0$ GeV/c (lower panels). The distributions are shown for the most central collisions (0-5% centrality class) obtained from the analysis of the 2011 Pb–Pb data.

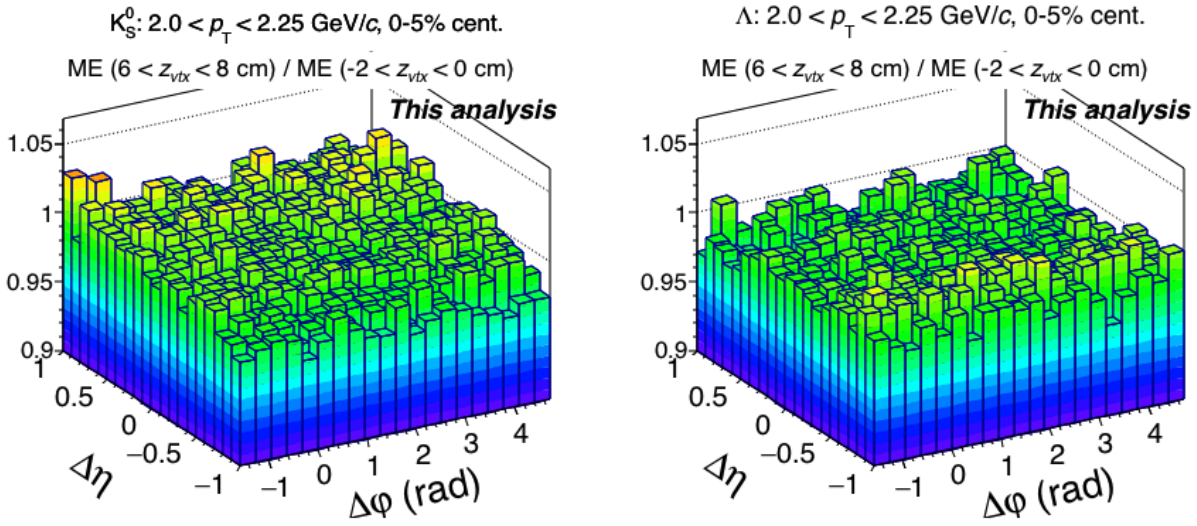

Figure 3.25: Ratio of the mixed event angular correlation distribution obtained for $6 < z_{\rm vtx} < 8$ cm to the one corresponding to $-2 < z_{\rm vtx} < 0$ cm. We present the results for the $\rm K^0_S$ candidates (left panel) and Λ candidates (right panel).

For the event mixing, the V0 candidates are selected in an invariant mass range from 0.398 to 0.598 GeV/c^2 for $\rm K^0_S$ candidates and from 1.065 to 1.165 GeV/c^2 for Λ candidates. The distributions corresponding to the mixed-event are also corrected for the non-flatness of the centrality distribution (as seen in Figure 3.23) and the η and $p_{\rm T}$-dependence of the V0's efficiency following the same procedure as done previously for the raw angular correlations. Once the mixed-event distributions are obtained, the combinatorial background of the V0 candidates is subtracted, in a statistical way, as follows:

$$\frac{d^2N_{\rm ME}}{d\Delta\varphi d\Delta\eta} = \frac{d^2N_{\rm ME,Candidates}}{d\Delta\varphi d\Delta\eta}(\pm 4\sigma) - \frac{d^2N_{\rm ME,Background}}{d\Delta\varphi d\Delta\eta}(|5-9|\sigma). \tag{3.8}$$

To correct the raw angular distributions, the obtained mixed-events distributions are normalized to *one* by the factor $N_0 \approx {\rm d}^2N_{\rm ME}/{\rm d}\Delta\varphi{\rm d}\Delta\eta(0,0|z_{\rm vtx,i})$. The resulting distribution is called *pair-acceptance efficiency* (see Figure 3.24). The purpose of the normalization to one is that the trigger-associated pair is more likely to be reconstructed when these particles are emitted very close in $\Delta\eta$, thus their detection efficiency as a pair is one. Consequently, as soon as their separation in pseudo-rapidity increases, then the pair-efficiency will decrease.

In Figure 3.24, the mixed-event distributions of $\rm K^0_S$ and Λ are plotted in three different $p_{\rm T}$ intervals for the 0–5% centrality and for one $z_{\rm vtx}$ range ($-2 < z_{\rm vtx} < 0$ cm). The distributions present a triangular shape in $\Delta\eta$ meaning that the acceptance of correlated pairs with large distance in pseudo-rapidity is more limited than the acceptance of pairs with smaller $\Delta\eta$ which have the largest probability to be reconstructed. With a finer $\Delta\varphi$ binning, regular structures could be observed in $\Delta\varphi$ that represent the loss of correlations at the boundaries between the TPC sectors.

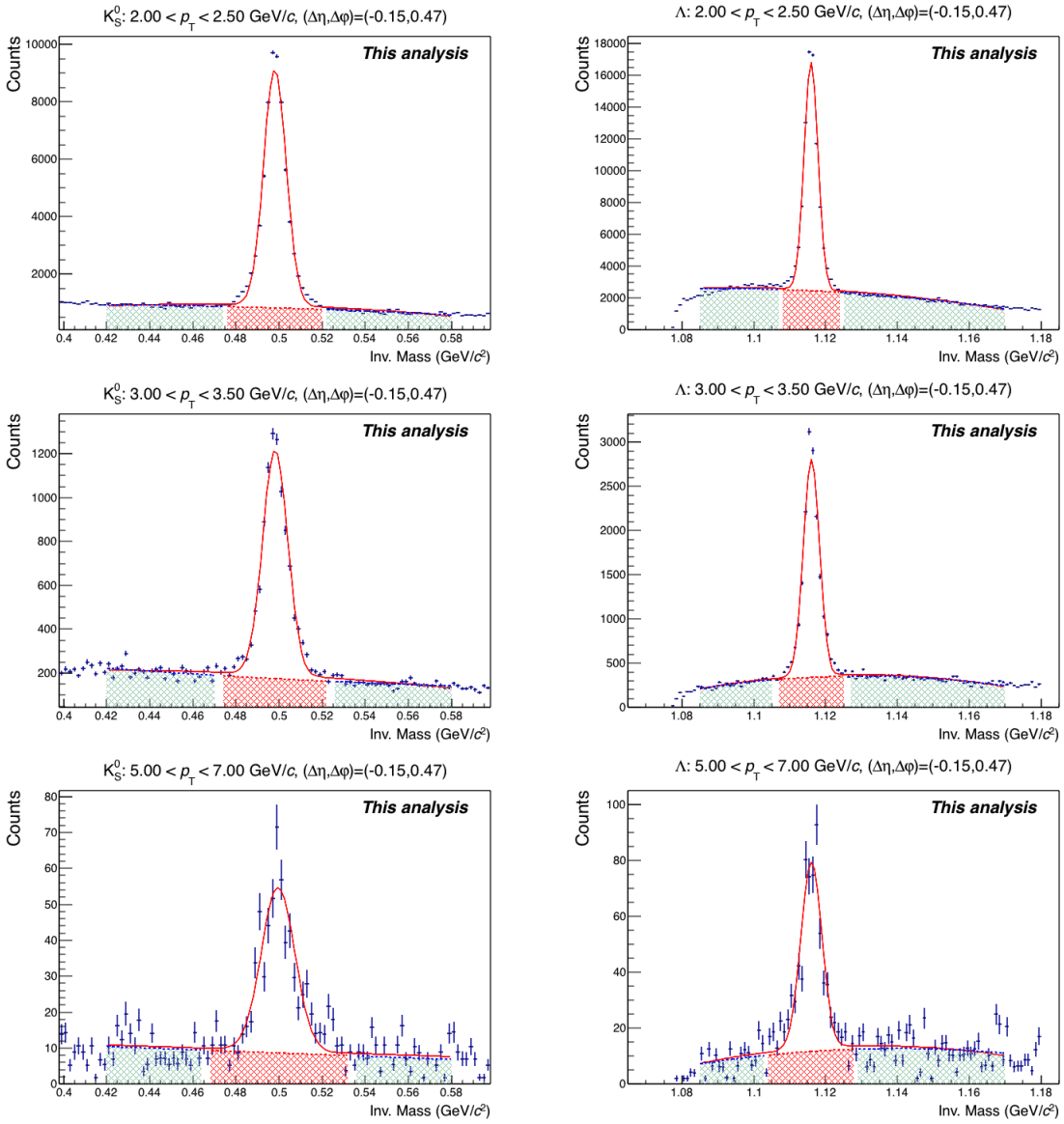

Figure 3.26: Fit of the invariant mass of K^0_S (left panels) and Λ (right panels) candidates in the centrality selection 0-10% for the same $(\Delta\varphi, \Delta\eta)$ bin with three different transverse momentum selections: $2.00 < p_\mathrm{T} < 2.50$ GeV/c (upper panels), $3.00 < p_\mathrm{T} < 5.50$ GeV/c (middle panels) and $5.00 < p_\mathrm{T} < 7.00$ GeV/c (lower panels).

Another point to notice in Figure 3.24 is that the shape of the mixed-event distributions is better defined in the low p_{T} ranges than for 5-7 GeV/c, as a consequence of a larger statistics available. With the used statistics of the trigger and of the associated particles, the mixed-events can be built with a very small relative error of less than 1% for most of the distributions while in the worse scenario it reaches relative errors of 3%.
The mixed distributions depend also slightly on the z_{vtx} interval as it can be seen in Figure 3.25 with the ratio of the mixed-event distributions of $\mathrm{K}^0_{\mathrm{S}}$ and Λ for two different z-vertex intervals.

◇ ***Summing over the primary vertex position***
Once the pair-acceptance correction is applied, the correlation distributions for a given centrality and p_{T}^{V0} bin are summed over the bins in vertex position in z.

$$\frac{\mathrm{d}^2 N_{\mathrm{Candidates}}}{\mathrm{d}\Delta\varphi\mathrm{d}\Delta\eta} = \sum_i \frac{\mathrm{d}^2 N_{\mathrm{Candidates}}/\mathrm{d}\Delta\varphi\mathrm{d}\Delta\eta \mid_{z_{\mathrm{vtx,i}}}}{\frac{1}{N_0}\,\mathrm{d}^2 N_{\mathrm{ME}}/\mathrm{d}\Delta\varphi\mathrm{d}\Delta\eta|_{z_{\mathrm{vtx,i}}}} \tag{3.9}$$

◇ ***Symmetrization***
In order to gain more statistics and to improve the shape of the angular correlation distributions, a symmetrization around the axis $\Delta\eta = 0$ is applied. It consists in obtaining the average value α of the bins in $(\Delta\varphi, \Delta\eta)$=(a,b) and $(\Delta\varphi, \Delta\eta)$=(a,-b).

◇ ***Signal extraction***
Since the associated $\mathrm{K}^0_{\mathrm{S}}$ and Λ candidates have a considerable contribution from combinatorial background under the invariant mass peak, we extract the signal (Sig$(\Delta\varphi, \Delta\eta)$) of the $\mathrm{K}^0_{\mathrm{S}}$ and Λ for each $(\Delta\varphi, \Delta\eta)$ bin.
We use a fitting procedure in two steps. First, a fit is applied to describe the invariant mass distribution as a sum of a Gaussian and a polynomial of order n (with $n = 0, 1, 2$), the latter represents the background in a certain restricted range around the mass peak. In the fitting procedure, the free parameters are the mean value (μ), the width (σ_{fit}) and an overall normalization factor of the signal peak, as well as the respective parameters for the polynomial describing the background. The shape of the background depends on the phase-space of the V0 candidate (see Figure 3.26). The second fit is performed only to the combinatorial background, in a region excluding the signal peak as represented by the shaded green area in Figure 3.26, to improve the description of the polynomial of order n. Then, the signal is extracted by integrating the bin content of the distribution over $\pm 4\sigma_{\mathrm{fit}}$ region around the nominal. In parallel, we use the fitting results extracted in the second step to estimate the amount of combinatorial background under the signal peak within the range $\pm 4\sigma_{\mathrm{fit}}$. The error associated to the background is calculated using the covariance matrix of the fit parameters. After, the estimated background is subtracted from the bin-counted signal.

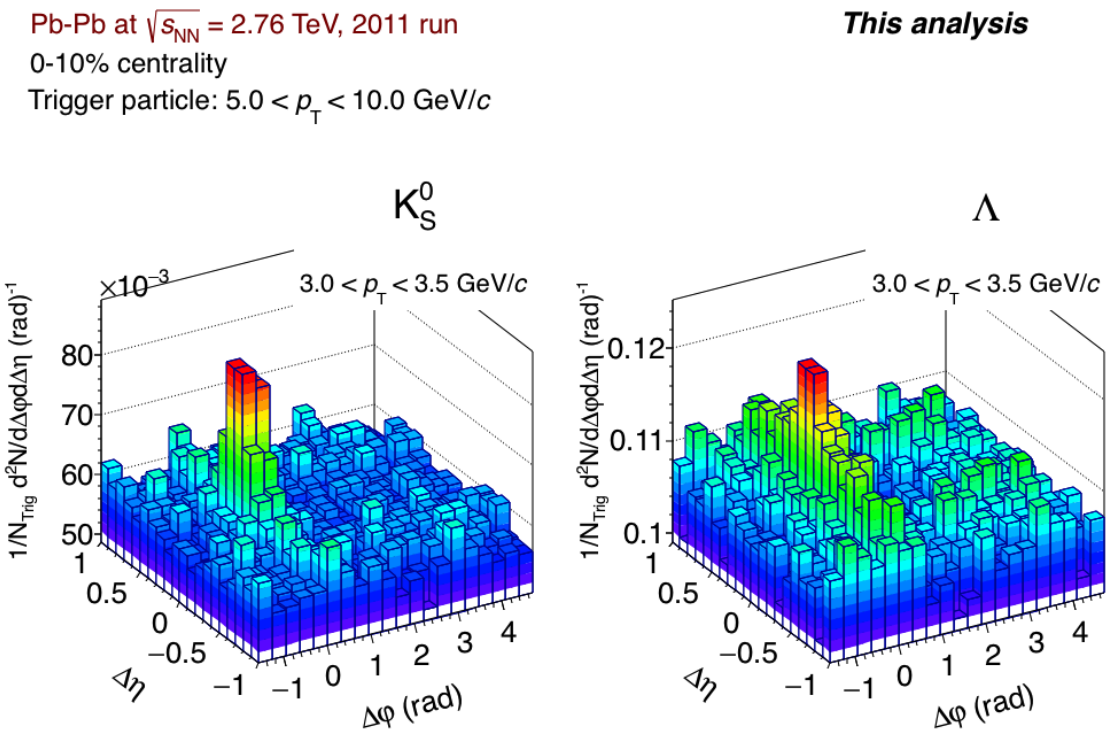

Figure 3.27: Corrected correlation distribution of K^0_S and Λ in the 0-10% centrality interval.

◇ ***Normalization***

Finally, the correlation function[6] is normalized to the total number of trigger particles N_{Trig} used within the centrality interval

$$\frac{1}{N_{\mathrm{Trig}}}\frac{\mathrm{d}^2N}{\mathrm{d}\Delta\varphi\mathrm{d}\Delta\eta} = \frac{1}{N_{\mathrm{Trig}}}\frac{1}{\mathrm{eff}\times\mathrm{Accep}\times\mathrm{B.R.}}\frac{\mathrm{d}^2N_{\mathrm{Sig}}}{\mathrm{d}\Delta\varphi\mathrm{d}\Delta\eta} \tag{3.10}$$

The correction to the trigger particle by the p_{T}-reconstruction efficiency is not needed because the final result is normalized to N_{Trig}.

In Figure 3.27, the final correlation distribution is shown for K^0_S and Λ within $3.0 < p_{\mathrm{T}} < 3.5$ GeV/c in the 0-10% centrality interval. The two-dimensional correlation distribution corresponding to the other transverse momentum selections for K^0_S and Λ and also for the 20-40% centrality selection can be seen in the Appendices *B* and *C*. A second distribution of K^0_S is shown in Figure 3.28 with a masked region from 0 to -1 in $\Delta\eta$ that corresponds to the symmetrization procedure. The enclosed areas are the selected regions where the yield-per-trigger in the bulk will be introduced and extracted in subsection 4.1.

[6] As a reminder, at this step the distributions are already corrected by the V0 reconstruction efficiency (eff × Accep × B.R.) and by the pair-acceptance efficiency

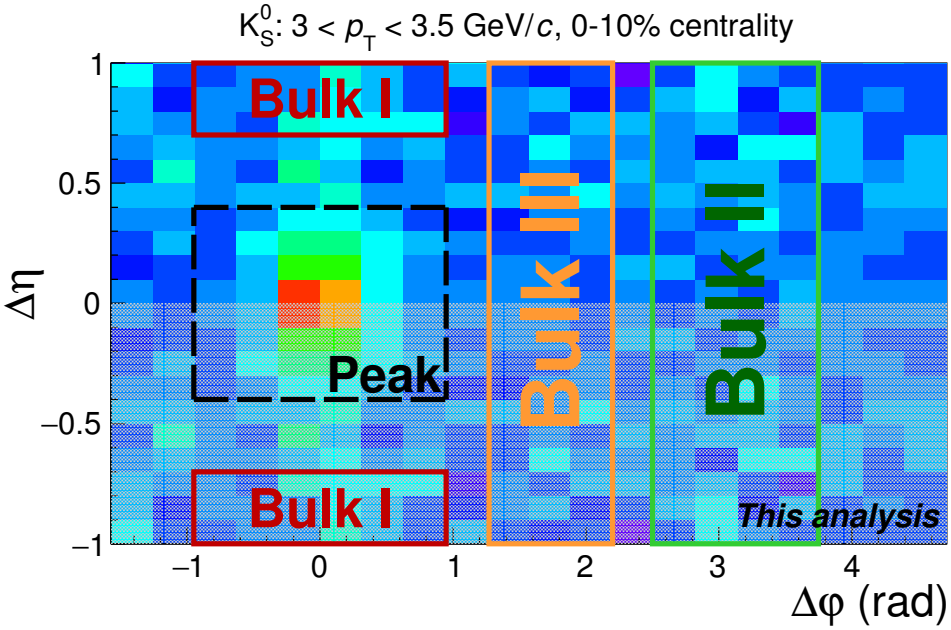

Figure 3.28: Corrected correlation distribution of K^0_S with the definitions of the different regions, bulk of matter and the correlated near-side peak, used to study the hadron production. These regions will be defined and described in next Chapter.

3.5.1 Tracking and reconstruction effects in $h^{\pm}$-V0 correlations

In this subsection, we will review the track splitting and track merging effects that can potentially affect the results on the angular correlation distributions. These two tracking footprints are generated by the reconstruction parameters and are not physical effects. In this subsection, we investigate these effects for both "TPC-only" tracks and "hybrid" tracks. Also, some words about the double V0 finding will be mentioned.

Track splitting

The track splitting effect refers to the situation when the signal along the detector (track) generated by one single particle can be associated to two different tracks at the reconstruction level. An extensive study has been performed to evaluate the influence of this effect (*track splitting*) on the results of the two-hadron angular correlations. It has been observed that depending on the track selection for the trigger particle, specifically requiring (or not) the cluster-to-track association in the first two layers of the ITS, some *fake correlations* between the trigger particle and the associated V0 particles can be introduced in the near-side peak of the correlation distributions. More details will be given in the next paragraphs.
As part of the tracking studies, first the selection of the trigger particle was chosen to be a TPC-only track (see trigger selection in Table 3.3). This selection allows the track to have for a distance to the primary vertex less constrained and also the track does not necessarily require to have hit(s) in the SPD. The tracking studies are performed in the following scenarios:

- ♢ **Correlation in the fraction of shared TPC clusters**
  This check is performed between the trigger particle and the daughter track form the V0 candidate to verify up to which extend these tracks can share some TPC clusters.
  The aforementioned correlations between the trigger particle and the positive daughter (proton) of Λ are shown in Figure 3.29. We select first the trigger particle as TPC-only track that have the same sign charge as the daughter track. The distributions are obtained by subtracting, in a statistically way, the combinatorial background of the Λ[7]. Only Λ candidates in the transverse momentum range $3 < p_{\mathrm{T}}^{\Lambda} < 7$ GeV/c are selected. The upper left panel contains the fraction of TPC clusters shared for the trigger particle and the daughter track. The distribution has a large quantity of tracks located around zero i.e. that do not share any TPC cluster at all. Few entries are located along the x- and the y-axis, meaning that there is a certain correlation with other particles but not between the trigger particle and the daughter track. However, a clear concentration of entries along the diagonal suggests some correlation between the two tracks.

- ♢ **Angular correlation between the trigger particle and the V0 daughter track**
  Since we are working now with secondary tracks, the angular correlation between the trigger track and the daughter track is obtained using a new definition of the angular position[8].

[7] The signal distributions is obtained by selecting the candidates in the invariant mass peak (signal plus background) and in the background. The distributions are subtracted afterward to keep only the signal.
[8] These correlations are not corrected by for pair acceptance efficiency.

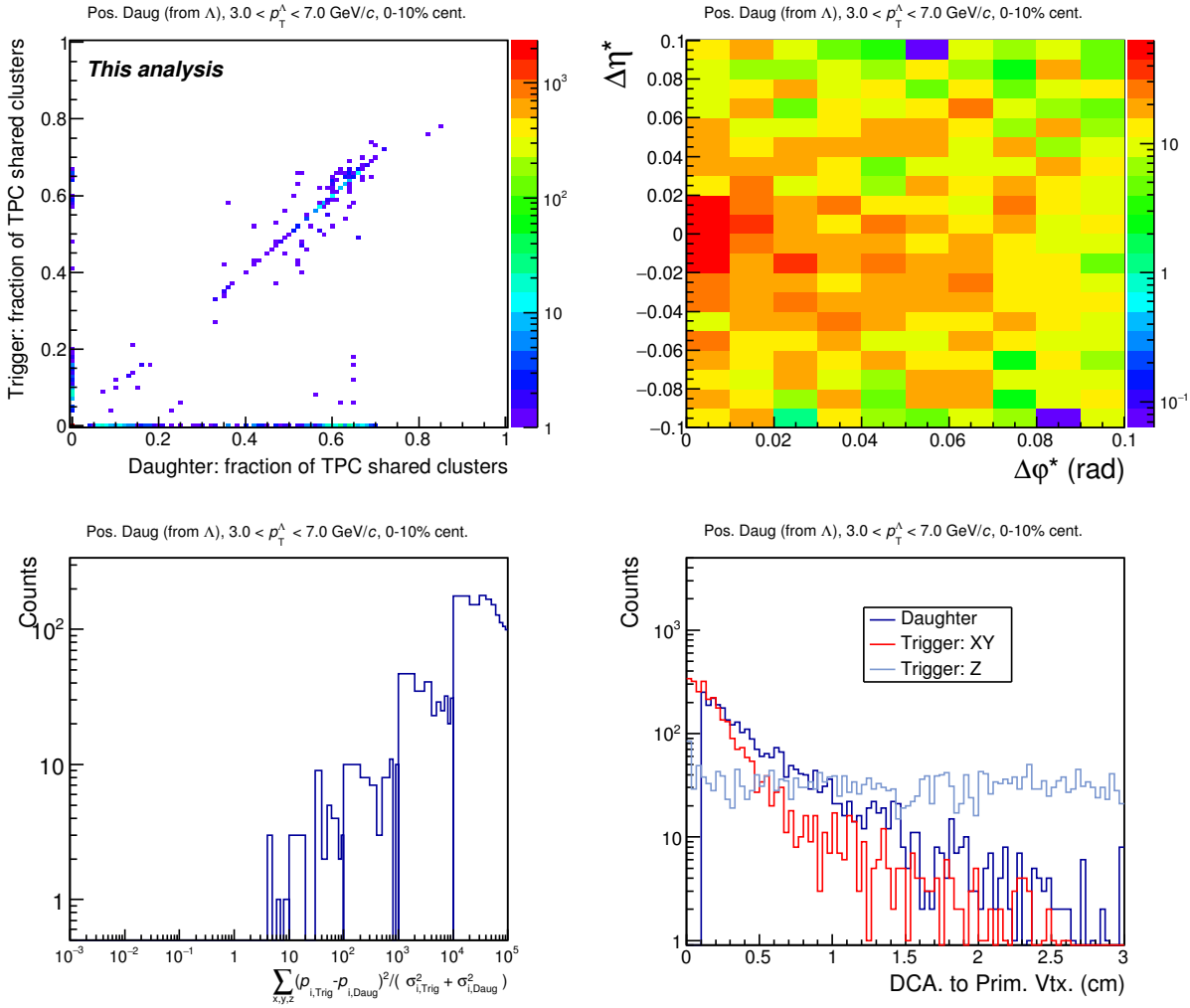

Figure 3.29: Correlation between the trigger particle (**TPC-only track**) and the daughter proton from a Λ candidate in the correlation peak as a function of several variables: the fraction of shared TPC clusters (upper left panel); the angular distribution $\Delta\eta^*$ vs $\Delta\varphi^*$ (upper right panel) with $\Delta\eta^* = \eta^*_{\rm Trig} - \eta^*_{\rm Daug}$ and $\Delta\varphi^* = \varphi^*_{\rm Trig} - \varphi^*_{\rm Daug}$; the sum of the difference in the momentum components of the trigger and daughter particle with respect to their momentum resolution (lower left panel); and the distance of closest approach to the primary vertex (lower right panel). These studies are performed with for Λ candidates in the $3 < p_{\rm T}^{\Lambda} < 7$ GeV/c range for the 0–10% centrality interval.

The approach implies the calculation of the pseudo-rapidity (η^*) and the azimuthal angle (φ^*) of the track by using the information of the track position at a certain TPC radius. The new angles are obtained with respect to the primary vertex position, assuming that the track would end up at the same position if it were a primary particle. In this calculation, one takes into account the track bending due to the magnetic field whose position denoted here as $\mathbf{x_{TPC}}$. The radial position in the TPC was taken to be $r_{\rm TPC} = 125$ cm, following the results from the HBT analysis for charged hadrons. Here, the inefficiency between the two tracks is the deepest at this TPC radius and the smearing in $\Delta\varphi^*$ is less [160].
The new angular positions in η^* is calculated as:

$$\eta^* = -\ln[\tan(\theta^*/2)] \qquad \text{with} \qquad \theta^* = \frac{\pi}{2} - \arctan\Big(\frac{\sqrt{z_{\mathbf{TPC}} - z_{\rm vtx}}}{r_{\rm TPC}}\Big) \tag{3.11}$$

thus the correlation between the trigger particle and the positive daughter track is $\Delta\eta^* = \eta^*_{\rm Trig} - \eta^*_{\rm Daug}$.
The angular distance $\Delta\varphi^*$ between the trigger particle and the daughter track is

$$\Delta\varphi^* = 2\arctan\Big(\frac{\delta^*_{\rm TPC}}{2\,r_{\rm TPC}}\Big) \tag{3.12}$$

where

$$\delta^*_{\rm TPC} = \sqrt{(x_{\rm TPC,Trig} - x_{\rm TPC,Daug})^2 + (y_{\rm TPC,Trig} - y_{\rm TPC,Daug})^2}. \tag{3.13}$$

In the upper right panel of Figure 3.29, we can observe the results on the $\Delta\eta^*$-$\Delta\varphi^*$ distribution. It is noticeable that a large density of particle is concentrated around $\Delta\eta^* \sim 0$ and $\Delta\varphi^* \sim 0$. Thus, suggesting to be possible fake correlations.

♢ **Momentum correlation between the trigger particle and the V0 daughter track**
Further comparisons between the trigger and the V0 daughter tracks were performed by calculating:

$$\chi^2 = \sum_{i=x,y,z} \frac{(p_{i,\rm Trig} - p_{i,\rm Daug})^2}{\sigma^2_{i,\rm Trig} + \sigma^2_{i,\rm Daug}}. \tag{3.14}$$

The previous relation helps estimating how close the tracks are in momentum space. The result is shown by the distribution of the lower left panel of Figure 3.29. The bin width is chosen to increase logarithmically. The upper bin thresholds 4, 10, 20, 30 can be consider as 2, 3, 4 and 5 standard deviations in momentum between the tracks. A large quantity of entries are above 30, therefore the pair of tracks (trigger-daughter particles) are not close in the momentum space.

♢ **Track distance of closest approach to the primary vertex**
In the lower right panel in Figure 3.29, the distance of closest approach (dca) of the track to the primary vertex is shown. For the trigger particle, the distance in the xy-plane and in the z-axis is presented, whereas the dca for the daughter particle is calculated with its three spatial components. One could expect that if the trigger track and the daughter track are generated by the same particle then the dca distributions could be similar.
From the previous figure, the distribution in the xy-plane for the trigger particle is similar

to the one of the daughter particle just in a small range from 0.1 to 0.3 cm. However, no clear conclusion can be done whether they are the same particle or not.

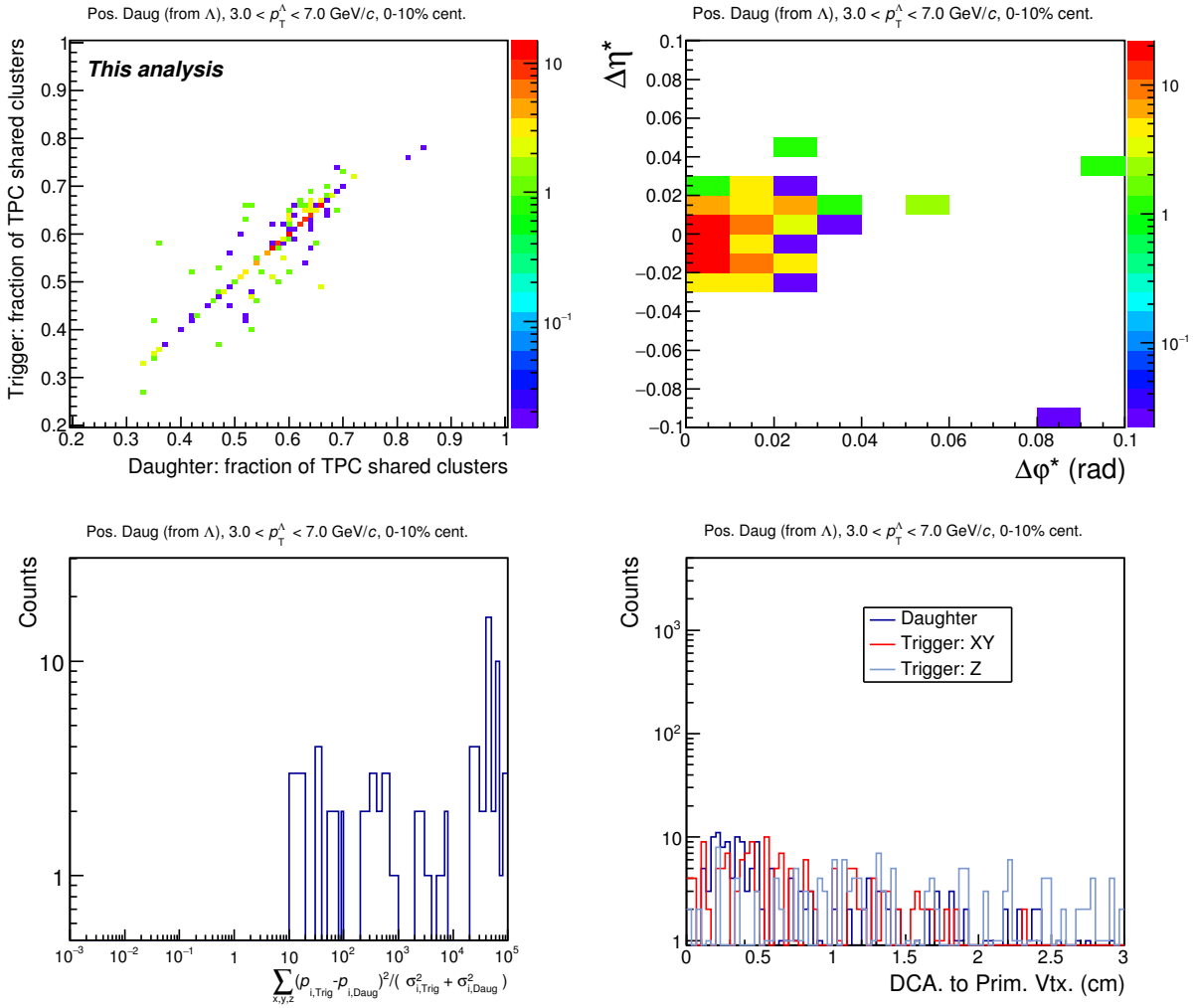

Figure 3.30: Same as Figure 3.29 but with a selection criteria requesting a **fraction of 0.2 shared clusters** between the trigger particle (**TPC-only track**) and the daughter proton from a Λ candidate in the correlation peak.

For investigating further the fake correlations, and following the same protocols as before, we select only track pairs where the trigger particle and the positive daughter track of Λ have a fraction of shared TPC clusters larger than 0.2, as shown in the upper left panel in Figure 3.30. In the upper right panel of the same figure, it is noticeable that these pairs are mostly located close in the $(\Delta\varphi^*, \Delta\eta^*)$-space, indicating that the clusters they share could originate from the same particle. This would imply that those clusters might be wrongly assigned in the reconstruction procedure. Although their momentum is different, since most of the entries have χ^2 values larger than 30 (see lower left panel), the trigger and daughter tracks have similar distributions of the distance to the primary vertex (see lower right panel).

Similar studies performed with the K^0_S hadron have shown that the effect appears to be more important for Λ than for K^0_S. This is due to the fact that the proton from Λ carries a large fraction of the momentum of the mother particle. It results in a straighter track which produces clusters that can also be assigned to the trigger tracks.

Also, Monte Carlo studies are also performed to better understand the track splitting effects on the angular correlation distributions. In this case, an additional condition is required: the trigger track and the daughter track are matched with the same production ID. In Figure 3.31, the $\Delta\eta^*$-$\Delta\varphi^*$ distribution in the right panel illustrates the fact that fake correlations under the peak can be produced by pair of tracks sharing a certain number of commonly associated clusters (left panel). In addition, we observe that the two upper distributions in Figure 3.30 present the same feature as the MC results here obtained.

The fake correlations are quantified Λ in the 0-10% centrality selection, only when the trigger is selected as TPC-only track. It has been found that the fake correlations introduced in the correlation peak depend strongly on the p_{T} of the associated particles. For example, in the case of $h^{\pm}$–Λ correlations (see Table 3.8), when the fraction of shared TPC clusters is larger than 0.3, the statistics of the fake correlations is of the order of 9% in the p_{T} range from 3–4 GeV/c and reaches up to about 40% for 5–7 GeV/c

The effect of track splitting on the angular correlation distributions was also studied in the case where the trigger particle is selected as hybrid track (see Figure 3.32). The previous observed diagonal in the fraction of shared TPC cluster distribution (upper left panel) has been almost removed. The concentration of particles around zero in $\Delta\eta^*$-$\Delta\varphi^*$ disappeared as well. Therefore, the selection of the hybrid tracks as trigger particles does not seem to bias angular correlations. Consequently, TPC-only tracks should be discarded as trigger particles.

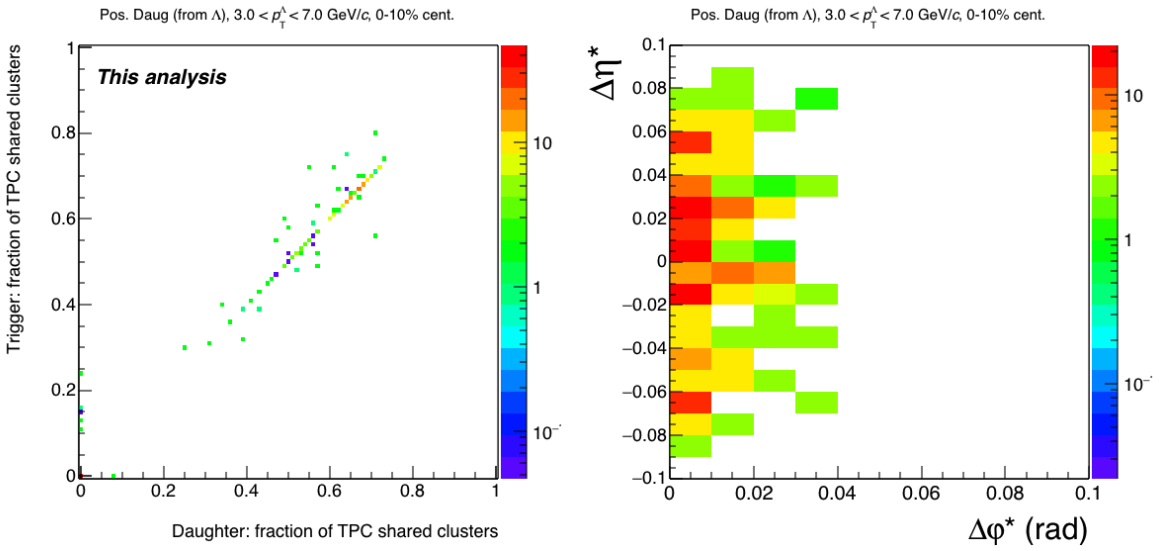

Figure 3.31: Monte Carlo studies about the correlation between the trigger particle (**TPC-only track**) and the daughter proton from a Λ candidate in the correlation peak. The distributions are obtained for the Monte Carlo matching between the two tracks. The left panel represents the fraction of shared TPC clusters assigned to the trigger particle and the daughter track. The right panel represents the angular distribution $\Delta\eta^*$ vs $\Delta\varphi^*$ between these two tracks. The selection is for the transverse momentum range $3 < p_{\mathrm{T}}^{\Lambda} < 7$ GeV/c and the 0–10% event centrality selection.

Table 3.8: Statistics for the h^+-Positive daughter track (from Λ candidate) for the $\Delta\eta^*$-$\Delta\varphi^*$ distributions (within $|\Delta\eta^*| < 0.1$ and $|\Delta\varphi^*| < 0.1$) for different selections in the shared of TPC clusters as function of p_{T}^{Λ}. The results are estimated for the 2011 Pb–Pb collisions at LHC energies.

0-10% centrality class			
p_{T}^{Λ} (GeV/c)	3-4	4-5	5-7
Fraction shared TPC clusters	———	Statistics	———
No cut	100%	100%	100%
> 0.3	8.6%	37.4%	44.8%
> 0.5	7.2%	34.9%	44.3%

Track merging

Another tracking effect that can possibly affect the angular correlation is *track merging*. It is due to the limited spatial resolution of the detector in η and φ, leading to situations where close clusters produced by different particles are associated to a single track as if they originated from a single particle. The performed studies have shown that track merging does not affect $h^{\pm}$-V0 correlations.

Double finding V0 candidates

The double finding V0 candidate refers to using the same track for two different V0's candidates. The inclusive analysis studies have shown this contribution is about 1%. Therefore, in this analysis, a negligible contribution is assumed for the region under the correlated peak.

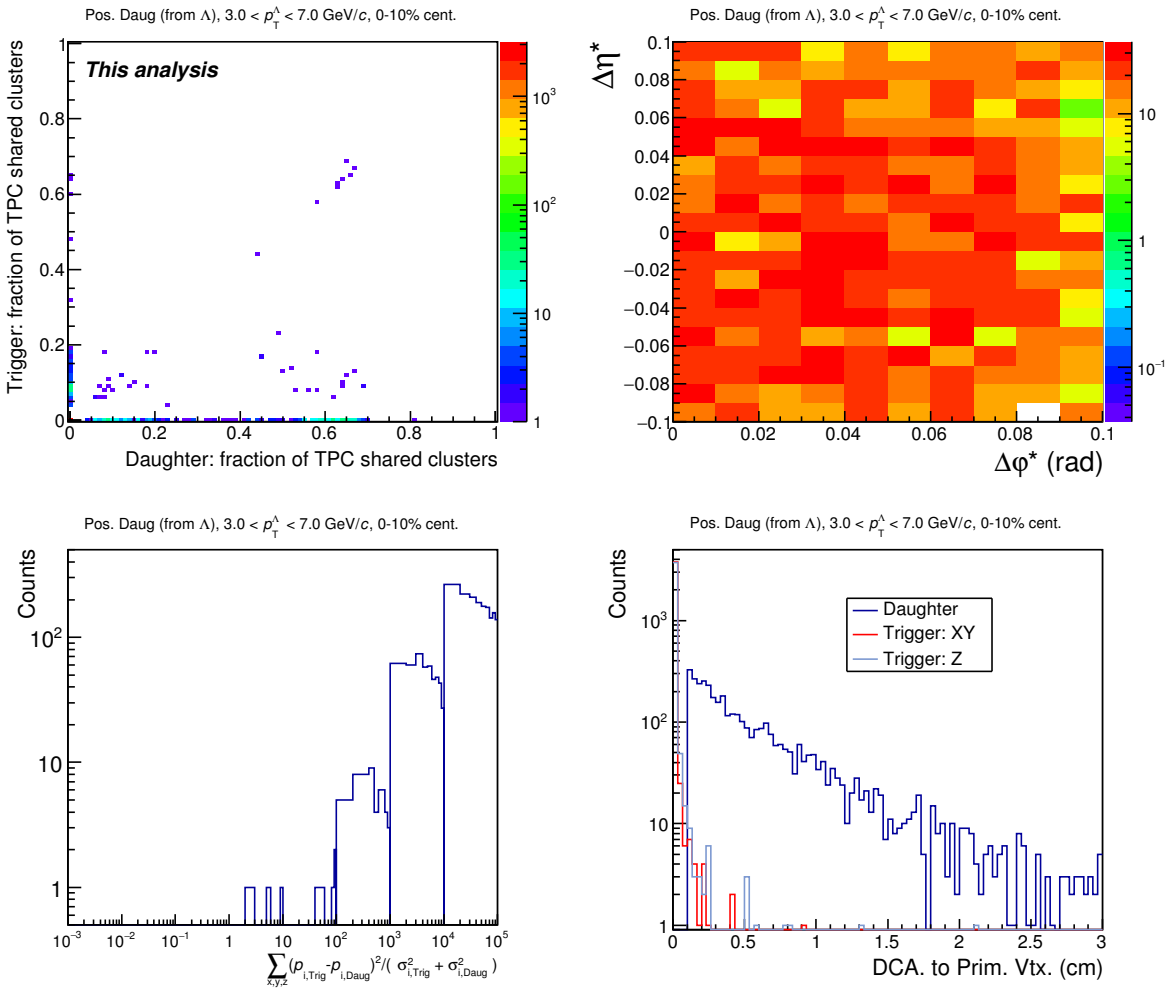

Figure 3.32: Correlation between the trigger particle (**hybrid track**) and the daughter proton from a Λ candidate in the correlation peak. Other distributions represent: the angular distribution $\Delta\eta^*$ vs $\Delta\varphi^*$ (upper right panel) with $\Delta\eta^* = \eta_{\rm Trig} - \eta_{\rm Daug}$ and $\Delta\varphi^* = \varphi_{\rm Trig} - \varphi_{\rm Daug}$; sum of the difference in the momentum components with respect to its momentum resolution (lower left panel); and the distance of closest approach to the primary vertex (lower right panel). These studies are performed with a selection in $3 < p_{\rm T}^{\Lambda} < 7$ GeV/c for the centrality interval 0–10%.

4. $\Lambda/\mathrm{K}^0_\mathrm{S}$ ratio as a function of p_T

As a thing is viewed so it appears.
Padma Sambhava

After introducing all the required elements to perform the two-hadron angular correlations, now it will be possible to study the relative production of baryons with respect to mesons. This will be assessed in regions of $\Delta\varphi, \Delta\eta$ where contributions from different dominant mechanisms are associated to, such as parton fragmentation or bulk effects. The central result for this dissertation of $\Lambda/\mathrm{K}^0_\mathrm{S}$ related to the aforementioned contributions in Pb–Pb collisions will be presented. The per-trigger yields of K^0_S will be obtained as well. Moreover, in this chapter the studies to evaluate the systematic uncertainties will be presented in detail.

4.1 Yield per trigger in the bulk regions

From the fully corrected $h^{\pm}$–V0 correlation distribution, the production of the uncorrelated V0 particles with respect to the trigger particle is extracted in several samples of, what is known as, the bulk. The bulk refers to the hadron production and contributions coming from all the interactions that are not related to hard-parton scatterings (jet-associated particles). The hadronization mechanism of the bulk matter supposes, as a first possibility, the theoretical model of parton coalescence. More, the bulk includes the flow effects from an expanding thermalized medium as well as the initial state fluctuations. The parton energy loss due to the interaction with the medium, via gluon radiation or elastic collisions, could also be considered as one of the ingredients in the bulk.
The hadron production normalized to the number of trigger particles (yield per trigger) in the bulk is obtained from three different regions in the two-hadron angular distribution that are indicated by the rectangles in Figure 3.28. These sampled regions need to be far from the trigger particle to avoid including particles produced by parton fragmentation. Potentially, the selected regions contain different types of physical processes that contribute together to the overall particle production, as mentioned before. Still, the right proportions of these individual contributions to the total yield are unknown since it is experimentally challenging to disentangle them. Then, the per-trigger yield in the bulk is extracted by the integration of the distribution within the following limits:

◇ Yield in Bulk I:

$$\frac{1}{N_{\mathrm{Trig}}}\frac{\mathrm{d}N^{\mathrm{Bulk\ I}}}{\mathrm{d}p_{\mathrm{T}}} = \int_{\Delta\eta=-1.0}^{\Delta\eta=-0.7}\int_{\Delta\varphi=-0.94}^{\Delta\varphi=0.94}\frac{1}{N_{\mathrm{Trig}}}\frac{\mathrm{d}^3N}{\mathrm{d}p_{\mathrm{T}}\,\mathrm{d}\Delta\varphi\,\mathrm{d}\Delta\eta}\,\mathrm{d}\Delta\varphi\,\mathrm{d}\Delta\eta + \int_{\Delta\eta=0.7}^{\Delta\eta=1.0}\int_{\Delta\varphi=-0.94}^{\Delta\varphi=0.94}\frac{1}{N_{\mathrm{Trig}}}\frac{\mathrm{d}^3N}{\mathrm{d}p_{\mathrm{T}}\,\mathrm{d}\Delta\varphi\,\mathrm{d}\Delta\eta}\,\mathrm{d}\Delta\varphi\,\mathrm{d}\Delta\eta.$$

For this selection, the elliptic flow and higher harmonic components have the largest contribution as a whole in $\Delta\varphi$ correlations.

◇ Yield in Bulk II:

$$\frac{1}{N_{\mathrm{Trig}}}\frac{\mathrm{d}N^{\mathrm{Bulk\ II}}}{\mathrm{d}p_{\mathrm{T}}} = \int_{\Delta\eta=-1.0}^{\Delta\eta=1.0}\int_{\Delta\varphi=2.51}^{\Delta\varphi=3.77}\frac{1}{N_{\mathrm{Trig}}}\frac{\mathrm{d}^3N}{\mathrm{d}p_{\mathrm{T}}\,\mathrm{d}\Delta\varphi\,\mathrm{d}\Delta\eta}\,\mathrm{d}\Delta\varphi\,\mathrm{d}\Delta\eta.$$

This region is usually called the "away side" in the $\Delta\varphi$ correlations.

◇ Yield in Bulk III:

$$\frac{1}{N_{\mathrm{Trig}}}\frac{\mathrm{d}N^{\mathrm{Bulk\ III}}}{\mathrm{d}p_{\mathrm{T}}} = \int_{\Delta\eta=-1.0}^{\Delta\eta=1.0}\int_{\Delta\varphi=1.21}^{\Delta\varphi=1.32}\frac{1}{N_{\mathrm{Trig}}}\frac{\mathrm{d}^3N}{\mathrm{d}p_{\mathrm{T}}\,\mathrm{d}\Delta\varphi\,\mathrm{d}\Delta\eta}\,\mathrm{d}\Delta\varphi\,\mathrm{d}\Delta\eta.$$

This part of the distribution contains the particles emitted in the orthogonal plane with respect to the trigger particle direction. Also, the magnitude of the summed contributions from elliptic flow and higher harmonics is expected to be the smallest as observed in [107].

The results of the per-trigger yield associated to the Bulk I region obtained with the ALICE data is illustrated in Figure 4.1 for the $\mathrm{K}^0_{\mathrm{S}}$ meson in the two Pb–Pb centrality intervals 0-10% and 20-40%. The statistical uncertainties are plotted as vertical lines in the distribution, the uncorrelated systematic uncertainties are shown as the blank boxes while the partially correlated systematic uncertainties are represented by the shadowed boxes. A complete description of the systematic contribution will be presented later in this chapter in section *E*.
The corresponding results for Λ is presented in Figure 4.2 in the same centrality interval 0-10% and 20-40% for Pb–Pb collisions. As it has been introduced in subsection *E*, their reconstructed raw yield contains some fraction of Λ coming from the Ξ decays: $\Xi^{\pm} \rightarrow \Lambda\pi^{\pm}$ and the $\Xi^0 \rightarrow \Lambda\pi^0$. From the inclusive analysis, it is known that approximately 20% of all measured Λ at the raw level are produced in these weak decays. On that account, in this analysis we assume that the feed-down contribution to the yield per trigger of Λ in the bulk has the same contribution as in the published analysis. Therefore, we apply the same correction factors as in [117] after integrating the signal in the selected bulk regions. As a reminder to the reader, we do not include $\overline{\Lambda}$ particles to extract the results in this study.
By sampling different $\Delta\eta \times \Delta\varphi$ regions in the bulk, we can explore the relative contributions of the different mechanisms contributing to the overall hadron production. Comparisons between the per-trigger yields obtained in the different bulk regions are performed by considering as the 'reference' the yield extracted in the Bulk III that contains all particles produced in the orthogonal direction with respect to the trigger particle emission.

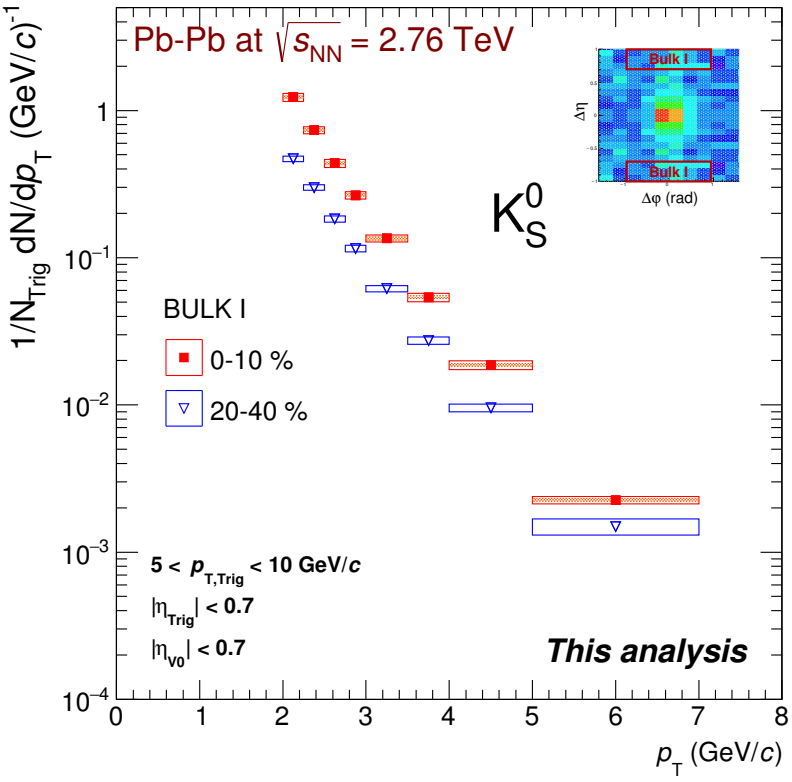

Figure 4.1: Per-trigger yield of K^0_S in the Bulk I sample for 0-10% and 20-40% centrality selections of the 2011 Pb–Pb collisions. The markers are located at the middle value of the p_T-bin. The horizontal extension of the boxes represents the p_T-bin width. Statistical uncertainties are plotted as vertical lines. The empty (shadowed) boxes stand for the uncorrelated (partially correlated) systematic uncertainties.

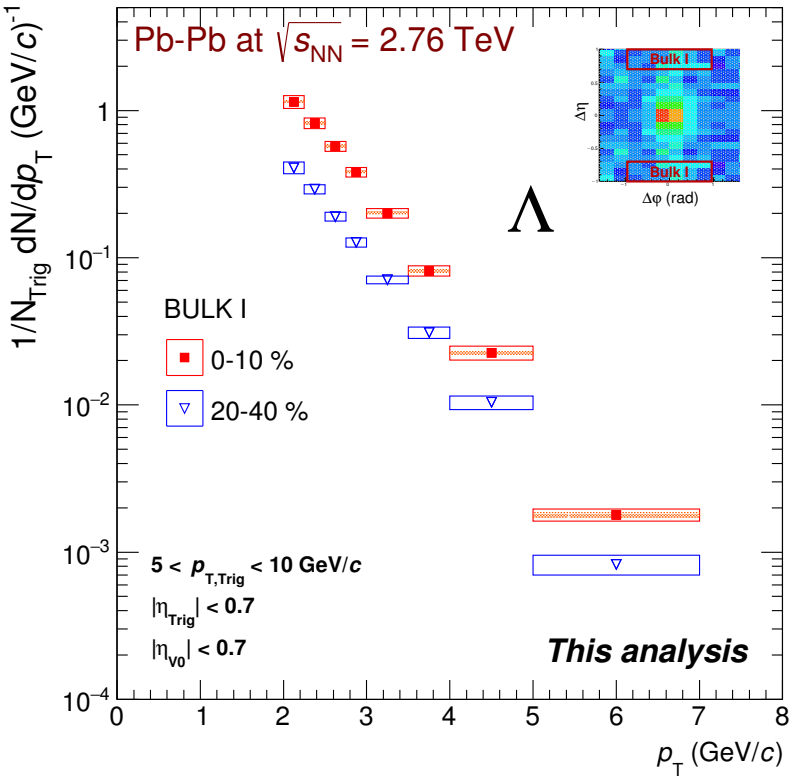

Figure 4.2: Yield per trigger of Λ ($\overline{\Lambda}$ not included) in the defined Bulk I region for the 2011 Pb–Pb collisions in the 0-10% and 20-40% centrality intervals. The horizontal bars are the p_{T}-bin width where the markers are located at the middle value of the p_{T}-bin. The statistical uncertainties are plotted as vertical lines. The empty (shadowed) boxes stands for the uncorrelated (partially correlated) systematic uncertainties.

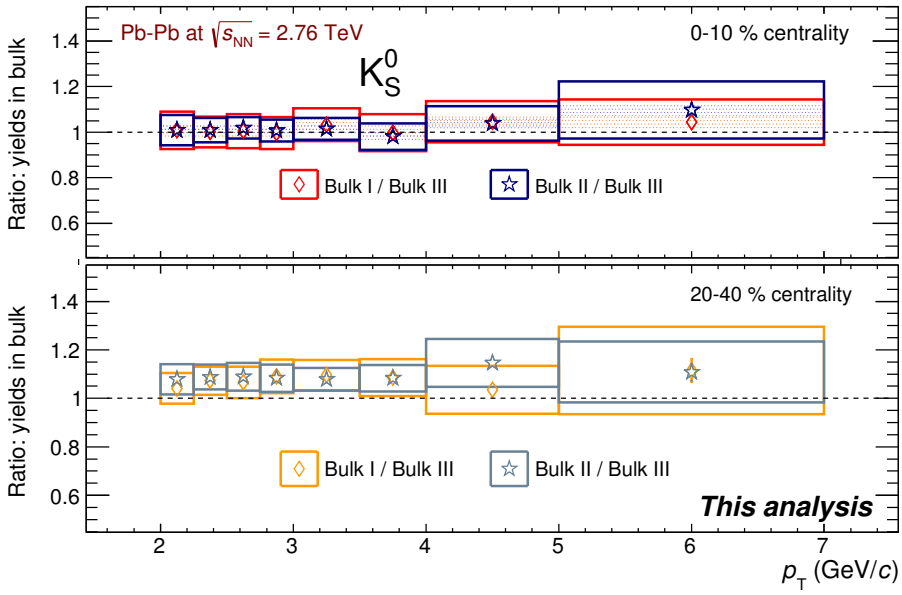

Figure 4.3: Ratio of the measured K^0_S per-trigger yield in the different bulk regions: Bulk I to Bulk III (empty diamond) and the Bulk II to Bulk III (empty star). The results are shown for Pb–Pb collisions at $\sqrt{s_{NN}} = 2.76$ TeV for 0-10% (upper panel) and 20-40% (lower panel) centrality selection. The uncertainty representation follows the convention in Figures 4.1 and 4.2.

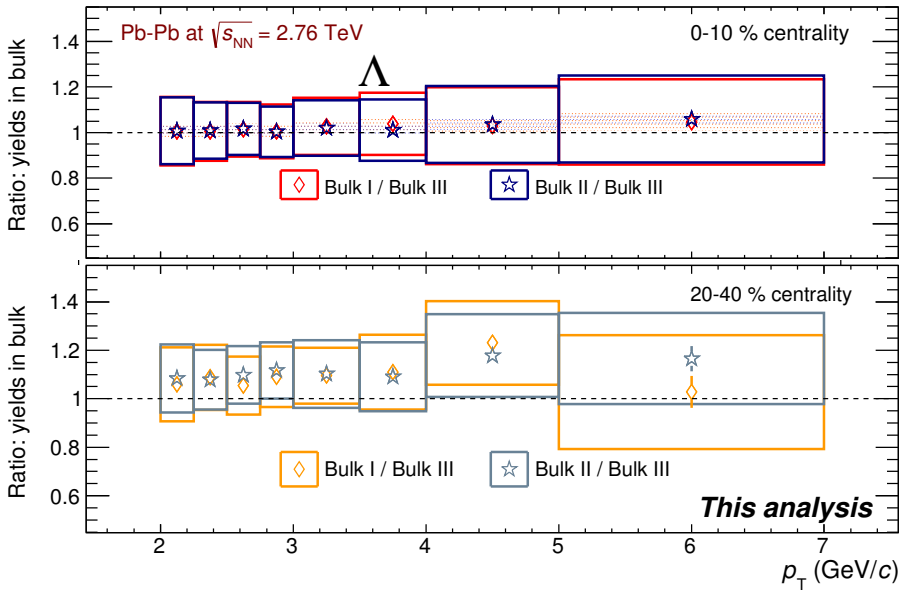

Figure 4.4: Ratio of the measured Λ per-trigger yield in the different bulk regions: Bulk I to Bulk III (empty diamond) and the Bulk II to Bulk III (empty star). The results are obtain for the centrality selection 0-10% (upper panel) and 20-40% (lower panel) in Pb–Pb collisions at $\sqrt{s_{NN}} = 2.76$ TeV. The uncertainty representation follows the convention in Figures 4.1 and 4.2.

The ratio of the bulk yields, Bulk I/Bulk III (empty diamond) and Bulk II/Bulk III (empty star), for the K^0_S are shown in Figure 4.3 in the most central and the semi-central Pb–Pb collisions. Before obtaining these results, the per-trigger yield is normalized to the $\Delta\varphi \times \Delta\eta$ area where it is extracted from. The correlated and uncorrelated systematic uncertainties are obtained by doing the ratio of the corresponding systematic uncertainties of the involved yields. A better approach could be assessed by evaluating the systematic contributions one by one to reduce their values. Similar results have been derived for the Λ particle which are plotted in Figure 4.4. Further discussions on these results will be developed in next chapter.

4.2 Yield per trigger in the correlated peak

The angular correlations have been widely applied to estimate the hadron production originated, in principle, from hard scatterings between partons. This kind of hadron production is translated into a large population of particles distributed close to the trigger particle around $\Delta\eta \approx 0$ and $\Delta\varphi \approx 0$. The resulting structure around the trigger particle is known as the *near-side peak*. In addition, a jet-like peak structure can also be seen at $\Delta\varphi \approx \pi$ (*away-side correlations*) created by the less energetic outgoing partons. However, in Au–Au collisions at RHIC energy it was observed that the away-side correlations disappear in the most central collisions [152], and for d+Au collisions its amplitude turns out to be slightly smaller than the one observed in proton-proton collisions [161, 162].
To be able to extract the production associated with high-p_T particles, one should rely on the assumption that the bulk effects (mainly flow) and the hadron production from parton fragmentation can be factorized, i.e., there is no connection/correlation between these two processes. Thus, the per-trigger yield associated to the fast parton fragmentation can be obtained by projecting the two-hadron angular distribution in: i) $\Delta\eta$-dimension or, ii) $\Delta\varphi$-dimension. In each case, the flow profile is different and so does the corresponding subtraction. In the next subsections we will review the previous two approaches by extracting the per-trigger yield of K^0_S and Λ only for the centrality interval 0-10%. To obtain the results in the 20-40% centrality interval, the same protocol as in central collisions should be followed. However, the results in semi-central collisions have been discarded since the Λ yield per trigger in the near-side (related to parton fragmentation) presents one bin off the trend for which it has not been possible to understand the origin up to now.

4.2.1 Projection in $\Delta\eta$

To study the yield per trigger in the $\Delta\eta$-correlated peak, we start by selecting a range in $\Delta\varphi$ around the near-side peak[1] defined for each p_T(V0) bin as

$$\frac{1}{N_{\text{Trig}}}\frac{\mathrm{d}N}{\mathrm{d}\Delta\eta} = \int_{-0.94}^{0.94}\frac{1}{N_{\text{Trig}}}\frac{\mathrm{d}^2N}{\mathrm{d}\Delta\varphi\,\mathrm{d}\Delta\eta}\,\mathrm{d}\Delta\varphi \tag{4.1}$$

$$= A^{\Delta\eta}\frac{1}{\sqrt{2\pi}\sigma_{\Delta\eta}}\exp\left[\frac{-0.5\,\Delta\eta^2}{\sigma^2_{\Delta\eta}}\right] + \text{Cte} \tag{4.2}$$

Commonly, the $\Delta\eta$-projection is fitted to a single Gaussian plus a constant. The last term of the

[1] From projecting in $\Delta\varphi$, we know beforehand the extension of the tails of the correlated peak in this variable.

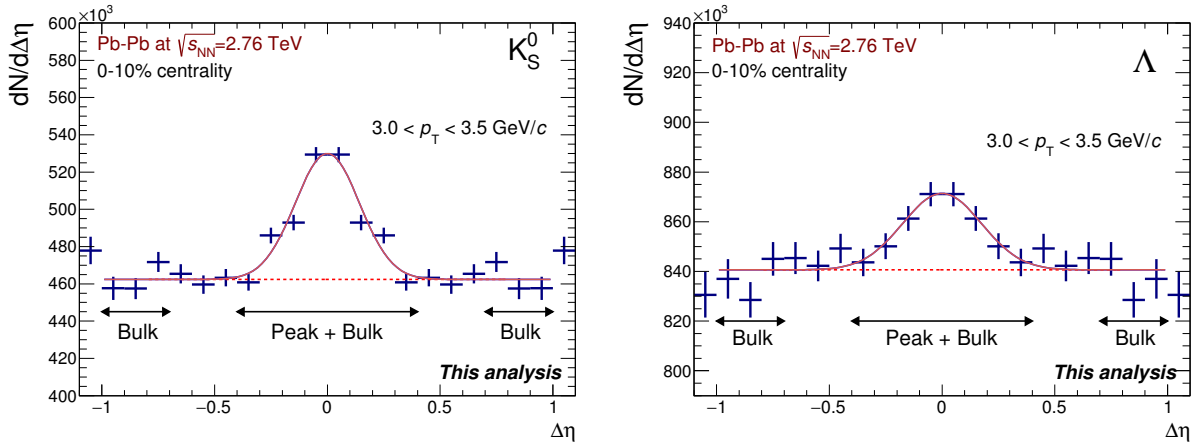

Figure 4.5: Illustration of the $\Delta\eta$-correlation distribution for K^0_S (left panel) and Λ (right panel) within the p_T-range from 3.0 to 3.5 GeV/c in the Pb–Pb 0-10% centrality interval. The production associated to the high-p_T particle (Gaussian peak) stands on top of a flat background originated from the flow contribution (dashed line).

expression 4.2 defines the flow contribution which experimentally has been measured for charged hadrons and it has been shown to be independent on the pseudo-rapidity range [163, 164] where the trigger and the associated particles are selected. By subtracting the constant value to the $\Delta\eta$-distribution, the fragmented-parton production is expected to remain.

Another possible approach to extract the yield per trigger in the near-side peak is the commonly known *eta gap* method [165]. The procedure considers a region of the bulk along the $\Delta\eta$-structure far from the signal of the correlated peak which is scaled to the acceptance of the peak, as it is presented in the following expression:

$$\frac{1}{N_{\text{Trig}}}\frac{\mathrm{d}N^{\Delta\eta}}{\mathrm{d}p_T} = \frac{1}{N_{\text{Trig}}}\int_{-0.4}^{0.4}\frac{\mathrm{d}^2N}{\mathrm{d}p_T\,\mathrm{d}\Delta\eta}\,\mathrm{d}\Delta\eta - \left(\frac{2\times0.4}{2\times0.3}\right)\frac{1}{N_{\text{Trig}}}\left\{\int_{\Delta\eta=0.7}^{\Delta\eta=1.0}\frac{\mathrm{d}^2N}{\mathrm{d}p_T\,\mathrm{d}\Delta\eta}\,\mathrm{d}\Delta\eta + \int_{\Delta\eta=-1.0}^{\Delta\eta=-0.7}\frac{\mathrm{d}^2N}{\mathrm{d}p_T\,\mathrm{d}\Delta\eta}\,\mathrm{d}\Delta\eta\right\} \quad (4.3)$$

The denominator inside the parenthesis accounts for the $\Delta\eta$-acceptance of the bulk in the selected range. In this analysis, it is from 0.7 to 1.0 and from -1.0 to -0.7 (right and left-side with respect to the peak). The numerator defines the $\Delta\eta$-extension of the peak. From Figure 4.5, it is noticeable the tails of the peak end around $\Delta\eta = \pm0.4$.

The two approaches are complementary and should lead to the same physics results. Unfortunately, the systematic studies performed for the $\Delta\eta$-projection resulted into large systematic uncertainties because it was not possible to control the background level for Λ over the accessible $\Delta\eta$ range and from p_T-bin to p_T-bin for $p_T < 4.0$ GeV/c (see Figure 4.6). In consequence, we did not apply this procedure.

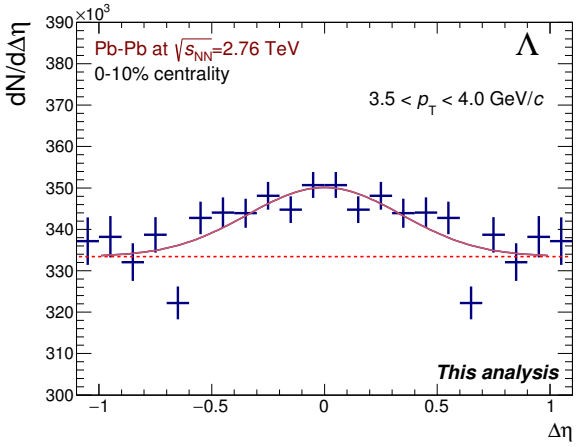

Figure 4.6: $h^{\pm}$-Λ correlation in $\Delta\eta$ with the associated particles in $3.5 < p_{\mathrm{T}} < 4.0$ GeV/c. The peak appears to be broad.

4.2.2 Projection in $\Delta\varphi$

As compared with the $\Delta\eta$-projection, the $\Delta\varphi$-projection allowed us to extract the yield per trigger correlated to the peak with a better precision on the systematic uncertainties. In a similar way, the correlation distribution in $\Delta\varphi$ is obtained by projecting the constructed two-dimensional correlations. From the previous studies of the $\Delta\eta$-projection (see subsection 4.2.1), the limits of regions are chosen to be $|\Delta\eta|$<0.4. Then, the $\Delta\varphi$-projection can be expressed as follows:

$$\frac{1}{N_{\mathrm{Trig}}}\frac{\mathrm{d}N}{\mathrm{d}\Delta\varphi} = \int_{-0.4}^{0.4}\frac{1}{N_{\mathrm{Trig}}}\frac{\mathrm{d}^2N}{\mathrm{d}\Delta\varphi\,\mathrm{d}\Delta\eta}\,\mathrm{d}\Delta\eta \tag{4.4}$$

To describe the overall $\Delta\varphi$-distribution, the production by parton fragmentation as a Gaussian function is considered, as well as, the background contamination originated from the pairs correlated via elliptic (and higher harmonic) flow and the contribution from the uncorrelated particle pairs. The previous formulation is expressed by the following terms:

$$\begin{aligned}\frac{1}{N_{\mathrm{Trig}}}\frac{\mathrm{d}N}{\mathrm{d}\Delta\varphi} &= A^{\Delta\varphi}\frac{1}{\sqrt{2\pi}\sigma_{\Delta\varphi}}\exp\left[\frac{-0.5\,\Delta\varphi^2}{\sigma^2_{\Delta\varphi}}\right] \\ &+ \beta\left\{1+\sum_{n=2}^{\infty}2<v_n^{\mathrm{Trig}}><v_n^{\mathrm{Assoc}}>\cos(n\Delta\varphi)\right\}\end{aligned} \tag{4.5}$$

As mentioned before, the anisotropic flow profile is different when we consider the $\Delta\varphi$-distribution. The profile is represented by the second term in the expression 4.5. It represents the nature of the anisotropic flow, coming from the initial anisotropy of the collision geometry, is showed with the dependence on $\Delta\varphi$ (as presented in subsection 1.6.3) [166, 167, 168]. The factor β is introduced to scale the anisotropic flow modulation to the lowest point in the $\Delta\varphi$ angular distribution. For the $h^{\pm}$-V0 correlation, the principal element of the anisotropic flow contribution comes from the amplitude of the elliptic flow, $< v_2^{\mathrm{Trig}} >$ and $< v_2^{\mathrm{Assoc}} >$, whose magnitudes are obtained from the independent anisotropic flow analyses in ALICE. The v_2 for charged particles is extracted with the event plane method [105, 107], whereas for identified particles the scalar product method is

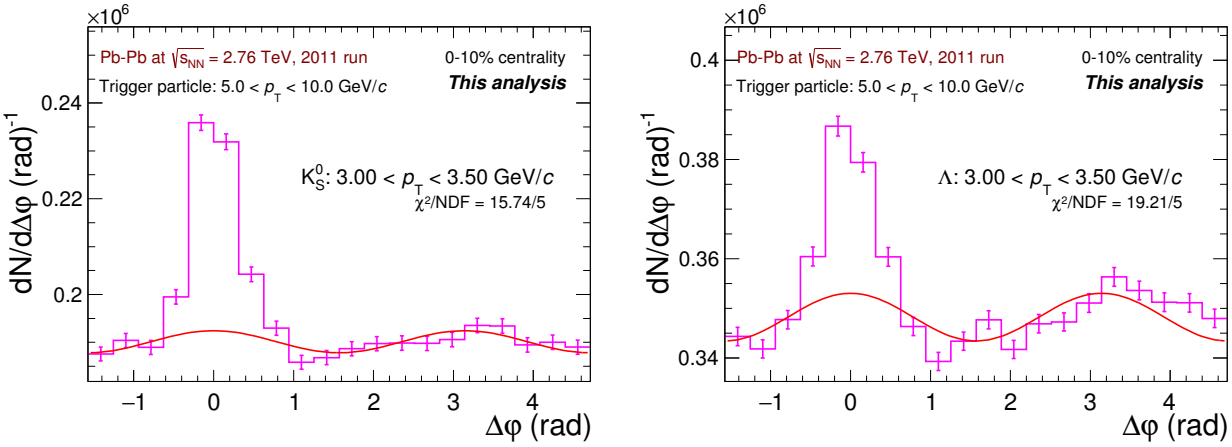

Figure 4.7: Illustration of the angular correlation distribution in $\Delta\varphi$ with K^0_S (left panel) and Λ (right panel) as the associated particles for Pb–Pb collisions at $\sqrt{s_{NN}} = 2.76$ TeV in the 0-10% centrality interval. The curve represents the elliptic flow contribution estimated as $2 < v_2^{Trig} >< v_2^{Assoc} > \cos(2\Delta\varphi)$.

used [112]. In the 0-5% centrality interval, the elliptic flow values extend approximately from 0.03 to 0.07 units of v_2 for the charged primary particles in the range $5 < p_T < 10$ GeV/c, and from 0.02 (0.04) to 0.07 (0.09) units of v_2 in the case of K^0_S (Λ) within the p_T-range 2-7 GeV/c (see Figures 1.8 and 1.9). The higher harmonics, v_n with $n \geq 3$, are not considered due to the lack of experimental measurements for K^0_S and Λ.

To subtract the anisotropic flow from the $\Delta\varphi$ angular correlations, first we fit the distributions[2] with the mathematical expression 4.5 to estimate the background level. During the fitting procedure, we consider $< v_2^{Trig} >$ and $< v_2^{Assoc} >$ as fixed parameters and initializing the Gaussian mean to zero. The free parameters taken into account for the fitting are: $A^{\Delta\varphi}$, $\sigma_{\Delta\varphi}$ and the normalization level β. An example of the fit result for K^0_S in the p_T-range from 3 to 3.5 GeV/c is shown in Figure 4.7 where the anisotropic flow contribution is represented with a red line. The magnitude of the elliptic flow contribution for the rest of the p_T-bins in the 0-10% centrality range can be observed in Appendices *D* and *E* for K^0_S and Λ, respectively.

Once the β parameter is obtained, then we proceed to subtract the elliptic flow contribution to the angular distribution and to integrate the yield per trigger within the limits $|\Delta\varphi| < 0.94$ as indicated in the following expression.

$$\frac{1}{N_{Trig}}\frac{dN^{\Delta\varphi}}{dp_T} = \frac{1}{N_{Trig}}\int_{-0.94}^{0.94}\frac{d}{dp_T}\left\{\frac{dN}{d\Delta\varphi} - \beta\left\{1 + 2 < v_2^{Trig} >< v_2^{Assoc} > \cos(2\Delta\varphi)\right\}\right\} d\Delta\varphi. \tag{4.6}$$

The per-trigger yields of K^0_S and Λ derived from this technique are plotted in Figure 4.8 for the centrality selection 0-10% in Pb–Pb collisions of the 2011 period. One important remark need to be done, as previously in the extraction of the production in the bulk as well as in the inclusive spectra, the Λ yields need to be corrected for the Ξ-decays contributions. However, the estima-

[2]In this thesis, $\Delta\varphi$-is not yet normalized to the number of trigger particles to avoid any conflict during the fitting procedure due to the management of small quantities.

tion of the feed-down correction of Λ coming from the direct process of parton fragmentation of Ξ in Pb–Pb collisions is still unknown. Therefore, in this dissertation work, we assume the feed-down contamination to Λ per-trigger yield in the near-side peak contributes in the same magnitude as in the inclusive results, then applying the same correction factors as for the bulk production. In Figure 4.8, we indicate the boundaries of the feed-down correction with the shadowed vertical bar around the Λ points of the yield per trigger. The upper limit of the shadowed bars represents when no feed-down correction is applied to the Λ production and the lower limit takes the maximum value of the feed-down contribution obtained in the inclusive Pb–Pb results in ALICE [117]. The last assumption considers that the Ξ baryon can be produced as well in correlation to the trigger particle by parton fragmentation whose production rate is not higher than the one obtained in the bulk.

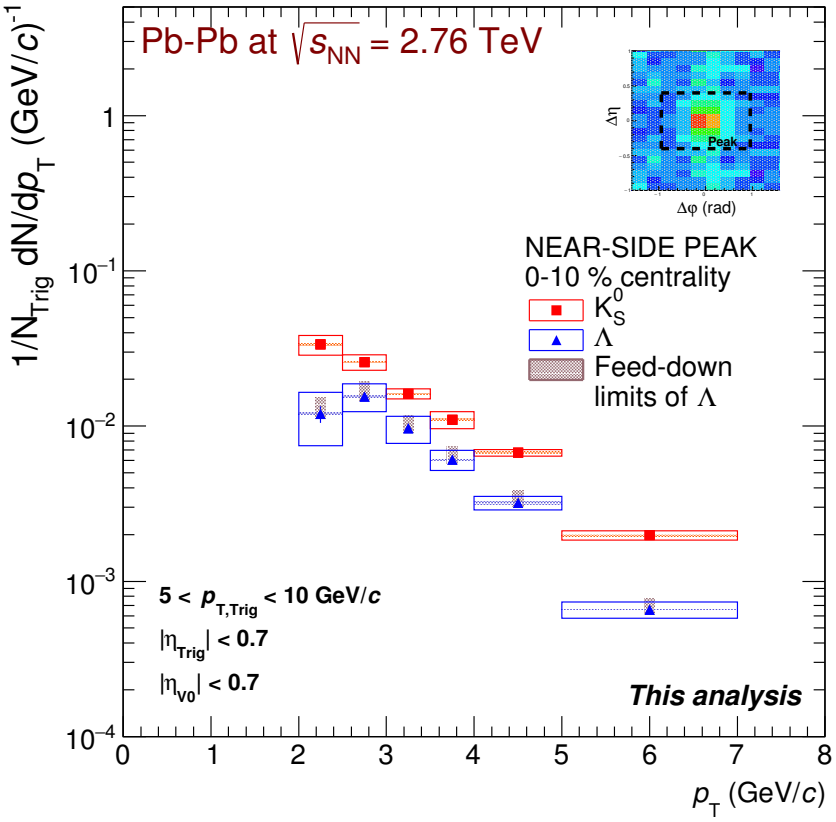

Figure 4.8: Yield associated in emission to a high-p_T particle, normalized to the number of trigger particles in the 0-10% centrality selection of Pb–Pb collisions at $\sqrt{s_{NN}} = 2.76$ TeV. The K^0_S production is represented with the filled squares, while the up-down triangles represent the Λ production. These results were obtained with the projection in $\Delta\varphi$. The horizontal bars are the p_T-bin width; the markers are located at middle value of the bin. The empty (filled) boxes indicates the contributions of the uncorrelated (partially correlated) systematic uncertainties.

4.3 Λ/K^0_S ratio in Bulk

The aim of this dissertation is not only to disentangle the hadron production according to the original processes but to study the origin of the baryon-to-meson enhancement in central heavy-ion collisions.
From the production extracted from Bulk I (see Figures 4.1 and 4.2), we derive the Λ/K^0_S in this bulk sample for the 0-10% and 20-40% centrality intervals of the Pb–Pb collisions taken from the 2011 data period. The results are plotted in Figure 4.9.

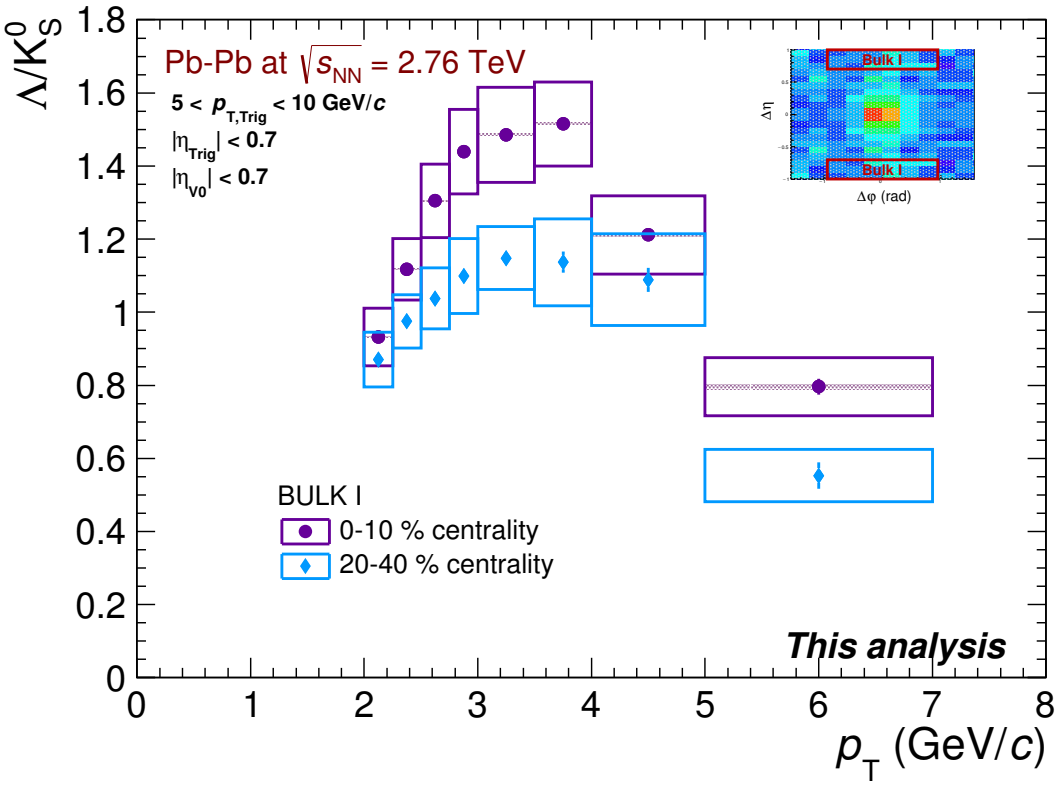

Figure 4.9: Λ/K^0_S ratio obtained from the particles produced in the **bulk I** for the centrality intervals 0-10% and 20-40% in Pb–Pb collisions at $\sqrt{s_{NN}}$ = 2.76 TeV for the 2011 run. The horizontal extension of the boxes represent the p_T-bin width. The markers are located at the middle value of the bin. The $\overline{\Lambda}$ is not included in the per-trigger yield extraction. The empty (filled) boxes indicates the contributions of the uncorrelated (partially correlated) systematic uncertainties.

4.4 Double ratio of the Λ/K^0_S in the different bulk samples

Continuing with the study of the baryon-to-meson ratio, we extend the results to the other sampled bulk regions defined in the two-hadron angular distribution (see section 4.1). We proceed to obtain the Λ/K^0_S ratio in each Bulk region, then we compare the results of Bulk I and Bulk II to Bulk III. In Figures 4.10 and 4.11, we show the double ratio of the Λ/K^0_S in the two centrality intervals (0-10% and 20-40%) where the results have been derived. The double ratio

includes the systematic uncertainties as well as the contribution from the partially correlated systematic uncertainty.

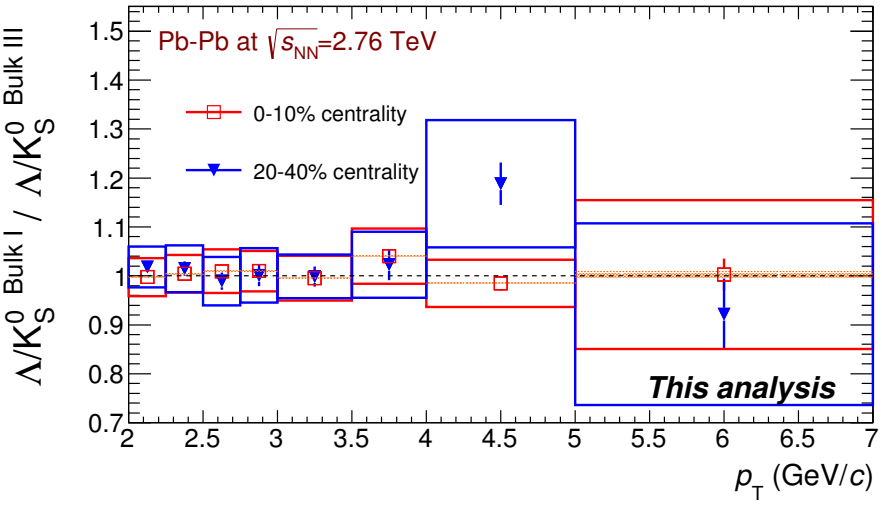

Figure 4.10: Double ratio of Λ/K^0_S in Bulk I to Bulk III. The results are presented for the 0-10% (open square) and 20-40% (up-side-down triangle) centrality intervals in 2011 Pb–Pb run. The $\overline{\Lambda}$ is not included in the single ratio results. The vertical lines are the statistical uncertainties. The empty (filled) boxes are the uncorrelated (partially correlated) systematic uncertainties.

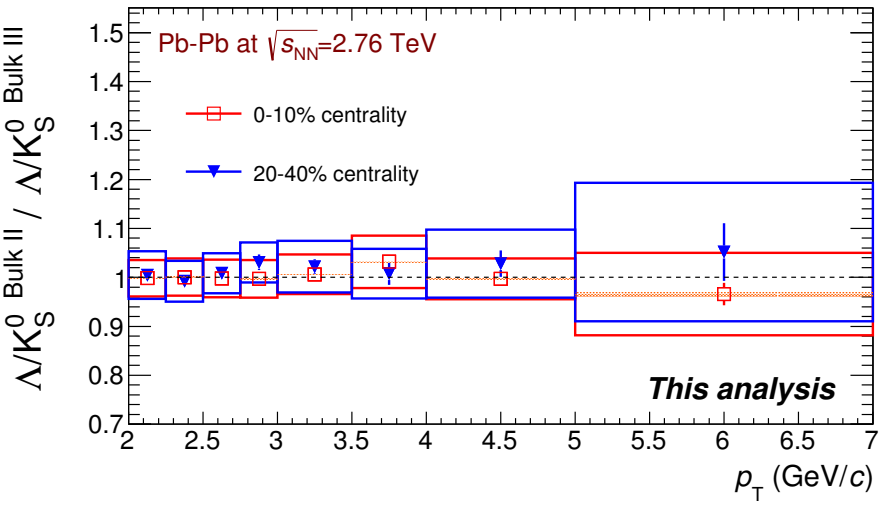

Figure 4.11: Double ratio of Λ/K^0_S in Bulk II to Bulk III. The results are presented in the centrality selections 0-10% (open square) and 20-40% (up-side-down triangle) for 2011 Pb–Pb collisions. The vertical lines are the statistical uncertainties. The empty (filled) boxes are the uncorrelated (partially correlated) systematic uncertainties.

4.5 Λ/K^0_S in the correlated peak

The principal ingredient to pursue the purpose of this doctoral work is to obtain the Λ/K^0_S ratio of particles related to the hadronization mechanism of parton fragmentation in Pb–Pb collisions at LHC energies.

Figure 4.12 shows the relative production of Λ with respect to K^0_S when these particles are emitted in association to a high-p_T charged particle in the near-side peak (expected to come from a hard-scattering process) with transverse momentum in $5 < p_T^{Trig} < 10$ GeV/c. The results are derived for the centrality 0-10% centrality selection in Pb–Pb collisions at $\sqrt{s_{NN}} = 2.76$ TeV from the yield per trigger of Figure 4.8. The results in the 20-40% centrality interval are not included since the Λ per-trigger yield showed a point off the trend which is not understood yet.

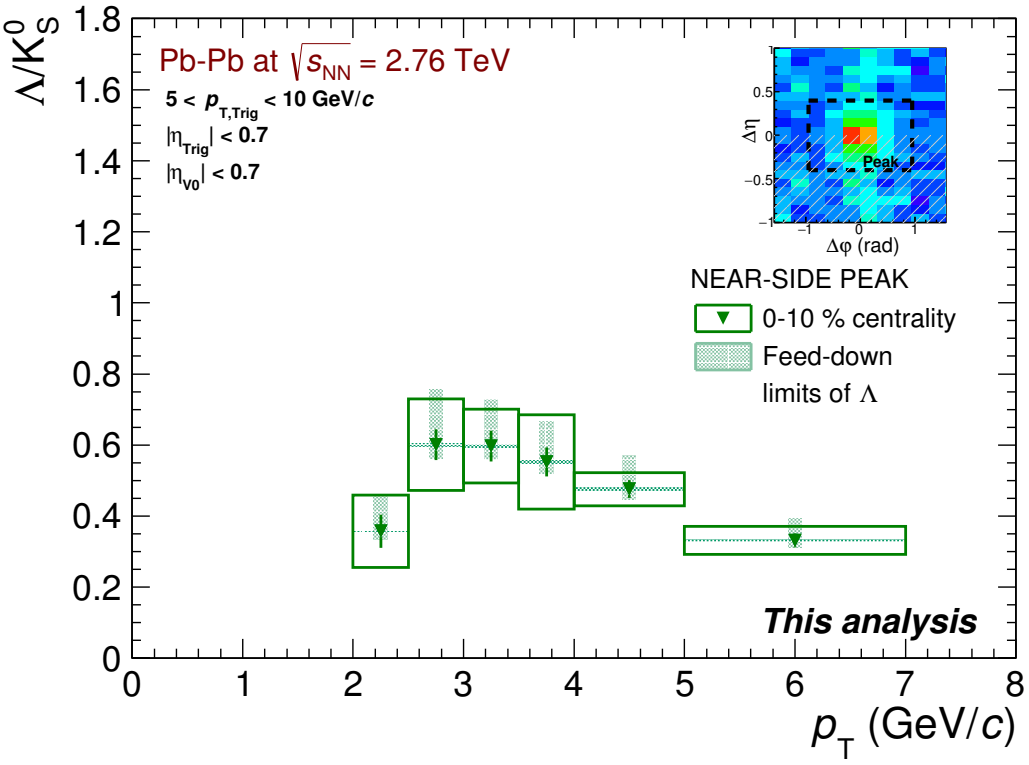

Figure 4.12: Λ/K^0_S ratio with particles emitted in association with a high-p_T particle in the near-side peak. The results are obtained with Pb–Pb collisions at $\sqrt{s_{NN}} = 2.76$ TeV for the 0-10% centrality selection. The markers are placed at the middle value of the bin. The horizontal bars represent the p_T-bin width. The statistical and systematic uncertainties are represented by vertical lines and boxes, respectively. The empty (filled) boxes indicates the contributions of the uncorrelated (partially correlated) systematic uncertainties. The projection in $\Delta\varphi$ was applied to extract the per-trigger yield. The $\overline{\Lambda}$ hadron is not included in the particle reconstruction.

4.6 Systematics studies

A substantial part for the experimental analysis performed in this dissertation is the estimation of the systematic uncertainties. After reviewing all the ingredients involved in the angular correlation analysis, we have classified the systematics studies in three different uncorrelated groups according to the nature of its selection:

Group 1 Event selection

Group 2 Angular correlation technique

Group 3 V0 particle reconstruction

The elements in each group are independent sources from the elements in another group.

4.6.1 Overview of the principles to follow for the systematic uncertainties

Uncorrelated systematics

For Group 1 and Group 2, the systematic selections are varied according to the values presented in Tables 4.1 and 4.2, respectively. The tables provide a first overview of the potential sources of systematic uncertainties that were investigated. More details on these contributions will be given in the next subsections. The selection of the systematic values for some of the elements (such as the centrality weight, the sampled region and the elliptic flow) are based on the own criteria gained with the experience on this analysis. For the rest of the selections, the values for the systematic studies are motivated by similar two-hadron correlation analyses from the ALICE collaboration. In Group 2, some systematic cuts are only applied to extract the yield associated to hard-parton scatterings, such as changing the bin-counting to a Gaussian fit and by considering other values of the elliptic flow for the trigger and associated particles.
In case of Group 3, the values corresponding to the topological cuts are determined via a 10% variation of the invariant raw yield with respect to the default value. The systematic cuts are evaluated separately for K^0_S and Λ, with the signal integrated within the transverse momentum range of these particle from 2 to 7 GeV/c. This selection criteria is biased in favor to the low-p_T values, implying that sometimes the deviation for the high-p_T values can be more than 10%.
A graphical representation of the percentile variation of the raw yield in Pb–Pb data is shown in Figure 4.13 with the cumulative frequency distribution (c.d.f.) for some of the topological selections. The value 1 for the c.d.f represents 100% of the reconstructed signal, when 0.9 is the 10% signal loss. The corresponding reconstructed Monte Carlo distribution for K^0_S and Λ are plotted as well. The combinatorial background from the side-bands of the K^0_S and the Λ are subtracted in a statistical way from the cumulative distributions for the experimental and Monte Carlo data.
From the distributions of Figure 4.13, we can observe that the signal loss of K^0_S and Λ is affected differently for a given topological cut hence also the systematic variations to apply to each particle. The full vertical arrows pointing to the data distributions are related to the ∼10% variation of the raw yield, therefore they represent the final systematic cut. The dashed horizontal arrows represent the range of values of the topological selection where the signal V0 particles is kept to evaluate the systematic uncertainties. For example, considering only the distance of closest approach between the daughter tracks (dca) (upper right panel in Figure 4.13),

the K^0_S systematic cut to be evaluated is indicated at dca < 0.3 cm that represent the 10% drop on the signal, thus keeping the K^0_S-sample in the range from 0 to 0.3 cm. The same procedure applies for Λ where the sample to keep for the systematic study belongs to the range 0-0.5 cm. Now, considering the distance to the primary vertex of daughter tracks, because of the asymmetrical decay of Λ, we vary the value for the positive daughter meanwhile the value for the negative daughter remains the same. Since K^0_S has a symmetric topological decay, the variations are applied at the same time for the two tracks.
A more detailed information about the variables to consider for the systematic studies of the topological and kinematical selection for the V0 reconstruction technique is listed in Table 4.3. The values of the systematic cuts to apply are also given.

Partially correlated systematics

From the evaluation of the systematic studies, we have determine one source of partially correlated systematics. This is the weighting factor in the centrality flattening correction (see Section 3.5) which leads to a partial correlation both between the K^0_S and Λ spectra and between p_T-bins for the each given species. The corresponding systematic studies are only applied for the central event where the centrality flattening correction only concerns.

Table 4.1: Systematic variations for the **Group 1** in the angular correlation analysis with the 2011 Pb–Pb data set.

Group 1 - Event selection	
Standard cuts	**Systematics variations**
Primary vertex position	
$\lvert z_{vtx}\rvert < 10$ cm	< 7 cm
Trigger particle	
Hybrid tracks	Global tracks

Table 4.2: **Group 2** of the systematic variations applied to the angular correlation analysis with the 2011 Pb–Pb data set.

Group 2 - Angular correlation technique	
Standard cuts	**Systematics variations**
Mixed events	
z_{vtx} bin width = 2 cm	= 1 cm
Sampled region	
No. bins $\Delta\eta = 30$,	No. bins $\Delta\eta = 40$,
No. bins $\Delta\varphi = 20$	No. bins $\Delta\varphi = 30$
Jet peak	
Bin counting in $\Delta\varphi$	Gaussian fit
Elliptic flow values	
Mean v_2	v_2 within uncertainties
	Weighted v_2 average

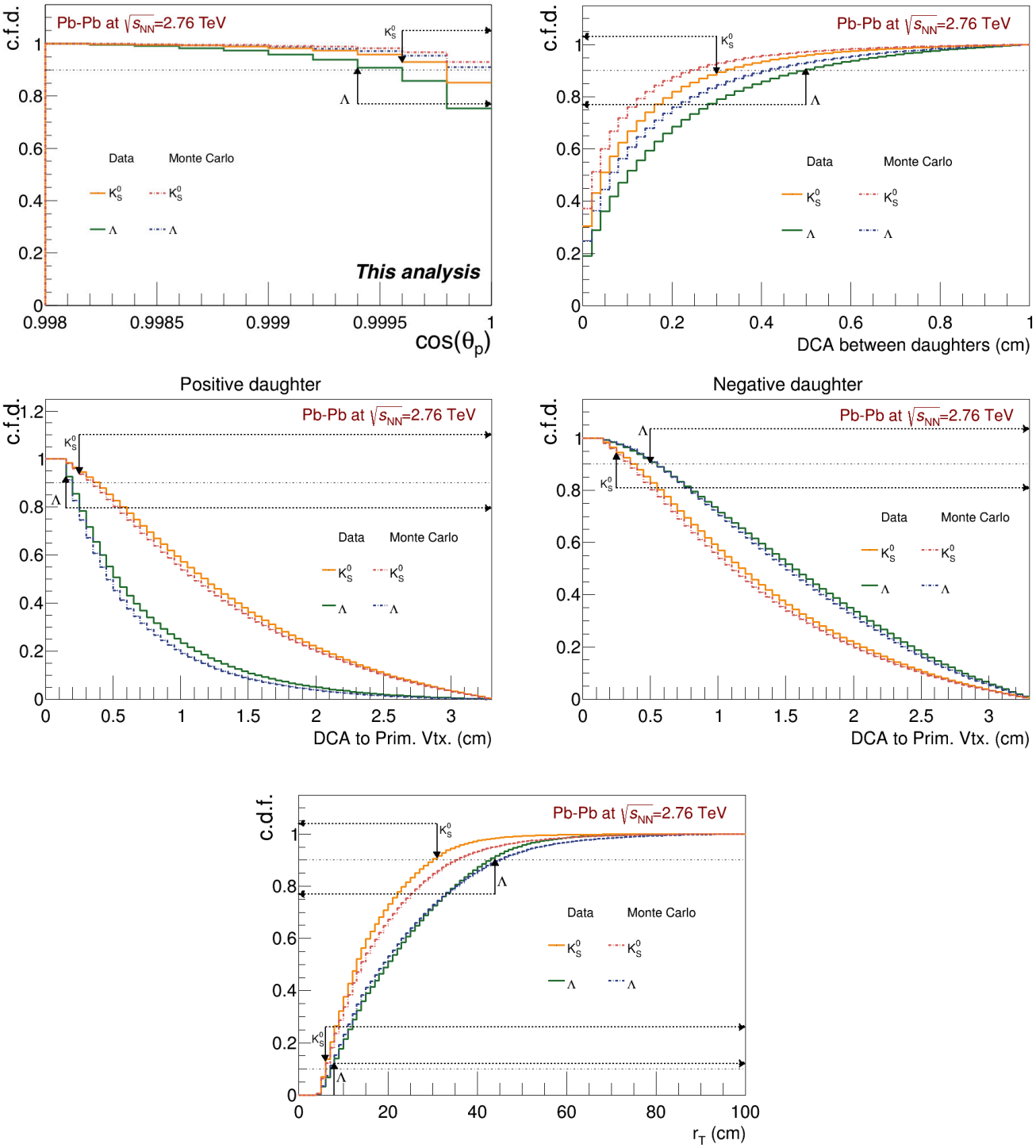

Figure 4.13: Cumulative frequency distributions (c.d.f) for the different V0 topological selections. The vertical arrows represent the systematic cuts to apply to K^0_S and Λ when a 10% variation is obtained in the raw inclusive yield integrated for the p_T-interval $2 < p_T < 7$ GeV/c. The horizontal dashed arrows indicate the range of values that are kept while doing the systematic variation of the topological selection for the systematic studies.

Table 4.3: Selections applied in the **Group 3** for the systematic studies performed in the angular correlation analysis in Pb–Pb collisions with the 2011 data set.

Group 3 - V0 reconstruction					
Standard cuts			**Systematics variations**		
	K^0_S		Λ		
	Syst. cut 1	**Syst. cut 2**	**Syst. cut 1**	**Syst. cut 2**	**Syst. cut 3**
Daughter track selection					
DCA between daughters $< 1.0\ \sigma$	$< 0.3\ \sigma$	—	$< 0.5\ \sigma$	—	—
DCA to the primary vertex (b) > 0.1 cm	$b > 0.25$ cm	—	$b_{\mathrm{pos(neg)}} >$ 0.1(0.5) cm	$b_{\mathrm{pos(neg)}} >$ 0.15(0.1) cm	—
Number of TPC crossed pad rows > 70	> 80	—	> 80	—	—
$p_T > 160$ MeV	No cut	> 0.5 GeV/c	No cut	$p_T^{\mathrm{pos(neg)}} >$ 1.7(0.16) GeV/c	$p_T^{\mathrm{pos(neg)}} >$ 0.16(0.3) GeV/c
V0 candidates					
Invariant mass selection $\pm 4\sigma$	$\pm 5\sigma$	$\pm 3\sigma$	$\pm 5\sigma$	$\pm 3\sigma$	—
CPA > 0.998	> 0.9996	—	> 0.9994	—	—
$\frac{l_T\, m}{p_T} < 3\, c\tau_{\mathrm{PDG}}$	$< 5\, c\tau_{\mathrm{PDG}}$	—	$< 5\, c\tau_{\mathrm{PDG}}$	—	—
Fiducial volume $5 < r_T < 100$ cm	$7 < r_T <$ 100 cm	$5 < r_T <$ 31 cm	$8 < r_T <$ 100 cm	$5 < r_T < 44$ cm	—

To evaluate the systematic uncertainties in this analysis, we examine one per one the contribution of each element by varying its nominal value while keeping the the other selections at their own default value. For example, for K^0_S, we vary the upper limit on the fiducial volume from 100 cm to 31 cm, while the lower value of r_T and the rest of the selections have the default value. It is also worth to mention that for each systematic variation in data, the same variation has been done in Monte Carlo to derive the corresponding eff $\times$ Accep. $\times$ B.R.; thus, correcting the yield for any signal loss in data which turns out to be important for the Group 3 of the systematic variations.
One last point to remark, the systematic uncertainties for the Λ/K^0_S is obtained with the systematic variation for K^0_S and Λ performed at the same time. Taking as an example the distance of closest approach between daughters, the systematic variation is applied as 0.3 cm for K^0_S and 0.5 cm for Λ, then the Λ/K^0_S ratio is obtained with the yields extracted with such variations.

4.6.2 Criteria to determine and combine the uncorrelated systematic uncertainties

The evaluation of the systematic uncertainties are performed by applying different criteria for each group.

Group 1 In this systematic group, we have only two components for the event selection. The total systematic uncertainty in this group (σ_{G1}) is calculated by the sum in quadratures of each individual deviation.

Group 2 The total systematic uncertainty corresponding to the angular correlation technique (σ_{G2}) is derived by applying different principles for the results in the bulk than for the near-side peak. In the bulk we have two elements for the assessment, consequently we will calculate σ_{G2} in the bulk as in Group 1, with the sum in quadratures of the deviations. In case for the jet, we have more number of contributions to the systematic uncertainty. Then evaluating σ_{G2} as the absolute maximum deviation in each p_T-bin will contain all the individual elements. This approach would not be overestimating the uncertainty as it would be by summing in quadratures of all the elements. Also the sources of systematic uncertainties in the near-side peak are not independent, e.g. the near-side peak shape for the Gaussian fit would depend on the flow subtraction.

Group 3 For the V0 particle reconstruction, the systematic studies involve a large number of variations for each part of the analysis, the bulk and the near-side peak. Here, we come again to the decision of not applying the sum in quadratures of all the deviations since it can lead to overestimating the systematic uncertainty since the contributions are not independent among each others. As a consequence, we decide to take the absolute maximum deviation to represent the systematic uncertainty in this group (σ_{G3}).

The total systematic uncertainty, as function of the associated particle p_T, is calculated as the quadratic sum of these individual contributions since independence between groups have been assumed.

$$\sigma_{Tot}(p_T) = \sqrt{\sigma^2_{G1}(p_T) + \sigma^2_{G2}(p_T) + \sigma^2_{G3}(p_T) + \sigma^2_{Mat.Budget} + \sigma^2_{FD}} \tag{4.7}$$

In the last expression the σ^2_{FD} term is only used for the Λ per-trigger yield and for the baryon-to-meson ratio. The uncertainties corresponding to the material budget contribution and the Λ feed-down correction are taken from the publications [169] and [117], respectively.

4.6.3 Detailed list of the systematic uncertainties

In this subsection, we will see in more detail how the contribution of each systematic source affects the per-trigger yields and the Λ/K^0_S in the two regions, the near-side peak and the bulk.

G1 - Primary vertex selection

By restricting the primary vertex position down to $|z_{vtx}| < 7$ cm, we obtain a more uniform particle acceptance in the detector. The systematic cut represent about 30% reduction in the number of selected Pb–Pb events. Due to the nature of the Gaussian distribution for the primary vertex, with mean value approximately at zero (see Figure 3.4), most of the events contributing to the two-hadron angular correlations comes from the primary vertex position range around ± 2 cm. Therefore, the results in the Bulk I are not strongly affected by this variation, leading to a systematic uncertainty of only 2% for K^0_S and less than 4% for Λ. For the near-side peak, their corresponding systematic uncertainties appear to have a larger contribution, up 6-13% (see Table 4.6).

G1 - Trigger particle selection

The selected tracks to perform the systematic studies for the trigger particle are named 'global tracks'. Its reconstruction requirements vary with respect to the hybrid track selection according to the specifications listed in Table 4.4. The main two differences between these two track selections are: i) the global tracks have always a tight constraint on the distance of closest approach to the primary vertex determined with the p_T-dependence selection, and ii) when there is no signal in none of the SPD layers, then the tracking requires to have a signal in the first SDD layer. Besides, the track splitting effects has been inspected in the $h^{\pm}$–V0 correlations also with the global track as trigger particle. This check follows the same procedure as previously applied for the hybrid tracks in subsection 3.5.1. The results have showed that none fake correlations are introduced in the angular correlation distribution, therefore it is reliable to consider this track selection in the systematic analysis.

It has been quantified that the yield per trigger in the bulk shows a 4% in the systematic contribution for the two hadrons, while the contributions decreases to 1% for the Λ/K^0_S result in the bulk. The trigger particle selection appears to have a large influence in the near-side results, especially on the Λ per-trigger yield at the low-p_T range and, as a consequence, in the Λ/K^0_S ratio (see upper panel in Figures 4.19 and 4.20). Below 3 GeV/c in the transverse momentum, the Λ systematic uncertainty reaches up to 20% variations with respect to the default values. In the rest of the p_T-range, the results have about 5% contribution to the uncertainties. The yield per trigger of the K^0_S in the near-side peak does not vary as significantly as for the Λ particle.

Table 4.4: Principal differences on the applied trigger particle selections between the hybrid tracks (default selection) and the global tracks (used for the systematic studies). Δ_{xy} and Δ_z are the impact parameters to the primary vertex in xy and z dimensions, respectively. *This selection is only applied for the sectors where the SPD ladders are not functioning.

	Hybrid track	**Global track**
SPD hit(s)	Yes	No
Hits in the first SDD layer*	—	Yes
Maximum distance to the primary SPD vertex d_{xy} (d_z)	$< 0.0105 + \frac{0.0350}{p_{\mathrm{T}}}$ cm (< 2 cm)	$< 0.0105 + \frac{0.0350}{p_{\mathrm{T}}}$ cm (< 2 cm)
Constrain to the primary SPD vertex*	$\left(\frac{\Delta_{xy}}{d_{xy}}\right)^2 + \left(\frac{\Delta_z}{d_z}\right)^2 < 1$	—

G2 - Mixed events

Applying the mixed-event correction, by obtaining systematically the same-event and the mixed-event distributions in a finer bin width of the primary vertex longitudinal position, shows to introduce a minor effect in the results. Around a 2% uncertainty is evaluated for the yield per trigger in the bulk as in the near-side peak for the two hadrons, $\mathrm{K}^0_{\mathrm{S}}$ and Λ. The baryon-to-meson ratio is affected by less than 2% in the bulk region and the correlated near-side peak.

G2 - Sampled region

The systematic studies in the bulk were performed by changing the $\Delta\eta$ and $\Delta\varphi$ bin-width at the same time. Evaluating the particle yield with slightly different boundaries leads the result to the following variations: less than 3% contribution for the per-trigger yields (for $\mathrm{K}^0_{\mathrm{S}}$ and for Λ) and the $\Lambda/\mathrm{K}^0_{\mathrm{S}}$ ratio in the bulk. However, the systematic uncertainty for the $\Lambda/\mathrm{K}^0_{\mathrm{S}}$ ratio in the bulk shows an augmentation to 6% in the transverse momentum above 5 GeV/c caused by the increase of the Λ production in this p_{T}-range.

For the near-side systematic studies, only the $\Delta\varphi$ bin-width was varied. The near-side peak production of the $\mathrm{K}^0_{\mathrm{S}}$ and Λ considers larger integration limits than in the relation 4.6, passing from ± 0.94 to ± 1.08. The $\Delta\eta$-range selection is kept at the same values (± 0.4). The major effects of this change are observed for the per-trigger yield of Λ (for the p_{T}-range below 3.5 GeV/c) which shows a reduction in the associated yield to the trigger particle down to $\sim$-12%. This outcome relates to the furthest $\Delta\varphi$ bins in the near-side region to consider in the yield per trigger extraction. This bins are under the curve that describes the elliptical flow contribution (as seen in the upper left panel in Figure E.1), therefore we subtract a larger quantity from the yield by applying the bin counting method. The $\mathrm{K}^0_{\mathrm{S}}$ yield does not show a large deviation (being below 5%) with this systematic cut.

Table 4.5: Contributions to the uncorrelated systematic uncertainties in the **bulk I**. The values corresponds to the centrality selection **0–10%** in Pb–Pb collisions at $\sqrt{s_{NN}} = 2.76$ TeV.

Source of systematic uncertainties	**Bulk**		
	K^0_S	Λ	Λ/K^0_S
— Group 1 —			
Primary vertex position	$< 2\%$	$< 1.5\%$ ($p_T < 5$ GeV/c) 4% ($p_T > 5$ GeV/c)	$< 1\%$ ($p_T < 5$ GeV/c) 1-3% ($p_T > 4$ GeV/c)
Trigger particle	$\sim 4\%$	$\sim 4\%$ ($p_T < 5$ GeV/c) 2% ($p_T > 5$ GeV/c)	$\lesssim 1\%$
Total G1 ($\sum \sigma_i^2$)	**3-5%**	**4-5%**	**$< 2\%$ ($p_T < 5$ GeV/c)** **4% ($p_T > 5$ GeV/c)**
— Group 2 —			
Mixed-events	$\lesssim 3\%$	$\sim 2\%$	$< 1.5\%$
Sampled region	$< 3\%$	1-2% ($p_T < 5$ GeV/c) 4% ($p_T > 5$ GeV/c)	$< 1.5\%$ ($p_T < 5$ GeV/c) 6% ($p_T > 5$ GeV/c)
Total G2 ($\sum \sigma_i^2$)	**2-4%**	**$\sim 2.5\%$ ($p_T < 5$ GeV/c)** **5% ($p_T > 5$ GeV/c)**	**$< 2\%$ ($p_T < 5$ GeV/c)** **6% ($p_T > 5$ GeV/c)**
— Group 3 —			
Daughter track selection			
DCA between daughters	$\sim 4\%$ ($p_T < 2.25$ GeV/c) $< 2\%$ ($p_T > 2.25$ GeV/c)	$< 3\%$	$< 2\%$
DCA to the primary vertex	$\lesssim 2\%$	$\leq 3.5\%$ ($p_T < 5$ GeV/c) 5% ($p_T > 5$ GeV/c)	$< 3\%$
No. TPC crossed pad rows	$< 1\%$	$< 3\%$	$< 2\%$
p_T	$< 2.5\%$	4-7% ($p_T < 2.5$ GeV/c) $< 3\%$ ($p_T > 2.5$ GeV/c)	4-7% ($p_T < 2.5$ GeV/c) $< 2\%$ ($p_T > 2.5$ GeV/c)
V0 candidates			
Invariant mass range	2-3%	$< 3\%$	$< 3\%$
CPA	$\lesssim 3\%$	4-6% ($p_T < 3$ GeV/c) $< 3\%$ ($p_T > 3$ GeV/c)	4-6% ($p_T < 2.75$ GeV/c) $< 3\%$ ($p_T > 2.75$ GeV/c)
$c\tau$	$< 1.5\%$	4-5% ($p_T < 3$ GeV/c) $< 3\%$ ($p_T > 3$ GeV/c)	2-5% ($p_T < 3.5$ GeV/c) $\sim 1\%$ ($p_T > 3.5$ GeV/c)
Fiducial volume	$< 1.5\%$ ($p_T < 4$ GeV/c) $\sim 3.5\%$ ($p_T > 4$ GeV/c)	3.5-9%	3-6%
Total G3 ($\max\{\sigma_i^2\}$)	**2-4%**	**4-9%**	**3.5-6%**
Material budget	**1.5%**	**3.4%**	**3.7%**
Feed-down correction	—	**5%**	**5%**
Total	**5-7%**	**8-12%**	**7-10%**

Table 4.6: Evaluated uncorrelated systematics uncertainties in the **near-side peak**. The values correspond to the centrality interval **0–10%** in Pb–Pb collisions at $\sqrt{s_{\rm NN}} = 2.76$ TeV.

Source of systematic uncertainties	**Near-side peak**		
	$\rm K^0_S$	Λ	$\Lambda/\rm K^0_S$
— Group 1 —			
Primary vertex position	$< 6\%$	2-7%	2-13%
Trigger particle	$< 7\%$	10-20% ($p_{\rm T} < 3$ GeV/c) 2-7% ($p_{\rm T} > 3$ GeV/c)	$\sim 18\%$ ($p_{\rm T} < 3$ GeV/c) 2-5% ($p_{\rm T} > 3$ GeV/c)
Total G1 ($\sum \sigma_i^2$)	$< \mathbf{7\%}$	**21% ($\mathbf{p_{\rm T} < 2.5}$ GeV/c)** **5-11% ($\mathbf{p_{\rm T} > 2.5}$ GeV/c)**	**13-18% ($\mathbf{p_{\rm T} < 4}$ GeV/c)** $< \mathbf{7\%}$ **($\mathbf{p_{\rm T} > 4}$ GeV/c)**
— Group 2 —			
Mixed-events	$< 2\%$	$< 2\%$	$< 2\%$
Sampled region	$< 5\%$	5-12% ($p_{\rm T} < 3.5$ GeV/c) $\sim 2.5\%$ ($p_{\rm T} > 3.5$ GeV/c)	11% ($p_{\rm T} < 2.5$ GeV/c) 2-5% ($p_{\rm T} > 2.5$ GeV/c)
Jet peak	11% ($p_{\rm T} < 2.5$ GeV/c) $\lesssim 14\%$ ($p_{\rm T} > 2.5$ GeV/c)	13% ($p_{\rm T} < 3$ GeV/c) $\sim 3.5\%$ ($p_{\rm T} > 3$ GeV/c)	$< 8\%$
Elliptical flow	8% ($p_{\rm T} < 2.5$ GeV/c) $\lesssim 4\%$ ($p_{\rm T} > 2.5$ GeV/c)	18% ($p_{\rm T} < 2.5$ GeV/c) 5-9% ($2.5 < p_{\rm T} < 4$ GeV/c) 1-3% ($p_{\rm T} > 4$ GeV/c)	9% ($p_{\rm T} < 2.5$ GeV/c) $< 5\%$ ($p_{\rm T} > 2.5$ GeV/c)
Total G2 ($\max\{\sigma_i^2\}$)	**2-12%**	**12-18% ($\mathbf{p_{\rm T} < 3}$ GeV/c)** **3-9% ($\mathbf{p_{\rm T} > 3}$ GeV/c)**	**4-11%**
— Group 3 —			
Daughter track selection			
DCA between daughters	5-8% ($p_{\rm T} < 3$ GeV/c) $< 2.5\%$ ($p_{\rm T} > 3$ GeV/c)	7-12% ($p_{\rm T} < 3.5$ GeV/c) $< 4\%$ ($p_{\rm T} > 3.5$ GeV/c)	2-6%
DCA to the primary vertex	7% ($p_{\rm T} < 2.5$ GeV/c) 2-4% ($2.5 < p_{\rm T} < 3.5$ GeV/c) $< 1\%$ ($p_{\rm T} > 3.5$ GeV/c)	24% ($p_{\rm T} < 2.5$ GeV/c) 2-6% ($p_{\rm T} > 2.5$ GeV/c)	16% ($p_{\rm T} < 2.5$ GeV/c) 2-9% ($p_{\rm T} > 2.5$ GeV/c)
No. TPC crossed pad rows	$< 2\%$	$< 3.5\%$	$< 2\%$
$p_{\rm T}$	$< 3\%$	5-16% ($p_{\rm T} < 3.5$ GeV/c) $< 3\%$ ($p_{\rm T} > 3.5$ GeV/c)	17% ($p_{\rm T} < 2.5$ GeV/c) 7% ($2.5 < p_{\rm T} < 3$ GeV/c) $< 4\%$ ($p_{\rm T} > 3$ GeV/c)
V0 candidates			
Invariant mass range	2-5%	12% ($p_{\rm T} < 2.5$ GeV/c) $< 4\%$ ($p_{\rm T} > 2.5$ GeV/c)	10% ($p_{\rm T} < 2.5$ GeV/c) $< 7\%$ ($p_{\rm T} > 2.5$ GeV/c)
CPA	$< 4\%$	$< 9\%$	$< 8\%$
$c\tau$	$< 2\%$	$< 6\%$	$< 7\%$
Fiducial volume	$< 10\%$	5-16% ($p_{\rm T} < 5$ GeV/c) 2% ($p_{\rm T} > 5$ GeV/c)	3% ($p_{\rm T} < 2.5$ GeV/c) 9-18% ($2.5 < p_{\rm T} < 4$ GeV/c) $\sim 4\%$ ($p_{\rm T} > 4$ GeV/c)
Total G3 ($\max\{\sigma_i^2\}$)	**3-10%**	**24% ($\mathbf{p_{\rm T} < 2.5}$ GeV/c)** **10-16% ($\mathbf{2.5 < p_{\rm T} < 5}$ GeV/c)** **5-6% ($\mathbf{p_{\rm T} > 5}$ GeV/c)**	**17-29% ($\mathbf{p_{\rm T} < 4}$ GeV/c)** $\sim$ **5% ($\mathbf{p_{\rm T} > 4}$ GeV/c)**
Material budget	**1.5%**	**3.4%**	**3.7%**
Feed-down correction	—	**5%**	**5%**
Total	**4-15%**	**10-38%**	**10-29%**

Fit to the near-side peak[3]

The default procedure to estimate the yield in the near-side peak is by bin-counting. But the systematic studies will implement another approach, as it is explained as follows. After the elliptic flow effects are subtracted, the hadron production associated to hard parton scatterings is phenomenologically described with a single Gaussian function around the peak in the $\Delta\varphi$-distribution, i.e. around $\Delta\varphi \approx 0$ (see Figure 4.14). The fitting procedure does not include any other function but the single Gaussian representation. The results are obtained by integrating the fit in the same $\Delta\varphi$ range as done for the correlation distribution (see limits in the mathematical expression 4.6). The integrated yield from the fit results, at low-p_T, in a positive variation with respect to the reference yield, extending up to 11% and 13% for K^0_S and Λ, respectively. As mentioned in the 'Sampled region' systematic study, the difference is originated by the $\Delta\varphi$-bins which have negative values (caused by the v_2 subtraction). In the p_T-range above 3 GeV/c, the variations in the per-trigger-yield are reduced to less than 4%. The larger effects observed in the per-trigger yield are cancelled out on the Λ/K^0_S ratio in the near-side peak, thus there are only small contribution to the Λ/K^0_S systematic uncertainties in all the p_T range, being less than 8%.

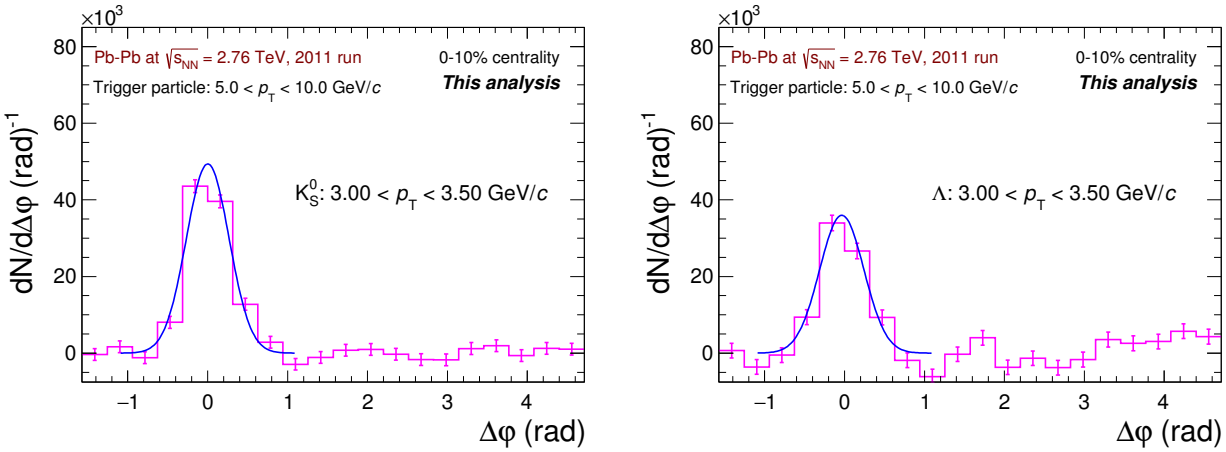

Figure 4.14: Gaussian fit to the near-side peak after the elliptic flow contribution is subtracted. The results are shown for the K^0_S (left panel) and Λ (right panel) for the most central collisions.

G2 - Elliptic flow subtraction[3]

The anisotropic flow is an essential element to obtain the per-trigger yield associated to the production by parton fragmentation, as expressed in Equation 4.6. The systematic study is performed by varying the elliptic flow values of the trigger and the associated particles at the same time in the same direction. The variations are obtained in two ways. The first one is achieved by adding (or subtracting) to the mean v_2 value the contributions from the respective statistical (σ_{stat}) and systematic (σ_{syst}) uncertainties, consistently for the charged trigger particles and the V0 particles, as follows

[3]This systematic study is only performed for the results in the near-side peak.

$$< v_2 >_{\text{syst. max.}} = < v_2 > + 3\sqrt{\sigma^2_{\text{stat}} + \sigma^2_{\text{syst}}}, \tag{4.8}$$

$$< v_2 >_{\text{syst. min.}} = < v_2 > - 3\sqrt{\sigma^2_{\text{stat}} + \sigma^2_{\text{syst}}}. \tag{4.9}$$

The factor 3 accounts for large deviation (3 standard deviation) of the elliptic flow values, following the criteria for the Group 2 about estimating the systematic uncertainty by taking the maximum deviation of all the applied cuts in the group. The systematic uncertainties of the trigger particle $\sigma_{\text{syst}}(v_2^{\text{Trig}})$ are taken from [105]. For the K^0_S and Λ, the systematic uncertainties are 0.001 and 0.002 units of v_2 [112], respectively, in the transverse momentum range and the centrality of the analysis. The second way of tackling the elliptic flow systematic studies is by calculating weighted v_2 values for the flow subtraction, using the number of trigger particles in the centrality intervals 0-5% and 5-10% as the weights.
The contributions originated from all these factors are illustrated in Figures 4.18, 4.19, and 4.20 (see middle panels). It is observed that the weighted v_2 provides larger deviations for p_{T} below 2.5 GeV/c (3.5 GeVc) for kaons (Λ) than considering the other two set of v_2 values (labeled as upper values and lower values in the graph). In the case of the Λ, this turns out to be the dominant systematic uncertainty, at the lowest p_{T}-bin, for the Group 2. At large p_{T} ($p_{\text{T}} > 3.5$ GeV/c), the elliptic flow variations affects all the results to a level below 5%.

G3 - Distance of closest approach between daughter tracks

Rejecting the V0 candidates by decreasing the limit in the distance of closest approach between the daughter tracks does not substantially change the final results, neither on the bulk nor on the production in the near-side peak, because a large amount of V0 candidates have daughter tracks significantly close in distance to the point of the decay vertex. It has been found that only at the lowest-p_{T} bin for the K^0_S production in the bulk, this systematic cut dominates over the other systematic variations with a 4% uncertainty related to the topological selections (Group 3).

G3 - Distance of closest approach to primary vertex for daughter tracks

Applying a larger rejection cut in the distance of closest approach to the primary vertex (b) position affects immediately more the most energetic daughter tracks because they do not experience large bending from the magnetic field. As a consequence, they are propagated at closer distance to the primary vertex than the low-p_{T} tracks and thus being rejected with this topological selection. This effect can be clearly seen in the per-trigger yield of Λ in the bulk when the cut is applied on the positive daughter, with the yield decreasing slowly as the p_{T} increases towards the highest value, reaching about 5% in the systematic uncertainty. The K^0_S yield in the bulk has less than a 2% impact.
The situation of the near-side results shows to be different, especially for Λ, affecting more the low-p_{T} particles. This is because the b distributions in the near-side peak are not the same as in the bulk. This systematic variation is dominant at the lowest p_{T}-bin for the two hadrons, reaching contributions of 7% for K^0_S and 24% for Λ.

G3 - Number of the TPC crossed pad rows

In the Pb–Pb data taken by ALICE, most of the daughter tracks have large number of TPC crossed pad rows (more than 100 out of 159 possible at most), therefore this fact is reflected in

the small variation observed from the systematic studies, less than 4%, for the yield per trigger and the baryon-to-meson obtained in the bulk and in the near-side peak as well.
A larger variation for the systematic cut is not possible due to the poor description of the Monte Carlo data to the experimental data.

G3 - Transverse momentum of daughter tracks
On the one hand, releasing the selection on the transverse momentum of the daughter tracks leads to the increase of the signal for low-p_T V0 candidates. Then, the kinematical properties of the negative daughter of Λ produce a larger impact on the baryon yield than for the meson. Selecting daughter tracks with no lower limit accepts up to 7% more Λ entering to the bulk per-trigger yield. Such cut brings the Λ yield in the near-side peak up to 16% higher with respect to the reference value in the same p_T-range below 2.5 GeV/c.
On the other hand, when moving the lower p_T-limit to higher values than the reference, the K^0_S yield per trigger decreases by 2% (3%) in the whole (lowest) p_T-range for the bulk (near-side peak). For the Λ daughter tracks, the shifting of the threshold is applied independently on each daughter due to the asymmetric topological decay. It results in a decrease of the yield between 4-7% for the lowest p_T-bins when the positive daughter track has $p_T > 1.7$ GeV/c. For the rest of the p_T-range this cut does not alter the per-trigger yield. Increasing the lower-p_T value for the negative track does not modify the yield in the bulk. In the near-side peak, the Λ yield per trigger decreases at most 5% in the p_T-range below 3.5 GeV/c. The variation in the Λ/K^0_S ratio originates from the variations of the Λ per-trigger yield in both the bulk and the near-side peak region.

G3 - Invariant mass range selection
The systematic procedure to follow considering in increasing and decreasing the mass range in the bin-counting for the signal extraction of the hadrons. The systematic range are chosen to be $\pm5\sigma$ and $\pm3\sigma$, with the σ being the detector mass resolution obtained from the fit to the invariant mass peak. In case of the bulk, this systematic cut leads to less than 3% contribution on all the three results we obtain in this analysis. The jet-associated production in the near-side peak has less than 12% variation for all the results here-performed as well.

G3 - Cosine of the pointing angle
The systematic cut in the cosine of the pointing angle affects in a minor scale the K^0_S production in the bulk and also in the correlated peak by less than 4%. However, the situation is different for Λ. In the bulk, this systematic cut dominates the Λ per-trigger yield in the p_T-range up to 2.75 GeV/c reaching up to 6% contribution. Then, the Λ/K^0_S ratio is also affected in the same p_T-range than the Λ baryon. The Λ near-side yield, the systematic variation is a bit larger than in the bulk.

G3 - Proper decay length $c\tau$
Increasing proper decay length does not have a large impact in detecting more hadrons due to the fact the $c\tau$ has an inverse exponential trend. As a reminder, the $c\tau_{PDG}$ values for K^0_S and Λ are 2.68 cm and 7.98 cm, respectively. We quantify a contribution less than 2% for K^0_S in the bulk production. The largest variation of Λ is at low-p_T with a 5% increase in the yield. The

effects are similar for the near-side peak yield for the two hadrons.

G3 - Fiducial volume

Studies on the fiducial volume selection are done by varying the upper and the lower boundaries where the reconstructed position of the V0 candidate decays. The K^0_S are mostly affected by reducing the upper threshold that leaves out the hadrons with higher momentum since these are the particles that decay further from the primary vertex. The evaluation of the rejection in the bulk is ∼3% for $p_T > 4$ GeV/c, while in the near-side peak is less than 10%. Similar situation happens to Λ where the rejection grows when the transverse momentum of the hadron increases being in magnitude of about ∼ 9% (16%) for the bulk (correlated peak) production.

Centrality weight

This source introduces a partially correlated systematic between the hadrons, K^0_S and Λ, and between the bin content in the p_T-spectra. The systematic studies on the centrality flattening are performed by decreasing the correction interval to 0.2% widths, within the 8.8%-10% centrality selection, instead of having one single interval of 1% covering the 9-10% centrality range. The centrality weight provides a minimum contribution to the systematic uncertainties. For the per-trigger yield in the bulk and in the near-side peak we obtain contribution of less than 3%, while the variation of the Λ/K^0_S ratio in these two regions is less than 1%. The systematic uncertainties for this cut is summarized in Table 4.7.

Table 4.7: Contributions of the partially correlated systematics uncertainties in the **bulk I** and in the **near-side peak** in the **0–10%** Pb–Pb collisions centrality interval.

Source of systematic uncertainties	**Bulk**		
	K^0_S	Λ	Λ/K^0_S
Centrality weight	∼ 2%	∼ 2%($p_T < 5$ GeV/c) ∼ 3%($p_T > 5$ GeV/c)	< 1%
Source of systematic uncertainties	**Near-side peak**		
	K^0_S	Λ	Λ/K^0_S
Centrality weight	< 2%	< 2%	< 1%

All the discussed contributions of the systematic studies, in the yield per trigger of K^0_S and Λ as well as the Λ/K^0_S (in the bulk and in the near-side peak), are summarized in Table 4.5 and Table 4.6 for the centrality interval 0-10%. The same contributions are illustrated from Figure 4.15 to Figure 4.20 showing the p_T-dependence of the systematic uncertainties.
The systematics uncertainties for the bulk results, the per-trigger yields of K^0_S and Λ and the Λ/K^0_S ratio, in the 20-40% centrality class are derived following the same approach that is presented in this chapter. Their contributions were found to be similar to the corresponding results in the 0-10% centrality interval, therefore no graphical representation on their p_T-differential systematic uncertainties is included in this thesis.

Adding some remarks, the size of the systematic uncertainties of the Λ/K^0_S obtained in the bulk have shown to be of the same magnitude as in the published measurements which have a maximal systematic uncertainty of 10%. On the other hand, the systematic uncertainties of the ratio in the near-side peak have more relative contribution than the ones in the bulk, since the analysis in this region calls for an extra step (anisotropic flow contribution and its dominant components) coming along with sizable systematic uncertainties.

In Figure 4.21, the contributions related to the uncorrelated and partially correlated systematic uncertainties are summarized for each of the obtained results in this analysis: the yield per trigger of K^0_S and Λ in the bulk and in the near-side peak, as well as, the corresponding Λ/K^0_S ratios. The relative statistical errors are also included in the figures.

In the next chapter, we will discuss the impact of the results obtained of the hadron production via the two-hadron angular correlation technique.

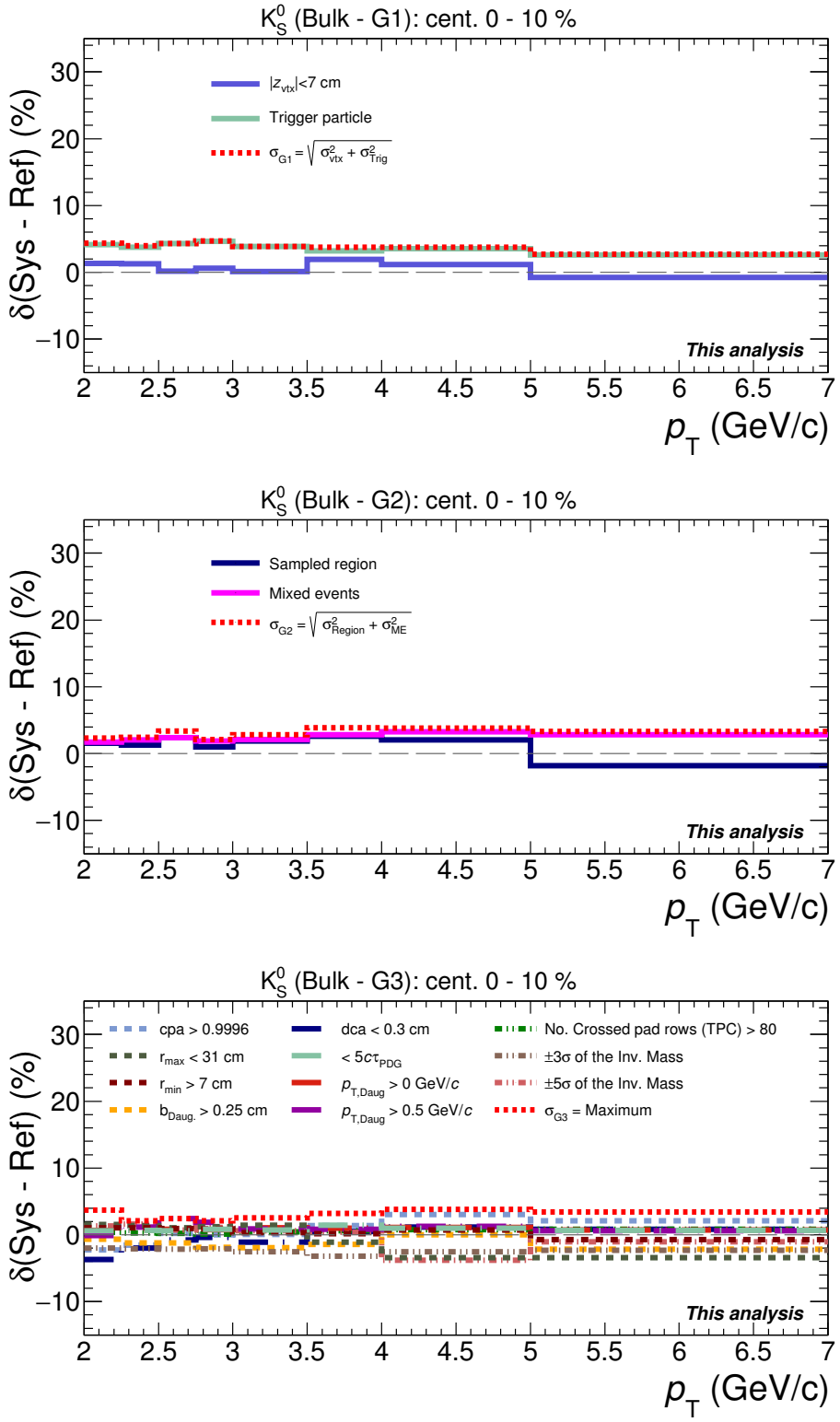

Figure 4.15: Systematics uncertainties for K^0_S of the yield per trigger the **Bulk I** in the centrality **0-10%**.

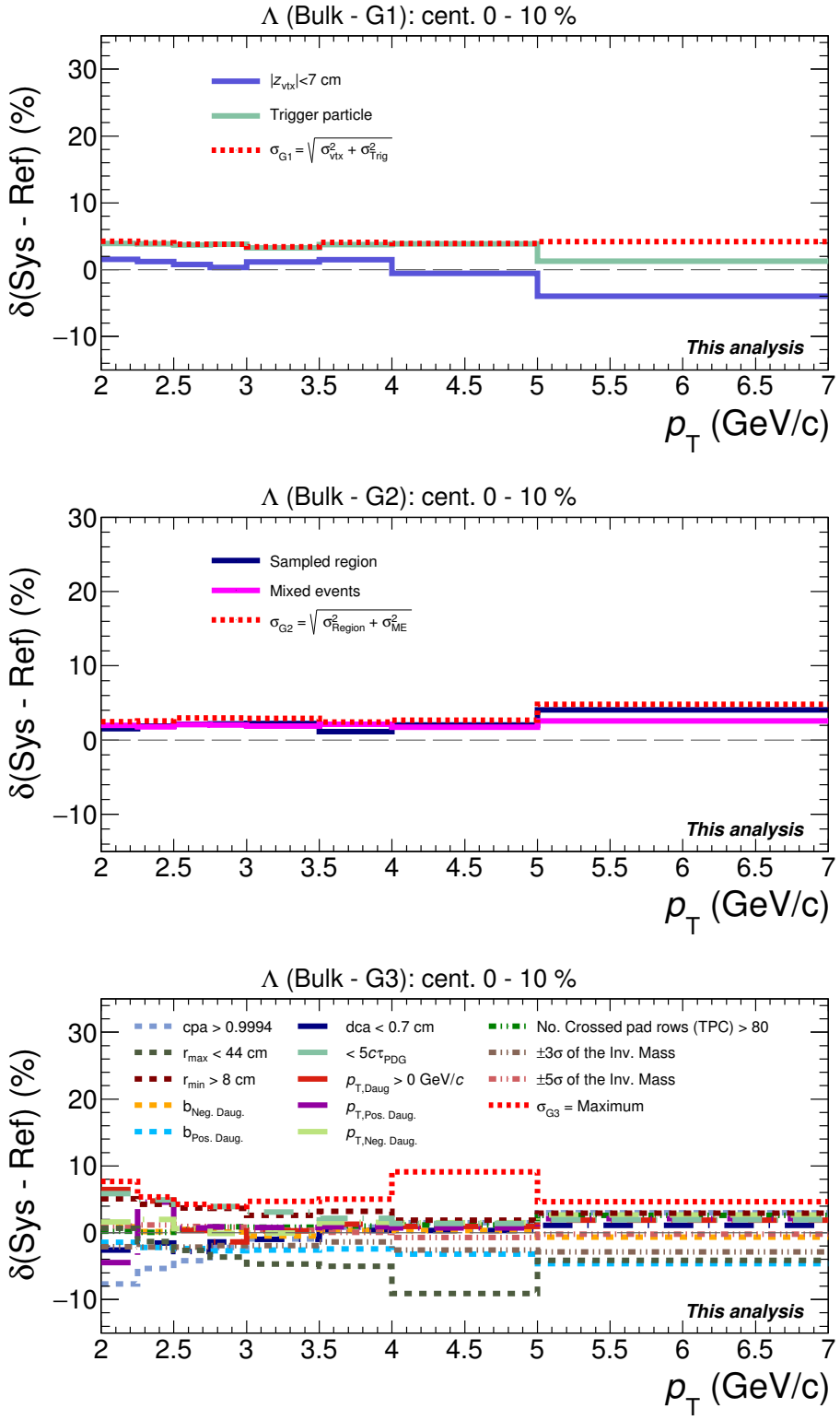

Figure 4.16: Systematics uncertainties for Λ of the yield per trigger the **Bulk I** in the centrality **0-10%**.

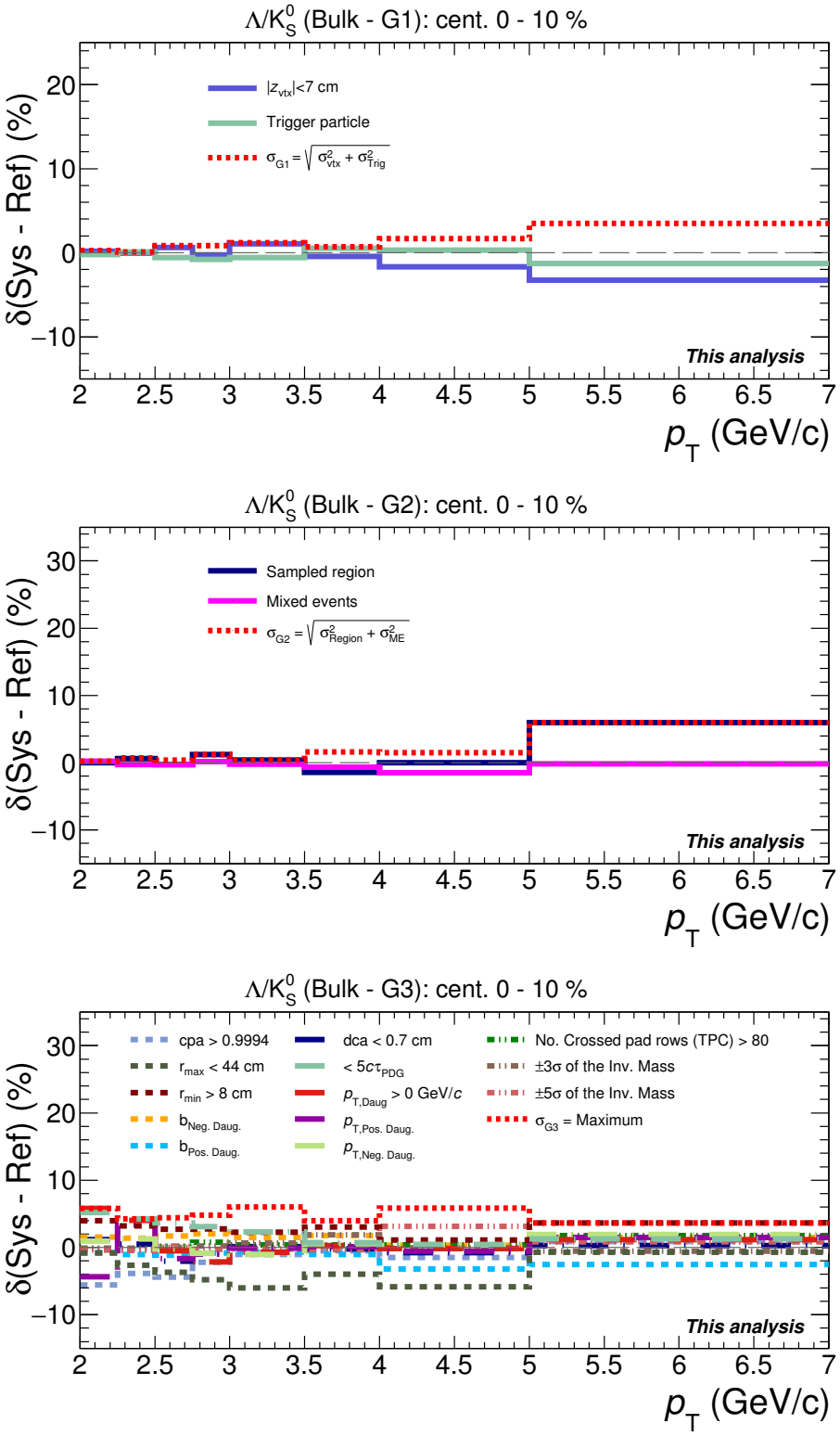

Figure 4.17: Systematics uncertainties for Λ/K^0_S ratio in **Bulk I** for the centrality **0-10%**.

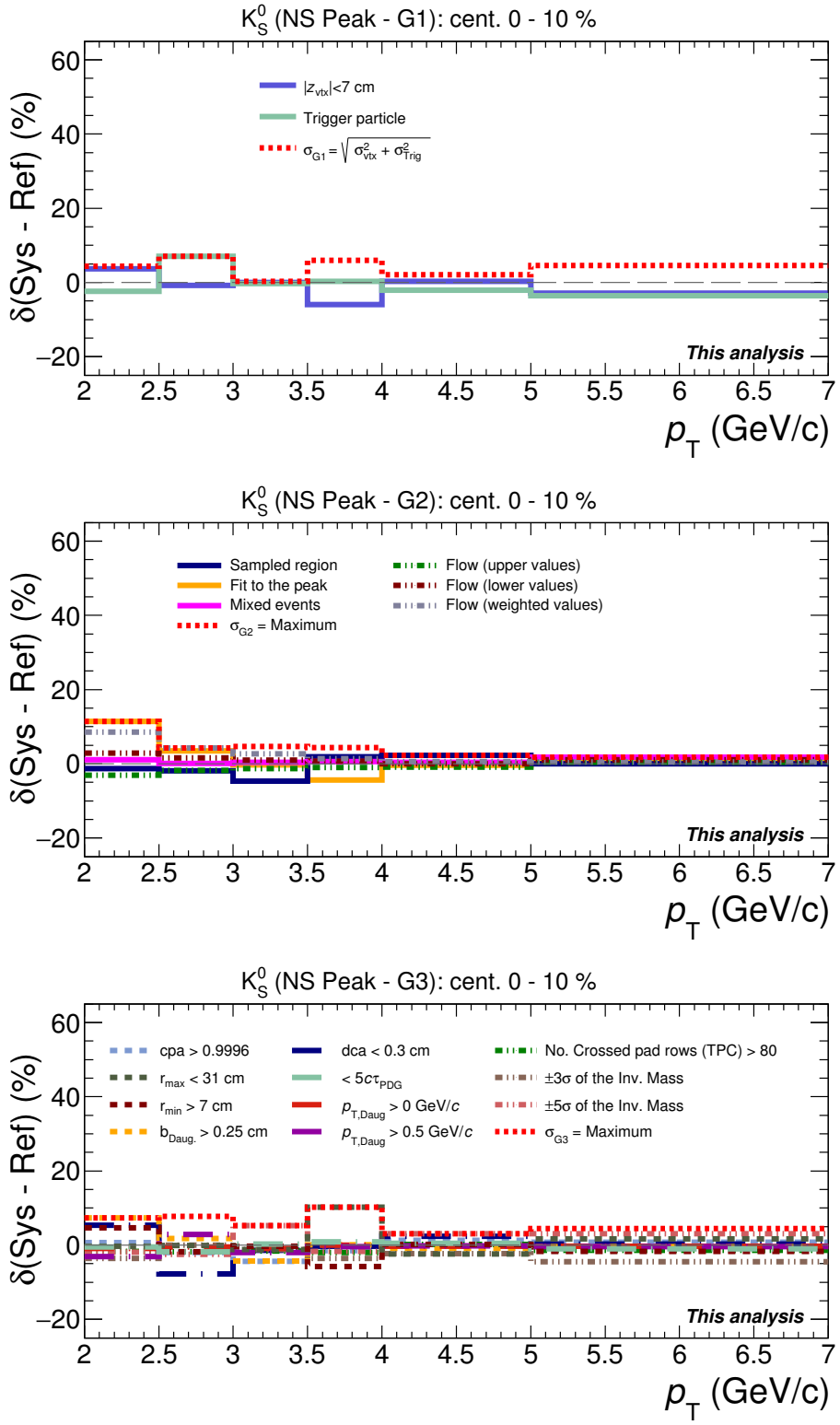

Figure 4.18: Systematics uncertainties for K^0_S per-trigger yield in the **near-side peak** (NS) for the centrality **0-10%**.

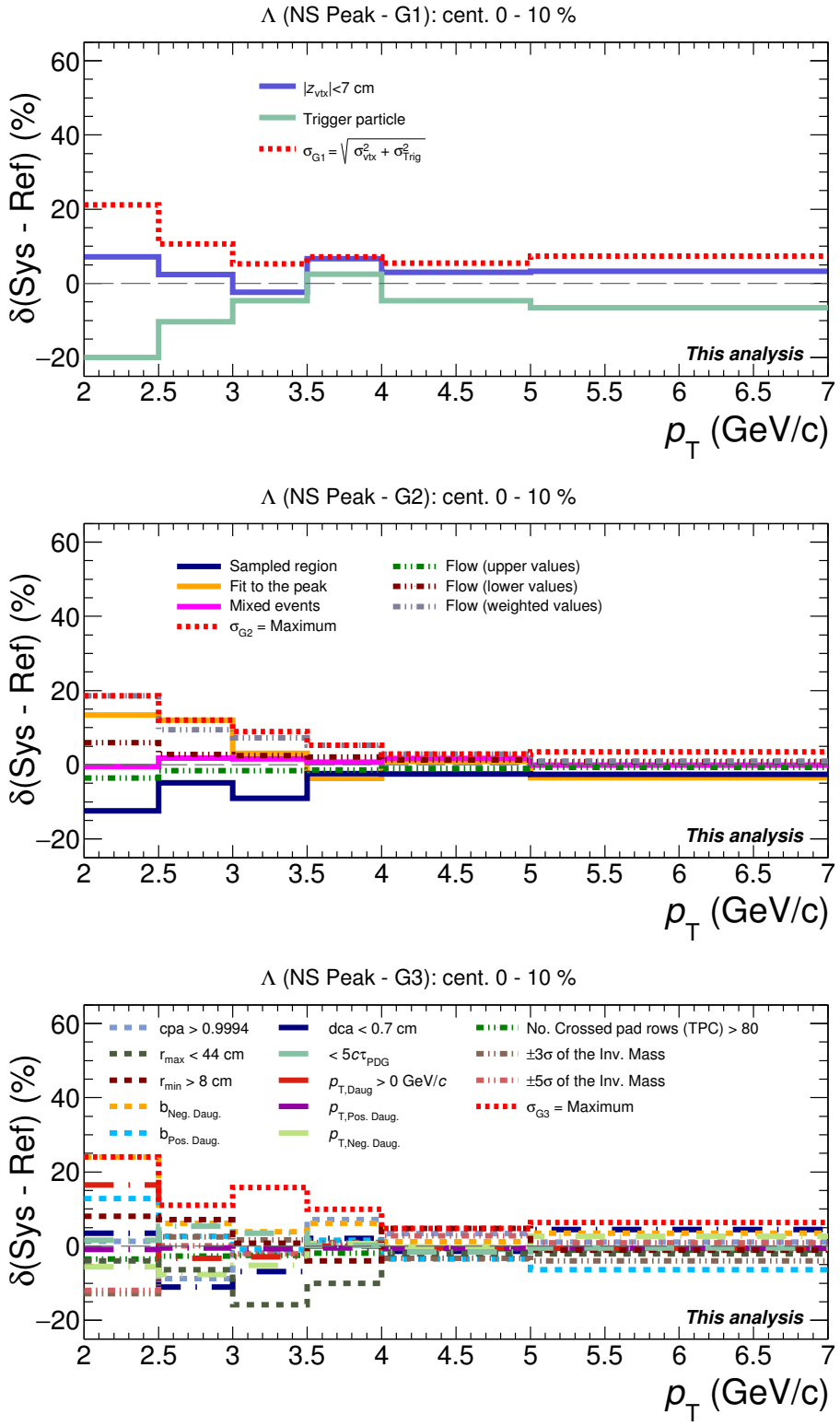

Figure 4.19: Systematics uncertainties for Λ per-trigger yield in the **near-side peak** (NS) for the centrality **0-10%**.

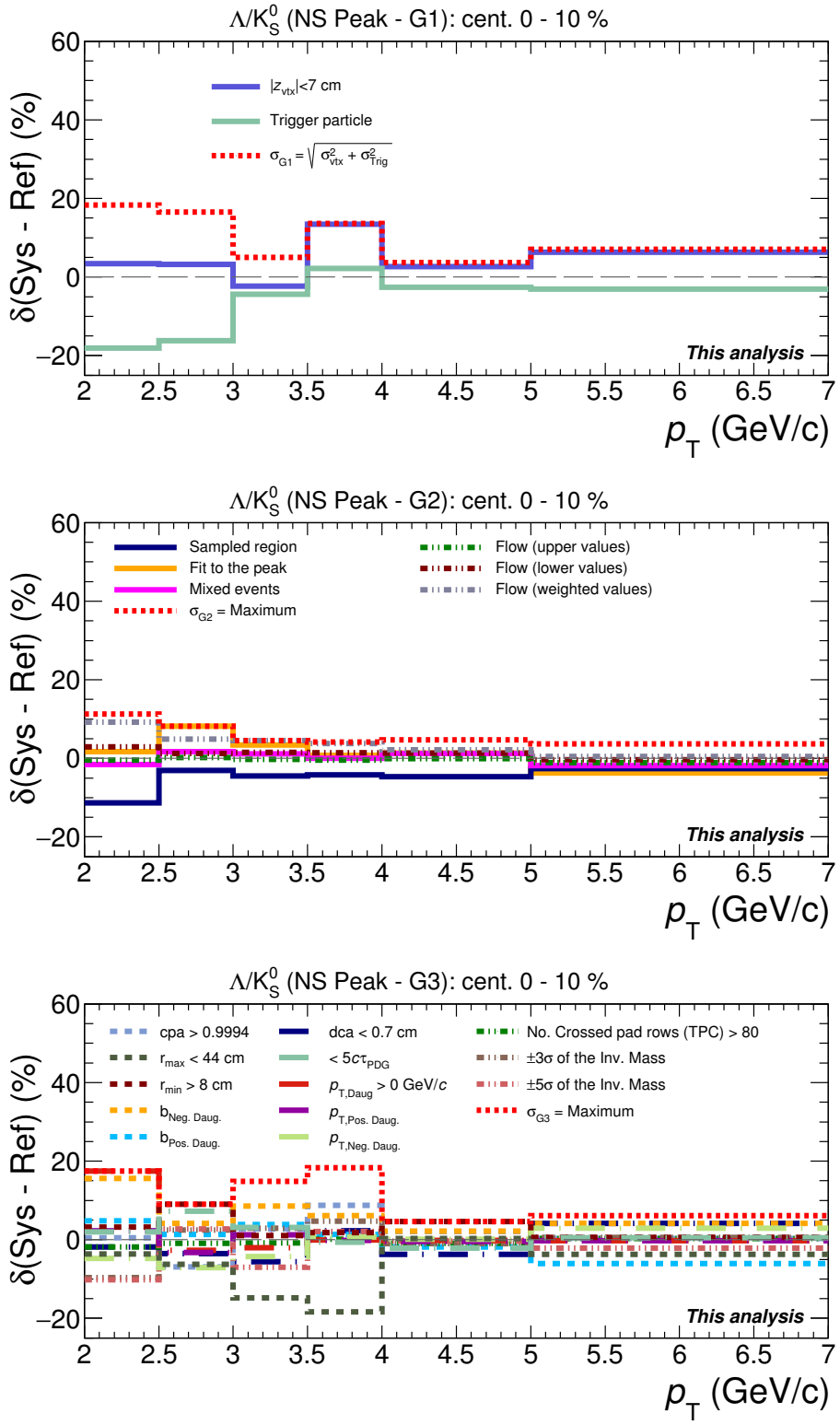

Figure 4.20: Systematics uncertainties for Λ/K^0_S ratio in the **near-side peak** (NS) for the centrality selection **0-10%**.

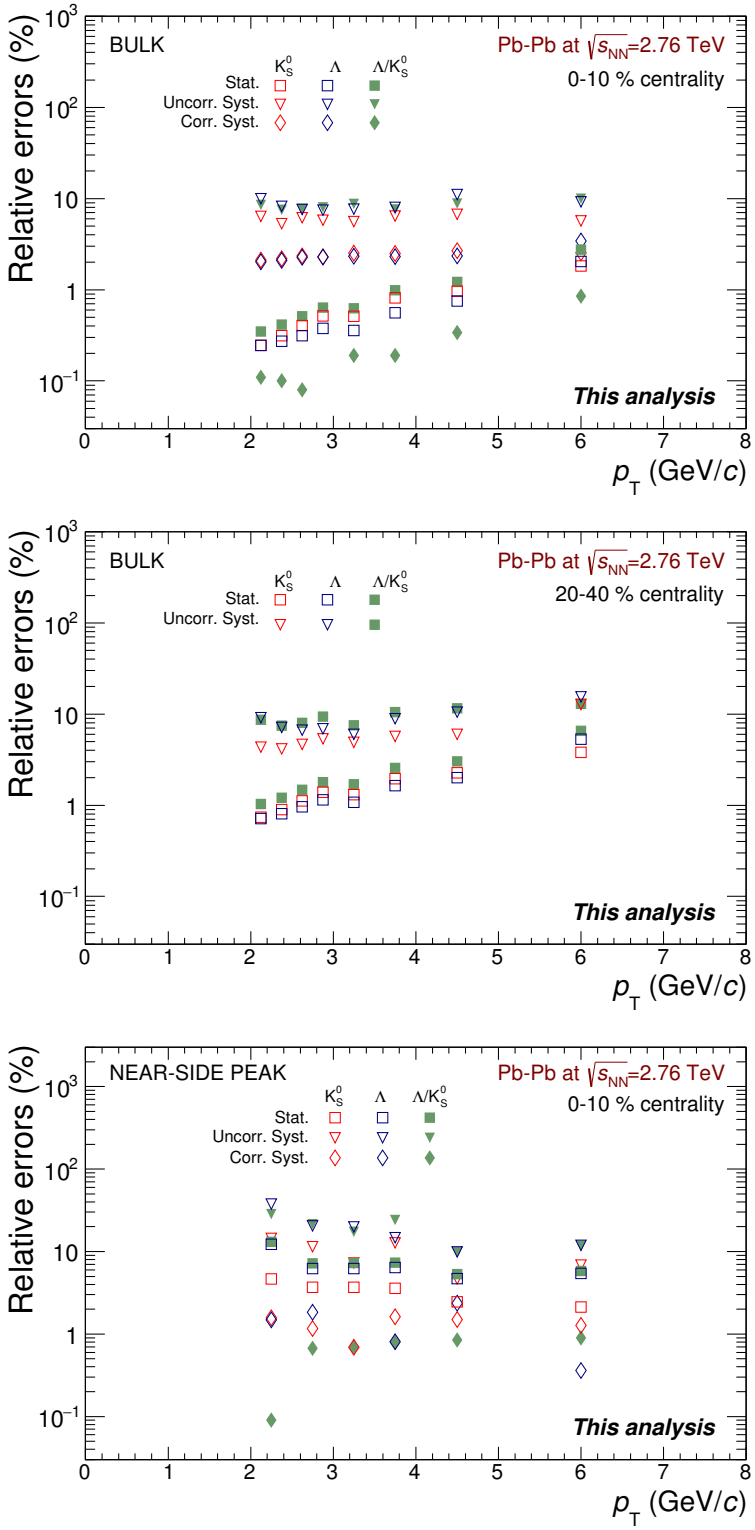

Figure 4.21: Contribution in percentage of the statistical errors and the uncorrelated (partially correlated) systematic uncertainties for each of the obtained results, per-trigger yield of K^0_S and Λ and the Λ/K^0_S ratio, in the bulk for the 0-10% (upper panel) and 20-40% (middle panel) centrality classes and in the near-side yield (lower panel).

5. Discussion

Along this chapter, we will discuss the results obtained for the per-trigger yields of associated K^0_S and Λ particles and the Λ/K^0_S ratios, extracted with the angular-correlation method as introduced previously. We will show in particular, that these results can contribute to a better understanding of hadronization mechanisms involved in high energy heavy ion collisions. Some perspectives following from these results will be also presented at the end of the chapter.

Topology of the two-hadron angular correlations

From the two-hadron angular correlation distributions, see Appendices *B* and *C*, we can qualitatively notice that the near-side peak, along the $\Delta\eta$-direction, is broader for the lowest p_T-range and its amplitude decreases with p_T. This trend has already been observed and quantified in hadron-hadron correlations measured with ALICE for Pb–Pb collisions by extracting the width $\sigma_{\Delta\eta}$ of the distributions [170]. One interesting point to notice in [170] is that the near-side peak has a larger extension in $\Delta\eta$ with respect to the one observed in $\Delta\varphi$. In the present analysis of $h^{\pm}$-V0 correlations, we observe qualitatively a similar feature. In addition, we could go one step further and try to distinguish separately the characteristic features of meson and baryon distributions. When we do so we find that baryons associated to the near-side peak (in the p_T-range below 3 GeV/c) seem to be distributed over a larger range in $\Delta\eta$ than mesons. Unfortunately, because of the fluctuations in the signal, it was extremely difficult to control the pedestal level in $\Delta\eta$, it was therefore not possible to quantify accurately these differences. A similar feature has been observed in the two-hadron angular correlation studies performed within the ALICE Collaboration, using protons and pions as associated particles [171]. In what follows we will discuss the possible physical mechanisms that produce such a difference between mesons and baryons in the $\Delta\eta$ near-side peak.

The longitudinal collective flow can modify the jet shape as proposed in [172] (see Figure 5.1). While particles produced from a hard-parton scattering traverse the medium, a momentum transfer from the medium to the hard parton can occur. In the case of the LHC energies, the pressure coming from the created dense medium could lead to a longitudinal expansion, therefore creating a distortion of the jet which in our analysis is approximated by the near-side peak. The Λ particles appear more affected by the longitudinal flow than K^0_S because they are heavier hadrons. Thus, Λ are distributed in a broader range along $\Delta\eta$, affecting more the low-p_T-range. The longitudinal flow is not the only possible reason for the long-$\Delta\eta$ correlations and the fading of the Λ $\Delta\eta$-peak. The long-range (pseudo)rapidity correlations are naturally developed in the Glasma flux-tubes picture [173], as a consequence of the formed flux tubes (with transverse size $1/Q^2$) at the early times of the collisions, and are eventually boosted by the radial flow during the final stage. Then, the observed two-hadron angular correlation distributions might indicate

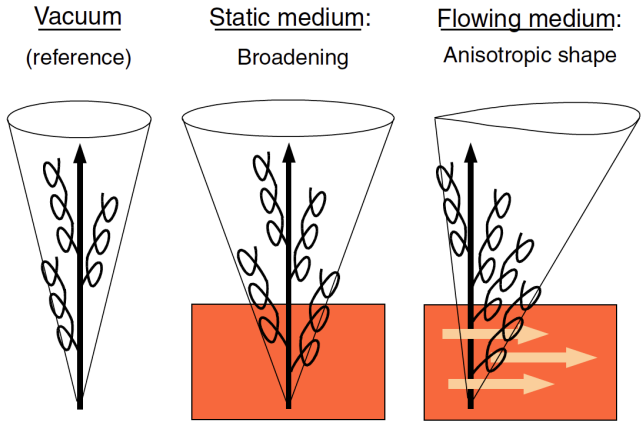

Figure 5.1: Jet emission in vacuum (left sketch), in the medium without (middle sketch) and with (right sketch) longitudinal collective flow. The latter effect leads to a distortion of the jet-shape [172].

that Λ baryons (extended in the long $\Delta\eta$-range) come from the early stages of the collisions more frequently as compared with K^0_S. This might indeed be expected since the flux tubes generated at the early-times store larger amounts of energy, therefore increasing the possibility to produce heavier hadrons, which at the end could favor the production of Λ with respect to K^0_S.

Yield per trigger of associated V0's: bulk and near-side peak

Figure 5.2 shows the yield per trigger of associated hadrons as a function of the transverse momentum for K^0_S (left panel) and Λ (right panel) in central (0-10%) Pb–Pb collisions. Comparing the distributions of the p_T-spectra for K^0_S and for Λ in the bulk (red markers) and in the near-side peak (blue markers), one can notice that the two hadron species show different inverse slope. This feature is naturally expected because the 'bulk' and 'near-side' particles are related to different production mechanisms. Since the bulk is essentially composed of hadrons coming from the expanding thermal source, a thermal distribution (exponential in p_T) boosted by the transverse flow is expected for the two centrality selections, 0-10% and 20-40%. On the other hand, the near-side peak originates mostly from the parton fragmentation process, and so a falling power-law p_T-spectrum could be expected for the yield per trigger of the associated particles.

Moreover, it is observed that for central collisions the near-side peak yield at the lowest p_T-bin is two orders of magnitude smaller with respect to the bulk particle production. At the highest-p_T bin, from 5 to 7 GeV/c, the contribution of parton fragmentation processes to the bulk region of the angular correlation distribution becomes quite substantial for K^0_S (as one can see in 5.2), thus, reflecting a transition in the dominant hadronization mechanism along the p_T-range. These results provide an additional constraint for theoretical models of particle production. The measured yield per trigger in the near-side peak can be used to test the theoretical predictions for the parton fragmentation production in Pb–Pb collisions at the LHC energies. On the other hand, the possibility to disentangle the contributions of parton fragmentation and bulk mechanisms,

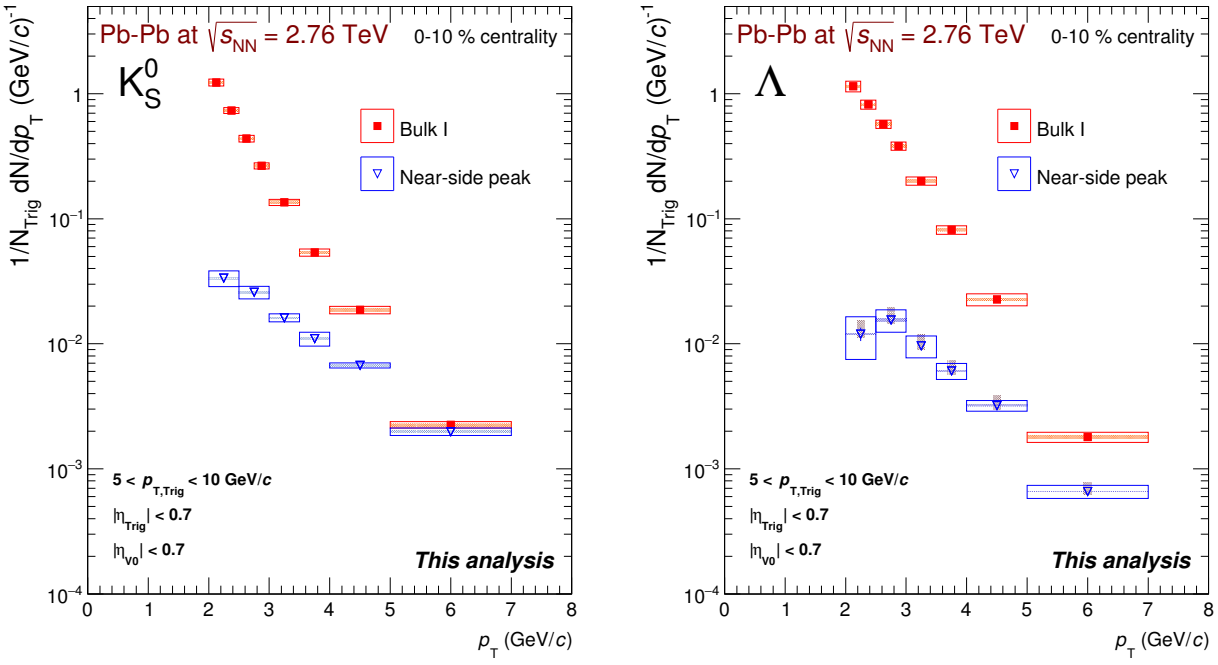

Figure 5.2: Per-trigger yield of associated hadrons as a function of the transverse momentum for K^0_S (left panel) and Λ (right panel). The distributions are shown separately for the particles emerging from the bulk and those produced in association to parton fragmentation. The results are presented for the 0-10% centrality selection in Pb–Pb collisions.

using the two-hadron angular correlation method, is helpful to better tune the parameters of theoretical models, for example the coalescence/recombination approaches [80, 88].
A comparison between particle yields coming from different bulk samples is shown in Figures 4.3 and 4.4 for K^0_S and Λ in the 0-10% and 20-40% centrality intervals. The ratios are obtained by considering the particle density in the BULK III sample (particles emitted orthogonally in φ with respect to the direction of the trigger particle) as the reference point for which, in average, the lowest flow contribution from v_2 and higher harmonics is expected. It is observed that, for the most central collisions, the results of the BULK I/BULK III and BULK II/BULK III yield ratios for the two strange hadrons are compatible with one. Therefore, the production rate is the same over all bulk regions. This shows that the transverse radial flow affects uniformly the particle production in this centrality range independently of their emission direction.
For the semi-peripheral events, the ratio of yields in some p_T-bins are systematically compatible with unity as observed for the central collisions, but for most of the p_T-bins the ratio lies around 1.1 along the whole p_T-range. This description holds for the two particles, K^0_S and Λ. The 10% increase can be understood from the $\Delta\varphi$-dependence of the elliptic flow profile. In other words, the particles emerging around $\Delta\varphi \approx 0$ ($\Delta\varphi \approx \pi$), that correspond to the BULK I (BULK II) region (see Figure 3.28), have a v_2 contribution typically 10% larger than its minimal contribution which is located at $\Delta\varphi \approx \pi/2$ (BULK III) (see figures in Appendices *D* and *E*).

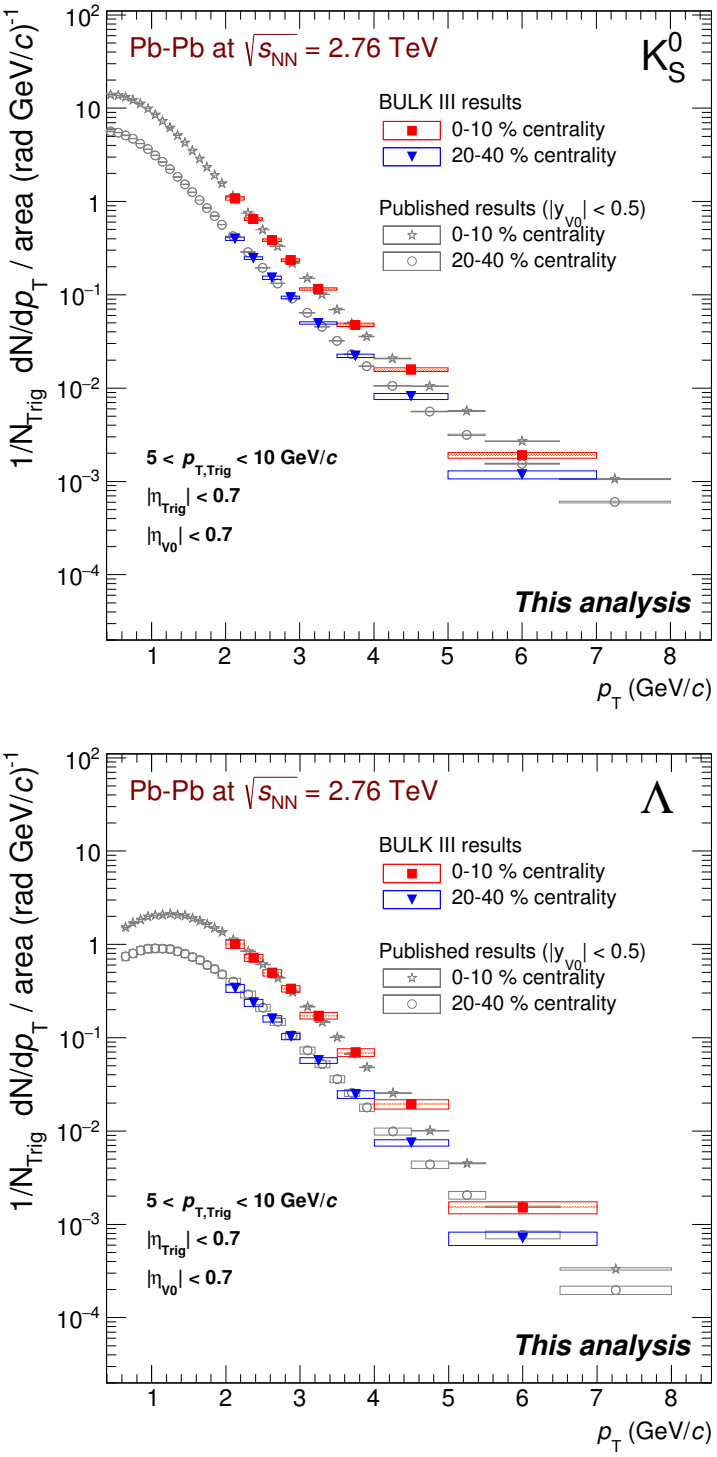

Figure 5.3: Comparison of the particle production density of K^0_S (upper panel) and Λ (lower panel) between the yield per trigger in BULK I (derived from the present analysis) and the ALICE inclusive results from [117].

Other comparisons of the per-trigger particle density in BULK I with respect to the inclusive spectra, taken from [117], are shown in Figure 5.3 for K^0_S and Λ. The inclusive spectra in the 0-10% centrality interval were derived from those measured for the 0-5% and 5-10% centrality classes. A normalization to the extension of inclusive particle acceptance ($y \times \varphi = 1.0 \times 2\pi$) was applied. It is observed that the BULK I particle density obtained with the two-hadron angular correlation distributions is compatible to that of the inclusive particle density for both K^0_S and Λ in the two centrality classes used for the analysis. This confirms the expectation that the bulk production essentially dominates the inclusive production. A small deviation in the K^0_S bulk yield per trigger with respect to the inclusive production is observed at the highest p_T-bin only for the 0-10% centrality class (see upper panel of Figure 5.3). This difference might be due to the fact that the production by parton fragmentation starts to be dominant for the K^0_S particle at this p_T.

Λ/K^0_S ratio: bulk and near-side peak

In Figure 5.4, one can see that the ALICE inclusive Λ/K^0_S ratio for Pb–Pb collisions at $\sqrt{s_{NN}} = 2.76$ TeV present an enhancement (which increases with centrality), with respect to the ratio in pp collisions [117]. This observation suggests that the phenomenon could be related to the collective effects in the QGP that are not present in pp collisions. To test this hypothesis and to see whether other effects such as in-medium modification of hard-processes could also contribute, the Λ/K^0_S results (in the bulk and in the near-side peak), performed in the present analysis with the two-hadron angular correlations, are included in the figure to compare their trend with the inclusive results.

Our results on the BULK I region for the two centrality classes display the same trend as the Pb–Pb inclusive results, describing the rise, reaching a maximum value with the same magnitude at approximately the same p_T value as the inclusive Λ/K^0_S ratio, and then decreasing in the same proportion. Furthermore, it is clearly seen that the Λ/K^0_S ratio obtained in the BULK I region is much larger in magnitude, over the whole p_T-range, than the Λ/K^0_S ratio obtained for hadrons associated to parton fragmentation, the latter approaching the inclusive pp results. The difference between the bulk and near-side peak ratio is largely above the experimental uncertainties even in the case where no feed-down correction is considered for the near-side Λ yield. Therefore, the conclusion is that the baryon-to-meson enhancement observed in heavy-ion collisions originates from the collective nature of the hadronization processes and expansion dynamics of the bulk.

Continuing with the discussion of the ratio in the bulk, Figures 4.10 and 4.11 in Chapter 4 show the double ratio of the Λ/K^0_S in BULK I to BULK III and BULK II to BULK III, respectively, for central and semi-peripheral Pb–Pb collisions. The derived results on the double ratio are consistent with unity for the two centrality intervals. Therefore, the similarity between the inclusive ALICE results and the ratio in the bulk discussed here holds independently of the bulk region the particles emerge from.

Coming back to the comparison between the Λ/K^0_S ratio related to parton fragmentation in central Pb–Pb collisions and the ALICE inclusive results obtained in pp collisions at $\sqrt{s} = 7$ TeV, as shown in Figure 5.4, our results are slightly higher than the inclusive pp ALICE results. This small difference, which remains within the systematic errors, might come from three facts: i)

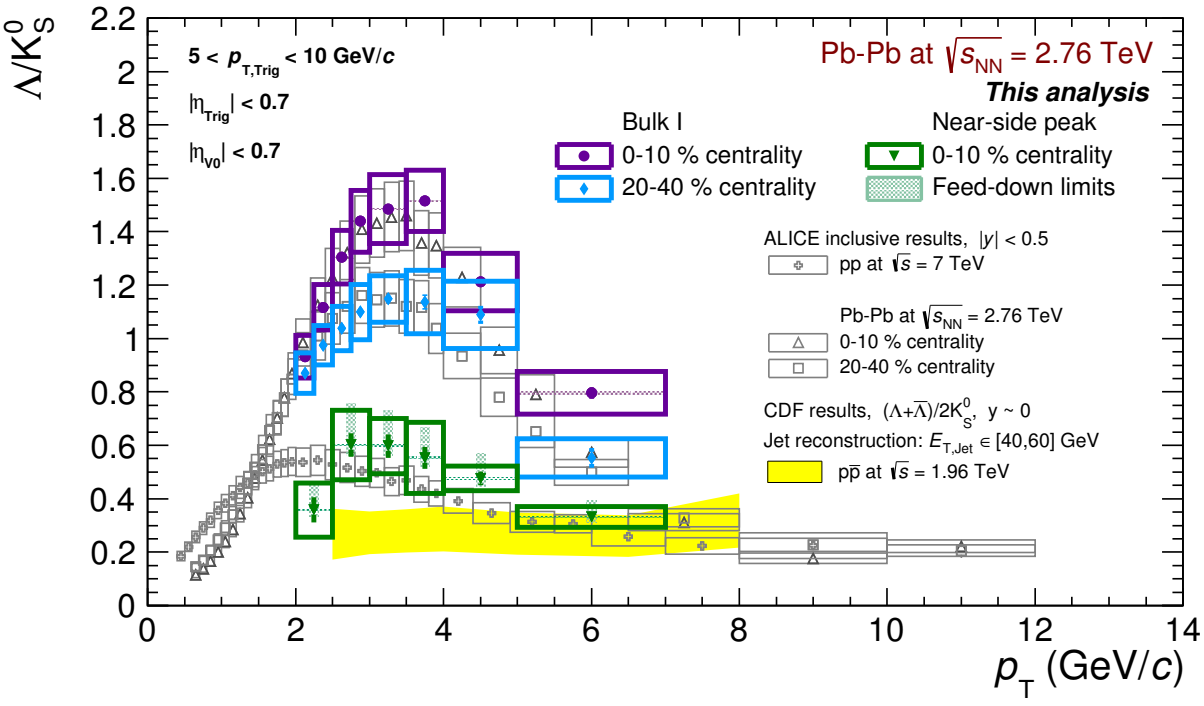

Figure 5.4: $\Lambda/\mathrm{K}^0_\mathrm{S}$ ratio as a function of p_T obtained in the bulk region and in the near-side peak using the two-hadron angular correlation technique. Comparisons with the ALICE inclusive results on pp (Pb–Pb) collisions at $\sqrt{s} = 7$ TeV ($\sqrt{s_\mathrm{NN}} = 2.76$ TeV) are included [117]. The vertical bars are the statistical uncertainties and the empty boxes correspond to the systematic uncertainties. The CDF result on $(\Lambda + \overline{\Lambda})/2\mathrm{K}^0_\mathrm{S}$ extracted from jets ($40 < E_\mathrm{T} < 60$ GeV) in $\mathrm{p\overline{p}}$ collisions at $\sqrt{s} = 1.96$ TeV are also shown as shaded area [174].

the triangular flow contribution still needs to be removed from the near-side yield, which seems to affect more baryons than mesons [106, 175], ii) the extracted v_2 values (in fact, v_n) could still be biased by contribution of non-flow effects and iii) by the breaking of the flow factorization [107] due to the method applied in the current analysis for the flow estimation. Moreover, the $\Lambda/\mathrm{K}^0_\mathrm{S}$ ratio in the near-side peak seems to start at a small amplitude, and immediately increasing to a maximum value as the one observed in the bulk, but placed at a lower p_T value ($p_\mathrm{T} \approx 2.75$ GeV/c) with respect to the Pb–Pb results. For the rest of the p_T-range, the ratio decreases as in pp collisions.

All these observations indicate that there is no modification of hadron production by hard-processes in the medium. However, recent measurements at LHC energies have suggested that possible bulk collective effects, as the ones observed in heavy-ion collisions, might develop in pp collisions. Then, one may raise the question whether *inclusive* $\Lambda/\mathrm{K}^0_\mathrm{S}$ ratios in pp collisions are the adequate reference to interpret our results. In ALICE, measurements of the K^0_S and Λ production related to parton fragmentation, either estimating it with the two-hadron angular correlation method or by reconstructing the jet of hadrons, are not yet available. For this reason, we compare our ratio in the near-side peak with measurements obtained by jet reconstruction at lower collisional energies provided by Fermilab experiments.

The CDF results on the $(\Lambda + \overline{\Lambda})/2\mathrm{K}^0_\mathrm{S}$ measured in reconstructed jets in $\mathrm{p\overline{p}}$ collisions at

$\sqrt{s} = 1.96$ TeV [174] are included in Figure 5.4. The CDF collaboration provides the $(\Lambda+\overline{\Lambda})/2\mathrm{K}^0_\mathrm{S}$ ratio for several intervals of the reconstructed-jet transverse energy (E_T). We have chosen the second class of the reconstructed jets ($40 < E_\mathrm{T} < 60$ GeV), represented by the shaded region that includes the systematic uncertainty range. It is important to mention that the trend of CDF results are E_T-independent within the p_T-range presented here. One can notice that the near-side-peak $\Lambda/\mathrm{K}^0_\mathrm{S}$ ratio in Pb–Pb collisions is approximately $2\sigma^{\Lambda/\mathrm{K}^0_\mathrm{S}}_{\mathrm{syst}}$ larger than the results obtained within jets in the p_T-range from 3-5 GeV/c. If such a difference persists when subtracting properly the triangular flow contribution to the background (see the last section of this chapter), then it would be a strong indication that there is an in-medium modification of parton fragmentation mechanisms. This could be also confirmed in ALICE by comparing the $\Lambda/\mathrm{K}^0_\mathrm{S}$ ratio extracted from jet reconstruction in pp collisions to the ratio of reconstructed jets in Pb–Pb.

Sapeta *et al.* modeled medium modification of the parton fragmentation in [127]. The authors proposed that the jet hadron-species may change because of an enhancement of the parton splitting, which affects the distribution of the invariant mass of partons at the end of the parton shower. This causes an increase of soft particles in the jet in comparison to the jets in vacuum. The aforementioned ingredient also changes the particle ratios in the medium with respect to the one obtained in the vacuum. This can be seen in Figure 5.5 for the proton over pion ratio for the in-medium modified jets (dashed blue line) that is twice larger than the ratio in vacuum jets (red line). It is worth to notice that this effect seems to be quite large, especially at high p_T. Considering again Figure 5.4, the value of the $\Lambda/\mathrm{K}^0_\mathrm{S}$ in the near-side peak at 5-7 GeV/c is already at the same level as the one in the reconstructed jets from the CDF results and it is expected to stay constant for higher-p_T values, contrary to the predicted baryon-to-meson ratio in the model of Sapeta *et al.*.

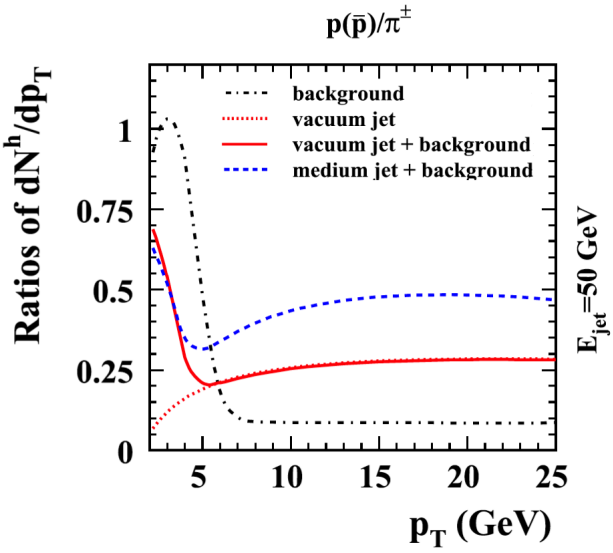

Figure 5.5: The particle ratio p/π obtained from the model in [127]. An enhancement due to medium effects of the baryon-to-meson ratio in jets is observed with respect to the ratio in vacuum jets.

Another interesting point to explore is the effect of the trigger particle selection in the Λ/K^0_S ratio in the near-side peak. The first check was implemented by choosing only the leading trigger particle in the whole event, i.e., the trigger particle with the highest p_T, still within the p_T-interval from 5 to 10 GeV/c. The second evaluation was made by removing the upper p_T-threshold for the trigger particle selection ($p_T^{Trig} > 5$ GeV/c). The two corresponding examinations appeared to result in similar Λ/K^0_S measurement in the near-side peak.

Perspectives

We have presented a complete analysis about the baryon-to-meson ratio depending on the hadron angle of emission with respect to the trigger particles. As perspectives, we propose the following points that appear relevant to us for future studies:

- ♢ The contribution of the triangular flow (and other higher harmonics) has not been taken into account in the present doctoral work because of the absence of experimental measurements in Pb–Pb collisions at the LHC energies. In the most central collisions, the v_3 values for charged particles have been found to be larger than the v_2 component. Therefore, including the triangular flow in the flow-modulated contribution to subtract from the $\Delta\varphi$-correlations would make the hadron yield in the near-side peak to decrease (see Figure 5.6). This would affect more the baryons than the mesons, as measured for π and p in ALICE [106] and for Λ and K^0_S in CMS [175]. Thus, one would expect a slight decrease of the Λ/K^0_S ratio in the near-side peak.

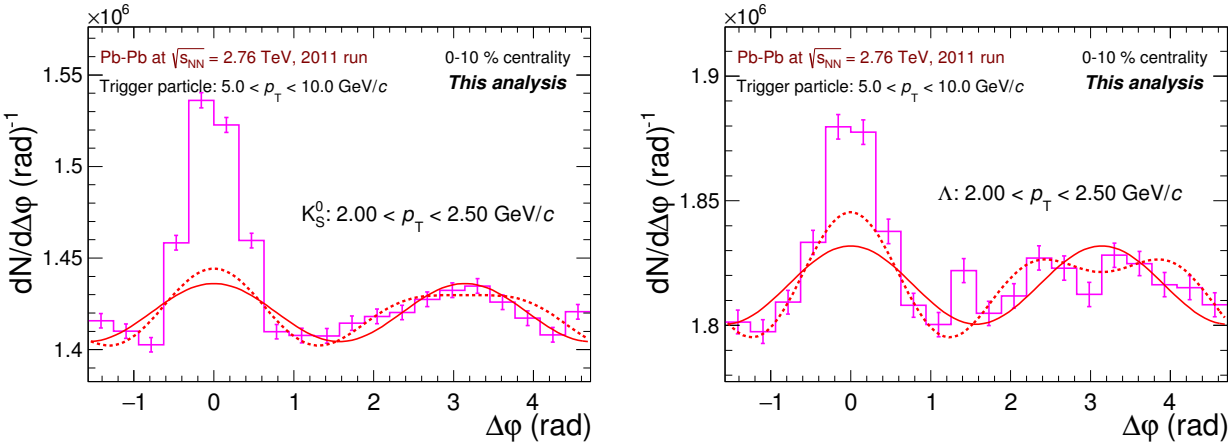

Figure 5.6: Angular correlation in $\Delta\varphi$ for K^0_S (left panel) and Λ (right panel) in the range $2 < p_T < 2.5$ GeV/c, in the most central Pb–Pb collisions. The continuous curve represents the elliptic flow (v_2) contribution. The dashed curve corresponds to an estimation of the $v_2 + v_3$ harmonics contribution, with the v_3 values for the associated particle taken from [175].

- ♢ An estimation of the Λ feed-down contribution coming from the Ξ produced out of hard-parton scattering (if possible in Pb–Pb collisions) is needed to have a better precision on the Λ-yield extraction in the near-side peak. One could try to determine the Ξ production

from direct measurements with reconstructed jets. However, large statistics of jets (or high-p_{T} particles) is needed to achieve such an estimation.

- ♢ The comparison of the $\Lambda/\mathrm{K}^0_{\mathrm{S}}$, in the near-side peak and in the bulk (sometimes referred to as underlying events), obtained for the different collision systems (pp, p–Pb and Pb–Pb) at the LHC can provide a more complete picture of the baryon-to-meson enhancement. More extended studies can be done by extracting the results with two different approaches, via the two-hadron angular correlation with high-p_{T} trigger particles (as used in this dissertation work) and with the jet-reconstruction technique. Results on the $\Lambda/\mathrm{K}^0_{\mathrm{S}}$ ratio extracted with jet reconstruction in ALICE have been obtained in p–Pb collisions [176] and studies are ongoing in Pb–Pb collisions [177, 178].
  One can also aim at comparing the results for: i) different p_{T}-ranges for the trigger particle selection and transverse energies for the reconstructed jet; ii) different centrality classes in Pb–Pb collisions and multiplicity intervals in pp and p–Pb collisions; iii) exploring different collision energies, at RHIC and LHC.

- ♢ It would be also interesting to compare different baryon-to-meson ratios related to the near-side peak and to bulk, such as p/π [158], $\Lambda/\mathrm{K}^0_{\mathrm{S}}$ (performed in this work), and p/ϕ, to study the chemical-composition dependence of the hadron-production mechanisms, at least, for Pb–Pb collisions. This would allow us to better constrain and possibly disentangle the relative contributions between soft- and hard-processes in heavy-ion collisions.

6. Summary and conclusions

Nowadays, from many measurements accumulated in heavy-ion collision experiments at several interaction energies, it is well established that strongly interacting matter at high energy density can form locally thermalized matter where the degrees of freedom are at the level of quarks and gluons, and consequently whose properties are very different from the ones of hadronic matter. After the stage of discovery and exploratory characterization of this state of matter, called quark-gluon plasma (QGP), we have today entered into a new generation of measurements aiming at more and more precise studies of its properties, in particular of its expansion dynamics and of its hadronization mechanisms.

One of the puzzling first-generation measurements obtained at RHIC and LHC energies during the exploratory campaign of the QGP investigation is the baryon-to-meson-ratio behavior as a function of p_{T}, especially the one of the $\Lambda/\mathrm{K}^0_{\mathrm{S}}$ ratio. For central Au–Au and Pb–Pb collisions, within the intermediate-p_{T} interval $2 < p_{\mathrm{T}} < 6$ GeV/c, such a ratio shows to be enhanced with respect to the equivalent ratio in pp collisions. This enhancement decreases when going from central to peripheral collisions, for which the $\Lambda/\mathrm{K}^0_{\mathrm{S}}$ matches the pp values. This behavior is thought to be related to the collective nature of the hadronization processes and of the expansion of the QGP, which is dominant in central collisions but appears to be less prominent in peripheral collisions and a priori absent in pp collisions. Various models involving different physics processes and dynamics have been proposed to explain such a feature, which seems to be the result of an interplay between soft phenomena dominating the low-p_{T} region and hard processes prevailing at high-p_{T}.

These theoretical interpretations are based on several complementary ideas as: i) the possibility to have parton coalescence or recombination from the QGP, ii) the influence of radial flow which reflects the strong collective dynamical behavior of the QGP, iii) other collective effects in the hadronization mechanisms (as developed for example in the EPOS model). In summary, the minimal interpretation of these first-generation inclusive measurements is that the enhancement of the baryon-to-meson ratios in central heavy-ion collisions at intermediate-p_{T} is most probably the consequence of the collective behavior of the bulk, but no conclusive scenario and no exact mechanism could be extracted from the comparison between these inclusive data and the models.

To be able to go a significant step forwards, a new generation of analyses was needed, based on more differential measurements whose objectives are the following: i) impose more severe and quantitative constraints to models, ii) validate the hypothesis that the enhancement of baryon-

to-meson ratio is essentially a 'soft sector' effect, i.e., related to the hadrons coming from the bulk, iii) conversely, invalidate this hypothesis by revealing other substantial contributions to the enhancement in 'the hard sector', among them a possible modification of the parton-parton hard interactions, the parton propagation and the parton fragmentation processes in the medium.

The differential analysis performed in this doctoral work has consisted in separating and evaluating the respective contributions of hard and soft processes to the K^0_S and Λ production in Pb–Pb collisions by means of the two-hadron angular correlation method. More precisely, this work has allowed us to disentangle on a statistical-basis the K^0_S and the Λ hadrons that are emitted in association with high-p_T particles ($5 < p_T^{Trig} < 10$ GeV/c), expected to be produced most-likely from hard-processes, from the particles emerging from the bulk. For each of these separated sources, the corresponding Λ/K^0_S ratios have beed derived as a function of p_T, for two different intervals of centrality of the collisions (0-10% and 20-40% centrality classes). These measurements were obtained with the ALICE Pb–Pb data at $\sqrt{s_{NN}} = 2.76$ TeV taken during the 2011 run.

The principal result of this work is that the Λ/K^0_S p_T-spectrum corresponding to the bulk matches the one obtained in the inclusive ALICE measurements, for both centrality classes. At intermediate-p_T, the Λ/K^0_S ratio is univocally distinct and larger than the one associated to hard processes, the latter being close (if not similar) to the inclusive measurement in pp collisions. Thus the first-level and principal conclusion of this analysis is that the enhancement of baryon-to-meson ratios observed in Pb–Pb collisions originates essentially (if not fully) from bulk effects, with barely (if not zero) contribution from hard processes, thus confirming the hypothesis derived from the inclusive measurements.

A second-level discussion requiring a sharper investigation could be the following. The fact that the Λ/K^0_S p_T-distribution associated to hard processes matches (within the experimental uncertainty) the inclusive Λ/K^0_S spectrum extracted in the pp system at the same collision energy indeed indicates, at the first order, that there is no modification of hadron production by hard processes in the medium. But the question is now to verify whether the *inclusive* spectrum of pp collisions is really the right reference for such a conclusion. Indeed, pp collisions also contains multi-parton interactions, which constitute the so-called underlying event, that can be considered as collective hadronization modes. Furthermore the recent LHC pp data suggest that some collective flow effects, such as the ones measured in heavy-ion collisions, might also develop, with much smaller amplitude, in pp collisions.

In principle, an appropriate reference should be the Λ/K^0_S ratio of particles produced only by hard processes and parton fragmentation in pp collisions. This ratio can be extracted with the two-hadron angular correlation technique (as implemented here) or with the jet-reconstruction technique. Unfortunately such measurements are not yet available in ALICE, and strictly speaking, with the data accumulated during the March 2011 ($\sim 34 \times 10^6$ events) and the February 2013 ($\sim 15 \times 10^6$ events) pp runs at $\sqrt{s} = 2.76$ TeV, the event statistics might not be enough to derive the Λ/K^0_S ratio associated to jets. To discern whether and how the possible collective effects in pp collisions might lead to a baryon-to-meson enhancement, other differential studies

need to be performed by separating the hadrons produced from the underlying event from the ones produced by hard-scatterings, as a function of the event multiplicity classes. One could indeed expect that the largest multiplicity class in pp might show a larger baryon-to-meson ratio because having the largest underlying events.

Due to the lack of such measurements at the LHC at the moment, we have compared our results to CDF measurements obtained with the jet reconstruction method in $\mathrm{p\overline{p}}$ collisions at $\sqrt{s} = 1.96$ TeV, which is a more suitable reference since it is expected to be fully dominated by hard processes. In the p_{T}-range from 2 to 5 GeV/c, the $\Lambda/\mathrm{K}^0_{\mathrm{S}}$ ratio in the near-side peak proves to be systematically above the one of CDF. If this deviation remains present with an improved subtraction of flow contribution from the two-hadron angular correlations (e.g. taking into account triangular harmonics), then it could reveal some interesting physics related to a modification of parton fragmentation in the medium. This could be further confirmed by comparing our results to the $\Lambda/\mathrm{K}^0_{\mathrm{S}}$ ratio that will be derived, in the future, with jet reconstruction from the ALICE data in pp and Pb–Pb collisions.

As a final remark, we hope that these first differential measurements of the $\Lambda/\mathrm{K}^0_{\mathrm{S}}$ ratio will trigger a lot of interest for phenomenological models like EPOS and recombination models, but also for models that would try to reproduce a possible modification of hard parton interactions and fragmentation in the medium. We look forward to see soon new theoretical curves on top of our experimental data, either showing a nice agreement or a large discrepancy but in any case helping, if not to solve the puzzle, at least to put many new pieces in the game.

"The astonishment which I had at first experience
on this discovery soon gave place to delight and rapture.
After so much time I spent in painful labour, to arrive at once
at the summit of my desires, was the most gratifying
consummation of my toils... and I beheld only the result."
Mary Shelly

A. Kinematical variables

The relativistic description of a particle in the spatial four vector coordinates $\mathbf{x}^\mu$ is defined as

$$\mathbf{x}^\mu = (ct, x, y, z) \tag{A.1}$$

A similar definition follows for the particle's kinematic that is described by the four-momentum vector $\mathbf{p}^\mu$

$$\begin{aligned} \mathbf{p}^\mu &= (E/c, p_x, p_y, p_z) && \text{(A.2)} \\ &= (E/c, p_\mathrm{T}, p_z). && \text{(A.3)} \end{aligned}$$

Note that E correspond to the particle energy and $p_\mathrm{T} = \sqrt{p_x^2 + p_y^2}$ is the transverse momentum. In natural units, $c = 1$ and $\hbar = 1$. If we consider the multiplication of the four momentum vector $\mathbf{p}^\mu$ with itself, for a given particle, we can obtain the particle mass:

$$\mathbf{p}^\mu \mathbf{p}_\mu = E^2 - |\vec{p}|^2 = m^2 \tag{A.4}$$

The variables named as the rapidity of a particle is expressed in terms of its energy and longitudinal momentum,

$$y = \frac{1}{2}\ln\left(\frac{E + p_z}{E - p_z}\right) = \frac{1}{2}\ln\left(\frac{1+\beta}{1-\beta}\right), \tag{A.5}$$

where $\beta = p_z/E$ represent the velocity of the particle. When considering the particle is emitted at an θ angle relative to the beam axis, the variable to describe this is the pseudo-rapidity

$$\eta = -\ln\tan(\theta/2) = \frac{1}{2}\ln\left(\frac{|p| + p_z}{|p| - p_z}\right). \tag{A.6}$$

The pseudo-rapidity is defined for any value of the mass, momentum and energy of the collision.

B. $h^{\pm}$-K^0_S angular correlations

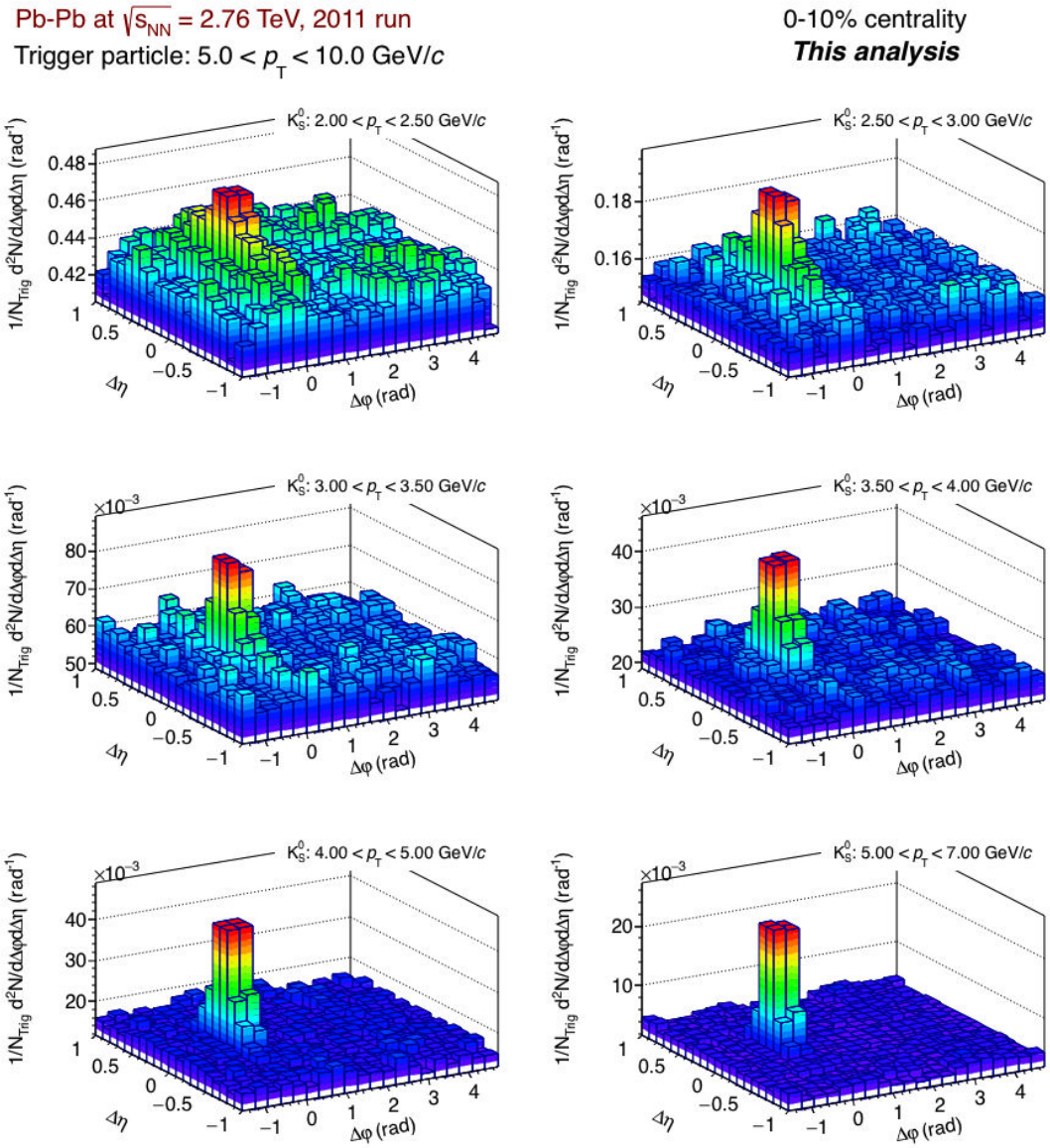

Figure B.1: Two-angular $h^{\pm}$-K^0_S correlations, for different p_T ranges, in the **0-10%** centrality interval for 2011 Pb–Pb collisions. The distributions are corrected with the K^0_S reconstruction efficiency and by the pair-acceptance efficiency applied with mixed-event distributions.

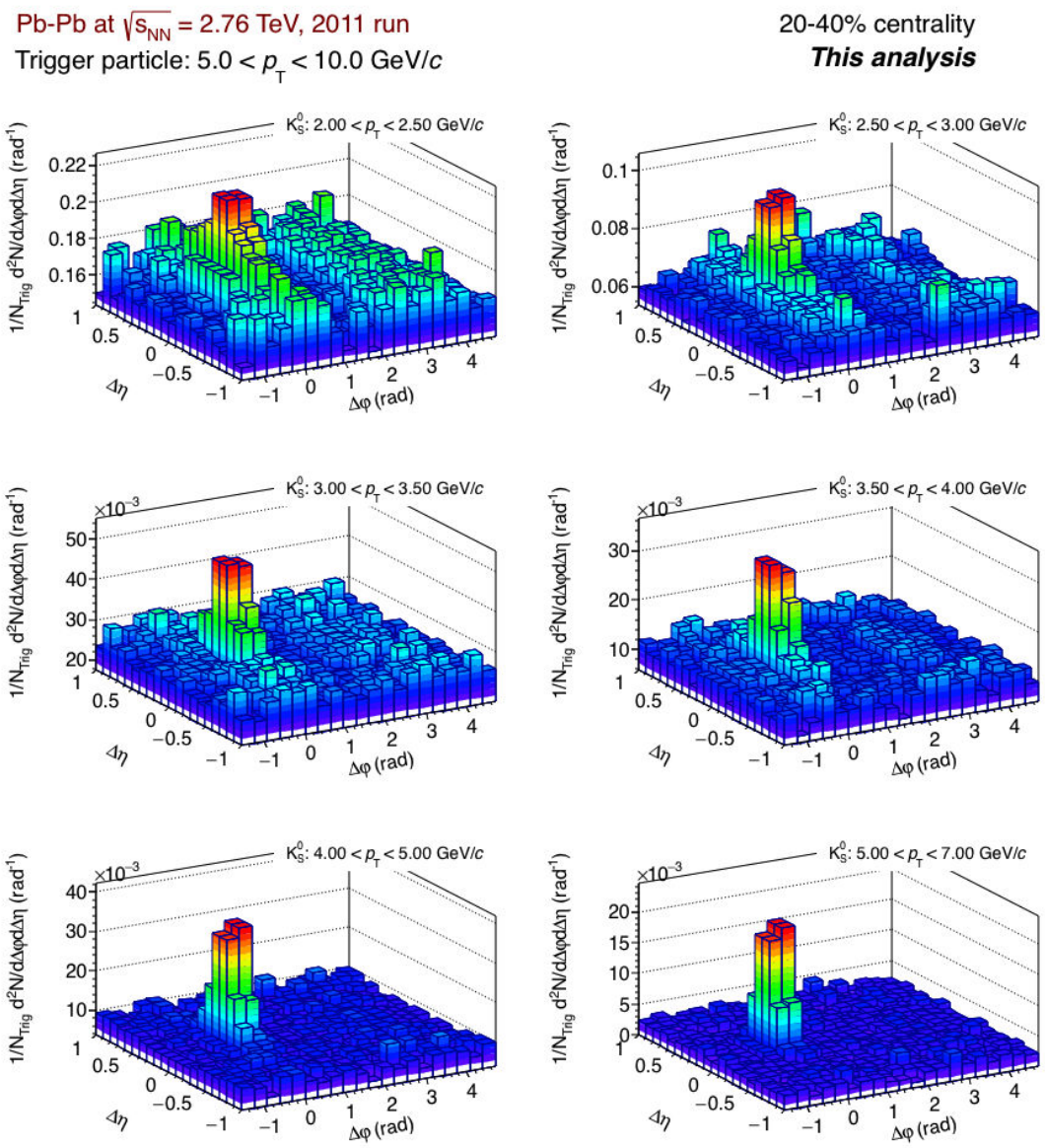

Figure B.2: Two-angular $h^{\pm}$-K^0_S correlations distributions in the **20-40%** centrality interval obtained with the 2011 Pb–Pb data. The angular correlations are shown for different p_T ranges. The distributions corrected with the K^0_S reconstruction efficiency and by the pair-acceptance efficiency applied with mixed-event distributions.

C. $h^{\pm}$-Λ angular correlations

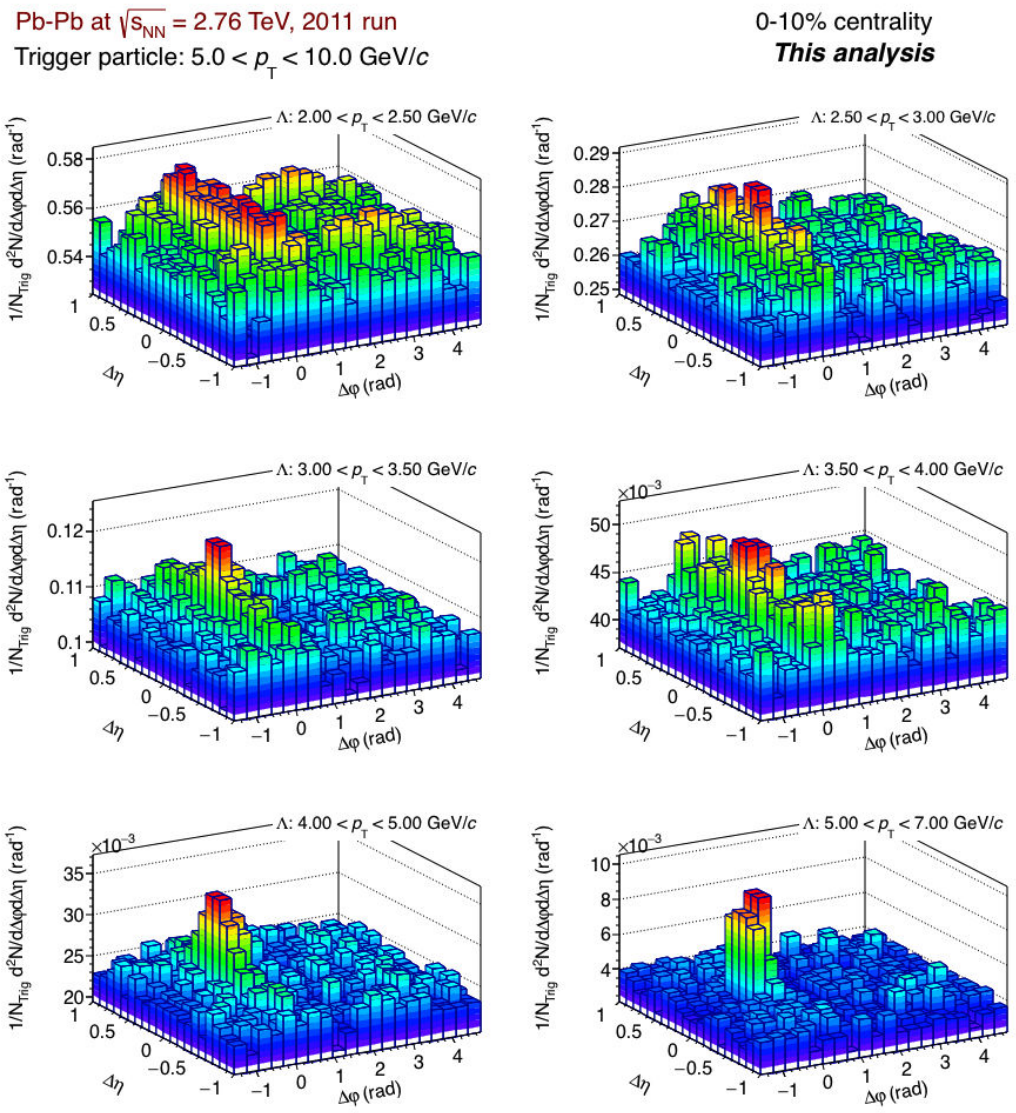

Figure C.1: Two-angular $h^{\pm}$-Λ correlation distributions, for different p_{T} ranges, obtained for the **0-10%** centrality interval using the 2011 Pb–Pb data. The distributions are corrected with the Λ reconstruction efficiency and by the pair-acceptance efficiency applied with mixed-events distributions.

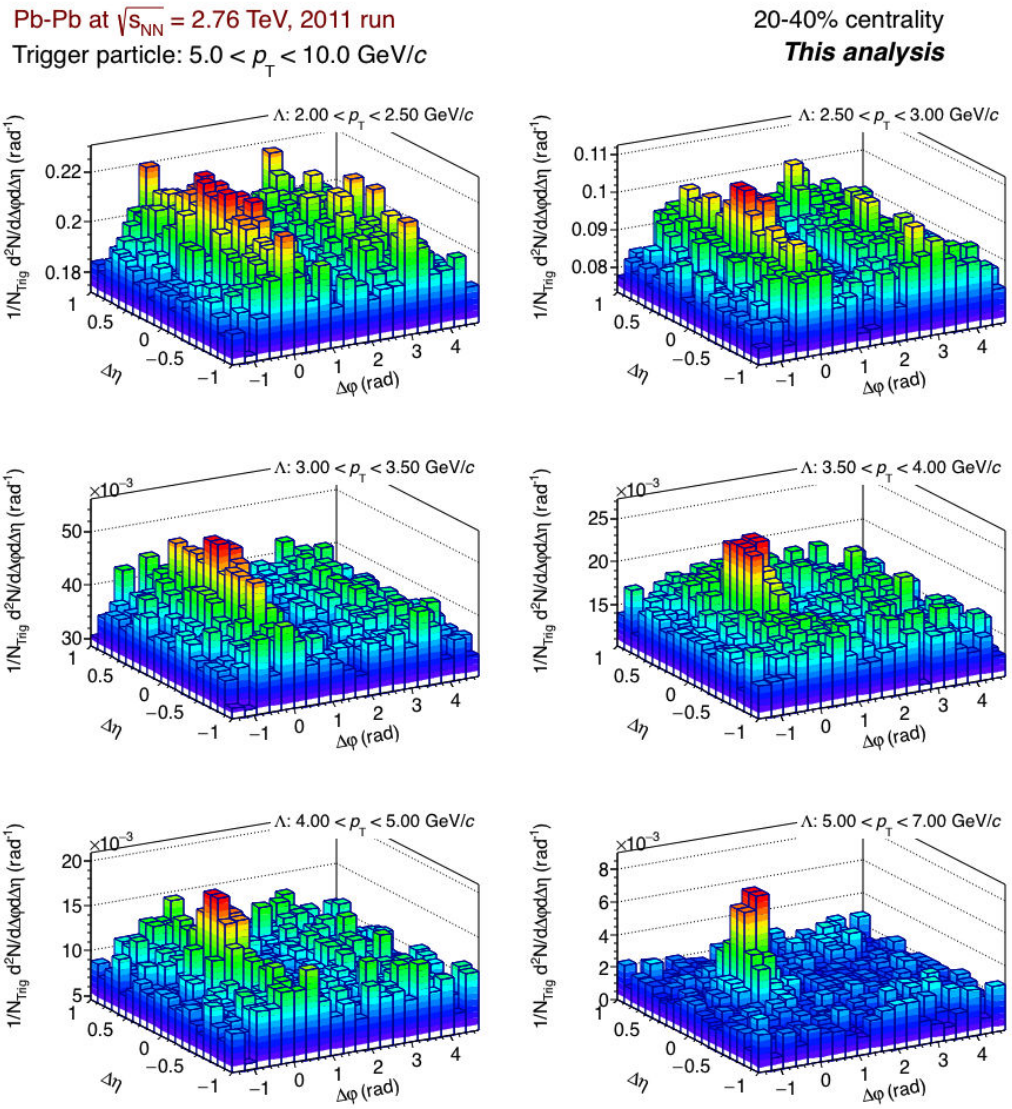

Figure C.2: Two-angular $h^{\pm}$-Λ correlation distributions, for different p_{T} ranges, obtained for the **20-40%** centrality class using the 2011 Pb–Pb data. The distributions are corrected with the Λ reconstruction efficiency and by the pair-acceptance efficiency applied with mixed-events distributions.

D. $h^{\pm}$-K^0_S correlations in $\Delta\varphi$

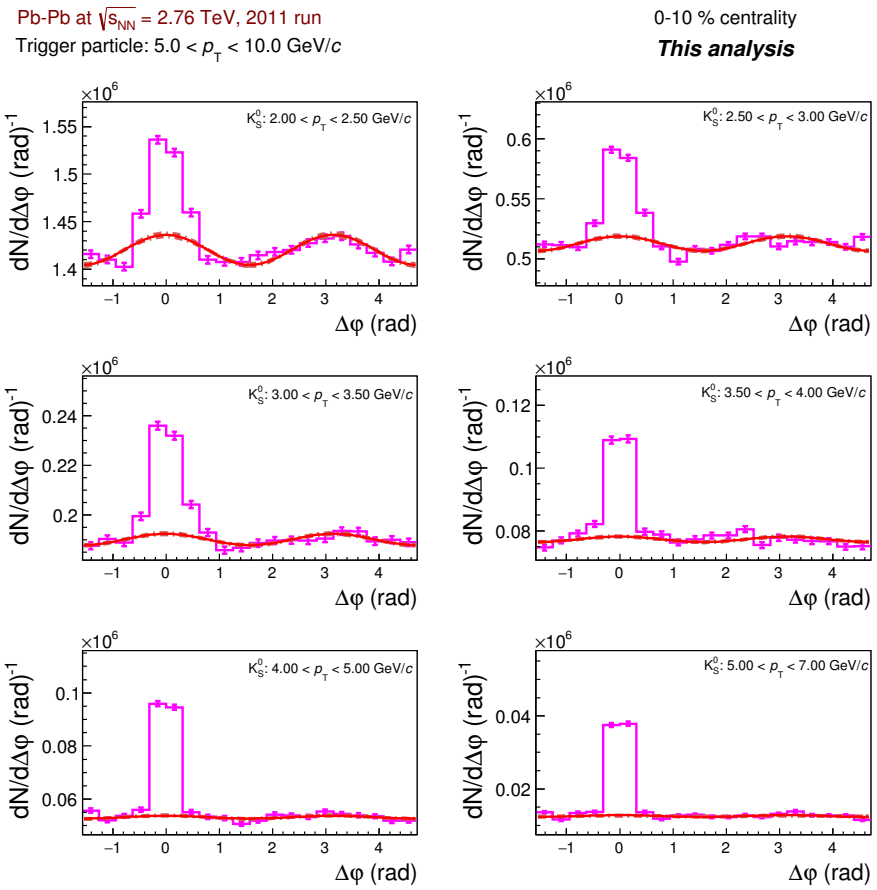

Figure D.1: $h^{\pm}$-K^0_S correlations in $\Delta\varphi$ for the **0-10%** centrality selection of Pb–Pb collisions. The distributions are shown for several p_T-ranges. The continuous curve represent the elliptic flow profile ($2 < v_2^{\mathrm{Trig}} >< v_2^{\mathrm{K}^0_\mathrm{S}} > \cos(2\Delta\varphi)$) whereas the dashed lines are the limits for the elliptic flow modulation in $\pm 3\sigma$ of the v_2 values.

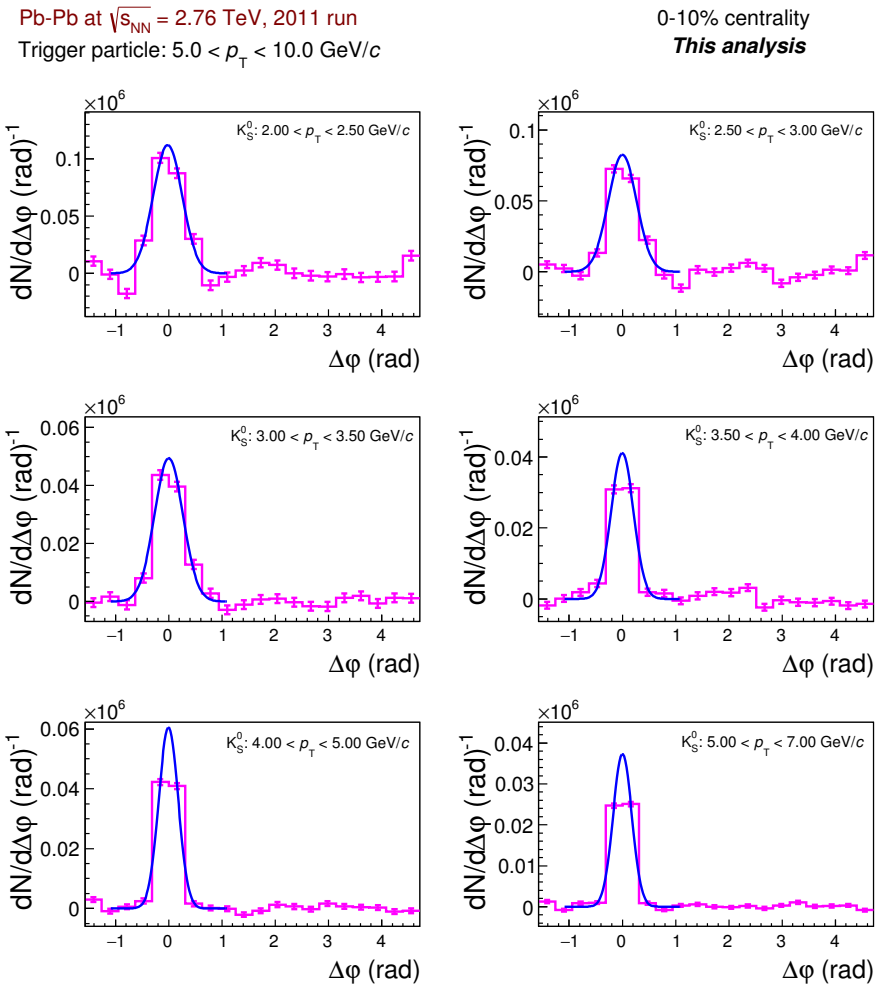

Figure D.2: $h^{\pm}$-K^0_S angular correlations in $\Delta\varphi$ after subtraction of the elliptic flow. The results are presented for the **0-10%** centrality class obtained with the 2011 Pb–Pb data. The Gaussian curve (in blue) describes the particle production related mostly to parton fragmentation.

E. $h^{\pm}$-Λ correlations in $\Delta\varphi$

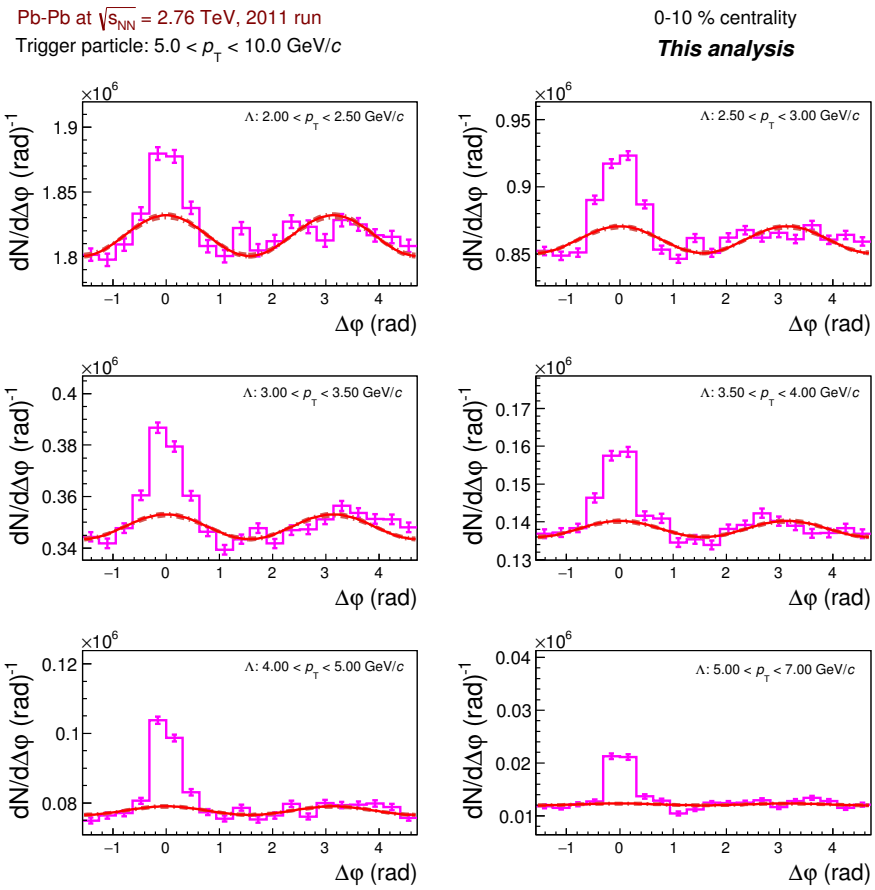

Figure E.1: $h^{\pm}$-Λ $\Delta\varphi$-correlations obtained for the **0-10%** centrality selection of Pb–Pb collisions. The distributions are shown for several p_{T}-ranges. The continuous curve represent the elliptic flow profile ($2 < v_2^{\mathrm{Trig}} >< v_2^{\Lambda} > \cos(2\Delta\varphi)$) whereas the dashed lines are the limits for the elliptic flow modulation in $\pm 3\sigma$ of the v_2 values .

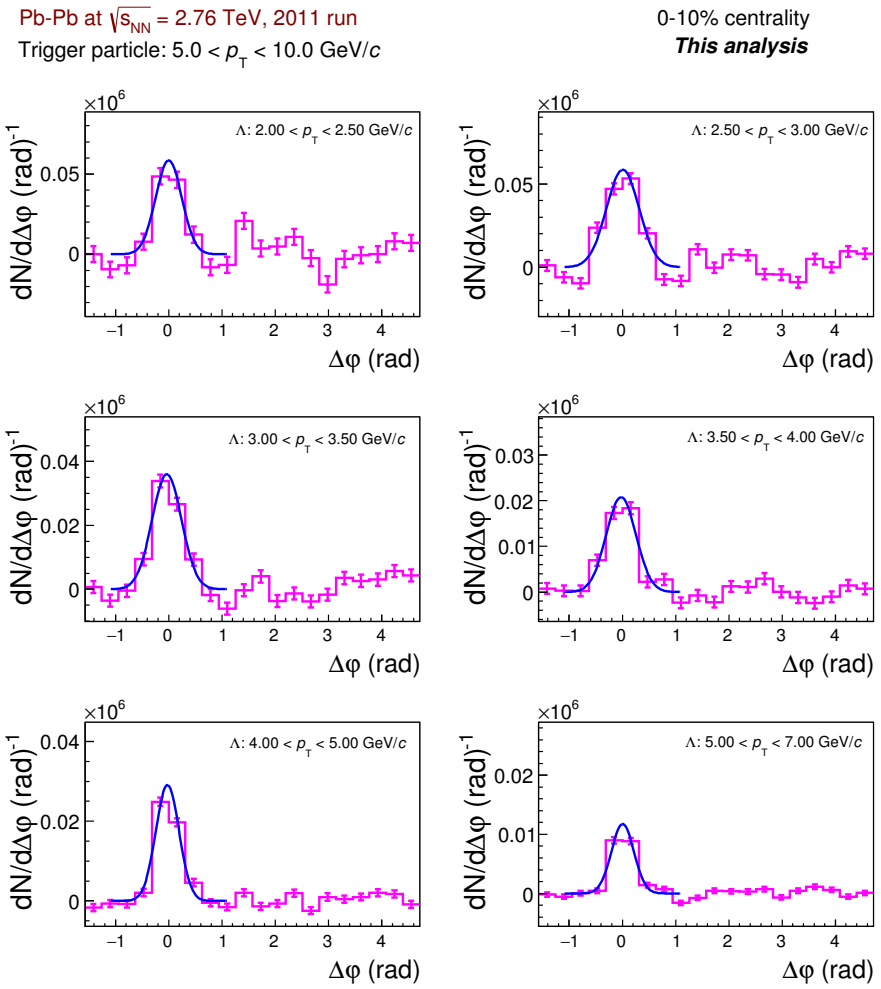

Figure E.2: $h^{\pm}$-Λ angular correlations in $\Delta\varphi$ after subtraction of the elliptic flow. The results are presented for the **0-10%** centrality class obtained with the 2011 Pb–Pb data. The Gaussian curve (in blue) describes the particle production related mostly to parton fragmentation.

Bibliography

[1] M. Gill and P. Pellegrin, *A Companion to Ancient Philosophy*. Blackwell Companions to Philosophy. Wiley, 2009. http://books.google.fr/books?id=EsCRCVJFZGAC.

[2] J. J. Thomson, "Cathode rays", *Phil.Mag.* **44** (1897) 293–316.

[3] J. J. Thomson, *Nobel Lecture: Carriers of Negative Electricity*. Elsevier Publishing Company, Amsterdam, 1967. http://www.nobelprize.org/nobel_prizes/physics/laureates/1936/anderson-lecture.pdf.

[4] H. Kragh, *Quantum Generations: A History of Physics in the Twentieth Century*. History and philosophy of science. Princeton University Press, 2002. http://books.google.fr/books?id=ELrFDIldlawC.

[5] D. Greenberger, K. Hentschel, and F. Weinert, *Compendium of Quantum Physics: Concepts, Experiments, History and Philosophy*. Physics and astronomy online library. Springer, 2009. http://books.google.fr/books?id=ekyAV8VtfuYC.

[6] E. Rutherford, "The Scattering of α and β Particles by Matter and the Structure of the Atom", *Philosophical Magazine Series 6* **21** (1911) 669–688.

[7] M. Planck, "On the Law of Distribution of Energy in the Normal Spectrum", *Annalen Phys.* **4** (1901) 553.

[8] M. Planck, *Nobel Lecture: The Genesis and Present State of Development of the Quantum Theory*. Elsevier Publishing Company, Amsterdam, 1967. http://www.nobelprize.org/nobel_prizes/physics/laureates/1918/planck-lecture.html.

[9] A. Einstein, "Über einen die Erzeugung und Verwandlung des Lichtes betreffenden heuristischen Gesichtspunkt", *Annalen der Physik* **322** 549–560.

[10] N. Bohr, *Nobel Lecture: The Structure of the Atom The Structure of the Atom* . Elsevier Publishing Company, Amsterdam, 1965. http://www.nobelprize.org/nobel_prizes/physics/laureates/1922/bohr-lecture.html.

[11] W. Pauli, *Nobel Lecture: Exclusion Principle and Quantum Mechanics*. Elsevier Publishing Company, Amsterdam, 1964. http://www.nobelprize.org/nobel_prizes/physics/laureates/1945/pauli-lecture.pdf.

[12] W. Heisenberg, *Nobel Lecture: The Development of Quantum Mechanics*. Elsevier Publishing Company, Amsterdam, 1965. http://www.nobelprize.org/nobel_prizes/

physics/laureates/1932/heisenberg-lecture.pdf.

[13] E. Schrödinger, *Nobel Lecture: The Fundamental Idea of Wave Mechanics*. Elsevier Publishing Company, Amsterdam, 1965. http://www.nobelprize.org/nobel_prizes/physics/laureates/1933/schrodinger-lecture.pdf.

[14] P. A. M. Dirac, "The quantum theory of the electron", *Proceedings of the Royal Society of London. Series A* **117** no. 778, (1928) 610–624.

[15] P. A. M. Dirac, "A theory of electrons and protons", *Proceedings of the Royal Society of London. Series A* **126** no. 801, (1930) 360–365.

[16] C. D. Anderson, *Nobel Lecture: The production and properties of positrons*. Elsevier Publishing Company, Amsterdam, 1965. http://www.nobelprize.org/nobel_prizes/physics/laureates/1936/anderson-lecture.pdf.

[17] J. Chadwick, "Possible Existence of a Neutron", *Nature* **129** (1932) 312.

[18] S. Bilenky, "Neutrino. History of a unique particle", *Eur.Phys.J.* **H38** (2013) 345–404, arXiv:1210.3065 [hep-ph].

[19] C. Cowan, F. Reines, F. Harrison, H. Kruse, and A. McGuire, "Detection of the free neutrino: A Confirmation", *Science* **124** (1956) 103–104.

[20] D. Griffiths, *Introduction to Elementary Particles*. Physics textbook. Wiley, 2008.

[21] M. Gell-Mann, "The Eightfold Way: A Theory of strong interaction symmetry",.

[22] M. Gell-Mann, "Symmetries of baryons and mesons", *Phys.Rev.* **125** (1962) 1067–1084.

[23] F. Halzen and A. Martin, *Quarks and leptons: an introductory course in modern particle physics*. Wiley, 1984.

[24] H. Fritsch, "The history of QCD", *CERN Cour.* **52N8** (2012) 21–24.

[25] M. Gell-Mann, "A schematic model of baryons and mesons", *Physics Letters* **8** no. 3, (1964) 214 – 215.

[26] G. Zweig, "An SU(3) model for strong interaction symmetry and its breaking. Version 2",.

[27] M. Breidenbach, J. I. Friedman, H. W. Kendall, E. D. Bloom, D. H. Coward, H. DeStaebler, J. Drees, L. W. Mo, and R. E. Taylor, "Observed Behavior of Highly Inelastic Electron-Proton Scattering", *Phys. Rev. Lett.* **23** (Oct, 1969) 935–939.

[28] E. D. Bloom, D. H. Coward, H. DeStaebler, J. Drees, G. Miller, L. W. Mo, R. E. Taylor, M. Breidenbach, J. I. Friedman, G. C. Hartmann, and H. W. Kendall, "High-Energy Inelastic $e - p$ Scattering at 6° and 10°", *Phys. Rev. Lett.* **23** (Oct, 1969) 930–934.

[29] O. Greenberg, "The Color charge degree of freedom in particle physics", arXiv:0805.0289 [physics.hist-ph].

[30] M. Y. Han and Y. Nambu, "Three-triplet model with double SU(3) symmetry", *Phys. Rev.* **139** (Aug, 1965) B1006–B1010.

[31] CDF Collaboration, F. Abe *et al.*, "Observation of top quark production in $\bar{p}p$ collisions", *Phys.Rev.Lett.* **74** (1995) 2626–2631, arXiv:hep-ex/9503002 [hep-ex].

[32] D0 Collaboration, S. Abachi *et al.*, "Observation of the top quark", *Phys.Rev.Lett.* **74** (1995) 2632–2637, arXiv:hep-ex/9503003 [hep-ex].

[33] UA1 Collaboration, G. Arnison *et al.*, "Further Evidence for Charged Intermediate Vector Bosons at the SPS Collider", *Phys.Lett.* **B129** (1983) 273–282.

[34] UA2 Collaboration, M. Banner *et al.*, "Observation of Single Isolated Electrons of High Transverse Momentum in Events with Missing Transverse Energy at the CERN anti-p p Collider", *Phys.Lett.* **B122** (1983) 476–485.

[35] UA1 Collaboration, G. Arnison *et al.*, "Experimental observation of lepton pairs of invariant mass around 95 GeV/c^2 at the CERN SPS collider", *Phys.Lett.* **B126** (1983) 398 – 410.

[36] "New State of Matter created at CERN",. Issued on 10 Feb 2000.

[37] "Opening the door to the quark-gluon plasma", *CERN Cour.* **40N5** (June, 2000) 25–26.

[38] M. Gazdzicki, "Quark gluon plasma in A + A collisions at CERN SPS", arXiv:hep-ph/9806257 [hep-ph].

[39] M. Gazdzicki, "Strangeness and pion production as signals of QCD phase transition", *J.Phys.* **G23** (1997) 1881–1888, arXiv:nucl-th/9706036 [nucl-th].

[40] T. Ludlam and L. McLerran, "What have we learned from the Relativistic Heavy Ion Collider?", *Phys.Today* **56N10** (2003) 48–54.

[41] "Hunting the Quark Gluon Plasma." BNL -73847-2005 Formal Report, 2005. http://www0.bnl.gov/bnlweb/pubaf/pr/docs/Hunting-the-QGP.pdf.

[42] ATLAS Collaboration, G. Aad *et al.*, "Observation of a new particle in the search for the Standard Model Higgs boson with the ATLAS detector at the LHC", *Phys.Lett.* **B716** (2012) 1–29, arXiv:1207.7214 [hep-ex].

[43] CMS Collaboration, S. Chatrchyan *et al.*, "Observation of a new boson at a mass of 125 GeV with the CMS experiment at the LHC", *Phys.Lett.* **B716** (2012) 30–61, arXiv:1207.7235 [hep-ex].

[44] W. N. Cottingham and D. A. Greenwood, *An Introduction to the Standard Model of Particle Physics*. Cambridge University Press, second ed., 2007.

[45] W. Bietenholz and U.-J. Wiese, "An Introduction to Quantum Field Theory and the Standard Model of Particle Physics.".

[46] Particle Data Group Collaboration, J. Beringer *et al.*, "Review of Particle Physics (RPP)", *Phys. Rev.* **D86** (2012) 010001.

[47] M. H. Seymour, "Quantum chromodynamics", arXiv:hep-ph/0505192 [hep-ph].

[48] A. Pich, "Quantum chromodynamics", arXiv:hep-ph/9505231 [hep-ph].

[49] D. Gross, "Asymptotic freedom and QCD: A historical perspective", *Nucl.Phys.Proc.Suppl.* **135** (2004) 193–211.

[50] S. Bethke, "World Summary of α_s (2012)", *Nucl.Phys.Proc.Suppl.* **234** (10, 2013) 229–234, arXiv:1210.0325 [hep-ex].

[51] M. Kramer and F. Soler, "Large hadron collider phenomenology, proceedings of the fifty seventh Scottish Universities Summer School in Physics, St. Andrews, 17 August to 29 August 2003",.

[52] B. Friman, C. Hohne, J. Knoll, S. Leupold, J. Randrup, *et al.*, "The CBM physics book: Compressed baryonic matter in laboratory experiments", *Lect.Notes Phys.* **814** (2011) 1–980.

[53] F. Karsch, "Lattice QCD at high temperature and the QGP", *AIP Conf.Proc.* **842** (2006) 20–28, arXiv:hep-lat/0601013 [hep-lat].

[54] S. Borsanyi, Z. Fodor, C. Hoelbling, S. D. Katz, S. Krieg, *et al.*, "Full result for the QCD equation of state with 2+1 flavors", *Phys.Lett.* **B730** (2014) 99–104, arXiv:1309.5258 [hep-lat].

[55] A. Bazavov, T. Bhattacharya, M. Cheng, C. DeTar, H. Ding, *et al.*, "The chiral and deconfinement aspects of the QCD transition", *Phys.Rev.* **D85** (2012) 054503, arXiv:1111.1710 [hep-lat].

[56] A. Ohnishi, "Phase diagram and heavy-ion collisions: Overview", *Prog.Theor.Phys.Suppl.* **193** (2012) 1–10, arXiv:1112.3210 [nucl-th].

[57] G. Odyniec, "The RHIC Beam Energy Scan program in STAR and what's next ...", *J.Phys.Conf.Ser.* **455** (2013) 012037.

[58] B. Frimann, C. Hoehne, J. Knoll, S. Leupold, J. Randrup, R. Rapp, and P. E. Senger, *The CBM Physics Book - Compressed Baryonic Matter in Laboratory Experiments*. FAIR Projec, 06, 2010. https://www-alt.gsi.de/documents/DOC-2009-Sep-120.html.

[59] V. Toneev, "The NICA/MPD Project at JINR (Dubna)", *PoS* **CPOD07** (2007) 057, arXiv:0709.1459 [nucl-ex].

[60] A. Sissakian, A. Sorin, V. Kekelidze, I. Meshkov, A. Kovalenko, *et al.*, "Progress of the NICA project", *PoS* **CPOD2009** (2009) 051.

[61] K. Fukushima and T. Hatsuda, "The phase diagram of dense QCD", *Rept.Prog.Phys.* **74**

(2011) 014001, arXiv:1005.4814 [hep-ph].

[62] K. Rajagopal, "The Phases of QCD in heavy-ion collisions and compact stars", *Acta Phys.Polon.* **B31** (2000) 3021, arXiv:hep-ph/0009058 [hep-ph].

[63] M. G. Alford, A. Schmitt, K. Rajagopal, and T. Schäfer, "Color superconductivity in dense quark matter", *Rev.Mod.Phys.* **80** (2008) 1455–1515, arXiv:0709.4635 [hep-ph].

[64] Wuppertal-Budapest Collaboration, S. Borsanyi, G. Endrodi, Z. Fodor, C. Hoelbling, S. Katz, *et al.*, "Transition temperature and the equation of state from lattice QCD, Wuppertal-Budapest results", *Acta Phys.Polon.Supp.* **4** (2011) 593–602, arXiv:1109.5032 [hep-lat].

[65] HERA Combined Structure Functions Working Group Collaboration, C. Gwenlan, "Combined HERA Deep Inelastic Scattering Data and NLO QCD Fits", *Nucl.Phys.Proc.Suppl.* **191** (2009) 5–15, arXiv:0902.1807 [hep-ex].

[66] ZEUS Collaboration, H1 Collaboration, A. Cooper-Sarkar, "PDF Fits at HERA", *PoS* **EPS-HEP2011** (2011) 320, arXiv:1112.2107 [hep-ph].

[67] E. Iancu, "QCD in heavy-ion collisions", arXiv:1205.0579 [hep-ph].

[68] R. Venugopalan, "From HERA to LHC through the Color Glass Condensate." http://www.desy.de/~heralhc/proceedings/wg4venugopalan.pdf.

[69] F. Gelis, "Color Glass Condensate and Glasma", *Int.J.Mod.Phys.* **A28** (2013) 1330001, arXiv:1211.3327 [hep-ph].

[70] C. Nonaka and S. A. Bass, "Space-time evolution of bulk QCD matter", *Phys.Rev.* **C75** (2007) 014902, arXiv:nucl-th/0607018 [nucl-th].

[71] R. Vogt, "Ultrarelativistic heavy-ion collisions",.

[72] S. Sarkar, H. Satz, and B. Sinha, *The Physics of the Quark-Gluon Plasma: Introductory Lectures*. Lecture Notes in Physics. Springer, 2009. http://books.google.fr/books?id=1WPV0NSenZ4C.

[73] K. Johnson, "The M.I.T. Bag Model", *Acta Phys.Polon.* **B6** (1975) 865.

[74] R. Field and R. Feynman, "A Parametrization of the Properties of Quark Jets", *Nucl.Phys.* **B136** (1978) 1.

[75] ATLAS Collaboration, G. Aad *et al.*, "Measurement of the jet fragmentation function and transverse profile in proton-proton collisions at a center-of-mass energy of 7 TeV with the ATLAS detector", *Eur.Phys.J.* **C71** (2011) 1795, arXiv:1109.5816 [hep-ex].

[76] S.-i. Nam and C.-W. Kao, "Fragmentation functions and parton distribution functions for the pion with the nonlocal interactions", *Phys.Rev.* **D85** (2012) 034023, arXiv:1111.4444 [hep-ph].

[77] T. Sjostrand, "Jet fragmentation of multiparton configurations in a string framework", *Nuclear Physics B* **248** no. 2, (1984) 469 – 502.

[78] B. Andersson, G. Gustafson, G. Ingelman, and T. Sjostrand, "Parton Fragmentation and String Dynamics", *Phys.Rept.* **97** (1983) 31–145.

[79] B. Andersson, G. Gustafson, and T. Sjostrand, "Baryon Production in Jet Fragmentation and Υ Decay", *Phys.Scripta* **32** (1985) 574.

[80] R. J. Fries, V. Greco, and P. Sorensen, "Coalescence Models For Hadron Formation From Quark Gluon Plasma", *Ann. Rev. Nucl. Part. Sci.* **58** (2008) 177–205, arXiv:0807.4939 [nucl-th].

[81] V. Greco, C. M. Ko, and P. Levai, "Parton coalescence and anti-proton / pion anomaly at RHIC", *Phys. Rev. Lett.* **90** (2003) 202302, arXiv:nucl-th/0301093 [nucl-th].

[82] P. Levai, "Strange hadron ratios from quark coalescence at RHIC and LHC", *J. Phys.* **G35** (2008) 044041, arXiv:0806.0133 [nucl-th].

[83] R. C. Hwa and C. B. Yang, "Recombination of shower partons at high p(T) in heavy ion collisions", *Phys. Rev.* **C70** (2004) 024905, arXiv:nucl-th/0401001 [nucl-th].

[84] R. J. Fries, B. Muller, C. Nonaka, and S. A. Bass, "Hadronization in heavy ion collisions: Recombination and fragmentation of partons", *Phys. Rev. Lett.* **90** (2003) 202303, arXiv:nucl-th/0301087 [nucl-th].

[85] V. Greco, C. M. Ko, and I. Vitev, "Hadron production from quark coalescence and jet fragmentation in intermediate energy collisions at RHIC", *Phys. Rev.* **C71** (2005) 041901, arXiv:nucl-th/0412043 [nucl-th].

[86] V. Greco, C. M. Ko, and P. Levai, "Parton coalescence at RHIC", *Phys. Rev.* **C68** (2003) 034904, arXiv:nucl-th/0305024 [nucl-th].

[87] R. C. Hwa and C. B. Yang, "Production of strange particles at intermediate pT in central Au+Au collisions at high energies", *Phys. Rev.* **C75** (2007) 054904, arXiv:nucl-th/0602024 [nucl-th].

[88] R. C. Hwa and L. Zhu, "Multi-minijet Contribution to Hadronic Spectra and Correlations in Pb-Pb Collisions at 2.76 TeV and beyond", arXiv:1202.2091 [nucl-th].

[89] R. C. Hwa and L. Zhu, "Spectra of Identified Hadrons in Pb-Pb Collisions at LHC", *Phys.Rev.* **C84** (2011) 064914, arXiv:1109.6300 [nucl-th].

[90] N. Herrmann, J. Wessels, and T. Wienold, "Collective flow in heavy ion collisions", *Ann.Rev.Nucl.Part.Sci.* **49** (1999) 581–632.

[91] J.-Y. Ollitrault, "Relativistic hydrodynamics for heavy-ion collisions", *Eur.J.Phys.* **29** (2008) 275–302, arXiv:0708.2433 [nucl-th].

[92] J.-Y. Ollitrault, "Anisotropy as a signature of transverse collective flow", *Phys. Rev. D* **46** (Jul, 1992) 229–245.

[93] T. Hirano, U. W. Heinz, D. Kharzeev, R. Lacey, and Y. Nara, "Hadronic dissipative effects on elliptic flow in ultrarelativistic heavy-ion collisions", *Phys.Lett.* **B636** (2006) 299–304, arXiv:nucl-th/0511046.

[94] R. Fries and B. Muller, "Heavy ions at LHC: Theoretical issues", *Eur.Phys.J.* **C34** (2004) S279–S285, arXiv:nucl-th/0307043 [nucl-th].

[95] A. M. Poskanzer and S. A. Voloshin, "Methods for analyzing anisotropic flow in relativistic nuclear collisions", *Phys. Rev.* **C58** (1998) 1671–1678, arXiv:nucl-ex/9805001 [nucl-ex].

[96] ALICE Collaboration, K. Aamodt *et al.*, "Higher harmonic anisotropic flow measurements of charged particles in Pb-Pb collisions at $\sqrt{s_{NN}}$=2.76 TeV", *Phys. Rev. Lett.* **107** (2011) 032301, arXiv:1105.3865 [nucl-ex].

[97] A. Bilandzic, R. Snellings, and S. Voloshin, "Flow analysis with cumulants: Direct calculations", *Phys. Rev.* **C83** (2011) 044913, arXiv:1010.0233 [nucl-ex].

[98] STAR Collaboration, C. Adler *et al.*, "Elliptic flow from two and four particle correlations in Au+Au collisions at $\sqrt{s_{NN}}$ = 130-GeV", *Phys. Rev.* **C66** (2002) 034904, arXiv:nucl-ex/0206001 [nucl-ex].

[99] R. Stock, *Relativistic Heavy Ion Physics*. Landolt-Börnstein - Group I Elementary Particles, Nuclei and Atoms : Numerical Data and Functional Relationships in Science and Technology. Springer, Berlin, 2010.

[100] M. Luzum and J.-Y. Ollitrault, "Eliminating experimental bias in anisotropic-flow measurements of high-energy nuclear collisions", *Phys. Rev.* **C87** no. 4, (2013) 044907, arXiv:1209.2323 [nucl-ex].

[101] STAR Collaboration, B. Abelev *et al.*, "Mass, quark-number, and $\sqrt{s_{NN}}$ dependence of the second and fourth flow harmonics in ultra-relativistic nucleus-nucleus collisions", *Phys.Rev.* **C75** (2007) 054906, arXiv:nucl-ex/0701010 [nucl-ex].

[102] STAR Collaboration, B. Abelev *et al.*, "Centrality dependence of charged hadron and strange hadron elliptic flow from $\sqrt{s_{NN}}$ = 200 GeV Au + Au collisions", *Phys.Rev.* **C77** (2008) 054901, arXiv:0801.3466 [nucl-ex].

[103] D. Teaney, J. Lauret, and E. V. Shuryak, "Flow at the SPS and RHIC as a quark gluon plasma signature", *Phys.Rev.Lett.* **86** (May, 2001) 4783–4786, arXiv:nucl-th/0011058 [nucl-th].

[104] P. Huovinen, P. Kolb, U. W. Heinz, P. Ruuskanen, and S. Voloshin, "Radial and elliptic flow at RHIC: Further predictions", *Phys.Lett.* **B503** (2001) 58–64, arXiv:hep-ph/0101136 [hep-ph].

[105] ALICE Collaboration, K. Aamodt *et al.*, "Elliptic flow of charged particles in Pb-Pb collisions at 2.76 TeV", *Phys. Rev. Lett.* **105** (2010) 252302, arXiv:1011.3914 [nucl-ex].

[106] ALICE Collaboration, B. Abelev *et al.*, "Anisotropic flow of charged hadrons, pions and (anti-)protons measured at high transverse momentum in Pb-Pb collisions at $\sqrt{s_{NN}}$=2.76 TeV", *Phys. Lett.* **B719** (2013) 18–28, arXiv:1205.5761 [nucl-ex].

[107] ALICE Collaboration, K. Aamodt *et al.*, "Harmonic decomposition of two-particle angular correlations in Pb-Pb collisions at $\sqrt{s_{NN}}$ = 2.76 TeV", *Phys. Lett.* **B708** (2012) 249–264, arXiv:1109.2501 [nucl-ex].

[108] CMS Collaboration, S. Chatrchyan *et al.*, "Azimuthal Anisotropy of Charged Particles at High Transverse Momenta in Pb-Pb Collisions at $\sqrt{s_{NN}}$=2.76 TeV", *Phys. Rev. Lett.* **109** (Jul, 2012) 022301.

[109] CMS Collaboration, S. Chatrchyan *et al.*, "Measurement of higher-order harmonic azimuthal anisotropy in PbPb collisions at $\sqrt{s_{NN}}$ = 2.76 TeV", *Phys. Rev. C* **89** (Apr, 2014) 044906.

[110] ATLAS Collaboration, G. Aad *et al.*, "Measurement of the azimuthal anisotropy for charged particle production in $\sqrt{s_{NN}}$ = 2.76 TeV lead-lead collisions with the ATLAS detector", *Phys. Rev. C* **86** (Jul, 2012) 014907.

[111] B. Żabiński for the ATLAS Collaboration, "Charged Particle Multiplicity and Correlations in Heavy Ion Collisions in the ATLAS Experiment", *Acta Phys.Polon.* **B44** no. 7, (2013) 1691–1702.

[112] ALICE Collaboration, B. Abelev *et al.*, "Elliptic flow of identified hadrons in Pb-Pb collisions at $\sqrt{s_{\rm NN}}$ = 2.76 TeV", arXiv:1405.4632 [nucl-ex].

[113] ATLAS Collaboration, G. Aad *et al.*, "Measurement of long-range pseudorapidity correlations and azimuthal harmonics in $\sqrt{s_{NN}}$ = 5.02 TeV proton-lead collisions with the ATLAS detector", *Phys. Rev. C* **90** (Oct, 2014) 044906.

[114] S. Chatrchyan *et al.*, "Observation of long-range, near-side angular correlations in pPb collisions at the {LHC}", *Physics Letters B* **718** no. 3, (2013) 795 – 814.

[115] ALICE Collaboration, B. Abelev *et al.*, "Long-range angular correlations of π, K and p in p-Pb collisions at $\sqrt{s_{\rm NN}}$ = 5.02 TeV", *Phys.Lett.* **B726** (2013) 164–177, arXiv:1307.3237 [nucl-ex].

[116] K. Dusling and R. Venugopalan, "Comparison of the color glass condensate to dihadron correlations in proton-proton and proton-nucleus collisions", *Phys.Rev.* **D87** no. 9, (2013) 094034, arXiv:1302.7018 [hep-ph].

[117] ALICE Collaboration, B. Abelev *et al.*, "K^0_S and Λ production in Pb-Pb collisions at $\sqrt{s_{NN}}$ = 2.76 TeV", *Phys. Rev. Lett.* **111** (2013) 222301, arXiv:1307.5530 [nucl-ex].

[118] ALICE Collaboration, B. Abelev *et al.*, "Production of charged pions, kaons and protons at large transverse momenta in pp and Pb–Pb collisions at $\sqrt{s_{\rm NN}}$ =2.76 TeV", *Phys.Lett.* **B736** (2014) 196–207, arXiv:1401.1250 [nucl-ex].

[119] PHENIX Collaboration, K. Adcox *et al.*, "Single identified hadron spectra from $\sqrt{s_{NN}}$ = 130 GeV Au+Au collisions", *Phys. Rev.* **C69** (2004) 024904, arXiv:nucl-ex/0307010 [nucl-ex].

[120] STAR Collaboration, B. Abelev *et al.*, "Identified baryon and meson distributions at large transverse momenta from Au+Au collisions at $\sqrt{s_{NN}}$ = 200-GeV", *Phys. Rev. Lett.* **97** (2006) 152301, arXiv:nucl-ex/0606003 [nucl-ex].

[121] ALICE Collaboration, B. Abelev *et al.*, "Pion, Kaon, and Proton Production in Central Pb–Pb Collisions at $\sqrt{s_{NN}}$ = 2.76 TeV", *Phys. Rev. Lett.* **109** (2012) 252301, arXiv:1208.1974 [hep-ex].

[122] ALICE Collaboration, B. Abelev *et al.*, "Centrality dependence of π, K, p production in Pb-Pb collisions at $\sqrt{s_{NN}}$ = 2.76 TeV", *Phys.Rev.* **C88** no. 4, (2013) 044910, arXiv:1303.0737 [hep-ex].

[123] T. Sakaguchi for the PHENIX Collaboration, "High p_T identified hadron ratios in $\sqrt{s_{NN}}$=200GeV Au+Au Collisions", *Nucl.Phys.* **A715** (2003) 757–760, arXiv:nucl-ex/0209030 [nucl-ex].

[124] K. Werner, "Lambda-to-Kaon Ratio Enhancement in Heavy Ion Collisions at Several TeV", *Phys. Rev. Lett.* **109** (2012) 102301, arXiv:1204.1394 [nucl-th].

[125] K. Werner, I. Karpenko, M. Bleicher, T. Pierog, and S. Porteboeuf-Houssais, "Jets, Bulk Matter, and their Interaction in Heavy Ion Collisions at Several TeV", *Phys.Rev.* **C85** (2012) 064907, arXiv:1203.5704 [nucl-th].

[126] V. Topor Pop, M. Gyulassy, J. Barrette, and C. Gale, "Baryon anomaly and strong color fields in Pb+Pb collisions at 2.76A TeV at the CERN Large Hadron Collider", *Phys.Rev.* **C84** (2011) 044909, arXiv:1105.3940 [hep-ph].

[127] S. Sapeta and U. A. Wiedemann, "Jet hadrochemistry as a characteristics of jet quenching", *Eur.Phys.J.* **C55** (2008) 293–302, arXiv:0707.3494 [hep-ph].

[128] ALICE Collaboration, B. Abelev *et al.*, "Multiplicity Dependence of Pion, Kaon, Proton and Lambda Production in p-Pb Collisions at $\sqrt{s_{NN}}$ = 5.02 TeV", *Phys.Lett.* **B728** (2014) 25–38, arXiv:1307.6796 [nucl-ex].

[129] L. Evans and P. Bryant, "LHC Machine", *JINST* **3** (2008) S08001.

[130] R. Bailey and P. Collier, "Standard Filling Schemes for Various LHC Operation Modes", Tech. Rep. LHC-PROJECT-NOTE-323, CERN, Geneva, Sep, 2003.

[131] R. Alemany-Fernandez *et al.*, "Operation and Configuration of the LHC in Run 1", 2013. http://cds.cern.ch/record/1631030?ln=en.

[132] ALICE Collaboration, B. Abelev *et al.*, "Performance of the ALICE Experiment at the CERN LHC", *Int.J.Mod.Phys.* **A29** (2014) 1430044, arXiv:1402.4476 [nucl-ex].

[133] J. J. Goodson and R. McCarthy, *Search for Supersymmetry in States with Large Missing Transverse Momentum and Three Leptons including a Z-Boson*. PhD thesis, Stony Brook U., May, 2012. Presented 17 Apr 2012.

[134] ALICE Collaboration, F. Carminati *et al.*, "ALICE: Physics performance report, volume I", *J. Phys.* **G30** (2004) 1517–1763.

[135] ALICE Collaboration, K. Aamodt *et al.*, "The ALICE experiment at the CERN LHC", *JINST* **3** (2008) S08002.

[136] ALICE Collaboration, B. Alessandro *et al.*, "ALICE: Physics performance report, volume II", *J. Phys.* **G32** (2006) 1295–2040.

[137] ALICE Collaboration, E. Abbas *et al.*, "Performance of the ALICE VZERO system", *JINST* **8** (2013) P10016, arXiv:1306.3130 [nucl-ex].

[138] Y. Zoccarato, W. Tromeur, S. Aguilar, R. Alfaro, E. Almaraz Avina, *et al.*, "Front end electronics and first results of the ALICE V0 detector", *Nucl.Instrum.Meth.* **A626-627** (2011) 90–96.

[139] ALICE Collaboration, G. Dellacasa *et al.*, "ALICE technical design report of the zero degree calorimeter (ZDC)",.

[140] N. De Marco, R. Arnaldi, E. Chiavassa, A. Ferretti, M. Gagliardi, *et al.*, "Performance of the zero degree calorimeters for the ALICE experiment", *IEEE Trans.Nucl.Sci.* **54** (2007) 567–573.

[141] ALICE Collaboration, G. Dellacasa *et al.*, "ALICE technical design report of the inner tracking system (ITS)", *CERN-LHCC-99-12* (1999) 356. https://aliceinfo.cern.ch/ITS/sites/aliceinfo.cern.ch.ITS/files/documents/ITS_TDR.pdf.

[142] G. A. Rinella, A. Kluge, M. Krivda, and A. S. P. D. project, "The level 0 pixel trigger system for the alice experiment", *Journal of Instrumentation* **2** no. 01, (2007) P01007. http://stacks.iop.org/1748-0221/2/i=01/a=P01007.

[143] ALICE Collaboration, G. Dellacasa *et al.*, "ALICE: Technical design report of the time projection chamber", 2000. https://cds.cern.ch/record/451098/files/open-2000-183.pdf.

[144] ALICE Collaboration, C. Garabatos, "The ALICE TPC", *Nucl.Instrum.Meth.* **A535** (2004) 197–200.

[145] ALICE Collaboration, B. Nilsen, L. Vannucci, and N. Bustreo, "Finding the vertex position using the SPD in stand alone mode and the effects of the off-axis vertexm pt.1", 2001.

[146] ALICE Collaboration, Y. Belikov, K. Safarík, and B. Batyunya, "Kalman Filtering Application for Track Recognition and Reconstruction in ALICE Tracking System", 1997.

[147] A. Maire and C. Kuhn, *Production des baryons multi-étranges au LHC dans les collisions proton-proton avec l'expérience ALICE*. PhD thesis, Strasbourg U., 2011. Presented 13 Oct 2011.

[148] A. Akindinov, A. Alici, A. Agostinelli, P. Antonioli, S. Arcelli, *et al.*, "Performance of the ALICE Time-Of-Flight detector at the LHC", *Eur.Phys.J.Plus* **128** (2013) 44.

[149] ALICE Collaboration, S. Beole *et al.*, "ALICE technical design report: Detector for high momentum PID", 1998.

[150] STAR Collaboration, B. Abelev *et al.*, "Long range rapidity correlations and jet production in high energy nuclear collisions", *Phys.Rev.* **C80** (2009) 064912, arXiv:0909.0191 [nucl-ex].

[151] CMS Collaboration, V. Khachatryan *et al.*, "Observation of Long-Range Near-Side Angular Correlations in Proton-Proton Collisions at the LHC", *JHEP* **1009** (2010) 091, arXiv:1009.4122 [hep-ex].

[152] STAR Collaboration, C. Adler *et al.*, "Disappearance of back-to-back high p_T hadron correlations in central Au+Au collisions at $\sqrt{s_{NN}}$ = 200-GeV", *Phys.Rev.Lett.* **90** (2003) 082302, arXiv:nucl-ex/0210033 [nucl-ex].

[153] M. Kopytine for the STAR Collaboration, "In-medium minijet dissipation in Au+Au collisions at $\sqrt{s_{NN}}$ = 130-GeV and $\sqrt{s_{NN}}$ = 200-GeV studied with charge independent two particle number fluctuations and correlations", arXiv:nucl-ex/0403011 [nucl-ex].

[154] ALICE Collaboration, K. Aamodt *et al.*, "Particle-yield modification in jet-like azimuthal di-hadron correlations in Pb-Pb collisions at $\sqrt{s_{NN}}$ = 2.76 TeV", *Phys.Rev.Lett.* **108** (10, 2012) 092301, arXiv:1110.0121.

[155] ALICE Collaboration, B. Abelev *et al.*, "Centrality determination of Pb-Pb collisions at $\sqrt{s_{NN}}$ = 2.76 TeV with ALICE", *Phys. Rev.* **C88** (2013) 044909, arXiv:1301.4361 [nucl-ex].

[156] ALICE Collaboration, B. Abelev *et al.*, "Measurement of the Cross Section for Electromagnetic Dissociation with Neutron Emission in Pb-Pb Collisions at $\sqrt{s_{NN}}$ = 2.76 TeV", *Phys. Rev. Lett.* **109** (2012) 252302, arXiv:1203.2436 [nucl-ex].

[157] M. L. Miller, K. Reygers, S. J. Sanders, and P. Steinberg, "Glauber modeling in high energy nuclear collisions", *Ann. Rev. Nucl. Part. Sci.* **57** (2007) 205–243, arXiv:nucl-ex/0701025 [nucl-ex].

[158] M. Veldhoen for the ALICE Collaboration, "p/π Ratio in Di-Hadron Correlations", *Nucl.Phys.* **A910-911** (2013) 306–309, arXiv:1207.7195.

[159] L. Hanratty, P. Jones, and L. Barnby, Λ *and* K^0_S *production in Pb-Pb and pp collisions*

with ALICE at the LHC. PhD thesis, Birmingham U., Jun, 2014. Presented 15 Aug 2014.

[160] J. Gramling and J. Stachel, *Azimuthally Sensitive Hanbury Brown–Twiss Interferometry measured with the ALICE Experiment*. PhD thesis, Heidelberg U., Dec, 2012. Presented 13 Dec 2012.

[161] STAR Collaboration, M. M. Aggarwal *et al.*, "Azimuthal di-hadron correlations in d+Au and Au+Au collisions at $\sqrt{s_{NN}} = 200$ GeV from STAR", *Phys.Rev.* **C82** (2010) 024912, arXiv:1004.2377 [nucl-ex].

[162] STAR Collaboration, J. Adams *et al.*, "Evidence from d+Au measurements for final-state suppression of high p_T hadrons in Au+Au collisions at RHIC", *Phys.Rev.Lett.* **91** (2003) 072304, arXiv:nucl-ex/0306024 [nucl-ex].

[163] A. Hansen for the ALICE Collaboration, "Study of pseudorapidity dependence of the anisotropic flow with ALICE at the LHC", *Nucl.Phys.* **A904-905** (2013) 523c–526c, arXiv:1210.7095 [nucl-ex].

[164] ATLAS Collaboration, G. Aad *et al.*, "Measurement of flow harmonics with multi-particle cumulants in Pb+Pb collisions at $\sqrt{s_{NN}} = 2.76$ TeV with the ATLAS detector", *Eur.Phys.J.* **C74** no. 11, (2014) 3157, arXiv:1408.4342 [hep-ex].

[165] A. Morsch for the ALICE Collaboration, "Jet-like near-side peak shapes in Pb-Pb collisions at $\sqrt{s_{NN}}$=2.76 TeV with ALICE", arXiv:1207.7187 [nucl-ex].

[166] N. N. Ajitanand, J. M. Alexander, P. Chung, W. G. Holzmann, M. Issah, R. A. Lacey, A. Shevel, A. Taranenko, and P. Danielewicz, "Decomposition of harmonic and jet contributions to particle-pair correlations at ultra-relativistic energies", *Phys.Rev.* **C72** (2005) 011902, arXiv:nucl-ex/0501025 [nucl-ex].

[167] PHENIX Collaboration, S. Adler *et al.*, "Dense-Medium Modifications to Jet-Induced Hadron Pair Distributions in Au+Au Collisions at $\sqrt{s_{NN}} = 200$ GeV", *Phys.Rev.Lett.* **97** (2006) 052301, arXiv:nucl-ex/0507004 [nucl-ex].

[168] J.Bielcikova, S.Esumi, K.Filimonov, S.Voloshin, and J.P.Wurm, "Elliptic flow contribution to two particle correlations at different orientations to the reaction plane", *Phys.Rev.* **C69** (2004) 021901, arXiv:nucl-ex/0311007 [nucl-ex].

[169] ALICE Collaboration, K. Aamodt *et al.*, "Strange particle production in proton-proton collisions at $\sqrt{s} = 0.9$ TeV with ALICE at the LHC", *Eur.Phys.J.* **C71** (2011) 1594, arXiv:1012.3257 [hep-ex].

[170] J. F. Grosse-Oetringhaus for the ALICE Collaboration, "Hadron Correlations Measured with ALICE", *Nucl.Phys.* **A910** (2013) 58–64, arXiv:1208.1445 [nucl-ex].

[171] To be published.

[172] N. Armesto, C. A. Salgado, and U. A. Wiedemann, "Measuring the collective flow with jets", *Phys.Rev.Lett.* **93** (2004) 242301, arXiv:hep-ph/0405301 [hep-ph].

[173] R. Venugopalan, "From many body wee parton dynamics to perfect fluid: a standard model for heavy ion collisions", *PoS* **ICHEP2010** (12, 2010) 567, arXiv:1012.4699 [hep-ph].

[174] CDF Collaboration, T. Aaltonen *et al.*, "Production of K^0_S, $K^{*\pm}(892)$ and $\phi^0(1020)$ in minimum bias events and K^0_S and Λ^0 in jets in $p\bar{p}$ collisions at $\sqrt{s}$=1.96 TeV", *Phys.Rev.* **D88** (2013) 092005, arXiv:1308.3371 [hep-ex].

[175] CMS Collaboration, V. Khachatryan *et al.*, "Long-range two-particle correlations of strange hadrons with charged particles in pPb and PbPb collisions at LHC energies", *Phys.Lett.* **B742** (09, 2015) 200–224, arXiv:1409.3392 [nucl-ex].

[176] X. Zhang for ALICE Collaboration, "K^0_S and Λ Production in Charged Particle Jets in p–Pb Collisions at $\sqrt{s_{NN}} = 5.02$ TeV with ALICE", *Nucl.Phys.* **A931** (2014) 444–448, arXiv:1408.2672 [hep-ex].

[177] A. Zimmermann for the ALICE Collaboration, "Production of strange particles in charged jets in p–Pb and Pb–Pb collisions measured with ALICE at the LHC.".

[178] V. Kučera for the ALICE Collaboration, "Production of strange particles in charged jets in Pb–Pb and p–Pb collisions measured with ALICE", *J.Phys.Conf.Ser.* **612** no. 1, (2015) 012013.

Résumé

Introduction

Plusieurs générations d'expériences d'ions lourds ultra-relativistes, à différentes énergies d'interaction (auprès des accélérateurs SPS, RHIC et LHC) ont permis de prouver que la matière en interaction forte à haute densité d'énergie existait sous la forme d'un état où les quarks et les gluons étaient déconfinés, un état appelé le plasma de quarks et de gluons (QGP). La Chromodynamique quantique (QCD) sur réseau prédit que la transition de phase entre la matière hadronique et le QGP se produit à une température critique T_c située entre 145 et 185 MeV. Initialement, le QGP était supposé être un gaz presque parfait de quarks et de gluons. Aujourd'hui, la comparaison entre les mesures expérimentales et les modèles théoriques indique que le QGP est un plasma fortement couplé dont les constituants ont un très faible libre parcours moyen et un comportement collectif marqué. Il a également été montré que cet état de la matière absorbait une fraction importante de l'énergie des partons rapides qui la traversent. Les représentations théoriques du QGP le décrivent comme un milieu en équilibre thermodynamique local, dont le rapport entre la viscosité de cisaillement et la densité d'énergie est faible. Il s'agirait donc d'un liquide presque parfait.

Les collisions d'ions lourds ultra-relativistes permettent de créer un volume de densité d'énergie élevée et comprenant un grand nombre de constituants. C'est de cette région, qui consiste en de la matière en équilibre thermique local, que provient 90% des hadrons produits (hadrons de basse ou de moyenne impulsion transverse). Selon toutes les observations, c'est ce volume de matière, appelé *bulk* (dont les mécanismes de hadronisation et la dynamique d'expansion sont soumis à de fort effets collectifs), qui est le siège du QGP, aussi longtemps que sa température reste au-dessus de T_c. Les dimensions du *bulk* et par conséquent les phénomènes collectifs associés au QGP diminuent lorsque l'on passe des collisions centrales aux collisions périphériques et sont, au premier ordre, censés disparaitre dans les collisions proton-proton (pp). Les mesures relatives aux collisions pp sont donc utilisées comme références hadroniques. Cependant, des études récentes montrent que la situation dans les collisions pp du LHC pourrait être plus complexe et impliquer également des effets collectifs.

À partir des mesures inclusives réalisées au LHC et précédemment au RHIC, dans le domaine des impulsions transverses intermédiaires ($2 < p_{\mathrm{T}} < 6$ GeV/c), une augmentation de la production relative de baryons et de mésons (rapport $\Lambda/\mathrm{K}^0_{\mathrm{S}}$ en particulier) a été observée dans les collisions d'ions lourds par rapport aux collisions pp. Cet accroissement diminue progressivement entre les collisions les plus centrales et les plus périphériques. Pour ces dernières, le rapport baryon/méson devient comparable à celui mesuré en pp. Au départ, ces mesures étaient généralement interprétées comme des preuves directes que des mécanismes de recombinaison (ou coalescence) de partons jouaient un rôle majeur, en compétition avec les processus de fragmentation de partons,

dans le scénario de formation des hadrons, mettant ainsi en évidence un niveau élevé de degrés de liberté partoniques dans le système. Aujourd'hui, sans privilégier une explication en particulier, ces caractéristiques suggèrent au moins que l'accroissement du rapport baryon/méson dans les collisions d'ions lourds est un effet de *bulk*, produit par des phénomènes collectifs aussi bien au niveau des mécanismes de hadronisation qu'au niveau de la dynamique d'expansion (flot radial) du QGP.

Le but de ce travail de thèse est de valider expérimentalement cette hypothèse et d'examiner si cet effet peut provenir également d'autres phénomènes, qui ne seraient pas liés au comportement collectif du *bulk* mais plutôt à une modification des processus durs entre partons et des mécanismes de fragmentation de partons dans le milieu. Pour atteindre cet objectif, des mesures différentielles sont nécessaires et réalisées dans ce travail au moyen de corrélations angulaires entre hadrons. En utilisant cette méthode, il est possible de distinguer les hadrons issus de la fragmentation d'un parton (créé lors d'un processus dur entre deux partons) des hadrons émergeant du *bulk*. Les premiers sont sélectionnés en associant leur émission à celle d'une particule chargée de haut p_{T} (appelée particule *trigger*). Cette particule est supposée faire partie d'un jet de hadrons provenant de la fragmentation d'un parton. La direction d'émission de ces hadrons associés à une particule *trigger* doit donc se trouver dans une fenêtre en angle azimutal et en pseudorapidité autour de la direction d'émission de la particule *trigger*. Les hadrons que l'on définit comme provenant du *bulk* doivent quant à eux avoir une direction d'émission bien en dehors de la zone d'émission de la particule de haut p_{T}.

Ce travail de thèse se fonde sur l'analyse de données de collisions Pb–Pb délivrées par le LHC à une énergie de $\sqrt{s_{\mathrm{NN}}} = 2.76$ TeV et enregistrées par l'expérience ALICE (A Large Ion Collider Experiment) en 2011. Les distributions des corrélations di-hadrons sont obtenues avec, comme *trigger*, des particules chargées primaires de $5 < p_{\mathrm{T}} < 10$ GeV/c et comme particules associées les hadrons étranges Λ et $\mathrm{K}^0_{\mathrm{S}}$ dans le domaine $2 < p_{\mathrm{T}} < 7$ GeV/c. Pour établir le rapport baryon/méson, le choix s'est porté sur les Λ et $\mathrm{K}^0_{\mathrm{S}}$ car ils peuvent être mesurés sur un vaste domaine de p_{T} en n'utilisant qu'une seule méthode fondée sur la reconstruction topologique de leur désintégration faible. Les résultats, relatifs au *bulk* et à la production par fragmentation, sont présentés pour deux intervalles en centralité (classes 0-10% et 20-40%). Ils sont ensuite comparés à des mesures inclusives réalisées pour des collisions Pb–Pb et pp dans ALICE ainsi qu'à des résultats de l'expérience CDF pour des jets sélectionnés dans des collisions proton-antiproton.

Corrélation angulaire entre deux hadrons

La méthode de corrélation angulaire entre deux hadrons est une puissante technique pour investiguer la production des hadrons dans différents systèmes de collisions. Pour les collisions d'ions lourds, cette méthode permet aussi de fournir des informations sur les propriétés du milieu dense formé. Dans cette section, nous décrirons les sélections et la procédure utilisée pour construire les distributions de corrélations angulaires en considérant les particules chargées de haut p_{T} comme les particules *trigger* et les hadrons $\mathrm{K}^0_{\mathrm{S}}$ et Λ comme les particules associées. En sélectionnant les particules primaires de haut p_{T}, nous espérons isoler les hadrons produits par fragmentation d'un parton issu d'une interaction dure entre deux partons. La distribution des corrélations angulaires sera extraite à partir des données de collisions Pb–Pb prises durant l'année 2011.

Sélection des événements

Les événements ont été sélectionnés sur la base d'un déclenchement en ligne fondé sur la mesure des particules détectées en coïncidence entre les détecteurs VZERO et SPD (un déclenchement dit de biais minimum (MB)), complété par la présence de signaux dans les deux détecteurs ZDC (MBZ). Pour les données de la campagne de collisions Pb–Pb de 2011, le but était de se focaliser sur les événements de haute multiplicité. Il y avait donc deux déclenchements en ligne dédiés à cela, selon le seuil placé au niveau du VZERO: 0-10% (collisions centrales) et 0-50% (collisions semi-centrales). Voir tableau 3.1. Une sélection hors ligne est également appliquée par la suite, avec les mêmes conditions.

Les événements doivent avoir un vertex primaire ($|z^{trk}_{vtx}|$) situé à moins de 10 cm de distance du centre du détecteur afin de s'assurer d'une acceptance uniforme en pseudorapidité $|\eta| < 1$. De plus, pour les données 2011, il était requis que le vertex primaire reconstruit avec les clusters des deux couches internes de l'ITS (SPD) (z^{SPD}_{vtx}) ne soit pas éloigné de plus de 0.5 cm du vertex primaire reconstruit au moyen des traces, i.e., $|z^{trk}_{vtx} - z^{\mathrm{SPD}}_{vtx}| < 0.5$ cm, afin d'éviter les biais potentiels pouvant être causés par un empilement de vertex en raison de l'accroissement de la luminosité de 0.03×10^{27} cm^{-2}s^{-1} dans le run 2010 à 0.5×10^{27} cm^{-2}s^{-1} dans le run 2011.

Le nombre total d'événements était de 14×10^6 pour les données 2010 et de 25×10^6 pour les données 2011 dans le domaine de centralité 0-40%. La centralité de la collision était déterminée par le VZERO et les calorimètres à zéro degré (ZDC) [155].

Sélection des particules *trigger* ($h^{\pm}$)

L'étude des corrélations angulaires présentée dans ce travail est effectuée en utilisant les particules chargées primaires de haut p_{T} comme particules *trigger*. La sélection des traces des particules *trigger* est effectuée suivant les critères énumérés dans la seconde colonne du tableau 3.3. Les traces sélectionnées sont communément appelés traces hybrides car différentes qualités de traces sont combinées afin de s'assurer de l'uniformité de la région $(\varphi - \eta)$ dans les zones où des détecteurs du SPD étaient inopérationnels. Parmi les conditions nécessaires pour garder une bonne qualité de trace, nous exigeons que la trace contienne au moins un cluster dans le SPD. D'un point de vue cinématique, les particules chargées primaires sont sélectionnées dans le domaine d'impulsion transverse compris entre 5 et 10 GeV/c et l'intervalle de pseudo-rapidité entre ± 0.7 afin de maintenir une couverture uniforme de l'acceptance du détecteur.

Sélection des particules associées ($\mathrm{K}^0_{\mathrm{S}}$ and Λ)

Les hadrons étranges et neutres $\mathrm{K}^0_{\mathrm{S}}$ et Λ sont connus sous le nom de particules "V0" car le plus grand rapport d'embranchement de leur désintégration correspond à l'émission de particules filles dont l'une est négative et l'autre positive, laissant une empreinte en forme de V dans le détecteur. Dans la suite nous utiliserons donc ce vocabulaire pour nommer ces hadrons.

Dans ALICE, les particules V0 sont reconstruites grâce à la topologie de leur désintégration faible $\mathrm{K}^0_{\mathrm{S}} \to \pi^+\pi^-$ et $\Lambda \to \mathrm{p}\pi^-$. Après que deux traces correspondant à des charges électriques opposées aient été sélectionnées dans la TPC, on calcule la distance de plus courte approche (DCA) entre ces traces, déterminant ainsi le lieu de désintégration du candidat V0. Les combinaisons de paires de traces dont la DCA est supérieure à un seuil fixé sont rejetées. D'autres sélections sont appliquées aux candidats V0. Les informations concernant chaque particule fille sont propagées jusqu'au vertex primaire de la collision. On peut ainsi rejeter les particules filles candidates qui ont une trop faible distance de plus courte approche par rapport au vertex principal, évitant ainsi de confondre des particules secondaires avec des particules primaires. En utilisant l'information sur les composants de l'impulsion des particules filles candidates et les lois de conservation de l'énergie et de l'impulsion, on peut reconstruire l'impulsion et la masse invariante du candidat V0. Afin d'être certain de ne garder que des V0 provenant du vertex primaire de la collision, on s'assure que la direction du vecteur impulsion du V0 pointe vers le vertex primaire en appliquant une coupure sur le cosinus de l'angle de "pointage" ($\cos(\theta_p)$). Une représentation graphique de la désintégration d'un $\mathrm{K}^0_{\mathrm{S}}$ est représenté sur la figure 3.11.

L'avantage d'utiliser ces particules étranges pour notre étude réside dans le fait que l'on peut appliquer la même technique d'identification à la fois pour les $\mathrm{K}^0_{\mathrm{S}}$ et pour les Λ, et ce sur un vaste domaine d'impulsion transverse: de 0.4 GeV/c (0.6 GeV/c pour les Λ) jusqu'à 12 GeV/c les collisions Pb–Pb dans ALICE. Ceci permet d'avoir un contrôle optimisé des incertitudes systématiques.

Les coupures par défaut utilisées pour la sélection des particules filles et des candidats V0 sont énumérées dans le tableau 3.6. Une sélection fondée sur les variables de Armenteros-Podolanski a été également appliquée mais uniquement pour la mesure des $\mathrm{K}^0_{\mathrm{S}}$ afin d'éviter le bruit de fond des

Λ et anti-Λ dans le spectre de masse invariante des K^0_S. Les variables de Armenteros-Podolanski, p_T^{arm} et α^{arm}, sont fondées sur les propriétés élémentaires des désintégration à deux corps. Ici, p_T^{arm} est la projection de l'impulsion de la particule fille positive (respectivement négative) sur le plan perpendiculaire à l'impulsion du V0, et $\alpha^{arm} = (p_{\parallel}^{+} - p_{\parallel}^{-})/(p_{\parallel}^{+} + p_{\parallel}^{-})$, où $p_{\parallel}^{+}$ $(p_{\parallel}^{-})$ est la projection de l'impulsion positive (respectivement négative) de la particule fille sur l'impulsion du V0. Pour sélectionner les K^0_S, la condition $p_T^{arm} > 0.2|\alpha^{arm}|$ est nécessaire (voir figure 3.13). La position dans le plan transverse, r_T, du vertex secondaire reconstruit doit se situer dans un volume fiduciaire limité par un rayon entre 5 et 100 cm. La valeur basse est choisie pour minimiser les effets systématiques introduits par les corrections d'efficacité. Pour réduire encore d'avantage le bruit de fond, une condition sur la longueur de vol du V0 dans le plan transverse a été introduite.

Les distributions de corrélations angulaires à deux hadrons ont été obtenues pour les K^0_S et les Λ pour des impulsions transverses dans le domaine 2-7 GeV/c, c'est-à-dire la région dans laquelle a été observé l'accroissement du rapport baryon/méson dans les données inclusives Pb–Pb.

Évaluation du facteur "Efficacité×Acceptance×B.R." des candidats V0

L'efficacité de reconstruction des particules K^0_S et Λ a été étudiée à l'aide de simulations Monte Carlo, en utilisant le générateur d'événements HIJING et le code GEANT 3. Elle a été évaluée comme le rapport défini par l'équation *R1*. Le dénominateur correspond au nombre total des hadrons générés dans le Monte Carlo avec une pseudo-rapidité comprise entre -0.7 et $+0.7$. Les baryons Λ produits par la désintégration des Σ^0 ont été considérés, dans cette simulation, comme des particules primaires. Le numérateur de l'équation *R1* est le nombre de particules reconstruites satisfaisant aux coupures de sélection, nécessaires pour réduire le bruit de fond combinatoire, et dont l'identité correspond à celle de la particule générée dans le Monte Carlo. Les résultats obtenus montrent une dépendance du facteur eff × Accep. × B.R. en fonction de la pseudo-rapidité de la particule, qui est plus prononcée pour des valeurs élevées de $|\eta|$ et à des impulsions transverses en-dessous de 4 GeV/c (voir figure 3.20).

$$\text{eff} \times \text{Accep.} \times \text{B.R.}\ (p_T) \;=\; \frac{\text{particules associées MC}\ (p_T \mid |\eta_{Gen}| < 0.7)}{\text{particules générées MC}\ (p_T \mid |\eta_{Gen}| < 0.7)}. \qquad (R1)$$

Notons qu'une sélection en masse invariante de $\pm 4\sigma$ a été considérée pour l'obtention du numérateur de l'équation *R1*, comme cela a été le cas pour l'extraction du signal dans les données expérimentales. Les valeurs de σ proviennent de l'ajustement des distributions en masse invariante.

Contribution due à la désintégration des hypérons Ξ en particules Λ (feed-down)

Les désintégrations des hypérons multi-étranges Ξ et Ω contribuent à la production des baryons Λ. Une fraction des Λ produits via ces désintégrations survit aux coupures topologiques utilisées dans l'analyse pour sélectionner les particules Λ primaires. Il est donc important de corriger les taux de production bruts des Λ de la contribution due aux désintégrations des Ξ et des Ω, appelée contribution de feed-down.

Une estimation de la contribution des Λ de feed-down provenant des hypérons Ξ^- et Ξ^0 est présentée dans [117]. Les résultats montrent que la contribution de feed-down est d'environ $\sim 25\%$ à $p_{\mathrm{T}}^{\Lambda} \sim 1$ GeV/c et elle décroît jusqu'à $\sim 10\%$ à haut p_{T}, avec une incertitude estimée à 5% sur tout le domaine en p_{T}. De plus, il a été constaté que cette contribution de feed-down est indépendante de la centralité de la collision. Notons que la contribution de feed-down provenant des désintégrations des Ω est negligeable, en raison des taux de production relativement faibles de ces hadrons.

Construction des corrélations angulaires $h^{\pm}$-V0

Les corrélations angulaires $h^{\pm}$-V0 sont extraites pour deux classes de centralité (0–10%, 20–40%), et dans huit différents intervalles en impulsion transverse des hadrons associées. Pour un intervalle donné en position du vertex primaire, de 2 cm de largeur, les corrélations angulaires brutes, en angle azimutal et en pseudo-rapidité, entre les particules *trigger* et les candidats V0 sont construites comme suit (voir figure 3.22) :

$$\Delta\varphi = \varphi_{\mathrm{Trig}} - \varphi_{\mathrm{Assoc}} \text{ and } \Delta\eta = \eta_{\mathrm{Trig}} - \eta_{\mathrm{Assoc}}.$$

Les corrélations angulaires brutes sont corrigées en appliquant les deux facteurs suivants :

1. Un facteur de pondération pour tenir compte de la non-uniformité de l'intervalle en centralité 9-10%.

2. L'efficacité de reconstruction (eff × Accep × B.R.) en fonction de la pseudo-rapidité et de l'impulsion transverse, comme cela est visible sur la figure 3.20. Afin d'éviter les effets de fluctuations en η, l'efficacité intégrée en η a été utilisée dans le domaine où celle-ci est à peu près constante.

Correction des effets d'acceptance de paires de particules à l'aide de la méthode de mélange des événements. Une fois les particules *trigger* et les hadrons associés sélectionnés, une correction est appliquée aux distributions bidimensionnelles (φ, η) des corrélations angulaires pour tenir compte des pertes de paires "*trigger* - particule associée" dues à l'acceptance limitée du détecteur. Ces pertes se produisent, par exemple, lorsque les particules finales (particules *trigger* ou particules filles des V0) traversent les bords des secteurs de la TPC ou se retrouvent, simplement, en dehors de l'acceptance du détecteur ($|\eta| > 0.8$). Dans les deux cas, les particules ne peuvent alors être reconstruites.

La correction des effets d'acceptance de paires de particules est appliquée en utilisant la technique dite de mélange des événements. Ceci est effectué pour les différents intervalles (mentionnés précédemment) en centralité, en position du vertex primaire et en impusion transverse des particules associées. Pour construire les distributions correspondant au mélange des événements, l'écart, en φ et en η, entre les particules *trigger* et les candidats V0 provenant de deux événements différents (ev_1 and ev_2) est calculé comme suit :

$$\Delta\varphi_{\mathrm{ME}} = \varphi_{\mathrm{Trig}}|_{\mathrm{ev}_1} - \varphi_{\mathrm{Assoc}}|_{\mathrm{ev}_2} \text{ and } \Delta\eta_{\mathrm{ME}} = \eta_{\mathrm{Trig}}|_{\mathrm{ev}_1} - \eta_{\mathrm{Assoc}}|_{\mathrm{ev}_2}.$$

Les événements ev_1 and ev_2 appartiennent au même intervalle en centralité et en position du vertex primaire, afin de s'assurer que l'acceptance du détecteur est similaire pour les deux événements.

Pour corriger les distributions angulaires brutes, les distributions obtenues avec la technique de mélange des événements sont normalisées à 1 en appliquant le facteur $N_0 \approx \mathrm{d}^2N_{\mathrm{ME}}/\mathrm{d}\Delta\varphi\mathrm{d}\Delta\eta(0,0|z_{\mathrm{vtx,i}})$.

Extraction du signal. Les candidats $\mathrm{K}^0_{\mathrm{S}}$ et Λ comprenant un important bruit de fond combinatoire, leur signal est extrait pour chaque bin $(\Delta\varphi, \Delta\eta)$.

Nous utilisons une procédure d'ajustement en deux étapes. Un premier ajustement est réalisé pour décrire la distribution en masse invariante comme la somme d'une gaussienne et d'un polynôme d'ordre n (avec $n = 0, 1, 2$). Ce dernier représente le bruit de fond combinatoire dans un domaine restreint autour de la masse du pic correspondant au signal. Le second ajustement est effectué uniquement pour le bruit de fond combinatoire, dans une région excluant le signal, afin d'améliorer la description du polynôme d'ordre n.

Le signal est ensuite extrait en additionant les contenus de chaque bin de l'histogramme de la masse invariante dans une région de $\pm 4\sigma_{\mathrm{fit}}$ autour de la valeur nominale de la masse de la particule reconstruite. En parallèle, nous estimons la quantité de bruit de fond combinatoire sous le pic du signal dans le même domaine de $\pm 4\sigma_{\mathrm{fit}}$. La contribution du bruit de fond ainsi obtenue est soustraite, bin par bin, de l'histogramme pour extraire le signal.

Enfin, la fonction de corrélation est normalisée au nombre total de particules *trigger* N_{Trig} utilisé pour chaque classe de centralité.

Taux de production par *trigger* : pour le *bulk* et pour le pic à proximité du *trigger*

Après avoir introduit tous les éléments nécessaires à l'établissement de corrélations angulaires à deux hadrons, il est désormais possible d'étudier la production de baryons relativement aux mésons. Cela sera évalué dans des régions de $\Delta\varphi, \Delta\eta$ où les mécanismes dominants sont tantôt la fragmentation de parton tantôt les effets de *bulk*.

Taux de production par *trigger* dans le *bulk*

À partir de la distribution complètement corrigée de corrélations $h^{\pm}$–V0, la production de particules V0 décorrélées de la particule *trigger* est estimée dans plusieurs régions $\Delta\varphi, \Delta\eta$ caractéristiques de ce que l'on appelle le *bulk*. Le *bulk* fait référence à ce qui constitue la partie majeure du système formé à la collision et par conséquence, à la population de particules dominante issue de celle-ci. On l'associe aux hadrons et effets produits dans des interactions qui ne sont pas reliées aux diffusions dures de partons (i.e. exclusion faite des jets). Les mécanismes d'hadronisation de la matière contenue dans le *bulk* suppose, comme possibilité naturelle, la coalescence de partons. A cela s'ajoute le fait que le *bulk* est sensible aux effets de flot issus du milieu thermalisé en expansion mais également aux effets des fluctuations de l'état initial; les pertes d'énergie des partons, quant à elles, dues à l'interaction avec le milieu, qu'il s'agisse de radiations de gluons ou de collisions élastiques, peuvent également être considérées comme parties prenantes du *bulk*.

Le taux de production ramené au nombre de *triggers*, dans la région dénommée "Bulk I", est extrait par intégration de la distribution $\Delta\varphi, \Delta\eta$ dans les limites suivantes :

(taux de production *in* Bulk I)

$$\begin{aligned}\frac{1}{N_{\mathrm{Trig}}}\frac{\mathrm{d}N^{\text{Bulk I}}}{\mathrm{d}p_{\mathrm{T}}} &= \int_{\Delta\eta=-1.0}^{\Delta\eta=-0.7}\int_{\Delta\varphi=-0.94}^{\Delta\varphi=0.94}\frac{1}{N_{\mathrm{Trig}}}\frac{\mathrm{d}^3N}{\mathrm{d}p_{\mathrm{T}}\,\mathrm{d}\Delta\varphi\,\mathrm{d}\Delta\eta}\,\mathrm{d}\Delta\varphi\,\mathrm{d}\Delta\eta \\ &+ \int_{\Delta\eta=0.7}^{\Delta\eta=1.0}\int_{\Delta\varphi=-0.94}^{\Delta\varphi=0.94}\frac{1}{N_{\mathrm{Trig}}}\frac{\mathrm{d}^3N}{\mathrm{d}p_{\mathrm{T}}\,\mathrm{d}\Delta\varphi\,\mathrm{d}\Delta\eta}\,\mathrm{d}\Delta\varphi\,\mathrm{d}\Delta\eta.\end{aligned}$$

Pour cette région *bulk I*, la contribution aux corrélations suivant $\Delta\varphi$ du flot elliptique et des harmoniques d'ordre supérieur est la plus importante.

Les résultats obtenus avec les données ALICE pour les taux de production par *trigger* des mésons K^0_S associés à la région *bulk I* sont illustrés avec la figure 4.1, pour deux intervalles en centralité des collisions Pb–Pb, 0-10% et 20-40%. Les incertitudes statistiques sont affichées comme des barres verticales, les incertitudes systématiques non-corrélées d'un intervalle de p_T à l'autre sont matérialisées par des rectangles vides et les incertitudes systématiques (partiellement) corrélées sont représentées par des rectangles colorés. Les résultats équivalents obtenus pour les Λ du *bulk I* sont donnés avec la figure 4.2, pour les mêmes intervalles 0-10% et 20-40%. Dans la présente analyse, l'hypothèse est faite que la population dans le *bulk* de Λ issus des $\Xi^{0,-}$ (*feed-down*) suit les mêmes proportions que ce qui est observé pour la production *inclusive*. Par conséquent, ce sont les mêmes facteurs de correction, tirés de l'analyse inclusive [117] qui sont appliqués ici pour le signal tiré de la région *bulk I*.

Taux de production par *trigger* dans le pic *near-side*

Les techniques de corrélations angulaires ont été fréquemment utilisées pour estimer la production hadronique associée, en principe, à des diffusions dures entre partons. Ce type de production se manifeste par une population de particules émises à proximité de la particule *trigger*, au voisinage de $\Delta\eta \approx 0$ et $\Delta\varphi \approx 0$. La structure résultante, proche de la particule *trigger*, sur la distribution de particules corrélées est connue sous la dénomination de pic *near-side*. En plus de ce pic, une structure caractéristique peut également ressortir à $\Delta\varphi \approx \pi$ (pic *away-side* de corrélations), structure créée par des partons s'échappant du système avec une moindre énergie et modulée par les effets du flot elliptique et des harmoniques d'ordre supérieur. Cependant, il a été observé, aux énergies du RHIC, que le pic *away-side* disparaît dans les collisions Au–Au les plus centrales [152] et que ce pic est de moindre amplitude pour les collisions d-Au, par comparaison aux collisions proton-proton [161, 162].

Afin d'évaluer la production associée à des particules de haut p_T, on doit s'appuyer sur l'hypothèse d'une factorisation possible entre les effets de *bulk* (essentiellement liés au flot) et la production de hadrons à partir de fragmentation de partons, ce qui revient à avancer l'indépendance entre ces deux types de processus. Dès lors, le taux de production par *trigger* associé à la fragmentation rapide de partons peut être obtenu en projetant la distribution 2D de corrélations angulaires à deux hadrons sur : i) la dimension $\Delta\eta$ ou ii) la dimension $\Delta\varphi$. Dans chaque cas de figure, le profil de flot est différent et, par voie de conséquence, la soustraction correspondante des effets du flot sera également différente. Dans la suite, seule la projection sur $\Delta\varphi$ sera explorée. La projection suivant cet axe nous permet en effet d'extraire le taux de production rattaché au pic *near-side* avec un meilleur contrôle des incertitudes systématiques.

Projection sur l'axe $\Delta\varphi$

La distribution des corrélations suivant $\Delta\varphi$ est dérivée pour une certaine plage de valeurs de $\Delta\eta$: conformément aux études précédentes relatives aux projections sur $\Delta\eta$ (voir sous-section 4.2.1), la projection sur le plan $\Delta\varphi$ est limitée à l'intervalle $|\Delta\eta|<0.4$. La projection sur $\Delta\varphi$ peut ainsi être exprimée comme suit :

$$\frac{1}{N_{\text{Trig}}}\frac{\mathrm{d}N}{\mathrm{d}\Delta\varphi} = \int_{-0.4}^{0.4}\frac{1}{N_{\text{Trig}}}\frac{\mathrm{d}^2N}{\mathrm{d}\Delta\varphi\,\mathrm{d}\Delta\eta}\,\mathrm{d}\Delta\eta \qquad (R2)$$

Pour décrire l'ensemble de la distribution $\Delta\varphi$, la production par fragmentation est assimilée à une fonction gaussienne, qui se superpose à un bruit de fond de paires $h^{\pm}$-V0, pour partie décorrélées (piédestal), et pour partie corrélées par l'entremise du flot (elliptique, triangulaire, ...). Une telle formulation prend alors la forme suivante :

$$\frac{1}{N_{\mathrm{Trig}}}\frac{\mathrm{d}N}{\mathrm{d}\Delta\varphi} = A^{\Delta\varphi}\frac{1}{\sqrt{2\pi}\sigma_{\Delta\varphi}}\exp\left[\frac{-0.5\,\Delta\varphi^2}{\sigma^2_{\Delta\varphi}}\right] + \beta\left\{1+\sum_{n=2}^{\infty} 2 < v_n^{\mathrm{Trig}} >< v_n^{\mathrm{Assoc}} > \cos(n\Delta\varphi)\right\} \qquad (R3)$$

Comme mentionné précédemment, le profil de flot anisotrope est caractéristique de la projection suivant $\Delta\varphi$. Ce profil est incarné par le second terme de l'expression *R3*. Il représente la nature du flot relié à l'anisotropie globale de la géométrie initiale de collision, et varie avec $\Delta\varphi$ (voir la sous-section 1.6.3) [166, 167, 168]. Le facteur β est introduit pour aligner la modulation du flot anisotrope sur le point le plus bas de la distribution angulaire suivant $\Delta\varphi$. Pour les corrélations $h^{\pm}$-V0, la principale composante du flot anisotrope provient du flot elliptique de chaque particule mise en jeu, $< v_2^{\mathrm{Trig}} >$ et $< v_2^{\mathrm{Assoc}} >$. Les magnitudes respectives de ces deux termes sont issues d'analyses ALICE indépendantes. Le terme v_2 pour les particules chargées est extrait par la méthode dite du "plan de l'événement" [105, 107], tandis que le terme pour les particules identifiées l'est à partir de la méthode dite du "produit scalaire" [112]. Dans l'intervalle de centralité 0-5%, les valeurs de flot elliptique s'étendent approximativement de 0.03 à 0.07 unités de v_2 pour les particules chargées primaires dans la plage $5 < p_{\mathrm{T}} < 10$ GeV/c, et de 0.02 (0.04) à 0.07 (0.09) unités dans le cas $\mathrm{K}^0_{\mathrm{S}}$ (Λ) sur la plage de p_{T} allant de 2 à 7 GeV/c (voir figures 1.8 et 1.9). Les harmoniques d'ordre supérieur, v_n avec $n \geq 3$, ne sont pas considérées ici, en raison de l'absence de mesures expérimentales existantes pour les $\mathrm{K}^0_{\mathrm{S}}$ et Λ.

Pour s'affranchir du flot anisotrope dans la distribution de corrélations angulaires suivant $\Delta\varphi$, on doit dans un premier temps ajuster les distributions[1] avec l'expression mathématique *R3* afin d'estimer le niveau de bruit de fond. À la réalisation de l'ajustement, les paramètres $< v_2^{\mathrm{Trig}} >$ et $< v_2^{\mathrm{Assoc}} >$ sont considérés comme des paramètres fixes; la valeur moyenne de la fonction gaussienne est établie à 0. Les paramètres laissés libres lors de l'ajustement sont : $A^{\Delta\varphi}$, $\sigma_{\Delta\varphi}$ et le facteur d'échelle β. Un exemple d'ajustement obtenu pour les $\mathrm{K}^0_{\mathrm{S}}$ sur un intervalle de p_{T} de 3 à 3.5 GeV/c est montré sur la figure 4.7, où le flot anisotrope résultant est représenté par une ligne rouge. Les valeurs du flot elliptique pour les autres intervalles en p_{T} de la centralité 0-10% sont disponibles en annexes, voir *D* et *E* pour les $\mathrm{K}^0_{\mathrm{S}}$ et Λ, respectivement.

Une fois le paramètre β obtenu, la contribution du flot elliptique est soustraite à la distribution angulaire puis on intègre le signal restant dans les limites $|\Delta\varphi| < 0.94$ comme indiqué dans

[1] À cette étape de l'analyse, la projection suivant $\Delta\varphi$ n'est pas encore normalisée au nombre de particules *trigger* et cela, pour éviter tout conflit pendant la procédure d'ajustement, en raison des petites quantités qu'il faudrait alors gérer.

l'expression suivante :

$$\frac{1}{N_{\mathrm{Trig}}}\frac{\mathrm{d}N^{\Delta\varphi}}{\mathrm{d}p_{\mathrm{T}}} = \frac{1}{N_{Trig}}\int_{-0.94}^{0.94}\frac{\mathrm{d}}{\mathrm{d}p_{\mathrm{T}}}\left\{\frac{\mathrm{d}N}{\mathrm{d}\Delta\varphi} - \beta\left\{1 + 2 < v_2^{Trig} >< v_2^{\mathrm{Assoc}} > \cos(2\Delta\varphi)\right\}\right\}\mathrm{d}\Delta\varphi. \tag{R4}$$

Les taux de production par *trigger* des $\mathrm{K}^0_{\mathrm{S}}$ et Λ dérivés à partir de cette technique sont rassemblés sur la figure 4.8, pour des centralités allant de 0 à 10% dans les collisions Pb–Pb de la période de données de 2011. Une remarque importante mérite d'être soulignée : comme précédemment pour l'évaluation de la production associée au *bulk*, les taux de production de Λ doivent être corrigés pour retirer les contributions des désintégrations de Ξ. Cependant, les corrections en *feed-down* demeurent encore indéterminées pour les Λ secondaires venant de Ξ issus eux-mêmes directement de la fragmentation de partons dans les collisions Pb–Pb. Par conséquent, dans ce travail, l'hypothèse par défaut est faite que la contamination en *feed-down* des Λ du pic *near-side* est de même magnitude que la contamination évaluée pour les Λ inclusifs. Il en découle une application des mêmes facteurs de corrections que ceux retenus pour la production de *bulk*.

Études systématiques

Une partie significative de travail mis en œuvre pour cette analyse expérimentale a consisté en l'estimation des incertitudes systématiques. Les études associées sont regroupées en trois ensembles indépendants, fonctions de la nature de la sélection étudiée.

Groupe 1 Sélection d'événements

Groupe 2 Technique de corrélations angulaires

Groupe 3 Reconstruction de particules V0

Les éléments de chaque groupe sont considérés comme des sources d'incertitudes indépendantes des sources de tout autre groupe.

Vue d'ensemble des principes suivis pour la détermination des incertitudes systématiques

Systématiques non-corrélées

Pour les groupes 1 et 2, les sélections sont systématiquement variées suivant les valeurs présentées respectivement dans les tableaux 4.1 et 4.2. Ces tableaux fournissent une première idée des sources potentielles d'incertitudes systématiques qui ont été retenues et testées. Dans le cas du groupe 3, les jeux de valeurs correspondant aux coupures topologiques sont établis suivant une variation de -10% de la valeur par défaut du signal brut de V0 reconstruit. Les valeurs des variations systématiques à appliquer sont ainsi évaluées séparément pour les $\mathrm{K}^0_{\mathrm{S}}$ et Λ, en considérant le signal brut intégré dans l'intervalle de p_{T} allant de 2 to 7 GeV/c. De plus amples informations vis-à-vis des variables à considérer pour les études systématiques rattachées à la reconstruction de V0 (sélections cinématiques et topologiques) sont disponibles dans le Table 4.3. Les valeurs numériques retenues pour les variations y sont également répertoriées.

Systématiques partiellement corrélées en p_{T} et en espèce

Parmi les sources d'incertitudes systématiques envisagées, une source partiellement corrélée a été identifiée. Il s'agit des facteurs de pondération associés au lissage en centralité (voir section 3.5); cela conduit en effet à une corrélation (partielle) entre les espèces V0, $\mathrm{K}^0_{\mathrm{S}}$ et Λ, mais aussi entre intervalles de p_{T} pour chaque espèce donnée. L'étude systématique qui en découle n'a été menée que pour les collisions centrales 0-10%, c'est-à-dire seulement là où le lissage en centralité était nécessaire.

Critères pour déterminer et combiner les incertitudes systématiques non-corrélées

L'évaluation des incertitudes systématiques est établie en appliquant différents critères pour chaque groupe.

Groupe 1 L'incertitude systématique totale dans ce groupe (σ_{G1}) est calculée comme la somme quadratique de chaque déviation individuelle.

Group 2 L'incertitude systématique totale à rattacher aux techniques de corrélations angulaires (σ_{G2}) est dérivée en appliquant différents critères, suivant que l'on considère les résultats du *bulk* ou du pic *near-side*. Pour le *bulk*, σ_{G2} est obtenue, comme pour le Groupe 1, par une somme quadratique des déviations individuelles. Dans le cas du pic *near-side*, σ_{G2} est évalué, pour chaque intervalle en p_{T}, comme la déviation maximale en valeur absolue parmi tous les éléments de groupe.

Groupe 3 En ce qui concerne la reconstruction des particules V0, il est décidé de prendre là aussi, pour chaque *bin* de p_{T}, la déviation maximale en valeur absolue parmi les sélections topologiques. Ce choix pour établir l'incertitude systématique σ_{G3} est retenu à la fois pour la production du *bulk* et celle de pic *near-side*.

L'incertitude systématique totale, fonction de l'impulsion de la particule associée $p_{\mathrm{T}}(\mathrm{V0})$, est calculée comme la somme quadratique des contributions individuelles des groupes, en raison de l'indépendance 2 à 2 entre groupes prise comme hypothèse.

$$\sigma_{\mathrm{Tot}}(p_{\mathrm{T}}) = \sqrt{\sigma^2_{\mathrm{G1}}(p_{\mathrm{T}}) + \sigma^2_{\mathrm{G2}}(p_{\mathrm{T}}) + \sigma^2_{\mathrm{G3}}(p_{\mathrm{T}}) + \sigma^2_{\mathrm{Mat.Budget}} + \sigma^2_{\mathrm{FD}}}$$

Dans l'expression ci-dessus, le terme σ^2_{FD} n'entre en ligne de compte que dans le cas des taux de production de Λ et dans celui du rapport baryon sur méson. Les incertitudes liées au budget de matière et celles attribuables aux corrections en *feed-down* des Λ sont respectivement tirées des publications ALICE [169] et [117].

Un résumé des incertitudes systématiques évaluées est présenté dans les tableaux synoptiques 4.5 et 4.6, pour les résultats du *bulk* et du pic *near-side*, respectivement.

Λ/K^0_S: dans les processus durs et *soft*

L'objectif premier de cette étude est non seulement de distinguer les différents modes de production de hadrons en fonction du processus initial mais aussi de comprendre l'origine de l'augmentation du rapport baryon sur méson dans les collisions centrales d'ions lourds. Et plus particulièrement, il s'agit ici de relier le rapport Λ/K^0_S à la fragmentation de parton en tant que mécanisme de hadronisation dans les collisions Pb–Pb aux énergies du LHC.

La figure 5.4 permet de constater que le rapport inclusif Λ/K^0_S, mesuré avec ALICE lors de collisions Pb–Pb collisions à $\sqrt{s_{NN}} = 2.76$ TeV, est plus élevé que celui extrait pour des collisions pp et augmente avec la centralité [117]. Cette observation suggère que le phénomène soit intimement lié aux effets collectifs associés au QGP, et par conséquent absent lors de collisions pp. Afin de vérifier cette hypothèse et de voir si d'autres effets, tels que la modification dans le milieu de processus durs, sont également à l'œuvre, les résultats provenant de notre analyse, et fondés sur les corrélations angulaires entre deux hadrons, sont superposés et leur allure peut ainsi être comparée aux mesures inclusives.

Nos résultats reportés pour deux intervalles en centralité et associés à la région dénotée *bulk I* présentent un comportement similaire à celui du rapport inclusif des collisions Pb–Pb: l'augmentation atteint la même valeur maximale pour un p_T identique puis décroît de la même façon. De plus, on peut observer sans la moindre ambiguité que le rapport extrait pour la région *bulk I* possède une amplitude plus importante sur l'ensemble de l'intervalle en p_T que celui obtenu pour des hadrons associés à la fragmentation de partons, ce dernier étant très proche des résultats inclusifs pour des collisions pp. La différence entre les rapports de type *bulk* et ceux proches du pic est très largement visible compte tenu des incertitudes expérimentales et même lorsque les corrections en "feed-down" associées aux taux de production des Λ sont incluses. Ceci permet de conclure que l'augmentation du rapport baryon sur méson observée pour les collisions d'ions lourds provient de la nature collective du système au moment de la hadronisation et de sa dynamique d'expansion.

La suite de la discussion relative au *bulk*, figures 4.10 et 4.11 du chapitre 4 se fonde sur le double rapport Λ/K^0_S des régions dénotés *bulk I* et *bulk III* puis *bulk II* et *bulk III* respectivement pour les collisions Pb–Pb centrales et semi-périphériques. Les rapports ainsi obtenus sont compatibles avec l'unité pour les deux intervalles en centralité. Ceci signifie que les similitudes avec les résultats inclusifs d'ALICE subsistent indépendamment de la région de l'espace des phases échantillonnée pour le *bulk*.

Si l'on considère à nouveau la comparaison entre le rapport $\Lambda/\mathrm{K}^0_\mathrm{S}$ associé à la fragmentation de parton dans les collisions Pb–Pb centrales et celui obtenu pour des collisions pp à $\sqrt{s} = 7$ TeV, présentés avec la figure 5.4, on constate que nos résultats sont légèrement supérieurs aux mesures pp inclusives. Une telle différence, qui reste cependant compatible avec les incertitudes systématiques, peut potentiellement être imputée à trois éléments: i) la composante triangulaire du flot ne peut encore être soustraite des taux de production proches du pic avec suffisamment de précision, ce qui semble plus altérer les baryons que les mésons [106, 175]; ii) les valeurs extraites pour le v_2 (ainsi que v_n) peuvent contenir un biais lié aux contributions de "non-flow" et iii) le principe de factorisation du flot [107] est difficilement applicable en raison de la méthode utilisée actuellement pour son estimation. Par ailleurs, le rapport $\Lambda/\mathrm{K}^0_\mathrm{S}$ dans la région proche du pic semble partir d'une valeur plus faible puis augmente jusqu'à un maximum, comme observé pour la région du *bulk*, mais situé cependant à une valeur en p_T plus faible ($p_\mathrm{T} \approx 2.75$ GeV/c) comparativement aux résultats Pb–Pb. Pour le reste de l'intervalle en p_T la décroissance du rapport est globalement équivalente à celle des collisions pp.

Ces différentes observations indiquent qu'il n'y a pas ou peu de modification de la production de hadrons associés aux processus durs en raison de la présence du milieu. Des mesures récentes aux énergies du LHC semblent cependant suggérer que des effets collectifs généralement associés au *bulk* lors de collisions d'ions lourds puisse être présents au sein de collisions pp (pour des multiplicités suffisamment élevées). On peut donc légitimement se poser la question de ce qui constitue une référence adéquate afin d'interpréter nos résultats. Les mesures de la production K^0_S et Λ relatives à la fragmentation de parton, estimées soit grâce aux corrélations angulaires entre deux hadrons, soit au moyen d'une véritable reconstruction des jets, ne sont pas encore disponibles. Il a par conséquent été choisi de comparer, provisoirement, les rapports extraits pour la région proche du pic avec des mesures bénéficiant d'une reconstruction de jets mais au Fermilab, c'est-à-dire pour une énergie dans le centre de masse plus faible.

Les résultats de CDF correspondant au rapport $(\Lambda+\overline{\Lambda})/2\mathrm{K}^0_\mathrm{S}$ mesurés au sein de jets reconstruits pour des collisions $\mathrm{p\overline{p}}$ à $\sqrt{s} = 1.96$ TeV [174] sont inclus dans la figure 5.4. La Collaboration CDF fournit ainsi un rapport $(\Lambda + \overline{\Lambda})/2\mathrm{K}^0_\mathrm{S}$ pour plusieurs intervalles d'énergie transverse (E_T) associée au jet reconstruit. Le second intervalle, correspondant aux jets reconstruits avec une énergie transverse comprise entre 40 et 60 GeV, est représenté par la zone grisée qui prend en compte l'incertitude systématique. Il est important de mentionner de surcroît que l'allure des résultats de CDF dépend pas de E_T pour l'intervalle en p_T présenté ici. On peut remarquer que le rapport $\Lambda/\mathrm{K}^0_\mathrm{S}$ de la région du pic mesuré pour les collisions Pb–Pb est supérieur et approximativement situé à 2σ de celui des jets dans l'intervalle $p_\mathrm{T} = 3$-5 GeV/c. Si une telle différence était amenée à être confirmée aux énergies du LHC une fois la soustraction de la contribution triangulaire du flot au bruit de fond (voir la dernière section du chapitre correspondant) réalisée de manière cohérente, cela constituerait une indication importante de la modification des mécanismes de fragmentation résultant de la présence du milieu. Cette confirmation pourrait être réalisée par ALICE en comparant le rapport $\Lambda/\mathrm{K}^0_\mathrm{S}$ extrait au sein de jets reconstruits pour des collisions pp d'une part et Pb–Pb d'autre part.

Une modélisation des modifications de la fragmentation de parton résultant de la présence du milieu est proposée par Sapeta *et al.* [127]. Les auteurs de ce modèle estiment que l'abondance relative des espèces de hadrons puisse être altérée en raison d'une augmentation de la probabilité d'embranchement des partons, ce qui affecte la distribution en masse invariante de ces partons en fin de gerbe. Ceci induit une augmentation du nombre de hadrons de faible p_{T} comparativement à ce qui se passerait pour des jets fragmentant dans le vide et conduirait à des différences entre les rapports de hadrons mesurés dans le milieu et ceux mesurés dans le vide. De telles conséquences sont visibles avec la figure 5.5 pour le rapport proton sur pion estimé pour des jets affectés par le milieu (ligne pointillée bleue) qui est deux fois plus élevé que ce même rapport estimé pour des jets dans le vide (ligne rouge). Remarquons que cet effet semble être assez significatif, notamment à haut p_{T}. Si l'on considère de nouveau la figure 5.4, la valeur du rapport $\Lambda/\mathrm{K}^0_{\mathrm{S}}$ dans la région du pic et autour de p_{T} 5-7 GeV/c est déjà assez proche de celle extraite au sein des jets reconstruits par CDF, et on peut supposer qu'elle reste constante à plus haut p_{T} contrairement aux prédictions pour le rapport baryon sur méson du modèle de Sapeta *et al.*.

Un autre aspect à explorer relève de l'influence du déclenchement qui dépend de la sélection de la particule pour le rapport $\Lambda/\mathrm{K}^0_{\mathrm{S}}$ proche du pic. Une première vérification a été réalisée en ne sélectionnant que la particule de plus haut p_{T} au sein de l'événement tout en conservant l'intervalle 5–10 GeV/c. La seconde vérification a consisté à ne plus considérer de borne supérieure pour la particule de déclenchement ($p_{\mathrm{T}}^{\mathrm{Trig}} > 5$ GeV/c). Ces deux vérifications ont conduit à des résultats similaires pour le rapport $\Lambda/\mathrm{K}^0_{\mathrm{S}}$ déterminé dans la région proche du pic.

Conclusion

Aujourd'hui, les nombreuses mesures accumulées dans le cadre des expériences d'ions lourds à diverses énergies d'interaction ont permis d'établir que la matière en interaction forte à haute densité d'énergie peut former un état de matière localement thermalisé dont les degrés de liberté sont au niveau des quarks et des gluons et possédant par conséquent des propriétés très différentes de celles de la matière hadronique. Après la phase de découverte puis de caractérisation exploratoire de cet état de la matière, appelé plasma de quarks et de gluons (QGP), nous sommes actuellement entrés dans une nouvelle génération de mesures destinées à des études de plus en plus précises des propriétés du QGP, en particulier de sa dynamique d'expansion et de ses mécanismes de hadronisation.

Parmi les mesures de première génération obtenues au RHIC et au LHC durant les campagnes d'exploration du QGP, l'une des plus troublantes est le comportement du rapport de production entre baryons et mésons en fonction de l'impulsion transverse, en particulier celui du rapport $\Lambda/\mathrm{K}^0_\mathrm{S}$. Pour des collisions centrales Au–Au et Pb–Pb, dans le domaine $2 < p_\mathrm{T} < 6$ GeV/c, cette quantité montre un fort accroissement par rapport à la même mesure dans les collisions pp. L'accroissement diminue lorsque l'on passe des collisions centrales aux collisions périphériques, pour lesquelles il s'apparente à la mesure en pp. On pense donc que ce comportement pourrait être attribué à la nature collective des processus de hadronisation et de l'expansion du QGP, dont le volume est maximal dans les collisions les plus centrales, diminue lorsque les collisions deviennent plus périphériques et finalement disparait pour les collisions pp. Plusieurs modèles, impliquant des processus physiques variés, ont été proposés pour expliquer ces observations expérimentales, qui semblent être le résultat de l'imbrication, à p_T intermédiaire, entre les processus "soft" qui dominent la région des faibles p_T et les processus durs qui prévalent à haut p_T.

Ces interprétations théoriques se fondent sur plusieurs idées complémentaires: i) la possibilité que se manifestent des processus de coalescence (ou recombinaison) au sein du QGP ii) l'influence du flot radial qui reflète le comportement collectif marqué du QGP iii) d'autres effets collectifs au niveau des processus de hadronisation (tels que modélisés par exemple dans EPOS). L'interprétation minimale que l'on peut faire de ces résultats inclusifs de première génération est que l'accroissement à p_T intermédiaire du rapport baryon/méson dans les collisions centrales d'ions lourds est probablement dû à la nature collective du *bulk* mais aucun scénario ni mécanisme physique en particulier n'ont pu être déduits de manière définitive de la comparaison entre les données expérimentales et les modèles.

Afin de pouvoir faire un pas important en avant, une nouvelle génération d'analyses était nécessaire, fondée sur des mesures différentielles dont les objectifs sont les suivants : i) imposer des con-

traintes plus sévères et plus quantitatives aux modèles ii) valider l'hypothèse que l'accroissement du rapport baryon/méson est essentiellement un effet provenant du secteur "soft", c'est-à-dire des hadrons issus du bulk. iii) au contraire, invalider cette hypothèse en mettant en évidence d'autres contributions substantielles à cet accroissement dans le secteur des processurs durs, parmi lesquelles une possible modification des interaction dures parton-parton et de la fragmentation de partons dans le milieu.

L'analyse différentielle réalisée dans ce travail de thèse a consisté à démêler les processus "soft" et les processus durs en évaluant leur contribution respective à la production de Λ et de K^0_S dans les collisions Pb–Pb, au moyen de la méthode des corrélations angulaires di-hadrons. Plus précisément, ce travail a permis de séparer, sur une base statistique, les Λ et K^0_S qui sont émis en association avec des particules de haut p_T ($5 < p_\mathrm{T} < 10$ GeV/c), censées être essentiellement produits à partir d'interaction dures, de ceux émergeant du bulk. Les rapport $\Lambda/\mathrm{K}^0_\mathrm{S}$ correspondant à chacune de ces sources disctinctes ont été extraits en fonction de p_T, pour deux intervalles en centralité (0-10% et 20-40%). Les mesures ont été obtenues à partir des données de collisions Pb–Pb à $\sqrt{s_\mathrm{NN}} = 2.76$ TeV prises durant le run 2011 avec ALICE.

Le principaux résultats peuvent être résumés ainsi: la distribution en p_T du rapport $\Lambda/\mathrm{K}^0_\mathrm{S}$ correspondant au bulk est identique à celui obtenu dans les mesures inclusives en Pb–Pb, et ce pour les deux classes de centralité. À p_T intermédiaire, le rapport $\Lambda/\mathrm{K}^0_\mathrm{S}$ est, sans équivoque, distinct et supérieur à celui associé aux processus durs, ce dernier étant proche (si ce n'est similaire) à celui correspondant aux mesures inclusives en pp. Ainsi, la conclusion de premier niveau est que l'accroissement du rapport baryon/méson observé dans les collisions Pb–Pb est dû essentiellement (si ce n'est totalement) aux effets de bulk, avec une contribution marginale (si ce n'est nulle) des processsus durs, confirmant ainsi les hypothèses dérivées de l'examen des mesures inclusives.

Une discussion de deuxième niveau, impliquant des investigations plus profondes, pourrait être la suivante. Le fait que la distribution en p_T du rapport $\Lambda/\mathrm{K}^0_\mathrm{S}$ associé aux processus durs corresponde (dans la limite des incertitudes expérimentales) au spectre $\Lambda/\mathrm{K}^0_\mathrm{S}$ inclusif extrait des collisions pp à la même énergie, indique, au premier ordre, qu'il n'y a pas de modification de la production de hadrons par processus durs dans le milieu. Mais la question est maintenant de vérifier si le spectre inclusif des collisions pp est réellement la référence correcte pour une telle conclusion. En effet les collisions pp sont également le théâtre d'interactions multi-partoniques, qui constituent ce que l'on nomme l'événement sous-jacent et qui s'apparentent à des modes de hadronisation collective. De plus, les données récentes du LHC suggèrent que des effets de flot collectif du même type que ceux observés dans les collisions Pb–Pb pourraient également se développer dans les collisions pp, mais avec une amplitude bien moindre.

En principe, une référence appropriée devrait être le rapport $\Lambda/\mathrm{K}^0_\mathrm{S}$ correspondant aux particules créées uniquement par interaction dure dans les collisions pp. Ce rapport peut être extrait en utilisant la méthode des corrélations angulaires à deux hadrons (comme dans cette thèse) ou en utilisant une technique consistant à reconstruire au préalable les jets. Malheureusement, ces mesures ne sont pas encore disponibles dans ALICE. Les données pp accumulées durant mars

2011 (environ 24×10^6 événements) et février 2013 (15×10^6 événements) ne représentent probablement pas une statistique suffisante pour extraire les rapports $\Lambda/\mathrm{K}^0_\mathrm{S}$ correspondant aux jets. Si l'on veut répondre à la question de savoir si et comment la présence d'effets collectifs dans une collision pp peut engendrer un accroissement des rapports baryon/méson, il faudra effectuer d'autres études différentielles, consistant à séparer les hadrons provenant de l'événement sous-jacent de ceux produits par interaction dure et ce en fonction de la classe de multiplicité de la collision. On peut en effet intuitivement s'attendre à ce que le rapport baryon/méson le plus élevé se produise pour la classe de multiplicité la plus élevée car celle-ci devrait correspondre aux événements sous-jacents les plus importants.

En raison de l'absence de telles mesures au LHC pour l'instant, nous avons comparé nos résultats à des mesures effectuées par l'expérience CDF en appliquant la méthode de reconstruction des jets pour sélectionner les processus durs dans des collisions proton-antiproton à $\sqrt{s} = 1.96$ TeV. Pour les raisons invoquées précédemment, ceci représente une référence plus adaptée puisque en principe totalement dominée par les processus durs. Dans le domaine de p_T entre 2 et 5 GeV/c, notre mesure du rapport $\Lambda/\mathrm{K}^0_\mathrm{S}$ correspondant aux processus durs est systématiquement plus élevé que celle de CDF. Si cette différence se confirmait après qu'une meilleure soustraction de la contribution du flot aux distributions des corrélations angulaires ait été faite (consistant à prendre en compte les harmoniques triangulaires), elle pourrait alors indiquer qu'il se produit une modification de la fragmentation des partons dans le milieu. Ceci pourrait être corroboré par la comparaison entre nos résultats et les rapports $\Lambda/\mathrm{K}^0_\mathrm{S}$ correspondant aux jets, qui seront bientôt extraits dans les collisions Pb–Pb et pp avec ALICE.

En guise de remarque finale, nous espérons que ces premières mesures différentielles concernant les rapports $\Lambda/\mathrm{K}^0_\mathrm{S}$ susciteront l'intérêt des approches théoriques phénoménologiques telles que celles suivies dans EPOS ou dans les modèles de recombinaison de partons, mais aussi l'intérêt de modèles qui essayeraient de reproduire une possible modification de la fragmentation de partons dans le milieu. Nous avons hâte de voir rapidement de nouvelles courbes théoriques comparées à nos points expérimentaux, montrant soit un bel accord soit de grosses divergences mais qui, dans tous les cas, contribueront, si ce n'est à résoudre le puzzle, au moins à en trouver de nouvelles pièces.

Xitzel SÁNCHEZ CASTRO

Production de mésons K^0_S et de baryons Lambda associés à des hadrons chargés de haut p_T dans les collisions Pb-Pb du LHC à $\sqrt{s_{NN}}$ = 2.76 TeV avec l'expérience ALICE

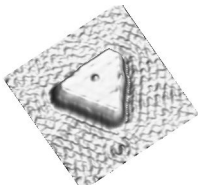

Résumé

Dans les collisions d'ions lourds ultra-relativistes (A-A), la matière se trouve dans des conditions extrêmes de densité d'énergie; elle forme un plasma de quarks et de gluons déconfinés. Aux énergies du RHIC et du LHC, le rapport baryon sur méson, tel Λ/K^0_S, prend des valeurs élevées sur une plage d'impulsions transverses intermédiaires pour les collisions centrales A-A. L'objectif de ce travail est de vérifier si la production accrue de baryons est seulement due à des effets collectifs au cœur du système formé ou s'il existe aussi un impact lié à une fragmentation des partons modifiée par le milieu. À l'aide de corrélations angulaires à deux hadrons, les K^0_S et Λ produits en association avec un hadron de haut p_T (processus durs) sont séparés de ceux issus du milieu thermalisé (processus softs). Les rapports Λ/K^0_S à relier aux mécanismes durs et softs sont établis; les résultats sont obtenus pour les collisions Pb-Pb à $\sqrt{s_{NN}}$ = 2.76 TeV enregistrées en 2011 avec l'expérience ALICE.

Mots clés: collisions d'ions lourds, plasma de quarks et de gluons, ALICE, rapport baryon sur méson, processus durs, fragmentation de partons, milieu thermalisé.

Résumé en anglais

In ultrarelativistic heavy-ion collisions, the QCD matter is under extreme conditions of energy density, forming a quark-gluon plasma (QGP), in which quarks and gluons are deconfined. At RHIC and LHC energies, a large baryon-to-meson ratio, like Λ/K^0_S, was observed within the transverse momentum range $2 < p_T < 6$ GeV/c for central heavy-ion collisions. The goal of this dissertation is to verify if the baryon-to-meson enhancement is only due to collective effects of the bulk of matter, and if there is also a contribution related to in-medium modifications of parton fragmentation.
With two-hadron angular correlations, the K^0_S and Λ produced in association to an energetic hadron (hard processes) are separated from those originated from the thermalised medium (soft processes). The differential Λ/K^0_S ratios related to the soft or hard production processes are extracted. The results are obtained for the Pb-Pb collisions at $\sqrt{s_{NN}}$ = 2.76 TeV recorded in 2011 with the ALICE experiment.

Keywords: heavy-ion collisions, quark-gluon plasma, ALICE, baryon-to-meson ratio, hard processes, parton fragmentation, thermalised medium, bulk